ENERGY LOSSES IN LOW-OFFSET ORGANIC SOLAR CELLS: FROM FUNDAMENTAL UNDERSTANDING TO CHARACTERIZATION CONSIDERATIONS

Kumulative Dissertation

zur Erlangung des akademischen Grades
"doctor rerum naturalium"
(Dr. rer. nat.)
in der Wissenschaftsdisziplin Experimentalphysik

eingereicht an der
Mathematisch-Naturwissenschaftlichen Fakultät
der Universität Potsdam

von

Bowen Sun

Ort und Tag der Disputation: 08.11.2023, Golm-Potsdam, Germany

SUPERVISORS:
Prof. Dr. Safa Shoaee
Prof. Dr. Dieter Neher

REVIEWERS:
Prof. Dr. Safa Shoaee
Prof. Dr. Dieter Neher
Prof. Dr. Jan Anton Koster

Published online on the
Publication Server of the University of Potsdam:
https://doi.org/10.25932/publishup-62143
https://nbn-resolving.org/urn:nbn:de:kobv:517-opus4-621430

日月出矣，而爝火不息

— <庄子·逍遥游>

ABSTRACT

Organic solar cells (OSCs) represent a new generation of solar cells with a range of captivating attributes including low-cost, light-weight, aesthetically pleasing appearance, and flexibility. Different from traditional silicon solar cells, the photon-electron conversion in OSCs is usually accomplished in an active layer formed by blending two kinds of organic molecules with different energy levels together (so-called bulk heterojunction, BHJ). During charge generation, electrons and holes in the photogenerated electron-hole pairs (excitons) are enriched in the electron-receiving (acceptor) and electron-donating (donor) molecules via a so-called charge transfer process, respectively. The energetic offsets between these two molecules provide the driving force for the charge transfer and consequently enable the harvesting of solar energy. However, while a large driving force benefits charge generation, and consequently the short-circuit current (J_{SC}) of the device, it introduces a reduction in the open-circuit voltage (V_{OC}). Traditionally, the active layers in OSCs are formed by a polymeric donor and a fullerene acceptor. More recently, the successfully synthesized non-fullerene acceptors (NFA) have enabled active layer blends with highly efficient charge generation with a low driving force (and often referred to as low-offset systems). These low-offset systems are highly attractive to the OSC community as they are promising for simultaneously benefitting both J_{SC} and V_{OC}. Thanks to NFAs and low-offset systems, the most state-of-the-art OSC has reached the power conversion efficiency (PCE) of 19.31%, closer and closer to the efficiency requirements for commercialization.

One of the main focuses of this thesis was a better understanding of the role of the energetic offset and each recombination channel on the performance of these low-offset systems as well as the interplays among the excited species. With the combination of a series of photoelectronic measurements in steady-state and transient conditions, morphological characterizations and simulations, a set of low-offset PM6:NFA blends with a wide range of device performance were studied in great detail. By systematically analyzing the losses via each loss channel at various bias conditions, an insightful understanding of the role of energetic offset in overall device performance is achieved. By performing current density – voltage characteristics (*J-V*), photoluminescence measurements and optical simulations, it was observed that the J_{SC} losses mainly originate from the exciton decay in the studied systems. With further characterizations on morphology and exciton diffusion combined with the *J-V* in large reverse bias, it was concluded that the excitons can efficiently diffuse to the donor:acceptor interface for all studied systems. Therefore, the exciton dissociation yield and the energetics at the donor:acceptor interface serve as the most dominating factors to explain the drastic differences in device performance in the studied systems. Interestingly, the exciton dissociation yield was found to be field dependent when the energetic offset becomes sufficiently small, acting as an additional limit to the fill factor (FF) of the device on top of the direct recombination of free charges. In these low-offset systems, the role of the interesting and frequently discussed effect called "exciton reformation" on device performance, which is a consequence of small energetic offset, was also discussed. With the analyses and characterizations of the studied systems, exciton reformation was found to help reduce the non-radiative voltage loss (ΔV_{nr}), but its benefit to V_{OC} overall, is limited. In addition,

while decreased energetic offset was observed to accelerate bimolecular recombination, this acceleration is not likely to be simply explained by exciton reformation, but rather it is accelerated via the decay of a “dark” state (such as charge transfer state (CT) and triplet excitons).

The second focus of the thesis was on the technical perspective for studying low-offset OSC systems, as well as that for OSC devices on industrial scales. Due to the high requisite level of characterization accuracy in the studies of OSCs and the sensitivity of OSC performance to fabrication conditions, the importance of employing appropriate characterization methods on device relevant samples, as well as correctly addressing the effect of characterization artifacts, was emphasized. This point was exemplified with two studies in this thesis. In the first study, two characterization techniques for energy level determination (spectro-electrochemistry and ultraviolet photoelectron spectroscopy (UPS)) were performed on an OSC system (PM6:Y6) fabricated from two different solvents (chloroform (CF) and o-xylene). Additionally, analyses were conducted to evaluate the measurement results obtained from the two characterization techniques on the films of the donor:acceptor blends and neat materials. The measurement results were then employed to explain the corresponding device performances. Compared to UPS, spectro-electrochemistry was found to be able to characterize the bulk of the PM6:Y6 blend, which is a better representation to the working devices and thus yield more reasonable measurement results. In addition, the energetics in PM6:Y6 blends from CF and o-xylene were found to be very similar, despite their substantial difference in V_{OC}. The difference in molecular orientation was demonstrated as the cause of the different V_{OC} values in the two blends, according to morphological measurements. In the second study, the influence of optical artifacts in differential absorption spectroscopy upon the change of sample configuration and active layer thickness was studied. As the thin-film solar cells such as OSCs are essentially low-finesse optical cavities, the manipulations of cavity effects to measurement results have been widely observed in optoelectronic measurements such as external photovoltaic quantum yield (EQE_{PV}) and photoluminescence (PL). Herein, it is exemplified and discussed thoroughly and systematically in terms of optical simulations and experiments, how optical artifacts can manipulate not only the measured spectra, but also the decay dynamics in various measurement conditions. For the sample system in this study (PM6:Y6), the measured spectrum was found to be strongly manipulated by optical artifacts when performing the measurement on full devices with active layers thicker than 150 nm. This matches the desired thickness range for active layers for industrial processing technologies, for instance, roll-to-roll processing. In some conditions, even the number of measured peaks can change due to optical artifacts. Therefore, it is of substantial relevance to correctly and carefully address the effect of optical artifacts and determine safe measurement windows, in order to correctly understand and analyze the experimental data. In the end of this study, a generalized methodology based on an inverse optical transfer matrix formalism was provided to correct the spectra and decay dynamics manipulated by optical artifacts. The results and proposed correction method in this study enables the reliable application of differential absorption spectroscopies on thick-junction operating devices with complex device configurations, and thus facilitate better understanding and progress in these organic solar cells. The results in this study can also be extended to other material systems in such thin-film-system-configurations such as perovskites and kesterites.

Overall, this thesis paves the way for a deeper understanding of the keys toward higher PCEs in low-offset OSC devices, from the perspectives of both device physics and characterization techniques. The significance of exciton dissociation and decay process at the donor:acceptor interface was emphasized. With the studies in this thesis, more detailed knowledge of the role of electric field in the exciton dissociation process, as well as the loss channels via the “dark” states upon the encounter of free charges, are proposed to be the key towards more efficient low-offset OSCs. In addition, methodologies are exemplified for appropriately employing suitable measurement techniques in safe measurement windows, and correctly addressing possible measurement artifacts, in order to ultimately propel the development of low-offset OSCs to achieve PCEs surpassing 20% in the industrial scale.

ZUSAMMENFASSUNG

Organische Solarzellen (OSC) stellen eine neue Generation von Solarmodulen dar, die durch eine Vielzahl faszinierender Merkmale gekennzeichnet sind, wie zum Beispiel niedrige Kosten, geringes Gewicht, ästhetisch ansprechendes Design und Flexibilität. Im Gegensatz zu herkömmlichen Silizium-Solarzellen findet bei OSCs die Umwandlung von Photonen in Elektronen in der Regel in einer aktiven Schicht statt. Diese Schicht entsteht durch die Vermischung zweier Arten organischer Moleküle mit unterschiedlichen Energieniveaus, was als "Bulk-Heterojunction"(BHJ) bezeichnet wird. Während der Ladungserzeugung werden Elektronen und Löcher in den photoerzeugten Elektron-Loch-Paaren (Exzitonen) in den Molekülen angereichert, die Elektronen aufnehmen (Akzeptor) bzw. abgeben (Donor). Dieser Prozess, der als Ladungstransfer bezeichnet wird, erfolgt aufgrund des energetischen Ausgleichs zwischen den beiden Molekülen und ermöglicht somit die Gewinnung elektrischer Energie. Eine hohe Antriebskraft begünstigt zwar die Ladungserzeugung und den Kurzschlussstrom (J_{SC}) des Devices, führt jedoch zu einer Verringerung der Leerlaufspannung (V_{OC}). Traditionell bestehen die aktiven Schichten in OSCs aus einem polymeren Donor und einem Fullerene-Akzeptor. In jüngster Zeit haben erfolgreich synthetisierte Non-Fullerene-Akzeptoren (NFA) Mischungen für aktive Schichten ermöglicht, die eine hocheffiziente Ladungserzeugung bei geringer Antriebskraft aufweisen (und werden oft als "Low-Offset-Systeme"bezeichnet). Diese Low-Offset-Systeme sind äußerst attraktiv für die OSC-Gemeinschaft, da sie vielversprechend sowohl für J_{SC} als auch für V_{OC} sind. Dank der NFAs und der Systeme mit geringem Offset hat die neueste Generation von OSCs einen Wirkungsgrad von 19,31% erreicht und nähert sich somit den Effizienzanforderungen für die Vermarktung immer weiter an.

Die beschriebene Forschungsarbeit fokussierte auf ein umfassenderes Verständnis der Rolle des Energieversatzes und der verschiedenen Rekombinationsmechanismen in Low-Offset-Systemen für organische Solarzellen. Mithilfe einer Kombination aus verschiedenen Messverfahren, Charakterisierungen und Simulationen wurde eine detaillierte Untersuchung von PM6:NFA-Mischungen mit geringem Versatz und einer Vielfalt an Bauteilen durchgeführt. Durch eine systematische Analyse der Verluste entlang verschiedener Verlustkanäle unter verschiedenen Spannungsbedingungen wurde ein aufschlussreiches Verständnis für die Rolle des Energieversatzes in Bezug auf die Gesamtleistung der Solarzelle erlangt. Es wurde festgestellt, dass die Verluste im Kurzschlussstrom (J_{SC}) hauptsächlich auf den Zerfall der Exzitonen zurückzuführen sind. Weitere Charakterisierungen der Morphologie und der Diffusion der Exzitonen in Verbindung mit Stromdichte-Spannungskennlinien zeigten, dass die Exzitonen effizient zur Grenzfläche zwischen Donator und Akzeptor diffundieren können. Die Ausbeute bei der Dissoziation der Exzitonen und die Energetik an der Donator-Akzeptor-Grenzfläche wurden als entscheidende Faktoren identifiziert, welche die Leistungsunterschiede zwischen den untersuchten Systemen erklären. Interessanterweise wurde festgestellt, dass die Dissoziationsausbeute der Exzitonen feldabhängig ist, wenn der Energieversatz ausreichend gering ist. Dies stellt eine weitere Begrenzung des Füllfaktors (FF) der Solarzelle dar, zusätzlich zur direkten Rekombination freier Ladungen. Auch der Einfluss des Effekts der Ëxzitonen-Reformationïn Systemen mit geringem Versatz wurde diskutiert. Dieser Effekt tritt aufgrund des geringen Energieversatzes auf und trägt zur Verringerung des nicht-

strahlenden Spannungsverlusts (ΔV_{nr}) bei. Es wurde jedoch festgestellt, dass der Nutzen für die Leerlaufspannung (V_{OC}) insgesamt begrenzt ist. Des Weiteren wurde beobachtet, dass ein geringerer Energieversatz die bimolekulare Rekombination beschleunigt. Diese Beschleunigung kann wahrscheinlich nicht allein durch die Bildung neuer Exzitonen erklärt werden, sondern resultiert aus dem Zerfall eines "dunklenSZustands wie beispielsweise einem Ladungstransferzustand (CT) oder Triplett-Exzitonen. Insgesamt trägt diese Arbeit zu einem tieferen Verständnis der Zusammenhänge zwischen Energieversatz, Rekombinationsprozessen und Leistung in Low-Offset-Systemen für organische Solarzellen bei. Die gewonnenen Erkenntnisse können dazu beitragen, die Entwicklung effizienter OSCs weiter voranzutreiben.

Der zweite Schwerpunkt der Arbeit lag auf der technischen Perspektive für die Untersuchung von Der zweite Schwerpunkt der Arbeit lag auf der technischen Perspektive zur Untersuchung von OSC-Systemen mit geringem Versatz und OSC-Devices im industriellen Maßstab. Angesichts der hohen Anforderungen an die präzise Charakterisierung von OSCs und der Empfindlichkeit der OSC-Leistung gegenüber Herstellungsbedingungen wurde betont, wie wichtig es ist, geeignete Charakterisierungsmethoden an gerätespezifischen Proben anzuwenden und die Auswirkungen von Charakterisierungsartefakten korrekt zu berücksichtigen. In dieser Arbeit wurden zwei Studien durchgeführt, um diesen Punkt zu verdeutlichen. In der ersten Studie wurden zwei Charakterisierungsmethoden, die Spektro-Elektrochemie und die Ultraviolett-Photoelektronen-Spektroskopie (UPS), an einem OSC-System (PM6:Y6) durchgeführt, das aus zwei verschiedenen Lösungsmitteln (Chloroform (CF) und o-Xylol) hergestellt wurde. Zusätzlich wurden Analysen durchgeführt, um die Messergebnisse beider Charakterisierungsmethoden an Filmen der Donor:Akzeptor-Mischungen und reinen Materialien zu bewerten. Die Ergebnisse wurden dann verwendet, um die entsprechenden Geräteleistungen zu erklären. Im Vergleich zur UPS wurde festgestellt, dass die Spektro-Elektrochemie in der Lage ist, die Zusammensetzung der PM6:Y6-Mischung genauer zu charakterisieren, was eine bessere Darstellung der funktionsfähigen Geräte ermöglicht und somit zu plausibleren Messergebnissen führt. Darüber hinaus wurde festgestellt, dass die energetischen Eigenschaften von PM6:Y6-Mischungen aus CF und o-Xylol trotz erheblicher Unterschiede in Bezug auf die Leerlaufspannung (V_{OC}) sehr ähnlich sind. Morphologische Messungen ergaben, dass der Unterschied in der molekularen Orientierung die Ursache für die unterschiedlichen V_{OC}-Werte in den beiden Mischungen ist. In der zweiten Studie wurde der Einfluss optischer Artefakte bei der Differentialabsorptionsspektroskopie in Abhängigkeit von der Probenkonfiguration und der Dicke der aktiven Schicht untersucht. Da Dünnschichtsolarzellen wie OSCs im Wesentlichen optische Hohlräume mit geringer Dicke sind, sind die Auswirkungen von Hohlraumeffekten auf Messergebnisse optoelektronischer Messungen wie der externen photovoltaischen Quanteneffizienz (EQE_{PV}) und der Photolumineszenz (PL) weit verbreitet. In dieser Studie wird ausführlich und systematisch erklärt, wie optische Artefakte nicht nur die gemessenen Spektren, sondern auch die Abklingdynamik unter verschiedenen Messbedingungen beeinflussen können. Anhand von optischen Simulationen und Experimenten wurde gezeigt, dass das gemessene Spektrum des untersuchten Probensystems (PM6:Y6) durch optische Artefakte stark beeinflusst wird, wenn die Messung an vollständigen Bauteilen mit aktiven Schichten von mehr als 150 nm Dicke durchgeführt wird. Dieser Dickenbereich entspricht den Anforderungen industrieller Verarbeitungstechnologien wie der Rolle-zu-Rolle-Verarbeitung. Unter bestimmten Bedingungen können optische Artefakte sogar die Anzahl der gemessenen Peaks verändern. Daher ist es von großer Bedeutung, die

Auswirkungen optischer Artefakte korrekt und sorgfältig zu berücksichtigen und sichere Messfenster zu bestimmen, um experimentelle Daten richtig zu verstehen und zu analysieren. Am Ende dieser Studie wurde eine verallgemeinerte Methode auf Basis des Formalismus der inversen optischen Transfermatrix zur Korrektur der durch optische Artefakte beeinflussten Spektren und Abklingdynamik vorgestellt. Die Ergebnisse und die vorgeschlagene Korrekturmethode ermöglichen eine zuverlässige Anwendung der Differentialabsorptionsspektroskopie auf Dickschicht-Solarzellen mit komplexen Bauteilstrukturen und tragen zu einem besseren Verständnis und Fortschritt bei organischen Solarzellen bei. Die Ergebnisse dieser Studie können auch auf andere Materialsysteme in solchen Dünnschichtsystemkonfigurationen wie Perowskit und Kesterit übertragen werden.

Insgesamt legt diese Arbeit den Grundstein für ein besseres Verständnis der Schlüsselfaktoren für höhere Effizienzen in OSC-Devices mit geringem Versatz, sowohl aus der Sicht der Physik der Solarzelle als auch der Charakterisierungstechniken. Die Bedeutung der Dissoziation von Exzitonen und des Zerfallsprozesses an der Grenzfläche zwischen Donator und Akzeptor wurde betont. Basierend auf den in dieser Arbeit durchgeführten Studien werden detailliertere Erkenntnisse über die Rolle des elektrischen Feldes im Prozess der Exzitonen-Dissoziation sowie über Verlustkanäle durch "dunkleS-Zustände bei der Wechselwirkung mit freien Ladungen als Schlüssel für effizientere Low-Offset-OSCs vorgeschlagen. Darüber hinaus werden Methoden für den angemessenen Einsatz geeigneter Messverfahren in sicheren Messfenstern und für die korrekte Behandlung möglicher Messartefakte aufgezeigt, um letztendlich die Entwicklung von Low-Offset-OSCs voranzutreiben und Effizienzen von über 20 % im industriellen Maßstab zu erreichen.

CONTRIBUTION STATEMENT

In the following, the publications involved in this thesis are listed, the contribution of each involved author is clarified.

N. Tokmoldin, B. Sun, F. Moruzzi, A. Patterson, O. Alqahtani, R. Wang, B. A. Collins, I.McCulloch, L. Lüer, C. J. Brabec, D. Neher, and S. Shoaee, "Elucidating How Low Energy Offset Matters to Performance of Nonfullerene Acceptor-Based Solar Cells," ACS Energy Letters 8, 2552-2560 (2023).

N.T., S.S. and D.N. planned the project. N.T fabricated the samples for optoelectronic measurements. N.T. and I fabricated the samples together for morphological measurements. N.T. and I performed the PL/EL, PLQY/ELQY, TDCF, BACE and UV-VIS measurements together, with N.T. being the lead. N.T. has performed the EQE_{PV} measurement. F.M. performed the CV measurements. A.P. and O.A. performed the morphological measurements (R-SOXS, STXM). R.W. performed the time-resolved photoluminescence measurement. I have participated in the data analysis and contributed interpretations and understandings to the data. B.A.C., I.M., L.L., C.J.B, D.N. and S.S provided interpretations to the measurements and results. D.N. and S.S. supervised the whole project. All co-authors contributed to the manuscript drafting.

D. Neusser, B. Sun, W. L. Tan, L. Thomsen, T. Schultz, L. Perdign-Toro, N. Koch, S. Shoaee, C. R. McNeill, D. Neher, and S. Ludwigs, "Spectroelectrochemically determined energy levels of PM6:Y6 blends and their relevance to solar cell performance," Journal of Materials Chemistry C 10, 11565-11578 (2022)

D.Neher. and S.L. planned the project. D.Neusser performed the spectroelectrochemistry measurement. I fabricated the devices and performed all the optoelectronic measurements (*J-V*, UV-VIS, EQE_{PV}, ELQY) with some assistance from L.P-T. W.L.T. and T.S. performed the GIWAXS and NEXAFS measurements. N.K., S.S., C.R.M., D.N., and S.L. provided understanding and interpretation to the data. D.N., and S.L. supervised the project.

B. Sun, N. Tokmoldin, O. Alqahtani, A. Patterson, C. S. P. De Castro, D. B. Riley, M. Pranav, A. Armin, F. Laquai, B. A. Collins, D. Neher, and S. Shoaee, "Toward More Efficient Organic Solar Cells: A Detailed Study of Loss Pathway and Its Impact on Overall Device Performance in Low-Offset Organic Solar Cells," Advanced Energy Materials, 2300980 (2023).

I planned the project with the help of S.S, drafted the manuscript and response letter to the reviewers. Experimentwise, I have fabricated all the samples and performed the optoelectronic measurements (with the assistance of N.T), including *J-V* measurements, UV-VIS spectroscopy, EQE_{PV}, PL/EL, PLQY/ELQY, TDCF, BACE measurements, analyzed and interpreted the data. O.A, A.P performed the morphological measurements (GIWAXS, AFM and R-SOXS), C.S.P.D.C performed the TRPL measurements. D.B.R. performed the plused-PLQY measurement. M.P. provided part of the *J-V* data and took part in some of the PL measurements. I have performed the optical-transfer materix simulations. A.A., F.L., B.A.C., D.N., and S.S. provided interpretations to the measurement results. S.S. and D.N. supervised the study. All co-authors have contributed to the menuscript drafting.

B. Sun, O. J. Sandberg, D. Neher, A. Armin, and S. Shoaee, "Wave Optics of Differential Absorption Spectroscopy in Thick-Junction Organic Solar Cells: Optical Artifacts and Correction Strategies," Physical Review Applied 17, 054016 (2022).

I planned the project with the supervision of S.S., drafted the manuscript and response letter to the reviewers. Experimentally, I have fabricated all samples and performed the PIA measurements. I have written the code for the proposed inverse transfer matrix formalism. O.J.S. and D.N. and A.A. contributed with suggestions and reviewing the manuscript.

_____

Supervisor: Prof. Dr. Safa Shoaee

Contents

IV Results and Conclusion

List of Figures

List of Tables

Part I

INTRODUCTION AND MOTIVATION

I. 1 Introduction

As burning carbon-based fuels (oil, coal, and natural gas etc.) is leading to more and more environmental issues such as CO_2 emission, global warming, and air pollution, it is vital that alternative green energy sources are employed to fulfill the increasing energy demands in modern societies. Solar energy, as one of the most abundant and sustainable energy sources, is considered as a very promising candidate. Photovoltaic (PV) technology enables the conversion of solar energy into electricity which is essential to our everyday life and serves as one of the most promising techniques for the generation of green energy. In 2022, the share of cumulative power capacity of solar photovoltaics reached 12.8% among all power generating technologies, an increase of around 7 times compared to that ten years ago. According to the international energy agency (IEA), the installed power capacity of solar PV is predicted to surpass that of coal by the year 2027. [1]

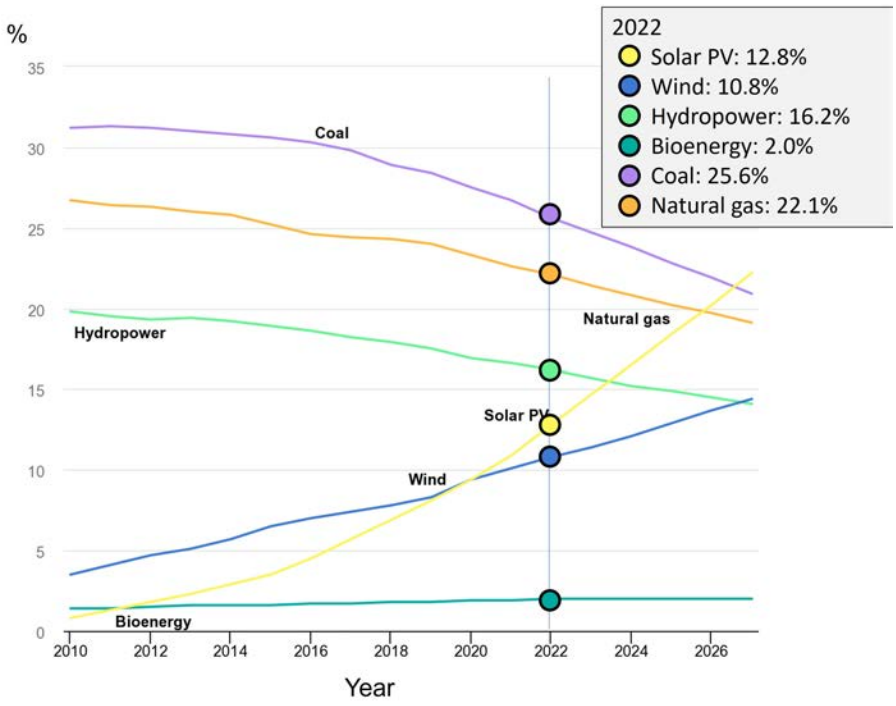

Figure I. 1.1: Share of cumulative power capacity by technology, 2010-2027.[1]

Most generally, photovoltaic power generation takes the form of centralized or distributed PV power stations. Centralized PV plants usually require a large piece of land and are usually located in deserts and Gobi areas, while distributed PV power stations are usually in the city, for instance, on the streets and the roof of the buildings and factories. Apart from the centralized and distributed PV plants, photovoltaic power generation techniques can also be used in other novel scenarios. For example, semi-transparent or colored solar cells can be used on windows and facades of buildings,

so-called building-integrated photovoltaics (BIPV). This is of great importance since buildings account for 30% of global energy consumption and 27% of greenhouse gas emissions, according to a report from International Energy Agency (IEA) in 2021 [2]. Additionally, solar cells can also be used in low-light environments to fulfill some indoor activities, for instance, to power the Internet of Things (IoT) ecosystems. Photovoltaics are also used in vehicles and satellites. In these novel application scenarios, solar cells are required to be lighted-weighted and good-looking, and with high power conversion efficiency (PCE).

So far, most of the solar panels in the market are silicon solar cells. While these silicon solar cells have high power conversion efficiencies and long service lifetime and are therefore suitable for traditional centralized and distributed PV power stations, they are, however, heavy, thick, rigid, and do not have an attractive appearance, thus cannot fulfill the requirements for novel application scenarios.

In this regard, organic solar cells (OSC) serve as a promising candidate for such scenarios. OSC devices are usually only hundreds of nanometers thick and are flexible. Moreover, the color of the OSCs can be tuned even to semitransparent (absorbing the light in invisible wavelength range), making them a good candidate in BIPV applications. The PCE of the state-of-the-art semitransparent organic solar cells (ST-OSCs) has surpassed 15% [3], and that of the best near-infrared absorbing OSC has reached the PCE of 9.91% [4].

OSCs usually consist of a polymeric donor and a small molecular acceptor. Since non-fullerene acceptors (NFAs) came into the game, the efficiency of organic solar cell has boosted to more than 19% in the past three years [5], pushing the organic solar cell technology closer and closer to commercialization. In fact, there are already some companies working on organic solar cells in the market, for instance, Heliatek from Germany, ARMOR from France, and infinityPV ApS from Denmark. Despite the progress made in organic solar cells, there are still significant challenges that need to be overcome before they can be commercialized.

The first issue comes from the PCE losses during upscaling and the realization of massive production. In the lab scale, the fabrication of organic solar cells is usually performed with spin coating, which is not suitable for large-scale production compared to techniques such as printing and roll-to-roll processing. Apart from the difference in fabrication procedure itself, one main difference is also on the active layer thickness. Nowadays, the thickness of the active layer in the most efficient organic solar cells is around 100 nm [5–8], however, a film thickness of around 300 nm is required for reproducible massive fabrications via printing and roll-to-roll processing [9]. As is pointed out by numerous studies, the performance of organic solar cells and quality of the active layer is very sensitive to the fabrication conditions of the devices and the active layer thickness, and many relevant physical parameters can change [10–13]. Therefore, it is not appropriate to translate the characterization results performed on lab-scaled devices to those fabricated via industrial processing methods, even if the active layer is from the same material. Therefore, it is vital to perform characterizations exactly on the samples processed with industrial methods. To study solar cells, it is relevant to know how many free charges can be generated upon photoexcitation and how fast these photo-generated charges are lost. In this regard, the characterizations of carrier density in the device upon photoexcitation and their decay are excessively relevant and informative. Such characterizations can be realized either optically or

electrically via techniques such as differential absorption spectroscopy or bias-assisted charge extraction (BACE). Differential absorption spectroscopy is a group of characterization methods which enables the measurement of the absorption of photo-excited states in the solar cells (such as excitons, charge transfer states, and free charges) and enable quantitative and quantitative analyses of these excited species [14–16]. With the introduction of the time component (so-called transient absorption spectroscopy), differential absorption spectroscopies can be employed to study the decay dynamics of these excited species. BACE is another powerful technique that can be applied to determine the carrier density and recombination rate in a solar cell by first generating free charges in the device and then extracting them out. Both techniques, while being very powerful, are based on assumptions which are only valid in certain conditions (for instance, when the active layer is within a certain thickness range) and may suffer from artifacts when these assumptions are violated, leading to falsified results. [17, 18] To apply these measurements on industrial processed organic solar cells and obtain reliable data, it is of great importance to carefully address whether these assumptions still hold and how much inaccuracy would be resulted upon the failure of these assumptions, and if possible, correct or compensate these inaccuracies.

Secondly, the PCE of state-of-the-art organic solar cells is still not high enough compared to the mainstream silicon solar cells in the market (PCE>25%)[19]. Efficient photon-electron conversion in organic solar cells is realized by blending of two materials with different energy levels (so-called donor and acceptor) on nanometer scale. For a long time, the efficiency of organic solar cells was limited to around 10% due to the underperformance of the acceptor (which is fullerene-based). In 2019, a new type of non-fullerene acceptor (NFA) came into the game and boosted the PCE of organic solar cells by over 15% [20]. Up to now, many state-of-the-art NFA solar cells are based on a type of fused-ring electron acceptors (FREAs) and have surpassed 19% efficiency [5]. To push the OSCs towards commercialization, it is vital to push the efficiency even further so that it competes with the main-stream silicon solar cells and its competitor perovskite solar cells. As mentioned above, the active layer of organic solar cells consists of two materials with different energy levels. The difference in the energy levels provides a driving force which assists the charge generation process. However, on the other hand, this driving force leads to an energy loss in the solar cell and lowers the PCE. Interestingly, it was found for FREA-systems that the required driving force for efficient charge generation is less compared to traditional fullerene-based systems [21, 22]. These OSC systems with low driving force are referred to as low-offset systems. While these low-offset systems are pointing to a path to further increase the PCE, a precise picture of the mechanism of photo-electron conversion under different operation conditions (e.g., different biases) of these systems is still missing. Moreover, the FREAs have now grown into a huge family upon the variation of chemical groups based on similar skeleton [23]. The structure-function relationship of FREAs has been observed to behave differently from that of fullerenes in terms of electro-optical and morphological properties [24]. It is also of great importance to understand in detail how the chemical structures of these FREAs affect the device performance and where exactly the losses come from when the devices underperform.

I. 2 Scope and Motivation

To response to the issues raised in the previous chapter, it is critical to understand both the underlying working principles of low-offset OSC devices and measurement techniques utilized for their characterization. In this thesis, the fundamental device physics of OSCs and theoretical backgrounds are firstly introduced in part ii, then in part iii, the experimental methods involved in this work is covered. Thereafter, the main results of this thesis is presented in part iv.

While low-offset OSCs based on NFA are presenting a promising future, the small energetic offset between donor and acceptor has been evidenced to play important role in many relevant optoelectronic processes in OSCs, including charge generation and recombination. Previous studies have demonstrated the repopulation of excitons from charge transfer (CT) states, as the energy levels of the two states are brought very close to each other [25]. The decay via S_1 state therefore serves as an additional loss pathway parallel to the CT decay. Chapter IV. 1 focuses on the effect of energetic offset to the effective bimolecular recombination rate. Herein an increase in apparent bimolecular recombination coefficient (k_2) upon the reduction of energetic offset was observed. More detailed analyses indicate that the reformation of S_1 alone does not explain the relationship between k_2 and energetic offset, and the role of recombination via "dark" states (such as CT and triplet excitons) should be considered for the recombination of photogenerated free carriers. Another information from chapter IV. 1 is the observed field-dependent charge generation, originating from field-dependent exciton dissociation, which will be revisited for more sample systems in chapter IV. 3 and discussed in greater detail.

The results in chapter IV. 1 presents drastic difference in device performance upon a small variation of the energetic offset by around 0.1 eV, calling for precise and careful analysis on the energetic levels in the active layer blends for a better understanding of low-offset systems. In chapter IV. 2, a thorough analysis of the energy levels and corresponding device performance on two OSC blends (based on the same material system) fabricated from two different solvents were performed with ultraviolet photoelectron spectroscopy (UPS) and spectro-electrochemistry. The measurement results in chapter IV. 2 show the importance of evaluating the energy levels on the blend which is better representative to operating device scenario. It is also important to measure the bulk of the active layer and therefore the results from surface sensitive characterizations are to be cautiously treated.

With the message from chapter IV. 2 in mind, the low-offset OSCs were revisited in chapter IV. 3 by getting the energetic offsets between excitons and CT states in the working devices. In chapter IV. 3, a systematic and detailed study for the loss channels to several PM6:NFA systems with different energetic offsets is presented. Herein, a series of NFAs were blended with the same polymer donor. These combinations yield a series of low-offset systems with different energetic offsets and a wide range of device performances. Detailed studies were performed to study the overall device performance

by evaluating the origination of losses from each loss channel under various bias conditions in each system. As a result, an insightful picture is given about what results in the different performances among these low-offset systems and the origin of each loss channel. Additionally, comparisons between FREAs with different halogen substituents were made to provide information about the structure-function relationships among the FREAs employed in this study. With the results in chapter IV. 3, it is demonstrated that the energetic condition at the donor:acceptor interface and exciton dissociation efficiency are the most decisive factors for the device performance. Furthermore the variation of halogen substituents in FREAs does not make a big difference to neither the probability that excitons find the donor:acceptor interface, nor the CT dissociation efficiency. Chapter IV. 3 helps providing the pathway toward record-breaking low-offset OSCs.

Finally, with the excitement for the promising commercialization of low-offset OSCs, another note is given in chapter IV. 4 from a technical perspective. Due to the low production efficiency of spin-coated devices, a change in fabrication technique and up-scaling is inevitable for the commercialization of OSCs. Compared to OSCs in lab scale, industrial compatible fabrication techniques such as roll-to-roll processing require thicker active layers. In chapter IV. 4, it is presented in detail how the change in geometry of the devices (e.g., the thickness of the active layer) can substantially change the extent of the influence of optical artifacts in a powerful characterization technique – differential absorption spectroscopy. In addition, correction approaches based on inverse optical transfer matrix formalism are proposed in terms of the experimental finding and simulations, to account for these inaccuracies so that reliable measurement results can still be generated for thick-junction devices.

This thesis paves the way toward the commercialization of OSCs from the perspective of device physics and characterization techniques.

Part II

FUNDAMENTALS

This chapter includes the relevant fundamentals for the analyses and interpretations involved in this study. In chapter II. 1, the basics of organic semiconductors are introduced. In chapter II. 2, the structure of organic solar cells is first introduced, then the basic processes of organic solar cells are explained in detail. Thereafter, the device physics in organic solar cells are introduced. In the end, in chapter II. 3, two important simulation models for OSC devices are presented, including an optical simulation and an electrical simulation formalism (namely optical transfer matrix and drift-diffusion).

II. 1 From inorganic semiconductors to organic semiconductors

Semiconductors has been considered as one of the most valuable materials in the past decades and plays an important role in many aspects of our modern life, such as economic, health, and national security.

The carrier density in semiconductors is responsive to external energy, such as radiation (photogeneration) or heat (thermal activation). The change in carrier density then consequently affects the conductivity of the semiconductor via the Drude-Sommerfeld free electron model (equation II. 1.1). At room temperature, the typical intrinsic conductivities for semiconductors are in the range from 10^{-4} to 10^{4} Ω^{-1} cm^{-1} [26].

$$\sigma = q \cdot n \cdot \mu \tag{II. 1.1}$$

where q is elementary charge, n the carrier density, and μ the mobility of charges.

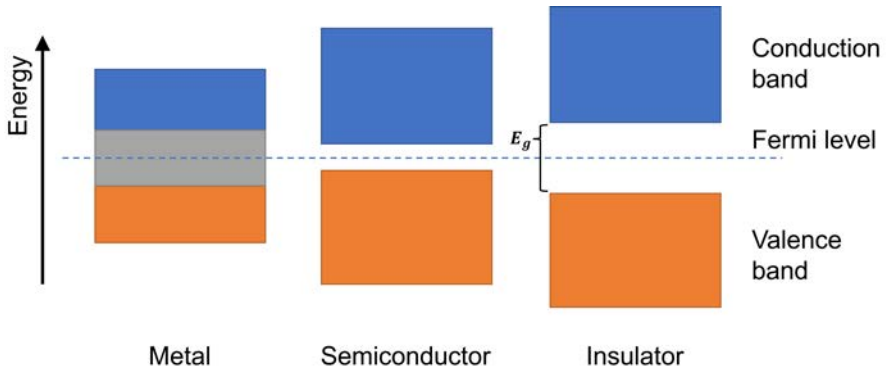

Figure II. 1.1: The scheme of energetic bandgaps of metals, semiconductors, and insulators.

In general, semiconductors can be classified into inorganic and organic semiconductors. Typical inorganic semiconductors are crystals or alloys including single compound semiconductors such as silicone (Si) and germanium (Ge), and compound semiconductors like gallium arsenide (GaAs), gallium nitride (GaN), and indium gallium arsenide ($In_xGa_{1-x}As$) etc., with the bandgap ranging from 0.36 eV to 3.44 eV [27]. Typical inorganic semiconductors have dielectric constants of ε_r = 13 to 16, much larger than those of typical organic semiconductors (ε_r= 3 to 6) [28, 29]. The low dielectric constants in organic semiconductors result in difference in the device configuration and detailed charge generation and recombination processes in OSC devices compared to traditional inorganic solar cell devices. II. 2 It is worth mentioning that the traditional inorganic semiconductor manufacturing industry can be excessively environmentally unfriendly due to the involvement of toxic elements such as arsenic, cadmium and lead [30].

Organic semiconductors on the other hand, are carbon-based organic small molecules or polymers with few heteroatoms such as sulfur, oxygen, nitrogen, and bromine. Unlike inorganic semiconductors which are brittle, rigid, and hard to process, organic semiconductors can be flexible and solution processable, making them more suitable in more diverse application scenarios and easier to process. The biggest difference between organic and atomic inorganic semiconductors is that organic semiconductors consist of molecules instead of atoms. Unlike inorganic semiconductors such as silicon, where the atoms are covalently bounded together [31], the molecules in organic semiconductors aggregate together due to Van de Waal forces [32]. From the molecular perspective, the molecules of organic semiconductors, no matter small molecular or polymeric, mainly consist of conjugated structure where electrons can resonate and delocalize. These conjugated structures are usually formed by alternating single and double carbon bonds, taking the form of linear shape or ring shape (such as single or fused aromatic rings) [33].

A simple conjugated structure can be exampled by 1,3-butadiene where four carbons are bounded with alternating single and double bonds on the backbone. The electron configuration of a single carbon atom is $1s^2 2s^2 2p^2$. In the backbone of 1,3-butadiene, the 2s and two 2p atomic orbitals hybrid and form three degenerate sp^2 orbitals taking a plane configuration and form strongly localized σ-bonds. The unhybridized *p* orbitals form the more delocalized π bonds. The coupling of the π bonds among the carbons in the conjugated segment enables the delocalization of the electrons in the molecule and thus the semiconductive property of the material.

In the carbon-based backbone of 1,3-butadiene, the in-phase and out-of-phase arrangement in the orbital wavefunctions form four molecular π-orbitals with different energies. The position where there is a switch between in the phase of the orbital wavefunctions (corresponding to the point where the possibility of finding an electron is zero) is called a “node”. The more the node, the higher the energy of the molecular orbital. Each molecular orbital contains two electrons, therefore in 1,3-butadiene, only the node = 0 and node = 1 orbitals can be filled. The molecular orbitals that are filled are called bonding π-orbitals and those not filled are called anti-bonding π-orbitals. The bonding π-orbital which has the highest energy is called highest occupied molecular orbital (HOMO), while the anti-bonding π-orbital which has the lowest energy is called lowest unoccupied molecular orbital (LUMO). The energy of each molecular orbital can be approximated with the linear combination of atomic orbitals (LCAO) model. The bandgap between HOMO and LUMO has been widely reported to be related to the length of the conjugated structure – the longer the conjugated segment, the lower the bandgap.

The transportation of charges between organic semiconductor molecules is enabled by intermolecular π-π stacking. [34] Each conjugated segment serves as an energetic state. In polymers, the planar conjugated structure can be disrupted due to, for instance, entropy driven coiling of the polymer chain, or kinks and twists formed by the rotation of the polymer chain. In addition, the degree of polymerization in polymer materials, chemical defects and presence of impurities also affects the lengths of the conjugation structures. As a result, a polymeric matrix consists of conjugated segments with different lengths and thus forms a distribution of energetic states (often referred as the energetic disorder) [35]. This characteristic leads to the unique "hopping mechanism" for charge transportation in organic semiconductors, which is different from that of inorganic semiconductors and metals (as will be introduced in more detail in section II. 2.2.3).

II. 2 Fundamentals of organic solar cells

As mentioned in the beginning of chapter II. 1, the carrier density in semiconductors can be populated via radiative activation process. More specifically, in the organic semiconducting active layers, upon the photon excitation, electrons can be excited from HOMO to LUMO and eventually form free charges. This enables the optoelectronic devices which convert photons to free charges, namely organic solar cells.

II. 2.1 Structure of Organic Solar Cells

A typical organic solar cell consists of active layer, electrodes (cathode and anode), and interlayers (Figure II. 2.1a). The active layer usually consists of a donor and an acceptor and is where charges are photogenerated. The cathode and anode are usually two metallic conductors with different chemical potentials. When connecting the cathode and anode together with a metal wire, the electrons in the two electrodes redistribute (driven by the difference in the work functions in the two electrodes) until an equilibrium is reached (Fermi level matching between the two electrodes). The redistribution of charges produces a built-in potential difference between the two electrodes and therefore creates a built-in field across the device. [29] The built-in field drives the photo-generated charges in the active layer to flow towards the electrodes and thus form a displacement current in the outside circuit, namely the photocurrent, which can be detected by an amperemeter in the outside circuit. A simple description of the displacement current, I_{displ}, can be given when considering the drift of the electrons and holes:

$$I_{\mathrm{displ}}(t) = \frac{qA}{d} \int_0^d \left(n_{\mathrm{e}}(x,t)\upsilon_{\mathrm{e}}(x,t) + n_{\mathrm{h}}(x,t)\upsilon_{\mathrm{h}}(x,t)\right) \tag{II. 2.1}$$

where A and d are the area and thickness of the device, respectively. n_{e} and n_{h} are the densities of electrons and holes, respectively. υ_{e} and υ_{h} are the drift velocities of electrons and holes, respectively.

Notably, it is always desired that holes flow towards the anode and electrons towards the cathode; thus charge carriers flowing towards and recombining at the “wrong” electrode result in energy losses. In this regard, interlayers (electron transport layer, ETL, and hole transport layer, HTL) are included in organic solar cells adjacent to the active layer. The HTL selectively allows for holes to pass through while blocking the electrons, and vice versa for the electron transport layer. The selectivity of interlayers is enabled by their energetic alignment with the active layer. As pictured in Figure 3, the HUMO (LUMO) of the ETL (HTL) is much deeper (shallower) than that of the active layer. In this way, the holes in the active layer cannot go through the ETL and reach the cathode (and vice versa for the electrons).

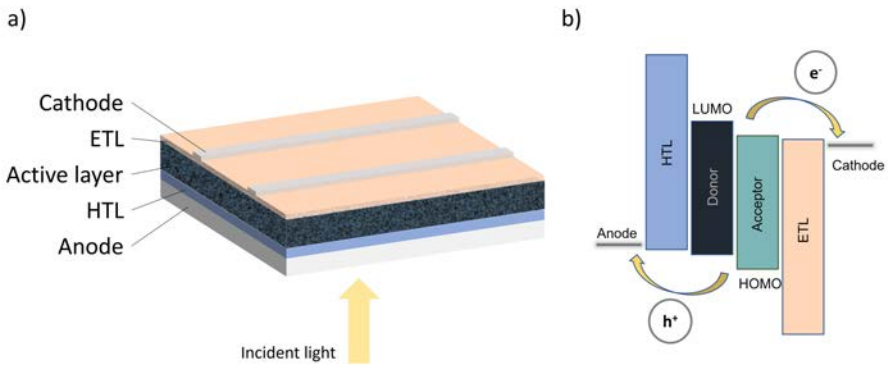

Figure II. 2.1: a) Structure of a typical conventional structured OSC device. The active layer is sandwiched between the two electrodes. Two interlayers, ETL and HTL, are employed between the active layer and electrodes to avoid photocarriers recombining at the wrong electrodes. b) The energetic diagram of the organic solar cell. The selectivity of the ETL and HTL is achieved by the design of energetic alignments. During the operation of the solar cell, the electrons and holes are collected at the cathode and anode, respectively.

II. 2.2 Basic Processes in Organic Solar Cells

Photo-electron conversion in organic semiconductors is not a simple one-step process. Figure II. 2.2 shows a simple and common model used for describing the generation and recombination processes in organic solar cells. From the incidence of photons, till the collection of free charges, several important processes must be considered, including: 1) the absorption of photons in the active layer, 2) the generation of charges, 3) the transportation of charges and, 4) the recombination of charges. Each process involves complicated underlying physical mechanisms and will be introduced in this section.

II. 2.2.1 Light absorption

The very first step of photon-electron conversion is the absorption of incident photons in the active layer. Since OSCs are thin-film systems, the distribution of the electromagnetic field upon incidence of light is subject to the multiple transmission, absorption, and reflection in each layer and at each interface in this thin-film system. Only a fraction of incident light can be absorbed by the active layer, the fraction of photons absorbed in the active layer compared to the incident photon flux (efficiency of photon absorption) is symbolized as η_{abs}. The situation of transmission, absorption and reflection in each layer and at each interface is subject to the wavelength of the incident light (λ_{in}) due to the wavelength-dependent complex refractive index ($\tilde{n}(\lambda) = n(\lambda) + i\kappa(\lambda)$) of each layer. Therefore, η_{abs} is a function of λ_{in}. The absorption of photons by the optoelectronic active layer in the solar cells result into the generation of excitons, which subsequently generate charges (more detailed charge generation process will be discussed in the next section II. 2.2.2). Therefore, the device has better chance for generating more charges when the absorption of the active layer matches the solar spectrum better. [36]

Notably, the absorption of incident light is not uniform in each position in the active layer, the spatial absorption profile of photons across the device was found in many experimental and simulation studies. For instance, Tress et al. [37] demonstrated a

considerable impact of photon absorption profile on the efficiency of charge collection when the electrons and holes have imbalanced mobilities (the concept of mobility will be discussed in more details in section II. 2.2.3).

It is worth to point out that, the thin-film system formed by the solar cell is, from an optical perspective, essentially a low finesse optical cavity where the multiple transmission and reflection of light among each layer result in the constructive and destructive waves (optical interference) in the optical cavity. As a result, the classic Beer Lambert's law fails to describe the actual distribution of electromagnetic waves in the active layer. Note that the situation of interference is subject to not only the wavelength of the incident light, but also the geometric of the optical cavity. This leads to different absorption spectra for the active layer when the same active layer is inserted in film stacks with different geometries [24]. The resulted cavity effect can result in optical artifacts in many optoelectronic measurements (will be discussed in greater detail in later sections II. 2.3.2, II. 3.1 and IV. 4). While the energy dissipation of the electromagnetic field in these optical cavities cannot be described by simply Beer Lambert's law, it can be computed via an optical transfer matrix formalism. The details about optical transfer matrix will be introduced in section II. 3.1.

II. 2.2.2 Charge generation

Upon photon excitation on semiconductors, excitons – a bounded electron-hole pair – can be generated. There are two types of excitons, so called Wannier-Mott exciton and Frenkel exciton. Wannier-Mott excitons are generated in materials with strong intermolecular interactions (e.g., in highly crystalline materials with large dielectric constant) and can be highly delocalized. The electron-hole pair in Wannier-Mott excitons are loosely bounded, consequently, the Wannier-Mott excitons can be easily separated into free charges at room temperature. [29, 38, 39]

As has been discussed in section II. 1, typical organic semiconductors have relatively low dielectric constants compared to inorganic semiconductors [29]. This results in a large binding energy in the electron-hole pair in the exciton (on the order of hundreds of meV) [29, 40]. The Frenkel excitons in OSCs typically live for tens to hundreds of picoseconds and can diffuse up to 20 nm before decaying to the ground state, depending on the material of interest [41–43]. To obtain free charges from these excitons, it is vital to separate the electron-hole pair before the excitons decay. To efficiently separate the excitons into free charges, a driving force is to be provided. In most organic solar cells, this is achieved by bringing two organic semiconductors with different HOMO and LUMO levels into contact. As depicted in Figure II. 2.1, the material with shallower HOMO and LUMO levels are called "donor", as it donates electrons, while the one with deeper HOMO and LUMO levels are called "acceptor", as it accepts the electrons. As the photo-generated exciton diffuses to the interface of the donor and acceptor, the offsets between the HOMO-HOMO and LUMO-LUMO of the donor and acceptor assist the exciton dissociation and dissociate the exciton into a so-called charge transfer (CT) state where the electron and hole sit on adjacent donor and acceptor molecules (donor for the hole and acceptor for the electron). The charges are thus now relatively more loosely bounded (compared to the exciton) which assists charge separated states (CS) to be generated more efficiently. The exciton dissociation rate can be described in the framework of the classic Marcus theory (equation II. 2.2) [44–47].

$$k_{\mathrm{exc,diss}} = \frac{2\pi}{\hbar} H^2 \frac{1}{\sqrt{4\pi\lambda_{\mathrm{re}} k_{\mathrm{B}} T}} exp(-\frac{(\Delta G + \lambda_{\mathrm{re}})^2}{4\lambda k_{\mathrm{B}} T}) \tag{II. 2.2}$$

where H is the electronic coupling between exciton and CT, ΔG is the change in Gibbs free energy upon exciton dissociation, λ_{re} is the reorganization energy.

Apart from providing the driving force, in order to achieve efficient charge generation, it is vital that the photogenerated excitons find the donor:acceptor interface before they decay. In presently state-of-the-art organic solar cells, this is achieved by blending the donor and acceptor to form a bulk heterojunction (BHJ). The fraction of excitons that successfully find the donor:acceptor interface and subsequently dissociate can be understood as exciton quenching efficiency, $\eta_{\mathrm{quen,exc}}$, defined by equation II. 2.3. [48]

$$\eta_{\mathrm{quen,exc}} = \frac{2L_{\mathrm{diff,exc}}\tau_{\mathrm{diss,exc}}}{d} \cdot \frac{sinh(\frac{d}{2L_{\mathrm{diff,exc}}})}{\tau_{\mathrm{diss,exc}} \cdot sinh(\frac{d}{2L_{\mathrm{diff,exc}}}) + \frac{D_{\mathrm{diff,exc}}}{L_{\mathrm{diff,exc}}} cosh(\frac{d}{2L_{\mathrm{diff,exc}}})} \tag{II. 2.3}$$

Where $D_{\mathrm{diff,exc}}$ and $L_{\mathrm{diff,exc}}$ are the exciton diffusion constant and exciton diffusion length, respectively; $\tau_{\mathrm{diss,exc}}$ the interface dissociation lifetime, and d the effective distance between two interfaces.

The dissociation of excitons results in the generation of more loosely bounded CT states which can be further separated and give free charges. However, the underlying physical mechanism for effective CT dissociation in highly efficient OSC systems is still not clear enough [49, 50]. From the perspective of energetics, the CT binding energy needs to be overcome when CT dissociates and form free charges. To realize the spontaneous CT dissociation, other factors must exist which compensate for the CT binding energy. Several possible factors have been proposed and studied, such as charge-quadrupole interactions [51, 52] and entropic contributions [53, 54].

It is worth mentioning that, the charge generation process has been observed to be field-dependent in many OSC systems and is attributed to a field-dependent CT dissociation rate [55–57]. One of the most famous models which accounts for the field-dependent CT dissociation is the Onsager-Braun model [58, 59], where k_{CT} is considered to be field-dependent and given by equation II. 2.4. In is worth mentioning that, despite the important insight of Onsager-Braun model in field-dependent charge generation behavior, it has been widely observed that reasonable CT lifetime cannot be obtained when applying Onsager-Braun model to explain experimental data measured in OSCs [57, 60–62].

$$k_{\mathrm{diss,CT}} = \upsilon \cdot exp(-\frac{\Delta E}{k_{\mathrm{B}} T}) \cdot (1 + b + \frac{d^2}{3} + \frac{d^3}{18} + ...) \tag{II. 2.4}$$

where υ is the separation attempt frequency, and b the effective field parameter given by $b = q^3/8\pi\varepsilon\varepsilon_o(k_{\mathrm{B}}T)^2$.

While the dissociation of exciton is usually considered as field-independent, some recent studies have presented evidence to field-dependent exciton dissociation in low-offset OSC systems [63–65]. The detailed mechanism is, however, still under debate. In chapter IV. 1 and IV. 3, more evidence for field-dependent exciton dissociation process in low-offset OSC systems will be presented and discussed.

Recently, extensive attention has been drawn to a fascinating phenomenon observed in a range of low-offset NFA-based OSC devices. These devices have demonstrated the remarkable ability to efficiently generate charges with a minimal amount of driving force, which is beneficial for the overall performance [23]. Quadrupole moments are suggested to be playing an important role in the efficient charge generation properties in these low-offset OSC systems [50, 66]. In addition, with decreased driving force leading to reduced energetic offset between S_1 and CT ($\Delta E_{S_1\text{-CT}}$), these low-offset OSC present different charge generation and recombination properties compared to the traditional OSC systems with large driving force. For example, Classen et al. [42] proposed a Boltzmann stationary-state equilibrium between S_1 and CT states which nicely explains the relationship between $\Delta E_{S_1\text{-CT}}$ and charge generation efficiency. An important consequence of this is the beneficial long-lived excitons which facilitates efficient charge generation. Other studies argue that $\Delta E_{S_1\text{-CT}}$ does not only change the equilibrium between S_1 and CT, but also the CT dissociation barrier [67]. Theoretical studied stressed the important role of $\Delta E_{S_1\text{-CT}}$ in the overall device performance [68], this topic will be discussed in more detail in chapter IV. 1 and IV. 3.

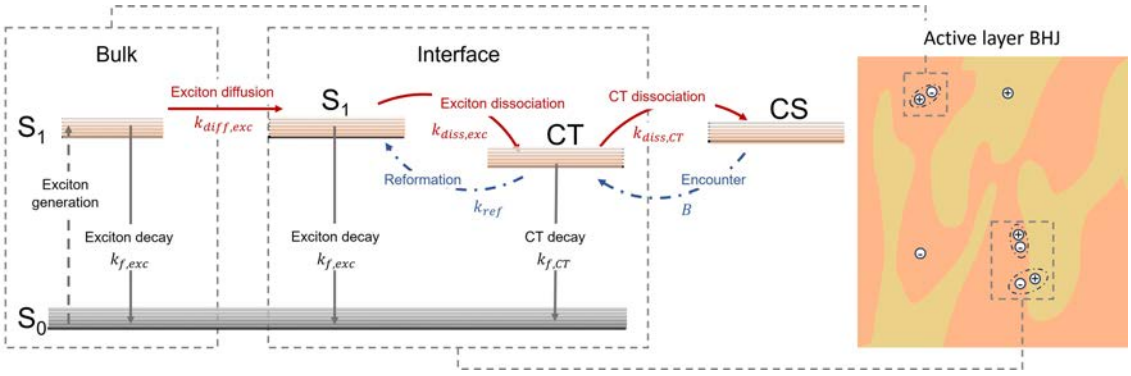

Figure II. 2.2: Energetic model showing the interplay and decay processes of S_1, CT and charge separated (CS) state. Singlet excitons are generated in the bulk or at the donor:acceptor interface upon illumination. The photogenerated excitons then diffuses to the donor:acceptor interface with a diffusion rate constant of $k_{\text{diff,exc}}$, or decay with the rate constant of $k_{\text{f,exc}}$. At the donor:acceptor interface, exciton dissociation can happen and form CT states due to the driving force created by the offset between HOMO-HOMO and LUMO-LUMO of the donor and acceptor, with the rate constant of $k_{\text{diss,exc}}$. The exciton dissociation process is in competition with exciton decay, similar to that of exciton diffusion. The CT state generated by exciton dissociation can then split to form free charge (CS). In the operation of an OSC device, CS can encounter each other and recombine again by reforming the CT states. Similar to the S_1 states, CT states also decay to ground state and with the rate of $k_{\text{f,CT}}$. In the systems with low energetic offset between S_1 and CT, the CT states can repopulate the S_1 state, with the reformation rate of k_{ref}.

II. 2.2.3 Charge Transportation

As introduced in chapter II. 1, in organic semiconductors, a disordered energetic landscape is formed in HOMO and LUMO. As is shown in Figure II. 2.3, the energy distribution of the energetic states, $\text{DOS}_{\text{Gauss}}$, in organic semiconductors show a disordered feature which is often described with a Gaussian model (equation II. 2.5) [69]. The center of the disorder ξ_0 represents the energy level where the most energetic state locates, and this energy is usually marked as ξ_0=0 [70]. The standard deviation of the Gaussian model,

σ, describes the shape of the distribution and is usually used as a parameter which evaluates the energetic disorder of the organic system[71].

$$DOS_{\text{Gauss}} = \frac{N_C}{(2\pi\sigma)^2} exp(-\frac{(\xi - \xi_0)^2}{2\sigma^2}) \tag{II. 2.5}$$

where N_C is the total density of states, σ the standard deviation of the DOS distribution, ξ and ξ_o are the energy of interest and the center of the DOS, respectively.

The transportation of photogenerated charges is realized by hopping of photocarriers among the localized states (hopping mechanism) [72, 73]. The hopping rate of carriers can be described by the Miller-Abraham model developed in 1960 [74]. As indicated from the Miller-Abraham model, efficient "hopping" from site *i* to *j* requires a close physical distance between the two states, as well as a higher or comparable energy level of site *i* compared to site *j*:

$$w_{ij} = \upsilon_0 \cdot exp(-2\gamma r_{ij}) \begin{cases} exp(-\frac{\xi_j - \xi_i}{k_B T}) & \xi_j \geq \xi_i; \\ 1 & \xi_j < \xi_i. \end{cases} \tag{II. 2.6}$$

where υ_o is the attempt hopping frequency, γ the inverse localization radius of the electron wavefunction that describes how well charges can tunnel from site *i* to *j* ; r_{ij} is the distance between the sites; ξ_j and ξ_i are the energy of site *i* and *j*, respectively.

Considering the charges are hopping in a Gaussian DOS within a Miller-Abraham framework, Heinz Bässler developed the Gaussian disorder model (GDM) in the year 1993 and explored the behavior of charges in such Gaussian DOS landscape via Monte Carlo simulations [69]. As suggested by the simulation, when a charge with high energy comes into the DOS distribution and hops forward, it tends to first lower its energy while finding the adjacent site to hop on, until a dynamic equilibrium is reached (the charge relaxes on a certain energy level), given sufficiently long lifetime of this carrier. The equilibrium energy ξ_∞ can be analytically obtained at zero electric field as σ^2/k_BT below ξ_o. However, the density of available states at this energy level is low and cannot result in efficient hopping and charge transportation; the major contribution to the transport level comes from the states at around $\sigma^2/2k_BT$ below ξ_o. [69, 75]

Under the GDM framework, mobility of charge can be described with a temperature and field-dependent expression (equation II. 2.7) [69, 76–78]. Equation II. 2.7 shows a non-Arrhenius type $1/T^2$ temperature dependence of mobility and a field dependence of $\mu(E) \sim exp(\beta\sqrt{E})$, which agrees to the Poole-Frenkel model [75, 79].

$$\mu_{\text{GDM}} = \mu_0 \cdot exp\left(-\left(\frac{2\sigma}{3k_BT}\right)^2\right) \times \begin{cases} exp\left[C\left(\left(\frac{\sigma}{k_BT}\right)^2 - \Sigma^2\right)\sqrt{E}\right] & \Sigma \geq 1.5 \\ exp\left[C\left(\left(\frac{\sigma}{k_BT}\right)^2 - 2.25\right)\sqrt{E}\right] & \Sigma < 1.5. \end{cases} \tag{II. 2.7}$$

where μ_o is the mobility at $T \to \infty$, C is a constant representing the spacing of the sites, and Σ describes the degree of positional disorder.

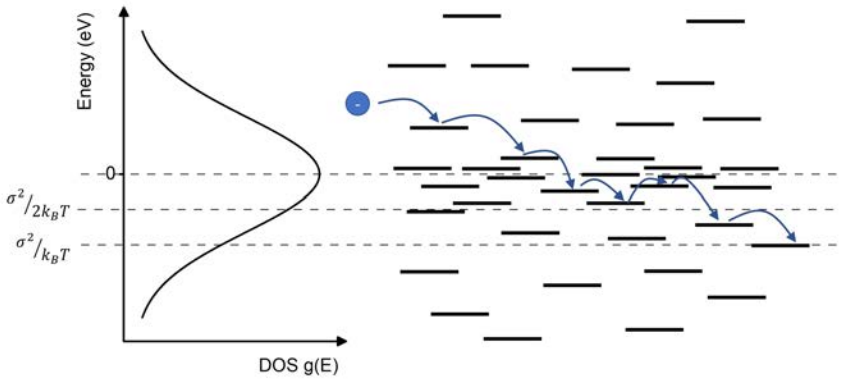

Figure II. 2.3: Charge transportation via hopping mechanism in a disordered density of states (DOS) in organic semiconductors.

The GDM model gives inspiring insights into the physics of charge transportation in disordered semiconductors. However, it neglects the effect of carrier density by assuming that the target site is always empty. As the carrier density increases, the excess carriers fill the low-energy states in the DOS and thus the mobility is higher than predicted in equation II. 2.7, given the same temperature and electric field. Such consideration was taken into account by Pasveer et al. [80] in 2005 in an extended Gaussian disorder model (EGDM).

Mobility of charges plays a vital role in achieving an efficient OSC device. As the photogenerated carrier will recombine and result in a loss of energy if not collected, the extraction and recombination of charges are in a competition once the photocarriers are generated. In this regard, high carrier mobilities benefits the device performance by facilitating the collection of free carriers.

II. 2.2.4 Loss channels of charges

As discussed in section II. 2.2.2, the photogeneration of free carriers in organic solar cells can be considered as a two-step process. The decay of excited states and thus carrier losses can occur during each step (depicted by the grey lines in Figure II. 2.2). In addition, upon encountering of free carriers, CT state is formed, which can decay to ground state or reform the exciton. The recombination rate, R, can be understood as the decay of carrier density over time, and be further described with an effective recombination coefficient and carrier density:

$$R = -\frac{dn}{dt} = \gamma n^{\delta} \tag{II. 2.8}$$

where n is the free carrier density, γ the recombination coefficient, and δ the recombination order. The value of the recombination order depends on the exact recombination mechanism.

II. 2.2.4.1 *Monomolecular recombination*

Monomolecular recombination is effectively a one-element process where only one particle is involved in the recombination process. In the case of monomolecular re-

combination, the value of δ in equation II. 2.8 is 1. In the framework of the energetic scheme shown in Figure II. 2.2, this particle is understood as an exciton or a geminate pair originated from the same photon (also named geminate recombination).

The recombination order can also be statistically observed to be 1, even though the recombination mechanism is not geminate. This is usually observed when a considerable amount of recombination center is involved in the recombination process. One example is the recombination between photogenerated charges with dark injection charges (which originates from the charge carrier diffusion from the metallic electrodes into the active layer). In low fluence condition, the apparent recombination order is 1, although the recombination mechanism falls in a non-geminate bimolecular recombination [81, 82]. Other examples include surface recombination and trap-assisted recombination, etc. [83, 84].

II. 2.2.4.2 *Bimolecular recombination*

As suggested by the name, bimolecular recombination is a two-element process and involves two species. Bimolecular recombination has been widely suggested as a main loss channel in many organic solar cells [84–87]. In the case of bimolecular recombination, the value of δ in equation II. 2.8 is 2, and γ is referred as the bimolecular recombination coefficient (usually denoted as k_2).

The recombination upon the encountering of electrons and holes was first described by Langevin and dubbed as the classic Langevin model. The Langevin recombination is based on two main assumptions: [88, 89] i) the electrons and holes are homogeneously distributed in homogeneous medium, and ii) bimolecular recombination occurs once the distance between an electron and a hole, a, is within their recombination cross-section (r_C). The radius of this recombination cross-section is defined in terms of the Coulomb potential between them (equation II. 2.9). [90]

$$r_C = \frac{q^2}{4\pi\epsilon\epsilon_0 k_B T} \tag{II. 2.9}$$

In the framework of classic Langevin recombination model, the Langevin bimolecular recombination coefficient (k_L) is given by [88, 91]:

$$k_L = \frac{q}{\epsilon\epsilon_0}(\mu_e + \mu_h), \tag{II. 2.10}$$

where μ_e and μ_h are the mobilities of electrons are holes, respectively.

The Langevin theory provides important insights to charge recombination mechanism. However, in real organic solar cells, neither of the two main assumptions in Langevin theorem is valid. A reduction is widely observed in actual bimolecular recombination rate coefficient k_2 compared to k_L. In this regard, k_2 can be described as the product of k_L and a Langevin reduction factor γ_L ($k_2 = \gamma_L \cdot k_L$). The exact value of γ_L was found to vary in a large range, depending on multiple influencing factors, including the materials used in active layer, additives, treatments, and other fabrication details [13, 16, 49, 92].

Almost all state-of-the-art organic solar cells consist of two materials – the donor and the acceptor. Upon the operation of organic solar cells, the holes and electrons are

restricted in donor and acceptor phase, respectively. Thus, recombination only happens at the donor:acceptor interface which reduces k_L. One theoretical work from Koster et al.[93] in 2006 suggested that in the scenario of BHJ configuration, the value of k_L is dictated by the slower carrier (equation II. 2.11). Other relations between k_L and charge mobilities have also been suggested, depending on detailed morphology circumstances [94, 95].

$$k_L = \frac{q}{\epsilon\epsilon_0} \cdot min(\mu_e, \mu_h), \tag{II. 2.11}$$

These models which relate k_L directly to mobilities assume an encounter-limited scenario. However, numerous studies have pointed out that the recombination in organic solar cells happens via an intermediate state (which is understood to be the CT state) [89, 96, 97]. Here the charge separated state (CS) and CT states are considered to be in an equilibrium with one another - meaning that the reformed CT states upon the encounter of free charges can re-split into free charges [89]. Note that due to the low external radiation efficiency (ERE) of CT states, the recombination process here upon the encountering of photogenerated free electrons and holes is supposed to be highly non-radiative [98]. However, some recent studies have found that in some low-offset NFA based systems, the excitons can be repopulated from the CT states. Consequently, in these systems, upon the encountering of free charges, part of the recombination also proceeds via excitons. As excitons generally have much higher ERE than CT states, the recombination in these systems are found to be much more radiative compared to that in high-offset systems, leading to low non-radiative losses [25, 98–100] (ΔV_{nr}) in these systems (will be discussed in more detail in section II. 2.3).

II. 2.2.4.3 *Trap-assisted recombination*

The trap-assisted recombination (also referred to as SRH recombination, which was first proposed by Shockley, Read and Hall in 1952 [101]) occurs via the traps within the bandgap which can be donor-like or acceptor-like. The donor-like traps are positively charged when occupied by a hole and neutral when empty, and vice versa for the acceptor-like traps. The SRH recombination is a two-step recombination process. During SRH recombination, one type of charge carrier is first captured by the traps, then this trapped carrier can either escape from the trap or recombine subsequently with the counter charge. The probability that the trapped carrier escapes from the trap depends how deep the trap is compared to the conduction band (for electrons) or valence band (for holes).

Taking acceptor-like traps as an example, the SRH recombination rate can be expressed as [102]:

$$R_{SRH}^{-} = k_{SRH}^{-} \cdot n_e \cdot n_h, \tag{II. 2.12}$$

where k_{SRH} is the effective SRH recombination rate coefficient; n_e and n_h are the densities of electrons and holes, respectively.

Considering traps with energy E_t, the effective SRH recombination coefficient via these acceptor-like traps, k_{SRH}^{-}, can then be described via equation II. 2.13.

$$k_{SRH}^{-} = \frac{C_e C_h N_t}{C_e(n_e + n_{e,1}) + C_h(n_h + n_{h,1})}, \tag{II. 2.13}$$

where N_t is the trap density at energy E_t, C_e and C_h are capture coefficients for electrons and holes, respectively. $n_{e,1} = N_C \cdot exp((E_t - E_C)/k_B T)$, and $n_{h,1} = N_V \cdot exp((E_V - E_t)/k_B T)$, where N_C and N_V are effective density of states on the conduction and valence band, respectively.

The effective recombination order of SRH recombination can vary between 1 and 2, depending on the depth of the traps compared to the conduction or valence band. In the case of mid-gap traps where the escaping of charges from the traps is highly inefficient, the traps effectively act as recombination centers. In this condition, $n_{e,1}$ and $n_{h,1}$ become negligible, then k_{SRH}^{-} can be approximated to $k_{SRH}^{-} \approx C_e C_h N_t / n \cdot (C_e + C_h)$ (assuming $n \approx p$), and thus the recombination rate R_{SRH}^{-} is in a linear relation with carrier density n. In this condition, δ=1 and the recombination is effectively monomolecular. Whereas when the traps are very close to the conduction or valence band, the trapped carriers can easily escape from the traps via thermal activation. In this scenario, the traps effectively simply reduce the mobility of the charge carriers rather than acting as recombination centers, and the recombination order is 2.

II. 2.3 Device Physics of Organic Solar Cells

II. 2.3.1 Equivalent Circuit Model

The electric behavior of an operating OSC device in an electric circuit can be described with an abstract model by considering the OSC device as a combination of several ideal electronic components. Figure II. 2.4 shows one of the most common and basic equivalent circuit models for describing organic solar cells. In the model presented, the electric characteristics of an OSC device is described with a combination of a current source, an ideal Shockley diode, a shunt resistor (R_{sh}) and a series resistor (R_s). In the following, the concepts behind these electronic components will be explained and discussed by linking them to the device physics of OSCs.

The current source provides a photocurrent density (J_{ph}) under illumination. Following the conservation law, for an operating solar cell device in the steady-state, the photo-generated free charge carriers are either extracted or they recombine. Hence, for each applied voltage, the relationship among current, recombination rate, and generation rate can be obtained in the form of equation II. 2.14 in the steady state condition:

$$J_{ph} = q \int_0^d (R - G)\, dx, \tag{II. 2.14}$$

where G and R are the generation and recombination rates of free carriers at a given position in the device.

As indicated from equation II. 2.14, under the steady-state operational conditions, at a fixed generation rate, the faster the free carriers move towards the electrodes to be extracted, the less chance they recombine. Starting from equation II. 2.14, Bartesaghi et al.[87] arrived at a dimensionless parameter θ for the evaluation of charge recombination

and extraction (equation II. 2.15), which is proportional to the ratio between the current densities of recombination and extraction (J_{rec} and J_{extr}, respectively).

$$\theta = \frac{k_2 G d^4}{\mu_e \mu_h (V_{int})^2} \propto \frac{J_{rec}}{J_{extr}} \tag{II. 2.15}$$

In a basic organic solar cell as shown in Figure II. 2.1, interlayers are employed between the active layer and the electrodes. Following Richardson-Schottky model, the injection current from the metal into the semiconductor layer via thermionic emission at the metal-semiconductor interface is given by: [31]

$$J_{inj} = A_G T^2 exp(-\frac{\Phi_{eff}}{k_B T})) \tag{II. 2.16}$$

where A_G is the effective Richardson constant, and Φ_{eff} the effective injection barrier which can be defined by the energetic difference between the HOMO (for hole injection) and LUMO (for electron injection) levels of the interlayer and the work function of the electrode.

Equation II. 2.16 indicates that the injection current is strongly related to the height of the effective injection barrier Φ_{eff}. Due to the designed energetic alignment between each layer in the device, the injection of holes (electrons) from the anode into the device is highly efficient (inefficient), and vice versa for the cathode. Therefore, when putting an OSC device into a circuit and applying a bias (V_{app}) to the device, efficient charge injection can be realized only when injecting holes from the anode and electrons from the cathodes (when V_{app} is larger than the built-in voltage, V_{bi}). In this regard, OSC devices are effectively also diodes. The diode characteristics of OSC devices are commonly represented with an ideal Shockley diode in the equivalent circuit model, and is analytically described with the Shockley diode equation: [102]

$$J(V) = J_0(exp(\frac{qV}{n_{id} k_B T}) - 1) - J_{ph}(V) \tag{II. 2.17}$$

where J_o is the dark saturation current density; n_{id} the ideality factor which is related to the exact recombination mechanism in the device [103], and J_{ph} the photocurrent density.

Practically however, OSC devices are not ideal diodes. In the equivalent circuit model shown in Figure II. 2.4, two main considerations are included for a better representation for the realistic scenario: 1) a series resistance (represented as R_s) is included for correcting the voltage drop in the electrodes and connecting cables, and 2) a shunt resistance (represented as R_{sh}) is included in parallel to the diode. The shunt current is usually considered to be related to the imperfections in the diode structure of the device, such as imperfect blocking effect of the interlayers (e.g., pin-holes or energetic issues) [102, 104]. The consideration of R_s and R_{sh} leads to a modified Shockley diode equation (equation II. 2.18) [29, 105, 106].

$$J(V) = J_0(exp(\frac{q(V_0 - JR_s)}{n_{id} k_B T}) - 1) + \frac{V - JR_S}{R_{sh}} - J_{ph}(V) \tag{II. 2.18}$$

It is important to acknowledge that although equations II. 2.17 and II. 2.18 offer valuable insights into the understanding of *J-V* characteristic of the devices, their direct

application for fitting actual experimental *J-V* data is often challenging and necessitates modifications [29]. For instance, Würfel and Neher et al. [105] have pointed out the importance of accounting for the impact of mobilities and recombination in low-mobility systems in the Shockley equations. Apart from the one shown in Figure II. 2.4, modified and more advanced equivalent circuit models have also been employed for the interpretation of different characterization techniques, as well as various simulations and analytical calculations [107–109].

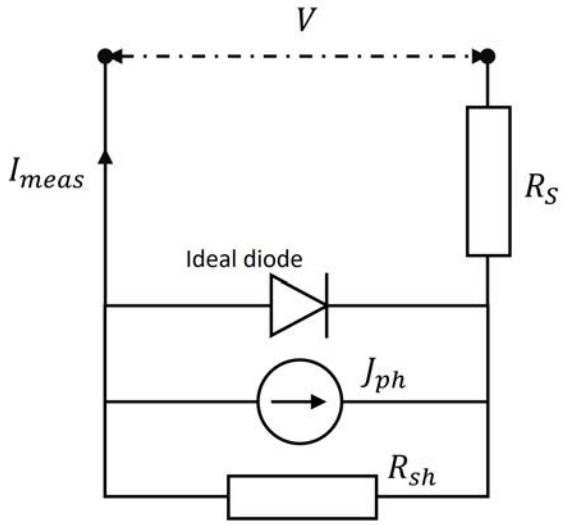

Figure II. 2.4: A simple equivalent circuit model for an OSC device.

II. 2.3.2 *J-V* Characteristics and Power Conversion Efficiency

The power conversion efficiency of an OSC device can be obtained from the ratio between the electrical output power density from the device (P_{out}) and the power density of incident radiation (P_{in}). The most well-established characterization for finding the maximum P_{out} of an OSC device is to put it in an electric circuit under illumination; apply various biases (V) and plot the measured current density (J_{light}) against the corresponding applied biases. In this way, a *J-V* characteristic of the device can be obtained (Figure II. 2.5). Getting the product of applied voltage and corresponding current density enables the calculation of the P_{out} at each bias, as mentioned in section II. 2.3.1, the recombination-to-extraction factor θ is subjective to applied bias. Hence, the P_{out} varies upon the change of the applied bias. Getting the P_{out} for each voltage condition, a maximum output power density can be found (denoted as P_{MPP}). The value of P_{MPP} is defined by three important parameters as shown in equation II. 2.19, namely short circuit current density, J_{SC}, open circuit voltage, V_{OC}, and the fill factor, FF, as marked in Figure II. 2.5. In Figure II. 2.5 the ratio between the areas of the dark and light red squares is the FF , it describes the “squareness” of the *J-V* plot and ranges between 0 and 1.

$$P_{MPP} = J_{MPP} \cdot V_{MPP} = J_{SC} \cdot V_{OC} \cdot FF \tag{II. 2.19}$$

$$PCE = \frac{P_{MPP}}{P_{in}} = \frac{J_{SC} \cdot V_{OC} \cdot FF}{P_{in}} \tag{II. 2.20}$$

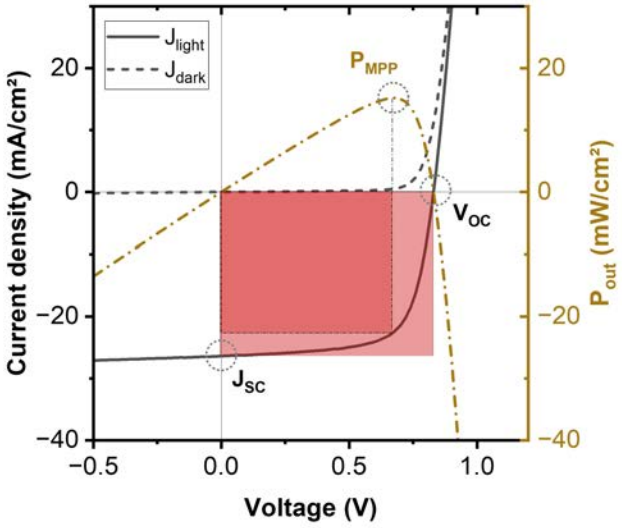

Figure II. 2.5: *J-V* characteristic of an organic solar cell (PM6:Y6) along with relevant parameters.

II. 2.3.2.1 *Short Circuit Current (J_{SC})*

J_{SC} corresponds to photocurrent density output from the device when the applied bias equals zero. In this condition, photogenerated free charges are collected with the help of the built-in field in the device. One of the most important measurements for understanding J_{SC} losses is the external photovoltaic quantum efficiency measurement (EQE_{PV}) which evaluates how efficiently incident photons are converted to electrons in a given organic solar cell at each incident wavelength.

EQE_{PV} measurements are usually performed at J_{SC} condition. The value of EQE_{PV} at each incident wavelength can be obtained with equation II. 2.21. Ideally, convoluting EQE_{PV} and AM 1.5G solar spectrum and integrating over the wavelength gives an integrated current density value J_{int} which equals to J_{SC} (equation II. 2.22).

$$EQE_{PV}(\lambda) = \frac{\#\ of\ collected\ charges}{\#\ of\ incident\ photons} = \frac{h \cdot c \cdot I(\lambda)}{q \cdot \lambda \cdot P_{in}(\lambda)} \qquad \text{(II. 2.21)}$$

where h is Planck constant, c the speed of light, I the measured current, q the elementary charge, and $P_{in}(\lambda)$ the incident light power at given incident wavelength which can be measured with a calibrated photodetector.

$$J_{int} = J_{SC} = \frac{q}{hc} \int \lambda \cdot EQE_{PV}(\lambda) \cdot E_{E,AM\,1.5}(\lambda)\, d\lambda \qquad \text{(II. 2.22)}$$

where $E_{E,AM\,1.5}(\lambda)$ is the standard AM1.5 solar spectral irradiance. [36]

As shown in equation II. 2.21, the value of EQE_{PV} at each incident wavelength depends on the measured current I. The value of I can be affected by many processes described in section II. 2.2, such as light absorption, exciton diffusion, exciton dissociation, CT dissociation, and charge extraction (the recombination of charges during charge extraction). In this regard, the EQE_{PV} can also be described with the efficiency of each basic process during the successful collection of free carriers:

$$EQE_{PV}(\lambda) = \eta_{abs}(\lambda) \cdot \eta_{ex,diff} \cdot \eta_{ex,diss} \cdot \eta_{CT,diss} \cdot \eta_{coll} \quad \text{(II. 2.23)}$$

where η_{abs}, $\eta_{ex,diff}$, $\eta_{ex,diss}$, $\eta_{CT,diss}$ are the efficiency for light absorption, exciton diffusion, exciton dissociation, and CT dissociation, respectively. η_{coll} is the collection efficiency of photogenerated free carriers and is related to the competition between the drift velocity and recombination rate of the photogenerated free carriers. An internal photovoltaic quantum efficiency (IQE_{PV}) is defined on the basis of equation II. 2.23 by correcting out the optical absorption term from $EQE_{PV}(\lambda)$, with

$$IQE_{PV} = \eta_{ex,diff} \cdot \eta_{ex,diss} \cdot \eta_{CT,diss} \cdot \eta_{coll}. \quad \text{(II. 2.24)}$$

Optical considerations are to be carefully taken into account when analyzing EQE_{PV} spectra to avoid falsify conclusions. For example, Grancini et al. [110] reported a photon-energy dependent IQE_{PV} spectrum of PCPDTBT:$PC_{[60]}BM$ as an evidence for the presence of hot-exciton effect in 2013, obtained by normalizing the EQE_{PV} spectrum by the film absorption. However, further studies clearly showed that the photon-energy dependent IQE_{PV} spectrum is a result of cavity effect and parasitic absorption [111, 112]. Another important scenario for optical consideration is when applying Marcus model and fitting the EQE_{PV} spectra to obtain the CT state energy (E_{CT}). Substantial error can be expected when cavity effect is not correctly addressed [113]. Apart from the analyses of EQE_{PV} spectra, such low finesse cavity effect is to be considered also for the understanding of other measurement techniques, such as differential absorption spectroscopies including transient absorption spectroscopy (TAS), photoinduced absorption spectroscopy (PIA), and charge modulation spectroscopy (CMS) etc., [17] as will be discussed in more detail in chapter IV. 4.

II. 2.3.2.2 *Open Circuit Voltage (V_{OC})*

V_{OC} evaluates the electrical potential capability of the device and is determined at the voltage condition where no current flows in an illuminated device due to the application of an external bias. In V_{OC} condition, no photogenerated charges can be extracted and all of them recombine in the solar cell, equation II. 2.25 can therefore be obtained, where the current density of charge generation, J_{gen}, equals that of recombination, J_{rec}.

$$J_{gen} = J_{rec} = qdR \quad \text{(II. 2.25)}$$

Meanwhile, in V_{OC} condition, connecting the Shockley diode equation (equation II. 2.17) and equation II. 2.25 yields

$$J_{gen}(V_{OC}) = J_{rec}(V_{OC}) = J_0 \cdot exp(\frac{qV_{OC}}{n_{id}k_BT}) - 1 \quad \text{(II. 2.26)}$$

Rewriting equation II. 2.26, an explicit expression for V_{OC} can be arrived (equation II. 2.27). J_{rec} (V_{OC}), which equals to J_{gen} (V_{OC}), can be experimentally determined from the saturation photocurrent at high reverse bias condition (J_{sat}), when the rate of free charge generation (the product of first four efficiencies in equation II. 2.23) is field-independent.

In the case that bimolecular recombination between free charges dominates the recombination process, n_{id} equals 1 and therefore is often omitted from equation II. 2.27. In usual operating conditions, $J_{gen}(V_{OC}) \gg J_0$, therefore the term of "1" is also often omitted.

$$V_{OC} = \frac{n_{id} k_B T}{q} \cdot ln\left(\frac{J_{gen}(V_{OC})}{J_0} + 1\right) \tag{II. 2.27}$$

J_0 in the Shockley diode equations represents the recombination current density in the cell at thermal equilibrium in the dark condition. When considering an ideal Shockley diode, all recombination occurs radiatively, and J_0 reaches its radiative limit, $J_{0,rad}$, with:

$$J_{0,rad} = q \cdot \int_0^{end} EQE_{PV}(E) \cdot \phi_{BB}(E)\, dE \tag{II. 2.28}$$

where ϕ_{BB} is the black body photon flux.

In realistic organic solar cells, most recombination proceeds via the CT states which has been widely observed to have a low emissivity [114]. Therefore, a large fraction of recombination occurs non-radiatively which deviates their J_0 from $J_{0,rad}$. The quantum yield of electroluminescence (ELQY), which quantifies the external radiative efficiency (ERE), can be experimentally determined to relate J_0 to $J_{0,rad}$ with $J_0 = J_{0,rad}/\mathrm{ELQY}$. Hence, equation II. 2.27 can be modified into equation II. 2.29 for realistic OSCs.

$$V_{OC} = \frac{k_B T}{q} \cdot ln\left(\frac{J_{gen}(V_{OC})}{J_{0,\,rad}} + ln(ELQY)\right) \tag{II. 2.29}$$

From the perspective of equation II. 2.29, V_{OC} of the device can be understood as the result of non-radiative voltage losses (ΔV_{nr}) from the radiative voltage limit ($V_{OC,rad}$), with ΔV_{nr} and $V_{OC,rad}$ in the forms of equations II. 2.30 and II. 2.31.

$$\Delta V_{nr} = -\frac{k_B T}{q} \cdot ln(\mathrm{ELQY}) \tag{II. 2.30}$$

$$V_{OC,rad} = \frac{k_B T}{q} \cdot ln\left(\frac{J_{gen}(V_{OC})}{J_{0,rad}}\right) \tag{II. 2.31}$$

Efforts have been made to understand and reduce the ΔV_{nr} in OSC systems. As the majority of free charge recombination proceeds via CT decay [25, 98], the emission efficiency of CT states plays a vital role in the value of V_{OC}. With the study of a large set of donor:acceptor combinations, Benduhn et al. [115] pointed out that the emission efficiency of CT states follow the energy-gap law [116], indicating the intrinsic link between ΔV_{nr} and electron-vibration coupling, and the inevitable non-radiative losses in OSC systems. Later studies from Chen et al. [117] reported systems disobeying energy-gap law between ΔV_{nr} and E_{CT} in low-offset OSC systems and found that the lower limit of ΔV_{nr} in these systems is defined by the PLQY of the pristine material with lower band-gap in the blend. This finding has induced the motivation in synthesizing highly luminescent NFA molecules [23, 118]. The avoidance of energy-gap law in low-offset systems can be explained by the re-population of exciton from CT states given a low energetic offset between S_1 and CT ($\Delta E_{S_1\text{-}CT}$) [25]. However, it is still under debate whether and to what extent the re-population process benefits the V_{OC} of the device. In addition, the role

of S_1-CT hybridization needs to be clarified [119]. As pointed out by Perdigón et al. [25], while the re-population of excitons significantly increases and dominates the ELQY due to the much higher emission efficiency of excitons compared to CT states, it does not immediately imply that most of the recombination proceed via exciton decay. On the contrary, in their detailed study on one of the most famous low-offset NFA systems, PM6:Y6, it was concluded that 99% of the recombination current is contributed by CT decay. In another study from Fritsch et al. [98], by tuning the $\Delta E_{S_1\text{-CT}}$ in an alloy-type ternary OSC system, it was pointed out that the V_{OC} was primarily defined by the CT states upon the shift of $\Delta E_{S_1\text{-CT}}$. Importantly, it was demonstrated in this work that re-population process reduces the ΔV_{nr} not because of the high emission efficiency of excitons, rather their strong absorption which reduces the $V_{OC,rad}$. The regime where V_{OC} is defined by the excitons can be entered when $\Delta E_{S_1\text{-CT}}$ is significantly small which, as mentioned in the last section, lead to a low J_{SC}.

II. 2.3.2.3 *Fill Factor (FF)*

FF mainly describes the field-dependence of photocurrent density ($J_{ph} = J_{light}\text{-}J_{dark}$) of the operating solar cell. More specifically, FF reflects the field-dependence of each term in equation II. 2.23.

The most important influencing factor for FF is the charge collection efficiency (η_{coll}) which describes the probability which a photogenerated can be collected and contribute to J_{ph}. When strong collection field presents in the device, the collection field benefits the drift of photocarriers to move towards their corresponding electrodes (holes towards the anode and electrons towards the cathode), leaving less chance for them to recombine, as indicated from equation II. 2.14. In this scenario, collection of photo-carriers is promoted. As V_{app} approaches from 0 V to V_{OC}, the applied voltage compensates the build-in voltage and reduces the collection field in the device. Hence, the drift velocities of photocarriers are reduced, making recombination of free charges the dominating process. From this perspective, the main difference between OSC devices with high and low FF is that in OSC devices with high FF, charge extraction is still highly efficient, even when the built-in field of the device is strongly compensated by V_{app}. η_{coll} can be affected by many factors, such as charge mobility, recombination rate coefficient, and fluence condition, etc. In this regard, Neher et al. [120] proposed a figure-of-merit α in 2016 to evaluate the effect of the competition between charge recombination and extraction on the FF of the device, given by equation II. 2.32. With α being smaller than 1, the device is a "Shockley type" (the *J-V* curve of the device follows the Shockley equation), while the device is transport limited when α is larger than 1.

$$\alpha^2 = \frac{q^2 k_2 G d^4}{4\mu_e \mu_h (k_B T)^2} \tag{II. 2.32}$$

Another major influencing factor for FF is the field-dependence of charge generation. A field-dependent charge generation behavior indicates a reducing free carrier generation efficiency with decreasing internal bias across the active layer which is detrimental to the “squareness” of the J-V characteristic and reduces FF. As mentioned in section II. 2.2.2, the observed field-dependent charge generation behavior in many systems were attributed to the field-dependent CT dissociation process and explained often in the framework of Onsager-Braun model. In several more recent studies, evidence for field-

dependent exciton dissociation was also observed for few low-offset systems. Since these low-offset NFA systems present unique behavior in the charge generation and recombination process while showing fascinating performance, it is vital to understand more about the loss channels and mechanisms for charges in these systems, as will be presented in greater detail in chapter IV. 1 and IV. 3.

II. 3 Simulations for Organic Solar Cells

II. 3.1 Optical Simulation - Optical Transfer Matrix

As mentioned in the last paragraph in section II. 2.2.1, the optical field distribution in a complex thin-film system like organic solar cell is neither uniform nor does it completely follow the Beer Lambert's law due to multi-reflections. In addition, the cavity interference results in Fabry-Perot oscillations in the transmission and reflection spectra of the sample [121], resulting in widely observable artifacts in optical pump and (or) probe experiments [17, 112, 113, 122, 123]. While it is challenging to experimentally eliminate such optical artifacts, corrections can be made in terms of optical simulations, such as optical transfer matrix calculations, as will be introduced and discussed in detail in this section.

The optical field distribution in such thin film systems can be calculated via optical transfer matrix, with knowledge on the structure of the thin-film system, as well as the thickness and optical constants of each layer. As shown in Figure II. 3.1, for a thin-film system, the optical transfer matrix considers two independent waves – forward and backward propagating plane waves ($E^{(+)}$ and $E^{(-)}$, respectively) – at each interface between two layers. The ($E^{(+)}$) and ($E^{(-)}$) take the form of

$$E(x) = E_0 \cdot exp(i \cdot \frac{2\pi\tilde{n}}{\lambda} \cdot x) \tag{II. 3.1}$$

where x the position in space, (E_0 is the amplitude of the wave, λ the wavelength, ñ the generalized complex refractive index of the medium which consists of real refractive index N and extinction coefficient K via

$$\tilde{n} = N + iK \tag{II. 3.2}$$

The four forward and backward-propagating waves at each interface can be related by a transmission matrix M which is defined by the optical constants of the two subject adjacent layers. Taking the i_{th} interface as example, this relationship can be expressed with

$$\begin{bmatrix} E^{(+)}_{i-1,r} \\ E^{(-)}_{i-1,r} \end{bmatrix} = M_{i-1,i} \begin{bmatrix} E^{(+)}_{i,l} \\ E^{(-)}_{i,l} \end{bmatrix} = \frac{1}{t_{i-1,i}} \begin{bmatrix} 1 & r_{i-1,i} \\ r_{i-1,i} & 1 \end{bmatrix} \begin{bmatrix} E^{(+)}_{i,l} \\ E^{(-)}_{i,l} \end{bmatrix} \tag{II. 3.3}$$

where $E^{(+)}_{i-1,r}$ and $E^{(-)}_{i-1,r}$ are the forward and backward waves at the right interface of the $(i\text{-}1)_{th}$ layer, respectively, $E^{(+)}_{i,l}$ and $E^{(-)}_{i,l}$ the forward and backward waves at the left interface of the i_{th} layer, respectively. $t_{i-1,i}$ and $r_{i-1,i}$ the transmission and reflection at the interface between $(i\text{-}1)_{th}$ and i_{th} layer, defined by the complex refractive index of the two layers

and angle of incidence at the interface (θ) via the Fresnel equations (equation II. 3.4a and b) [124], for parallel (p) polarization:

$$r_{p(i-1,i)} = \frac{\tilde{n}_{i-1} cos\theta_i - \tilde{n}_i cos\theta_{i-1}}{\tilde{n}_{i-1} cos\theta_i + \tilde{n}_i cos\theta_{i-1}} \tag{II. 3.4a}$$

$$t_{p(i-1,i)} = \frac{2\tilde{n}_{i-1} cos\theta_{i-1}}{\tilde{n}_{i-1} cos\theta_i + \tilde{n}_i cos\theta_{i-1}} \tag{II. 3.4b}$$

and for perpendicular (s) polarization:

$$r_{s(i-1,i)} = \frac{\tilde{n}_{i-1} cos\theta_{i-1} - \tilde{n}_i cos\theta_i}{\tilde{n}_{i-1} cos\theta_{i-1} + \tilde{n}_i cos\theta_i} \tag{II. 3.5a}$$

$$t_{s(i-1,i)} = \frac{2\tilde{n}_{i-1} cos\theta_{i-1}}{\tilde{n}_{i-1} cos\theta_{i-1} + \tilde{n}_i cos\theta_i} \tag{II. 3.5b}$$

On the other hand, the four waves at the two interfaces on each layer can be related to each other via a propagation matrix P which is defined by the extinction coefficient and thickness of the subject layer in the thin film stack, taking the i_{th} layer as an example,

$$\begin{bmatrix} E_{i,l}^{(+)} \\ E_{i,l}^{(-)} \end{bmatrix} = P_i \begin{bmatrix} E_{i,r}^{(+)} \\ E_{i,r}^{(-)} \end{bmatrix} = \begin{bmatrix} \phi_i^{-1} & 0 \\ 0 & \phi_i \end{bmatrix} \cdot \begin{bmatrix} E_{i,r}^{(+)} \\ E_{i,r}^{(-)} \end{bmatrix} \tag{II. 3.6}$$

where ϕ_i is the phase shift of the wave between E_l and E_r, taking the form of $\phi_i = e^{-jKL}$, where K and L are the extinction coefficient and thickness of layer i, respectively.

Relating equation II. 3.3 and II. 3.6 together enables a transfer matrix formalism to describe the relationship among the four waves on the left side of the first interface and the right side of the last interface of the whole thin film stack ($E_o^{(+)}$, $E_o^{(-)}$, $E_j^{(+)}$ and $E_j^{(-)}$):

$$\begin{bmatrix} E_0^{(+)} \\ E_0^{(-)} \end{bmatrix} = M_{0,1} \cdot P_1 \cdot M_{1,2} \cdot P_2 ... M_{j-2,j-1} \cdot P_{j-1} \cdot M_{j-1,j} \cdot \begin{bmatrix} E_j^{(+)} \\ E_j^{(-)} \end{bmatrix} = \begin{bmatrix} T_{11} & T_{12} \\ T_{21} & T_{22} \end{bmatrix} \cdot \begin{bmatrix} E_j^{(+)} \\ E_j^{(-)} \end{bmatrix} \tag{II. 3.7}$$

where $E_o^{(+)}$, $E_o^{(-)}$ and $E_j^{(+)}$ are essentially the incident wave, reflected wave, and transmitted wave of the whole stack, and $E_j^{(-)}$ equals to 0. Furthermore, $E_o^{(+)}$, $E_o^{(-)}$ and $E_j^{(+)}$ can be related to each other with the definition of transmission and reflection, with $R_{full} = E_0^{(-)}/E_0^{(+)}$ and $T_{full} = E_j^{(+)}/E_0^{(+)}$. Therefore, equation II. 3.7 can be rewritten as

$$\begin{bmatrix} 1 \\ R_{full} \end{bmatrix} = \begin{bmatrix} T_{11} & T_{12} \\ T_{21} & T_{22} \end{bmatrix} \cdot \begin{bmatrix} T_{full} \\ 0 \end{bmatrix} \tag{II. 3.8}$$

Expanding equation II. 3.8, the transmission and reflection of the full stack (T_{full} and R_{full}, respectively) can be expressed by the optical transfer matrix (equation II. 3.9 a and b). This means, optical transfer matrix formalism enables expressing T_{full} and R_{full} simply with the optical constants and thickness of each layer in the stack.

$$T_{\text{full}} = \frac{1}{T_{11}} \tag{II. 3.9a}$$

$$R_{\text{full}} = \frac{T_{21}}{T_{11}} \tag{II. 3.9b}$$

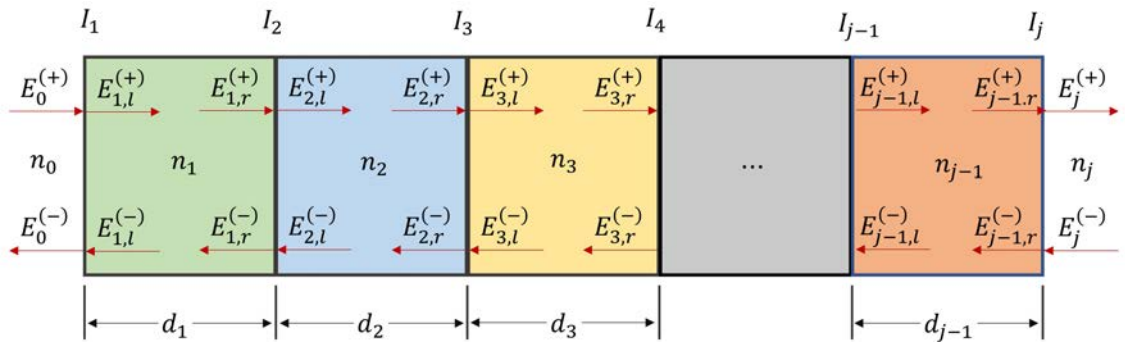

Figure II. 3.1: Scheme of optical transfer matrix calculation. Here a thin film system with *j*-1 layers is considered. n_1 to n_{j-1} are each layer in the film stack. n_0 and n_j are out of the thin film system (considered here as vacuum). I_1 to I_j are the interfaces between each two layers. $E^{(+)}$ and $E^{(-)}$ are the forward and backward waves, respectively.

With optical transfer matrix, one could calculate the plane wave distribution and thus absorption at each position in the device. The time average of the energy dissipated per second in layer *i* at position *x* at normal incidence is given by

$$P_i(x,\lambda) = \frac{1}{2} c \cdot \epsilon_0 \cdot \alpha_i(\lambda) \cdot N_i(\lambda) \cdot |E_i(x,\lambda)|^2 \tag{II. 3.10}$$

where α_i the absorption coefficient of layer *i* ($\alpha_i = (4\pi K_j/\lambda)$), N_i the real refractive index of the layer *i*, and $E_{i(x,\lambda)}$ the sum of the forward and backward propagating waves at position *x* in layer *i*.

Light absorption at each position in the device can then be converted to the distribution of photogeneration rate which could be used as one of the initial input files in the drift-diffusion model (vide infra). With the knowledge of the spectral density of the illumination, the charge generation rate at each position *x* in the active layer can therefore be obtained by integrating the energy dissipation over wavelengths, with the assumption that charge generation efficiency is unity:

$$G_i(x) = \int P_i(x,\lambda)\, d\lambda \tag{II. 3.11}$$

II. 3.2 Drift-Diffusion Simulation

The drift-diffusion model serves as a classical and powerful approach to study device physics in an organic solar cell. By considering charge transport and recombination process, drift-diffusion model enables the simulation of device performance with the

consideration of charge generation, transportation and recombination in the device, on the basis of the equivalent circuit model.

The primary consideration in drift-diffusion model is the continuity equation. The continuity equation relates the movement of electrons and holes to charge generation and recombination. During transportation of charges, electrons and holes may recombine via various decay mechanisms. Typical recombination mechanisms include bimolecular (band-to-band) recombination and trap-assisted recombination can be accounted for with the equations in section II. 2.2.4. The continuity equations can be expressed in the form of equations II. 3.12 a and b for electrons and holes, respectively.

$$\frac{\partial n_e(x)}{\partial t} - \frac{1}{q}\frac{\partial J_e(x)}{\partial x} = G(x) - R(x) \tag{II. 3.12a}$$

$$\frac{\partial n_h(x)}{\partial t} - \frac{1}{q}\frac{\partial J_h(x)}{\partial x} = G(x) - R(x) \tag{II. 3.12b}$$

where J_e and J_h are electron and hole current densities, respectively. G the charge generation rate, and R the charge recombination rate.

The movement of the charges in the simulated device can be described by the drift-diffusion equations. The drift-diffusion equation describes charge transportation in space driven by electric field and the density gradience of charges and can be described with equations II. 3.13 a and II. 3.13 b for electrons and holes, respectively.

$$J_e(x) = n_e(x)\mu_e\frac{dE_C(x)}{dx} + qD_e\frac{dn_e(x)}{dx} \tag{II. 3.13a}$$

$$J_h(x) = n_h(x)\mu_h\frac{dE_C(x)}{dx} + qD_h\frac{dn_h(x)}{dx} \tag{II. 3.13b}$$

where x represents the position in the device, n_e (n_h) is the electron (hole) density, μ_e (μ_h) is the electron (hole) mobility, E_C (E_V) is the conduction (valence) band potential, and D_e (D_h) is the diffusion coefficient for electrons (holes). The mobility and diffusion coefficient can be related to each other via Einstein relation:

$$D_{e(h)} = \frac{\mu_{e(h)}k_B T}{q}\eta_{e(h)} \tag{II. 3.14}$$

where $\eta_{n(p)}$ is a dimensionless coefficient accounting for the density of state (DOS) occupation for electrons or holes. In non-degenerate systems, the diffusion coefficient obeys the classical Einstein relation where $\eta_{n(p)}$=1.

The movement of the charges can result in change in the distribution of charges and therefore affect the field distribution. This can be described by the Poisson's equation:

$$\frac{\partial F}{\partial x} = \frac{1}{q}\frac{d^2E_{C,V}}{dx^2} = \frac{n_e(x) - n_h(x)}{\epsilon\epsilon_0} \tag{II. 3.15}$$

where F is the electric field, and E the potential energy.

Part III

EXPERIMENTAL

This chapter introduces the most important experimental methods involved in this thesis. Here involves not only the standardized experimental techniques such as basic device fabrications, current-voltage characteristics (*J*-*V*), photovoltaic external quantum yield (EQE_{PV}), and transmission/reflection spectroscopies (UV-VIS), but also more advanced spectroscopies including time-delayed collection field (TDCF), bias-assisted charge extraction (BACE) and photo-induced absorption. In addition, emission spectroscopies such as photoluminescence and electroluminescence also serve as important characterization techniques in this work.

III. 1 Experimental Methods

III. 1.1 Material and Sample Fabrication

The materials employed in this thesis can mainly be classified into two groups: namely the photosensitive organic semiconductors that form the active layer, and photo-insensitive organic semiconductors that form the interlayers. The active layers involved here consist of polymer donor and small molecular acceptor. Figure III. 1.1 shows the chemical structures of all materials in this thesis. PM6 (also often named as PBDB-T-2F) was used as the polymer donor, and the employed acceptors include o-IDTBR, Y5, Y6 and TPT10. All materials used in this thesis were purchased from 1-material Inc. As for the interlayer materials, PEDOT:PSS (aqueous solution, purchased from Clevios, AL4083) was used as the hole transport material, and PDINO was employed as the electron transport material. The full chemical names of all materials can be found in the chapter E.

All solar cells devices in this thesis were fabricated in the structure of glass/ITO/PEDOT:PSS/active layer/PDINO/Ag. To start the fabrication, patterned ITO substrates (Psiotec, UK) were firstly sonicated in Hellmanex (3%), deionized water, acetone and isopropanol for 20 min, 20 min, 5 min and 10 min, respectively. The cleaned ITO substrates were then further treated with O_2 plasma at 200 W for 4 min. Thereafter, aqueous PEDOT:PSS solution was first filtered through a 0.45 µm PTFE filter and spin coated on top of ITO to form a layer of around. The substrates were then immediately transferred to a glovebox to finish the rest of the solar cell fabrication procedure.

Solutions of donor:acceptor blend and interlayer were prepared, the blend of in chloroform in the total concentration of 12 mg/ml (0.5 vol% of 1-chloronaphtalene (CN) was added as additive for some of the systems). The weight ratio of donor and acceptor was 1:1.2. PDINO was dissolved in methanol in the concentration of 1 mg/ml. Both active layer and interlayer solutions were stirred at room temperature in the glovebox for 3 hours, then spin coated on top of PEDOT:PSS layer at 2000 rpm to form the active layer of $\sim$100 nm. For the systems where CN was added, the active layer was thermally annealed at 110 °C for 10 min. Thereafter, PDINO solution was spin coated on top of the active layer to form a $\sim$15 nm electron transport layer (ETL). The samples were sent into a thermal evaporator. Silver was thermally evaporated on top of the ETL through a patterned mask in a high vacuum atmosphere (1×10^{-6} mbar) to form the top contact and complete the device. The thickness of the top contact is 100 nm for normal devices and 35 nm for semitransparent devices. The overlapping area of the ITO and silver pattern defines the area of the device. The resulting device area was 0.06 cm^2 (for device characterizations in steady states) or 0.011 cm^2 (for TDCF and BACE).

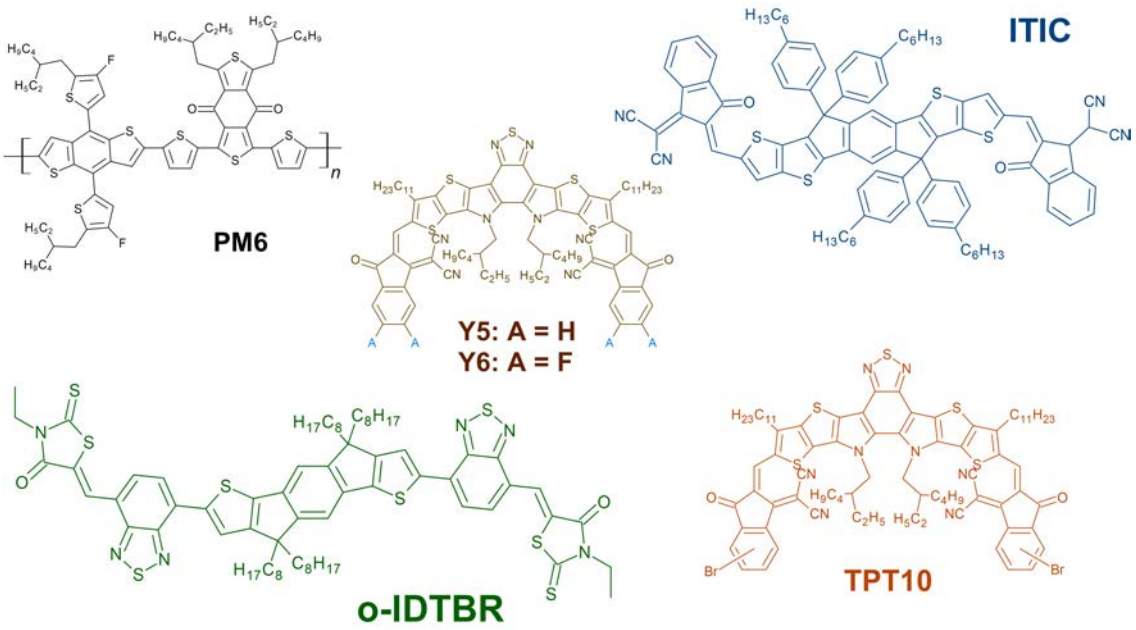

Figure III. 1.1: Employed donor and acceptors in this thesis. The full chemical names can be found in chapter E.

III. 1.2 Current Density-Voltage (*J-V*) Characterization

In JV characterization, a Newport Oriel Sol2A solar simulator was used as the light source to simulate the AM1.5G irradiation spectrum, with the fluence of 100 mW/cm^2. Keithley 2400 system was used to apply voltage on the devices and measure the current in two-wire mode. The *J-V* measurements were conducted in the N2 atmosphere. The illumination intensity was adjusted to the AM1.5G condition using a calibrated Si solar cell.

III. 1.3 External Photovoltaic Quantum Efficiency (EQE_{PV})

In photovoltaic external quantum efficiency (EQE_{PV}) measurement, the device was excited with monochromatic light with low fluence, while short circuit current (J_{SC}) was recorded. A Phillips Halogen lamp was used as the light source, the broadband white light was first input into a cornerstone monochromator and then guided to the sample via optical fiber. A ThorLabs MC2000 chopper system with a 2-blade chopper was place between the light source and the monochromator to modulate the light. The phase and frequency of the modulation was input into a Stanford Research system SR830 lock-in amplifier as an external reference. A lens was used between the output of the optical fiber and the sample to focus the monochromatic light into a small light spot which is smaller than the width of the device pixel. The electrical response (short circuit current) of the sample upon the excitation of modulated monochromatic light was first amplified by a Stanford Research system SR570 preamplifier and then input into the lock-in amplifier as the signal input. The absolute signal amplitude recognized by the lock-in amplifier was recorded to calculate the quantity of generated charges from the device. The photon flux

that was output from the optical fiber at each wavelength was calibrated with Newport Photodiodes (818-UV and 818-IR).

III. 1.4 Ultraviolet-visible optical absorption spectroscopy (UV-VIS)

The transmission and reflection spectra were measured by Varian Cary 5000 UV-vis-NIR spectrophotometer with an integrating sphere on a bare film sandwiched between two glass substrates.

III. 1.5 Photoluminescence (PL) and Photoluminescence Quantum Yield (PLQY)

The photoluminescence measurements were conducted on devices or bare films by exciting the sample with a 520 nm CW laser diode. The samples were place in front of the detector of an Andor Solis SR393i-B spectrograph system. The spectral signal of luminescence from the device was collected by a DU420A-BR-DD Si detector (for central wavelength of 800 nm) and a DU491A-1.7 InGaAs detector (for central wavelengths of 1100 and 1400 nm). In the measurement, long pass filters were placed between the detector and the sample to remove the excitation light from the detected spectra. When measuring the photoluminescence of a device at various applied biases, the voltage was applied to the device with a Keithley 2400 system in two-wire mode. A black mask was used on the sample to make sure that only specified area can be illuminated.

To measure PLQY, the sample (bare film) was first placed inside an integrating sphere, then the laser light was guided into the integrating sphere and shone right in the middle of the sample. The PL of the sample was output from the integrating sphere and guided to the detector. Quantification of photon absorbed by the sample was realized by getting the reduction of the peak signal at the excitation wavelength with and without the sample inside the integrating sphere.

III. 1.6 Electroluminescence (EL) and Electroluminescence Quantum Yield (ELQY)

In EL measurement, the sample device was placed in front of the detector of an Andor Solis SR393i-B spectrograph system, charges were injected into the device with a Keithley 2400 system in two-wire configuration at equivalent 1 sun condition (where injected current density Jinj equals the short circuit current of the device at 1 sun illumination). The spectral signal of luminescence from the device was collected by a DU420A-BR-DD Si detector (for central wavelength of 800 nm) and a DU491A-1.7 InGaAs detector (for central wavelengths of 1100 and 1400 nm).

For the quantification of emitted photon flux from the device, a Newport 818-UV silicon detector was put in front of the device and connected to a Keithley 485 picoampere

meter to quantify the photon flux emitted by the device. The detailed measurement approach was provided in the PhD thesis of Steffen Roland [125].

III. 1.7 Bias-Assisted Charge Extraction (BACE)

BACE serves as an important technique to study the carrier density in the active layer. In BACE measurements, the sample device is first illuminated by a laser while biased at V_{OC} condition, then the illumination is switched off while immediately switching the voltage from V_{OC} to V_{coll}, controlled by a Keysight 81150A function generator. To correct out the geometric capacitance of the device from the measured signal, a dark background measurement is to be performed. For the dark background measurement, the device is put in dark condition while zero volt is applied, then the same voltage step as that in the light condition was used by applying a collection bias of V_{coll}-V_{OC}, so that the dark displacement current can be corrected. With a Keysight Infiniium 9000 Series oscilloscope, the light and dark transient current was recorded, the transient photocurrent can consequently be obtained according to $I_{ph,trans} = I_{light,trans} - I_{dark,trans}$. By integrating $I_{ph,trans}$ over time, the total photogenerated charge in the device can be obtained via $Q_{ph} = \int_0^{end} I_{ph,trans}\, dt$, with the assumption that the electrons and holes have the same distribution profile. Then with the knowledge of the area of the device and active layer thickness, the photogenerated carrier density can be calculated.

$$\frac{Q_{ph}}{edA} = n = p \tag{III. 1.1}$$

For a device whose charge generation is independent of field, when put under illumination in steady-state in V_{OC} condition and, following equation applies which enables calculating charge recombination rate from saturation current density.

$$G = R = \frac{q}{d} \cdot J_{sat} \tag{III. 1.2}$$

Meanwhile, when assuming that the major recombination channel in the device at V_{OC} condition is bimolecular recombination, the charge recombination rate can be described by equation III. 1.2. Relating equations III. 1.1 to III. 1.3 together, the bimolecular recombination rate k_2 can be calculated.

$$R = k_2 \cdot n^2 \tag{III. 1.3}$$

III. 1.8 Time-Delayed Collection Field (TDCF)

TDCF is a charge extraction based characterization technique. In TDCF measurement, a short laser pulse (of ~6 ns) first illuminates the device while the device is pre-bias at V_{pre}, then after a certain delay time t_{delay}, a collection bias V_{coll} is applied to extract the charges. Similar to the BACE measurement, the transient currents during the application of the voltage functions are detected and recorded by a Keysight Infiniium 9000 Series oscilloscope. For each measurement, the same voltage function (from Keysight 81150A

function generator) is applied to the device in dark condition to correct the dark displacement current out from the light transient current signal. The transient photocurrent signal is therefore obtained from $I_{ph,trans} = I_{light,trans} - I_{dark,trans}$. The total amount of charge can therefore be obtained by integrating $I_{ph,trans}$ over time. Upon careful tuning the fluence of the laser pulse, V_{pre}, t_{delay} and V_{coll}, many important physical parameters of the device can be measured.

The field-dependence of charge generation can be measured by using a very low fluence (typically around 0.1 µJ/cm2) and a large collection voltage (typically larger than -2.5 eV), namely "TDCF-generation". t_{delay} is set to 6 ns, same as the width of the laser pulse. This means that the charge extraction starts immediately once the illumination is stopped. The low fluence and high V_{coll} ensures that all photogenerated charges can be extracted efficiently and thus bimolecular recombination is negligible. By scanning the value of V_{pre} (in the range between V_{coll} and V_{OC}), the field-dependence of charge generation can be measured.

Another important application of TDCF is to measure the bimolecular recombination rate (namely "TDCF-delay"). This is achieved by illuminating the device with high fluences (in the fluence condition where bimolecular recombination dominates) while biasing the device with V_{pre} close to the maximum power point voltage V_{MPP}. After the illumination, a series of t_{delay} is waited (typically ranging from 0 ns to 2000 ns) before V_{coll} is applied to collect the charges out. During V_{pre}, the photocarriers are extracted slowly and severe bimolecular recombination happens. Whereas during V_{coll}, the photocarriers are extracted efficiently. This results in a kink in the transient photocurrent when the delay time is over and V_{coll} is applied. In TDCF-delay it is assumed that all charges in the device can be extracted during the application of V_{coll} and recombination in between is negligible. Therefore, the integration of the transient photocurrent during the application of V_{coll} $Q_{ph,coll} = \int_{t_{delay}}^{end} I_{ph,coll}\, dt$ can be understood as "how many charges still present in the device after the device is biased at V_{pre} for t_{delay} after illumination". On the other hand, integrating the transient photocurrent in the entire range of time $Q_{ph,tot} = \int_{0}^{end} I_{ph}\, dt$ gives the amount of charges that are successfully extracted without undergoing bimolecular recombination. Knowing the geometry of the device, the number of charges $Q_{ph,coll}$ and $Q_{ph,tot}$ can be easily converted to carrier densities $n_{ph,coll}$ and n_{tot}. Thereafter, by getting the first derivative of n_{tot} over t_{delay}, the information of how much charges have recombined during each increment of t_{delay} (and thus the recombination rate R) can be obtained. Plotting R against $n_{ph,coll}$, and fitting the plot with $R = k_2 \cdot {n_{coll}}^2$, the bimolecular recombination coefficient k_2 can be obtained.

III. 1.9 Quasi-Steady State Photoinduced Absorption Spectroscopy (PIA)

The sample is pumped by a continuous-wave (cw) laser diode (Spectral Products) which is modulated by an optical chopper (Thorlabs MC2000B) at a frequency of 570 Hz. The excitation wavelength of the pump light is 405 nm. The probe light is sourced from a tungsten halogen lamp. The probe consequently goes through a monochromator (Spectral Products DK240) and an optical chopper before reaching the sample. The pump and probe light are aligned to overlap exactly on the sample. The transmitted probe light is collected by a Si or Ge photodiode (Thorlabs). A lock-in amplifier (Stanford

Research Systems, SR830) is connected to the photodiode (as input) and optical chopper (as reference) to minimize the noise from the environment, and to obtain the change in transmitted probe light ΔT as well as ground state transmission T_{gs}. When measuring ΔT, both pump and probe light are on, with the pump light being modulated. The optical chopper for the pump light is connected to the lock-in amplifier. When measuring T_{gs}, only probe light is on while being modulated. The optical chopper for the probe light is connected to the lock-in amplifier.

In PIA measurements, the transmission spectra of the sample are measured when the sample is in ground state or photo-illuminated, the resulted differential absorption spectra can therefore be obtained with $\Delta T = T_{exc} - T_g$. The $\Delta T > 0$ peaks are ground state bleach (GSB), corresponding to the bleaching of the ground state material, while the $\Delta T < 0$ peaks are the photoinduced absorption peaks, corresponding to the absorption of photo-excited states. The measurements can also be conducted in the reflection mode.

Part IV

RESULTS AND CONCLUSION

In this part, the experimental and simulation results in this thesis are presented. In chapters IV. 1 and IV. 3, the charge generation, recombination, as well as loss analyses for each *J-V* parameter are studied. Chapters IV. 2 and IV. 4 focus on the experimental considerations. Discussions, conclusions and outlooks are given in chapter IV. 5.

IV. 1 Elucidating How Low Energy Offset Matters to Performance of Non-fullerene Acceptor-Based Solar Cells

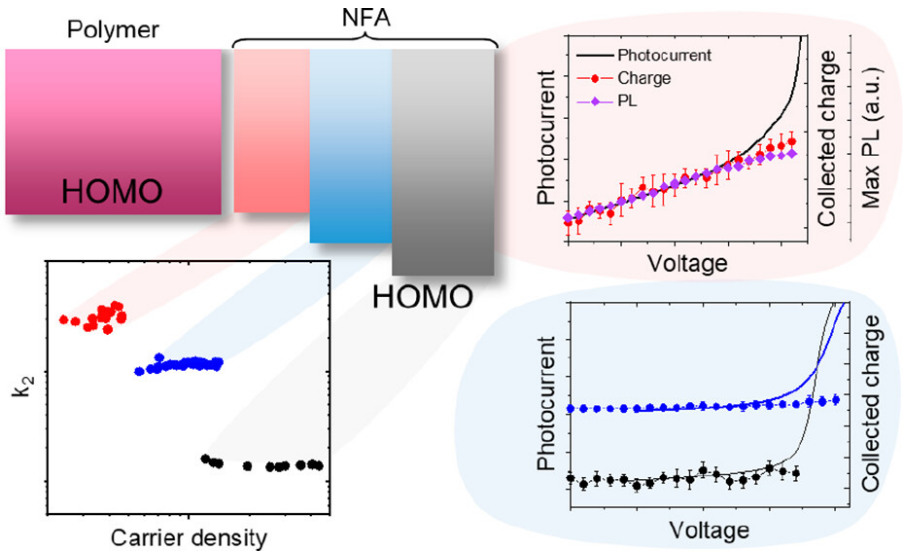

This chapter discusses about the relationship between the recombination rate and energetic offsets as well as its effect on FF in low-offset OSC systems.

This chapter is an adapted preprint of:
Nurlan Tokmoldin, **Bowen Sun**, Floriana Moruzzi, Acacia Patterson, Obaid Alqahtani, Rong Wang, Brian A. Collins, Iain McCulloch, Larry Lüer, Christoph J. Brabec, Dieter Neher, and Safa Shoaee. ACS Energy Letters 2023 8 (6), 2552-2560

IV. 1.1 Abstract

The energetic offset between the highest occupied molecular orbitals of the donor and acceptor components of organic photovoltaic blends is well-known to affect the device efficiency. It is well established that a decreasing offset increases the open-circuit voltage but reduces the short-circuit current, which has been explained by insufficient exciton dissociation. However, the impact of the offset on the fill-factor and underlying processes is less clear. Here, we study free charge generation and recombination in three different non-fullerene acceptors, Y6, ITIC and o-IDBTR, blended with the same donor polymer PM6. We demonstrate that a diminishing offset results in field-dependent charge generation related to field-assisted exciton dissociation. On the other hand, reformation of excitons from free charges is identified as an additional channel for charge recombination, which goes along with a substantial rise in the bimolecular recombination coefficient. In combination of these two effects, the fill-factor drops considerably with a decreasing energy offset. Using the comparison between PM6:ITIC and PM6:o-IDBTR, we show that bulk properties such as morphology and carrier mobilities can not fully explain the observed difference in performance, highlighting the importance of interfacial kinetics and thermodynamics in controlling the device efficiency, both through generation and recombination of charge carriers.

Keywords: HOMO-HOMO offset, field-dependent generation, exciton dissociation, bimolecular recombination, exciton reformation.

IV. 1.2 Introduction

Organic solar cells (OSCs) have seen a significant improvement in performance since the introduction of non-fullerene acceptors (NFAs) as one of the components of the bulk heterojunction (BHJ) layer [24, 126]. The ability to control the synthetic routes and, therefore, structure of these molecules yields a variety of important properties, including solubility, film morphology, charge carrier mobility and energetics [127, 128]. The energetic aspect is particularly important for a BHJ, as it affects charge generation across the interface between the donor (D) and the acceptor (A) materials [66, 129]. Whereas electron transfer from D to A has been previously regarded as the main mechanism of charge generation [130], the current general consensus underscores the predominant role of hole transfer from A to D in NFA-based blends due to the typically smaller acceptor bandgap and the considerable exciton contribution from the acceptor. In this picture, the offset between the highest occupied molecular orbital (HOMO) levels of the two blend components should play a critical role in charge generation, as it represents a driving force for the transition from a singlet exciton (S_1) to a charge transfer (CT) state [22, 131]. While earlier work reported efficient charge generation for vanishing HOMO offset, it is now well established that below a critical value ranging, according to various reports, from below 0.2 eV to ca. 0.5 eV the exciton dissociation efficiency decreases continusouly with decreasing offset [42, 66, 129]. This has been related to a decrease in the short circuit current (J_{SC}), which overcompensates the increase in open-circuit voltage (V_{OC}) with regard to device efficiency.

Another remarkable observation is a notable reduction in the fill factor (FF) with decreasing offset[129, 132, 133]. By definition, the FF summarizes all field-dependent loss

processes in an illuminated cell. In a BHJ solar cell, photocurrent generation is believed to proceed through three fundamental steps: (1) the formation of an interfacial CT state through exciton diffusion and dissociation at the D/A heterojunction, competing with the decay of the exciton to the ground state; (2) dissociation of the CT state into spatially separated independent charges (CS), competing with geminate recombination (GR); and (3) collection of the free charges at the electrodes, competing with nongeminate recombination (NGR) [85]. For large-offset systems it was shown that process 2 can be field-assisted and thereby cause a field dependence of free charge generation [58, 134].However, recent studies have provided evidence for a pronounced electric field dependence of step 1, exciton dissociation in systems with a low energy offset [63–65, 135]. Such a scenario requires that an appreciable energetic barrier exists between the S_1 and the CT states, which is indeed predicted by Marcus theory for the case of a small energy offset and a large reorganization energy. Electric field-induced barrier lowering would then be possible if the electric field reduces the CT state energy relative to the energy of S_1.

The final process determining the FF is process 3, the competition between free charge extraction and NRG. Surprisingly, the correlation between NRG and the blend energetics has been scarely explored. For field-independent free charge generation, a fill-factor figure-of-merit α, is defined as [120]:

$$\alpha = \sqrt{\frac{q^2 k_2 G d^4}{4\mu_e \mu_h (k_B T)^2}} = \sqrt{\frac{q k_2 J_{Gen} d^3}{4\mu_e \mu_h (k_B T)^2}} \tag{IV. 1.1}$$

where q is the elementary charge, k_2 is the bimolecular recombination coefficient, G and $J_{Gen}$are, respectively, the carrier generation rate and current density, d is the active layer thickness, $\mu_{e/h}$ are the electron/hole mobilities, k_B is the Boltzmann constant and T is the temperature. It is not expected that a direct correlation exists between the energy offset and the carrier mobilities. Therefore, if a lower offset system decreases the FF through increased NGR, it must be due to a higher k_2.

Here, we study the cause of the reduced FF for low offset systems. To this end, we selected three NFA based blends, where the HOMO offset is systematically reduced. By performing time-delayed collection field (TDCF) experiments, we observe a pronounced increase of the field dependence of free charge generation with decreasing HOMO offset. Steady-state and time resolved photoluminescence studies then prove field-assisted exciton dissociation as the main cause of this field dependence. At the same time, the bimolecular recombination coefficient is significantly enhanced. Space charge limited current measurements reveal no correlation between the energy offset and mobility, putting an emphasis on the Langevin reduction factor. We, then, find that a reduced HOMO offset can cause exciton reformation from free charges, providing an additional pathway for NGR.

IV. 1.3 Results

In this study, we blended the donor polymer PM6 (full compound names given in Supplementary) with three different small-molecule acceptors Y6, ITIC and o-IDTBR (Figures IV. 1.1 (a-d)). Figure IV. 1.1(e) demonstrates the energy levels of the neat materials as well as blend films obtained using cyclic voltammetry (see SI Figure A.1 for cyclic voltammetry

data, and the measurement details and comments in the Supplementary Notes; PM6 and Y6 energy levels were also reported by our group earlier [131]). The resulting HOMO-HOMO offsets range from -30 to ca. 400 meV. The performance of solar cells fabricated from these blends is shown in Figures IV. 1.1 (f-g) and Table IV. 1.1. The observed trend in the HOMO-HOMO offset correlates with the device performance, with the smallest offset PM6:o-IDTBR blend showing the largest V_{OC}, but the smallest FF and J_{SC}. The FF and J_{SC} gradually increase in the ITIC device and the highest values are obtained in the Y6 blend. Additionally, whereas the absorption in the PM6:Y6 blend is significantly red-shifted (Figure IV. 1.1(h)) – partially explaining the higher J_{SC}, the very close absorption spectra of PM6:ITIC and PM6:o-IDTBR make the comparison between the latter two systems particularly interesting.

Table IV. 1.1: Device performance characteristics of the studied NFA-based organic solar cells with the structure ITO/PEDOT:PSS/active layer (120 nm)/PDINN/Ag.

Active layer	V_{OC} [V]	J_{SC} [mA/cm^2]	FF%	PCE%
PM6:Y6	0.83	26.9	70.7	15.7
PM6:ITIC	1.00	15.1	64.3	10.1
PM6:o-IDTBR	1.13	7.1	49.9	4.0

To understand the change in the FF according to equation IV. 1.1, we first study the competition between charge recombination and extraction. We start with the measurement of the carrier recombination dynamics using the bias-assisted charge extraction (BACE) technique [136]. In this measurement, a device is held initially under illumination at open circuit, where a dynamic equilibrium is established between the carrier generation and recombination rates. As soon as the illumination is switched off, a reverse bias is immediately applied to the terminals to extract the charge carriers. To account for the displacement charge due to the change in voltage $\Delta V = V_{OC} - V_{coll}$, a measurement with the same voltage jump ΔV is also performed in the dark. The recombination order close to 2 is seen in all three blends, suggesting that bimolecular recombination is the dominate recombination mechanism for the free charge carriers. We note that determination of the correct carrier recombination rate for the BACE analysis requires the estimation of the carrier generation rate at the V_{OC} condition, which, generally speaking, may differ to the one at short circuit. The respective procedure for determination of the recombination rate and the bimolecular recombination coefficient is described in the Supporting Information, Figure A.2(a) and (b)). Figure IV. 1.2 shows the results for the three systems. Amongst them, PM6:o-IDBTR has the highest k_2, followed by PM6:ITIC and then PM6:Y6. According to equationIV. 1.1, k_2 directly affects the fill-factor figure-of-merit α, agreeing with the observed trend in FF (Table IV. 1.1). However, other factors such as charge carrier mobilities and generation rate, are also responsible in determining α.

Carrier mobilities for the studied systems were determined via the space-charge limited current (SCLC) measurements in single-carrier devices (Table IV. 1.2 and Figure A.3) [137]. Table IV. 1.2 lists the room-temperature mobilities and energetic disorder values for the neat materials and blends, obtained from fitting of the *J-V* and slope-V curves via the drift-diffusion model [137]. Looking at the two lower-offset systems, although the mobilities are much more imbalanced in PM6:o-IDTBR than in PM6:ITIC, the effective mobilities $\mu_{eff} = \sqrt{\mu_e \mu_h}$ for the two blends are identical: 1.3×10^{-4} cm^{2}V^{-1}s^{-1}. We remind the reader that the effective mobility, determined as the geometric mean of individual carrier

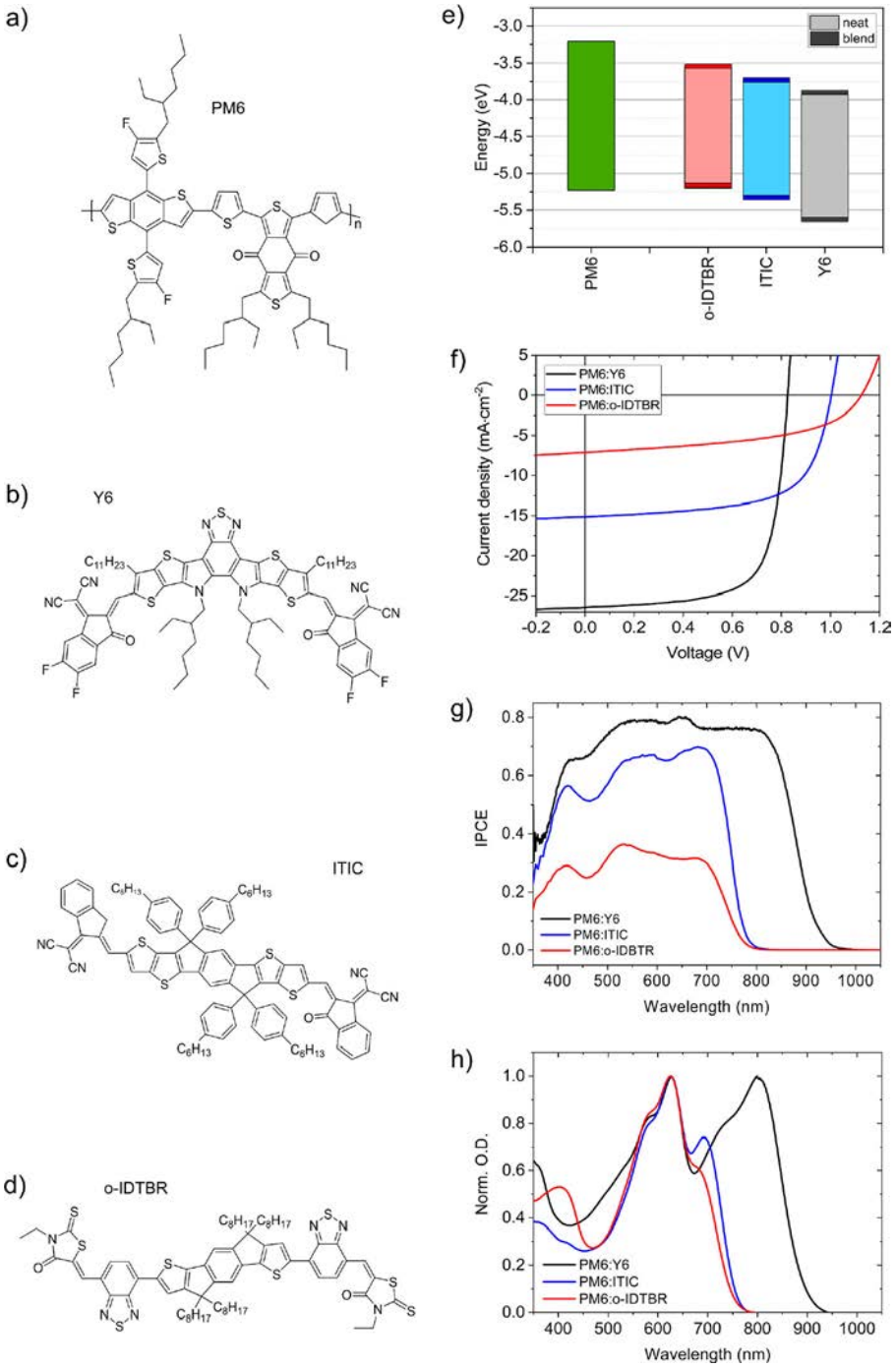

Figure IV. 1.1: a)-d) Chemical structures of materials used in the study: a) PM6, b) Y6, c) ITIC and d) o-IDTBR; e) energy levels of the studied materials determined via cyclic voltammetry (*C-V*) and UV-vis absorption spectroscopy, solid lines indicate the energy levels determined for the neat acceptors, whereas rectangular areas – for their blends with PM6 (the HOMO levels were determined from the measured LUMO levels and the optical bandgaps, see Figure A.1); f)-h) device performance of app. 120 nm thick junctions of PM6:Y6, PM6:ITIC and PM6:o-IDTBR (see experimental section for full details): f) current density vs. voltage (*J-V*) curves; g) spectra of incident photon-to-current conversion efficiency (IPCE); h) UV-vis absorption spectra of the studied blend films [25].

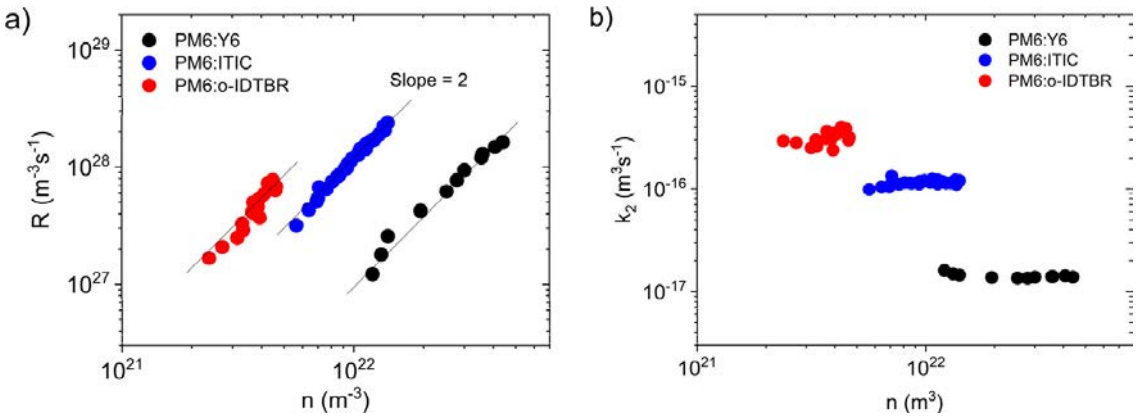

Figure IV. 1.2: Bias-assisted charge extraction (BACE) measurements of 140 nm thick devices: a) recombination rate R vs. carrier density n; b) bimolecular recombination coefficient k_2 vs. carrier density n.

mobilities, appears in equation.IV. 1.1 representing the efficiency of charge extraction. Additionally, it has been shown earlier that for blends with domain sizes of the order of tens of nanometers the encounter-limited bimolecular recombination coefficient is best described by the geometric mean of mobilities [91, 95].

Table IV. 1.2: Carrier mobilities and energetic disorder in neat NFAs and PM6-blended systems, determined using the space-charge limited current (SCLC) measurements.

Material	$\mu_{e,RT}$ $cm^2V^{-1}s^{-1}$	σ_e meV	$\mu_{h,RT}$ $cm^2V^{-1}s^{-1}$	σ_h meV
Neat Y6 [138]	2.4×10^{-3}	71.0	1.8×10^{-4}	74.0
PM6:Y6 [15]	8.4×10^{-4}	60.0	1.3×10^{-4}	74.0
Neat ITIC	4.7×10^{-4}	59.9	2.8×10^{-8}	68.5
PM6:ITIC	1.9×10^{-4}	63.1	9.3×10^{-5}	62.6
Neat o-IDTBR	1.1×10^{-4}	82.1	1.9×10^{-4}	73.1
PM6:o-IDTBR	3.4×10^{-5}	70.0	5.0×10^{-4}	54.4

Now turning to charge generation, we measured the efficiency of free charge generation (EGE) using the time-delayed collection field (TDCF) technique [136]. TDCF probes the amount of photogenerated charge at different applied biases in the low-light intensity regime avoiding bimolecular recombination (the extracted charge is strictly proportional to the laser fluence). In this experiment, the device is excited with a short laser pulse ($\sim$ 5 ns) while being held at a given pre-bias (V_{pre}). After a delay time of 6 ns all charges are extracted by applying a high reverse collection bias (Vcoll). Then, the total extracted charge (Q) is a direct measure of EGE under the chosen condition. Figure IV. 1.3 shows the results of such a measurement for PM6:ITIC and PM6:o-IDTBR, where V_{pre} is swept from reverse bias (-1 V) to V_{OC}. A similar measurement in PM6:Y6 has previously shown that charge generation in this blend is independent of the applied bias [50]. We find that in the PM6:ITIC device, charge generation does not depend on the field, however the PM6:o-IDTBR device shows a strong field dependence with fewer charges collected. To examine the extent of this behaviour, the voltage sweeping range for PM6:o-IDTBR was further widened to -7 V. Figure A.4 shows that charge generation remains field-dependent even up to -7 V.

The field-dependent charge generation in the o-IDTBR system can stem from field-dependent exciton dissociation and/or field-dependent CT dissociation. The lower charge generation efficiency may also originate from poor exciton dissociation. To probe, whether charge generation in PM6:o-IDTBR is driven by exciton or CT dissociation, we performed photoluminescence (PL) measurements on the device at different applied biases. PL quenching is an assay of exciton dissociation and by comparing the PL signal of neat and blend films with and without field, we address the exciton dissociation. Figures IV. 1.3 (a) and (b) show the overlap of the field-dependent PL with the TDCF generation curves for both blends. PM6:ITIC shows strong exciton quenching of the NFA excitons (Figure A.5(a)) and exhibits field-independent PL. On the other hand, in the absence of any field (at V_{OC}), PM6:o-IDTBR shows poor PL quenching (Figure A.5(b)); however, the PL has a strong field-dependence. It should be noted that, in spite of the small HOMO-HOMO offset, the exciton dissociation in PM6:o-IDTBR is still facilitated by the presence of PM6, since the PL of neat o-IDTBR is field-independent (Figure A.6). Consistent with these results are our field-dependent time resolved PL (TRPL) data for the PM6:o-IDTBR system. Figure IV. 1.3 shows the TRPL kinetics indicating a drop in the yield of intensity with increasing reverse bias. However, the decay time (corresponding to the CT dissociation) remains invariant, confirming that only exciton dissociation is field-dependent.

The small PL quenching in PM6:o-IDTBR in the absence of an electric field may be due to unfavourable morphology of the system, causing a competition between the exciton diffusion length and the domain size. Alternatively, emission may also take place from re-formed excitons (vide infra). To address this, we probed the morphology of PM6:o-IDTBR and, for comparison, PM6:ITIC, as well as the neat materials, using grazing-incidence wide-angle X-ray scattering (GIWAXS) and resonant soft X-ray scattering (RSoXS) measurements (Figure IV. 1.4 and A.7, Table IV. 1.3 and Supplementary Note). According to the GIWAXS results, o-IDTBR molecules show higher crystallinity and a closer π-πpacking than ITIC. Additionally, although crystallinity is disrupted upon blending of the acceptors with PM6, the π-πstacking of neat components with the preferential face-on orientation is preserved for both blends. The RSoXS measurements reveal that both blends feature a similar average domain size with the characteristic length LC of 60 nm, which is consistent with size and spacing of polymer fibrils seen in atomic force microscopy (AFM) images (see Figure A.8).

With this size scale, measuring and analyzing domain purity using scanning transmission X-ray microscopy (STXM) was limited by the instrumental resolution (Figure A.7). However, the relative domain purity was extracted from the RSoXS profiles analysing multiple energies and correcting for contrast differences and scattering symmetry (Figure A.7) [139]. From this analysis, the PM6:o-IDTBR blend has a significantly lower domain purity than the PM6:ITIC blend. More mixing between PM6 fibrils in the o-IDTBR blend films may enable increased interfacial interaction between charges compared to PM6:ITIC, which could rationalize the difference in bimolecular recombination for the two blends (Figure IV. 1.2) [140]. However, domain mixing has not been shown to result in field-dependent PL quenching and thus cannot explain the effects seen here on its own, although the role of a morphology-driven driving force for charge separation following initial exciton dissociation should also be considered (see Supplementary Note). The consistency of molecular crystallinity and domain size, however, suggests that morphology between the two blends is fundamentally similar.

Table IV. 1.3: Morphological parameters of PM6:ITIC and PM6:o-IDTBR, obtained via GIWAXS, RSoXS and STXM.

Blend	**Out-of-plane π-π d-spacing (nm)**	**Domain characteristic length (L_C) (nm)**	**Relative domain purity**
PM6:ITIC	Polymer: 0.36 NFA: 0.42	60	1
PM6:o-IDTBR	Polymer: 0.36 NFA: 0.34	60	0.65

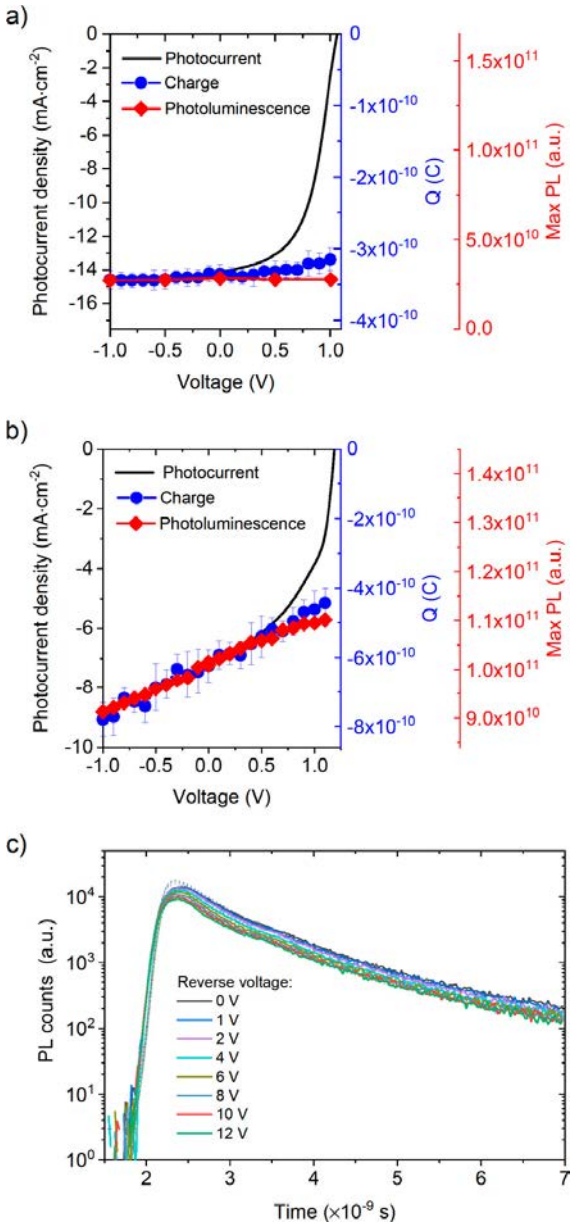

Figure IV. 1.3: Probing field-dependence in charge generation: a) overlap between photocurrent density vs. voltage, collected charge vs. voltage and photoluminescence vs. voltage curves for PM6:ITIC; b) overlap between photocurrent density vs. voltage, collected charge vs. voltage and photoluminescence vs. voltage curves for PM6:o-IDBTR; c) time-resolved photoluminescence decay of PM6:o-IDTBR.

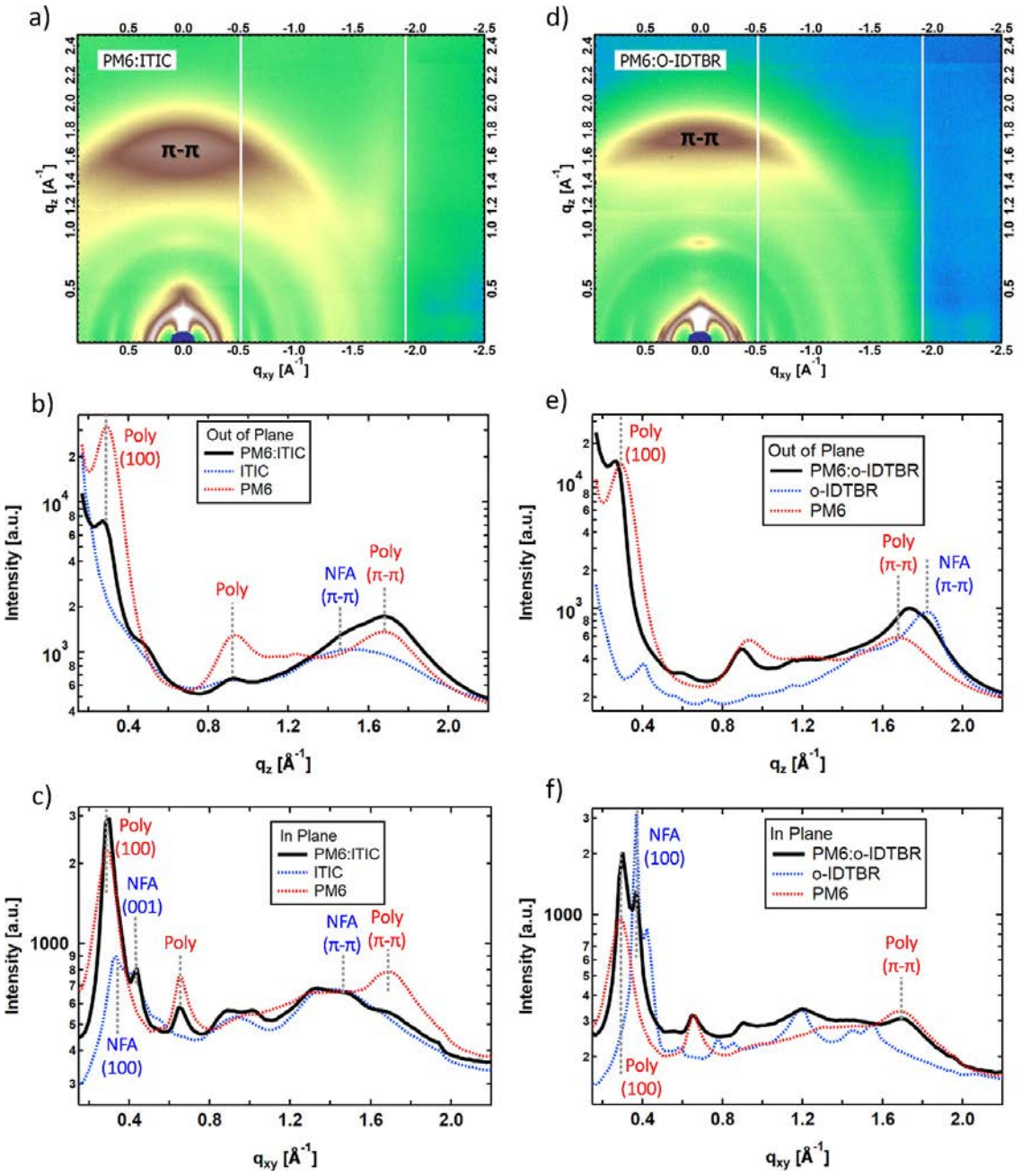

Figure IV. 1.4: Grazing-incidence wide-angle X-ray scattering (GIWAXS) data for PM6:ITIC and PM6:o-IDBTR.

In order to determine the nature and origin of PL in PM6:o-IDTBR, we consider reformation of excitons. For this purpose, we employ electroluminescence (EL) measurements, in which emission may take place exclusively via recombination of the injected free charges (through the CT state), avoiding emission from non-dissociated excitons upon photoexcitation. We have previously reported such measurements for PM6:Y6 [25]. Figure IV. 1.5 shows the comparison of the EL and PL spectra for PM6:ITIC and PM6:o-IDTBR. The equivalence in the spectral shapes for the o-IDTBR blend resembles EL and PL of a singlet exciton on o-IDTBR. In contrast, EL of the ITIC blend displays both singlet excitons (also observed in PL) and a red-shifted feature, which we assign to CT states [42].

By comparing the EL and PL quantum yields, we evaluate the efficiency of exciton reformation according to:

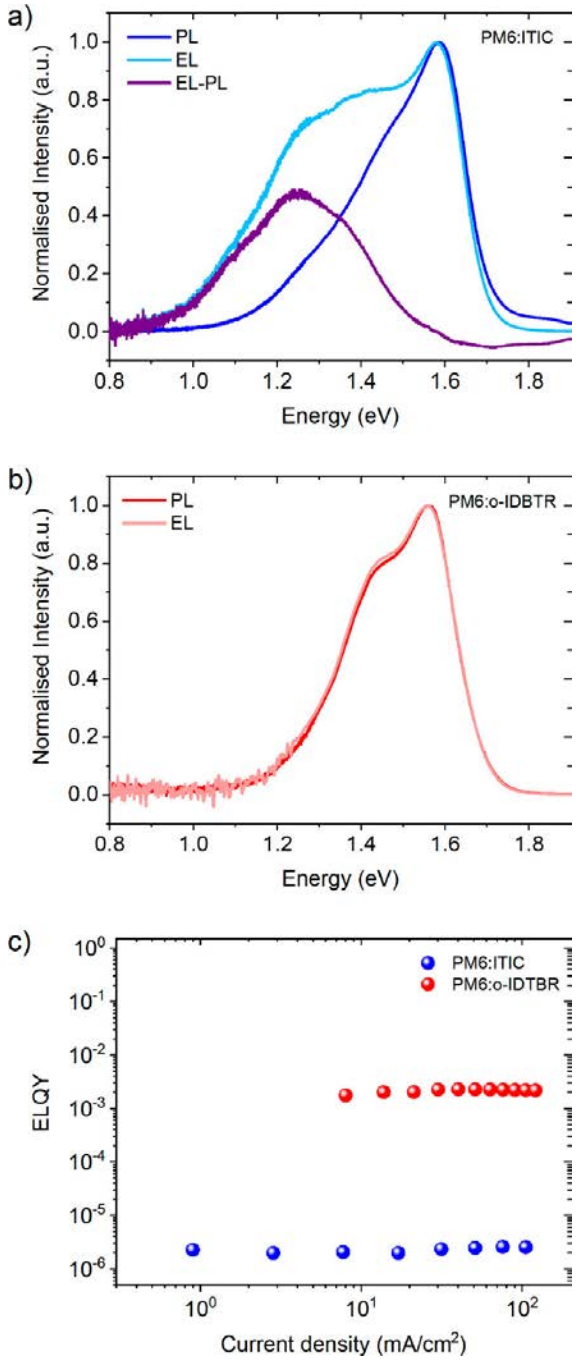

Figure IV. 1.5: Comparison of the PL and EL spectra of PM6-blended and neat ITIC and o-IDTBR; ELQY measurements in the studied blends.

$$\eta_{ex,ref} = \frac{ELQY_{PM6:A}}{PLQY_{PS:A}} \quad \text{(IV. 1.2)}$$

where $ELQY_{PM6:A}$ is the EL quantum yield of the blend, and $PLQY_{PS:A}$ is the PL quantum yield of the acceptor blended into polystyrene as an inert matrix with the same ratio as the studied D:A system [98]. Equation IV. 1.2 is based on the definition of the ELQY of the blend as a product of the probability of forming an exciton on the acceptor, which is the lower band-gap component of the blend, upon CT formation via charge injection (i.e. $\eta_{ex,ref}$) and the probability of photoluminescence from an exciton on the neat acceptor

having the same compositional fraction as in the studied blend (hence $PLQY_{PS:A}$). The ELQY measurements in PM6:ITIC and PM6:o-IDTBR are shown in Figure IV. 1.5(c). The respective $ELQY_{PM6:A}$ and $PLQY_{PS:A}$ values are given in Table IV. 1.4.

Table IV. 1.4: PLQY of polystyrene(PS):acceptor (A) samples and ELQY of the PM6:A blends.

Accepor	**$PLQY_{PS:A}$**	**$ELQY_{PM6:A}$**
Y6	7×10^{-3} [25]	3×10^{-5} [15]
ITIC	2×10^{-2}	3×10^{-6}
o-IDTBR	6×10^{-2}	2×10^{-3}

IV. 1.4 Discussion

The experimentally determined parameters of the studied OSC blends are summarized in Table IV. 1.5. The HOMO-HOMO offset in the studied systems appears to correlate strongly with FF through both charge generation and k_2. Significant reduction in the offset leads to field-dependent charge generation, faster recombination of free carriers and a contribution of singlet exciton reformation as one of the channels of bimolecular carrier recombination. Since the S_1 to CT energy separation can be approximated by the offset between the HOMO energies of the donor and the acceptor, the efficiency of S_1 reformation from the CT state is expected to rise for low offset systems (until the CT and S_1 hybridise). In this case, the charges would get an opportunity to recombine through reformed excitons.

Table IV. 1.5: Correlation between the HOMO-HOMO level offsets (ΔE_{HOMO}) obtained by the cyclic-voltammetry measurements, reformation efficiency ($\eta_{ex,ref}$), bimolecular recombination coefficient (k_2) and fill-factor figure-of-merit (α) in the PM6:Y6, PM6:ITIC and PM6:o-IDTBR organic solar cells.

Blend	**ΔE_{HOMO} meV**	**$\eta_{ex,ref}$**	**k_2**	**FF**
PM6:Y6	410	$\sim 4\times 10^{-3}$	$\sim 1\times 10^{-17}$	2.4
PM6:ITIC	70	$\sim 1\times 10^{-4}$	$\sim 1\times 10^{-16}$	14.0
PM6:o-IDTBR	-30	$\sim 3\times 10^{-2}$	$\sim 3\times 10^{-16}$	19.8

The correlation between k_2 and the HOMO-HOMO offset suggests that reducing the offset either increases the CT binding energy and thus the decay of the CT state, and/or it allows for a new decay channel through the reformed excitons. In particular, the latter channel becomes important when exciton dissociation is inefficient, as is the case for PM6:o-IDTBR. In this scenario exciton reformation can act as a channel for charge recombination in OSCs. Consequently, the bimolecular recombination rate equation, involving a single decay route via the CT state [141]:

$$R = k_{rec} n_{CS}^{\alpha} = \eta_{CT,diss} \cdot k_{f,CT} \cdot n_{CT} \tag{IV. 1.3}$$

transforms as follows:

$$R = k_{\text{rec}} n_{\text{CS}}^{\alpha} = \eta_{\text{CT,diss}} \cdot k_{\text{f,CT}} \cdot n_{\text{CT}} + \eta_{\text{ex,ref}} \cdot k_{\text{f,S}_1} \cdot n_{\text{S}_1} \quad \text{(IV. 1.4)}$$

where k_{rec} is the free carrier recombination coefficient which for purely bimolecular recombination is equivalent to k_2, αis the order of recombination, $k_{\text{f,CT}}$ is the CT-state decay rate, $k_{\text{f,S}_1}$ is the exciton decay rate, $\eta_{\text{CT,diss}}$ is the probability of charge generation, $\eta_{\text{ex,ref}}$ is the probability of exciton reformation and n_{S_1}, n_{CT}, and n_{CS} are the densities of singlet excitons, CT states and free charges, respectively. The respective state diagrams denoting electronic transitions between different states for the cases of large and small energy offsets is presented in Figure IV. 1.6.

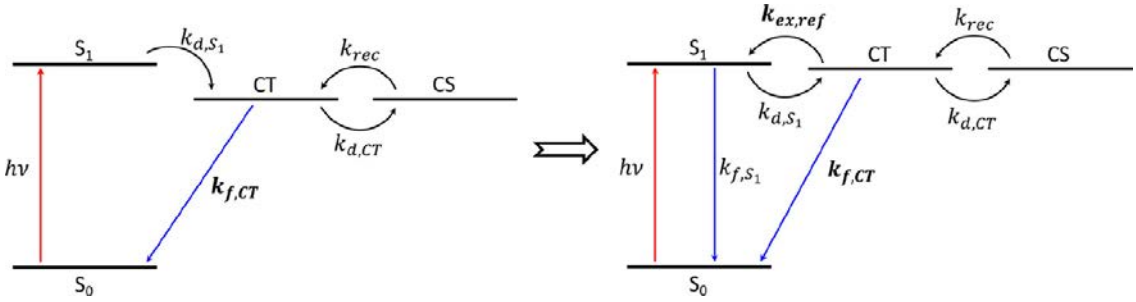

Figure IV. 1.6: State diagram of an organic solar cell with the low energy offset, indicating various transitions between the ground state singlet S_0, singlet exciton S_1, charge-transfer (CT) and charge-separated (CS) states: photon absorption under illumination ($h\nu$), carrier injection under external bias (J_{inj}), exciton decay ($k_{\text{f,S}_1}$), exciton dissociation to CT ($k_{\text{d,S}_1}$), CT decay ($k_{\text{f,CT}}$), CT dissociation into free carriers ($k_{\text{d,CT}}$), free carrier encounter to form CT (k_{rec}) and reformation of the singlet exciton ($k_{\text{ex,ref}}$).

It is important to point out that the enhanced exciton reformation with a lower energy offset cannot fully explain the rise in k_2, given also that the majority of recombination still proceeds via non-radiative channels, as evidenced by the ELQY measurements [25]. At the same time, we see a correlation between the energetic offset and the recombination reduction factor γfor the studied systems (obtained from k_2 and the Langevin recombination coefficient – see Supplementary Note 7). Since the reduction factor is typically assigned to the dynamics of the CT state (dissociation vs. decay) [141], this work highlights the role of the energetic offset influencing the kinetic rates at the interface.

Regarding the specific mechanisms of non-radiative recombination, relaxation to the molecular triplet state has previously been proposed as the major charge recombination mechanism in the PM6:Y6 blend [142]. This process occurs via back-charge transfer from the triplet CT to the triplet exciton state. In general, the dominant free charge recombination pathway is determined by the comparison between the back-charge transfer rate vs. intersystem crossing between the triplet CT and singlet CT states, as well as the rate of the triplet CT dissociation into free charges and the decay of the singlet CT to the ground state vs. its re-dissociation [141]. We note that equation IV. 1.4 as well as the state diagrams in Figure IV. 1.6 focus on singlet states and do not explicitly include the contribution of the triplet exciton and triplet CT state to the carrier recombination dynamics [143], however as mentioned above, their role should not be dismissed. Whilst we and others have shown the effect of spin statistics and polaron mediated triplet formation on the recombination rate of free carriers [141, 142, 144], at the same time we note that singlet reformation may only proceed via the singlet CT

state. As such, the efficiency of reformed excitons will not be affected by the omission of triplet statistics in the rate equation. Nevertheless, understanding the relationship between exciton reformation from free charges vs. CT binding energy, and the singlet-triplet interplay, is important to build a detailed picture of the charge generation and recombination processes in low offset systems. This work conveys the message that, in addition to triplet excitons and a singlet CT state, singlet excitons can also contribute to the bimolecular recombination channels, albeit in the current systems the S_1 channel is far away from dominating the loss pathway.

IV. 1.5 Conclusion

In conclusion, we show that decreasing the HOMO-HOMO offset in NFA-based OPVs not only reduces the free carrier generation efficiency but also speeds up free carrier recombination, as characterized by the bimolecular recombination coefficient k_2. We show that a significantly reduced energy level offset results in both field-dependent exciton dissociation as well as the activation of singlet exciton reformation as a new channel for bimolecular recombination. At the same time, although it is tempting to directly relate exciton reformation to charge recombination, one must also carefully consider the influence of other factors, affecting the efficiency of the excited state decay, such as the difference in the CT binding energies. Additionally, the growing field dependence in exciton dissociation, and thereby carrier generation, and the increased recombination coefficient with a diminishing energy offset result in a reduced FF, as exemplified by PM6:o-IDTBR. Finally, this study highlights the importance of optimizing blend energetics to drive further improvement in the performance of NFA-based organic solar cells through minimization of the total recombination losses.

IV. 2 Spectroelectrochemically Determined Energy Levels of PM6:Y6 Blends and Their Relevance to Solar Cell Performance

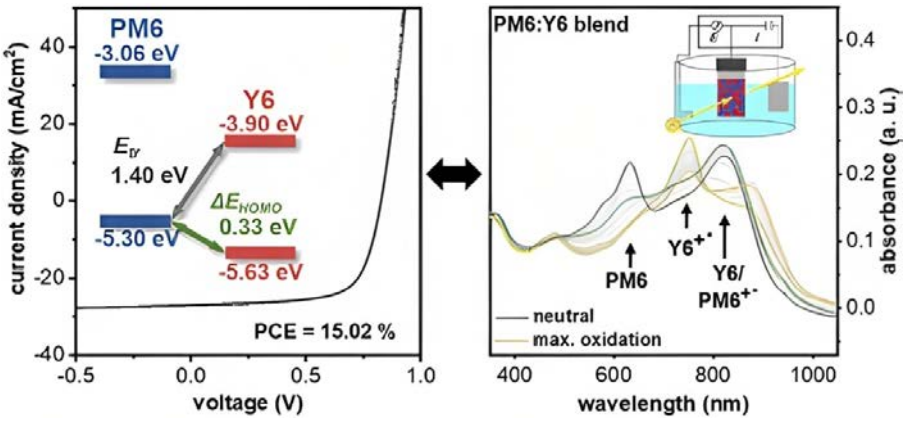

This work presents a systematic spectroelectrochemical approach to precisely determine frontier orbital energies of PM6:Y6 blends in device-relevant films and results are discussed regarding their impact on solar cell performance.

This chapter is an adapted preprint of:
David Neusser, **Bowen Sun**, Wen Liang Tan, Lars Thomsen, Thorsten Schultz, Lorena Perdigón-Toro, Norbert Koch, Safa Shoaee, Christopher R. McNeill, Dieter Neher and Sabine Ludwigs. J. Mater. Chem. C, 2022,10, 11565-11578

IV. 2.1 Abstract

Recent advances in organic solar cell performance have been mainly driven forward by combining high-performance p-type donor–acceptor copolymers (e.g.PM6) and non-fullerene small molecule acceptors (e.g.Y6) as bulk- heterojunction layers. A general observation in such devices is that the device performance, e.g., the open-circuit voltage, is strongly dependent on the processing solvent. While the morphology is a typically named key parameter, the energetics of donor–acceptor blends are equally important, but less straightforward to access in the active multicomponent layer. Here, we propose to use spectral onsets during electrochemical cycling in a systematic spectroelectrochemical study of blend films to access the redox behavior and the frontier orbital energy levels of the individual compounds. Our study reveals that the highest occupied molecular orbital offset (ΔE_{HOMO}) in PM6:Y6 blends is $\sim$ 0.3 eV, which is comparable to the binding energy of Y6 excitons and therefore implies a nearly zero driving force for the dissociation of Y6 excitons. Switching the PM6 orientation in the blend films from face-on to edge-on in bulk has only a minor influence on the positions of the energy levels, but shows significant differences in the open circuit voltage of the device. We explain this phenomenon by the different interfacial molecular orientations, which are known to affect the non-radiative decay rate of the charge-transfer state. We compare our results to ultraviolet photoelectron spectroscopy data, which shows distinct differences in the HOMO offsets in the PM6:Y6 blend compared to neat films. This highlights the necessity to measure the energy levels of the individual compounds in device-relevant blend films.

IV. 2.2 Introduction

The material class of organic semiconductors has seen significant advances in recent years due to their wide range of applications in the field of organic electronics and optoelectronics [145, 146] including organic solar cells (OSCs). [147–149] The typically high extinction coefficients and the possibility to tune optical properties via the design of chemical structures strengthen the interest in developing and optimizing new materials for OSCs. Within the photoactive layer, bulk-heterojunction solar cells (BHJs) combine an electron donor material (D) and an electron acceptor material (A) to maximize the harvest of the solar spectrum and allow for an efficient charge generation and separation at the D/A-interface [150, 151]. To improve the efficiency regarding light absorption and charge generation, both components need to be tuned in terms of energy level matching. Here, a balance between a reduction of the energy loss during charge transfer and a large enough highest occupied molecular orbital offset (ΔE_{HOMO}) to drive exciton dissociation needs to be found. [152] This aspect demonstrates that it is crucial to have a profound knowledge of the energy levels to achieve efficient devices. There are multiple methods available to determine the energy levels including cyclic voltammetry (*C-V*), ultraviolet photoelectron spectroscopy (UPS) or scanning tunneling spectroscopy. Serious discussions have unfolded about when it is reasonable to compare resulting energy levels from different experimental methods and when different data sources can be problematic. For example, it is quite common to combine the HOMO level derived from cyclic voltammetry or UPS with the optical bandgap to determine the lowest unoccupied molecular orbital (LUMO) level energy, which is, however, inappropriate

because of the large exciton binding energy of organic materials.9–11 Additionally, measurements on neat materials may not be suitable to explain the energetic properties of material blends. [153, 154] Microstructural order and morphology can be very unique in blends and therefore influence device-relevant parameters in a strong manner. Simply evaluating measurements on neat materials and translating them to material blends can therefore be a problematic approach. This work will deliver more insights into energy level determination in blend films and hence add more details to the prevailing discussions.

Due to its striking performance in solar cells, the present work is focused on thin films of the non-fullerene acceptor (NFA) molecule Y6 [20] (2,2'-((2Z,2'Z)-((12,13-bis(2-ethylhexyl)-3,9-diundecyl-12,13-dihydro-[1,2,5]thiadiazolo[3,4e] - thieno[2",3":4',5']thieno[2',3"4,5]pyrrolo [3,2-g] - thieno[2',3':4,5] - thieno[3,2-b]indole-2,10-diyl) bis(methanylylidene)) - bis(5,6-difluoro-3-oxo-2,3-dihydro-1H-indene-2,1-diylidene))-dimalononitrile), the conjugated donor polymer PM6 (poly[(2,6-(4,8-bis(5-(2-ethylhexyl-3-fluoro)thiophen-2-yl)-benzo[1,2-b:4,5b']dithiophene))-alt-(5,5-(1',3'-di-2-thienyl-5',7'-bis(2-ethylhexyl)benzo[1',2'-c:4',5'-c']di-thiophene-4,8-dione)])) and their blends PM6:Y6 (see Fig.IV. 2.1 for chemical structures).

One of the main achievements in the development of these high-performance materials was to tune the energy levels and shift the acceptor absorption to a region above 800 nm [127, 155, 156] (see Fig.IV. 2.1 c for the normalized absorbance spectrum). This way some of the limitations of previous state-of-the-art fullerene-based acceptor materials which had struggled for example with thermal and photochemical stability could be addressed. [157] The blue shift of the absorption peak of Y6 in the blend compared to that in the neat film is a commonly observed phenomenon. The position of this peak is influenced by the degree of aggregation and by the intermolecular arrangements in the solid state of Y6. [158] The exact decomposition of the absorption spectrum of Y6 in solution, neat film and blend in the contributions of different aggregates and non-aggregated molecules is the subject of ongoing further investigations and beyond the scope of this work.

The acceptor Y6 is designed following the well-established internal electronic push–pull character with alternating electron donating and withdrawing groups, [159–161] leading to an internal A–DA'D–A structure. The electron deficient core in the center is realized by a benzothiadiazole moiety surrounded by two planar arms which are slightly tilted because of the steric demands of the alkyl chains attached to the center. [20, 162] The exact attachment position and length of the alkyl chains were carefully adjusted and not only modify the solubility properties but also influence the packing structure and performance of the final devices. [163]

PM6 belongs to the thriving family of D/A copolymers based on polythiophenes. [164–166] Poly(3-hexylthiophene) (P3HT) being one of the most prominent polythiophenes is still considered to be a work horse in organic electronics applications. [147, 153, 167, 168] Latest developments in the field of D/A copolymers present the introduction of halogen atoms, especially fluorine, to be one of the structural modifications that dramatically improves the properties of donor materials based on polythiophenes. The D/A copolymer PM6 carries a benzodithiophene donor unit which allows for the attachment of two fluorine atoms per unit. These groups shift down the HOMO level and are therefore an effective approach for increasing the transport gap (E_{tr}) which has a direct positive influence on the V_{OC} and increases the power conversion efficiency of the solar cell. Besides the energetic aspects, the fluorine atoms increase the tendency to aggregate

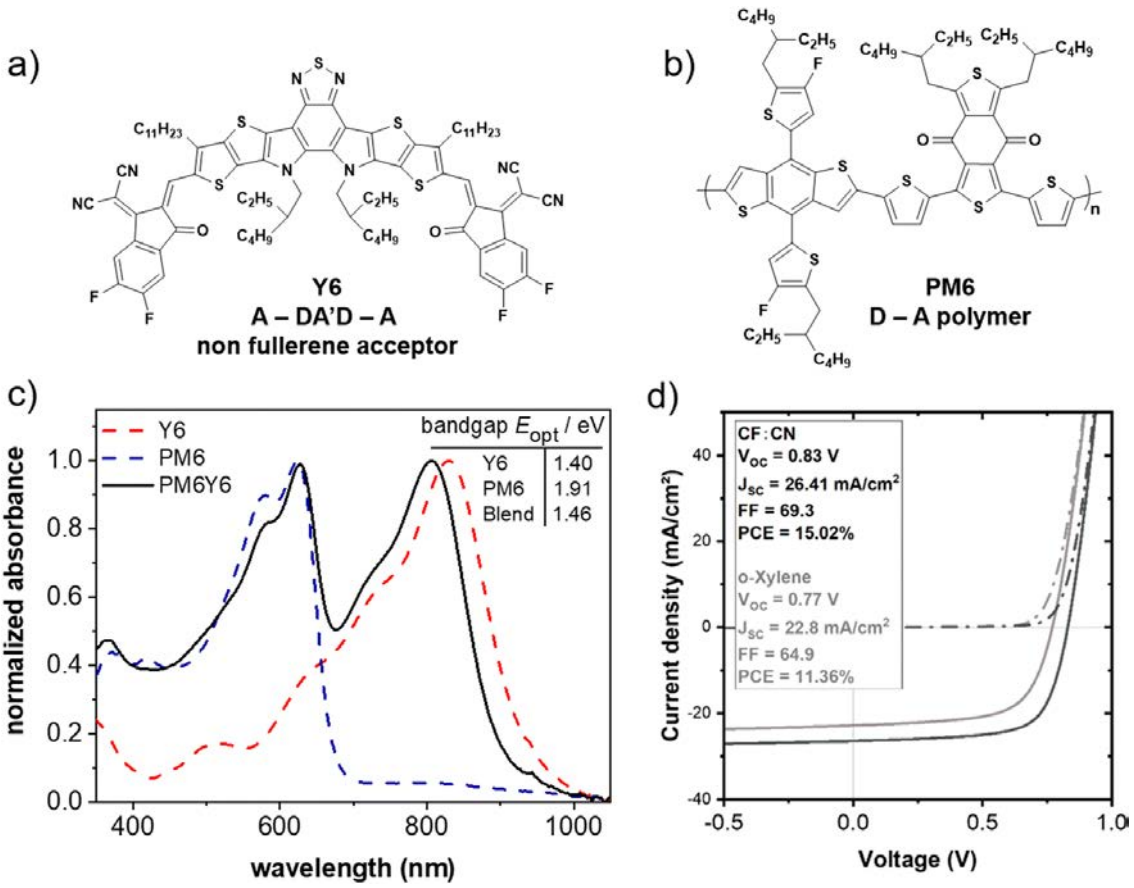

Figure IV. 2.1: Chemical structures of (a) Y6 and (b) PM6. The corresponding UV-vis absorption spectra in thin films processed from CF:CN (chloroform + 0.5 v% chloronaphthalene) are given in (c) showing Y6 in red, PM6 in blue and a blend of PM6:Y6 (1:1.2 wt%) in black. The device characteristics of PM6:Y6 BHJ solar cells processed from CF:CN (black line) and o-xylene (grey line) are presented in (d).

and π-π stack by inducing a stronger dipole moment and improve the crystallinity favoring charge transport properties in general. [165, 169] PM6's large bandgap leads to an absorption spectrum that perfectly complements the absorption spectrum of Y6. When processed in blends, the PM6:Y6 absorption spectrum covers a large part of the solar spectrum from around 350–1000 nm (see Fig.IV. 2.1 c), making these two materials a promising match for BHJ solar cells.

When fabricated into BHJ solar cells, the PM6:Y6 blends deliver an impressive power conversion efficiency of 15.7%, which is among the highest achieved in BHJ devices. [20, 170] This has been attributed to the negligible barrier for charge separation [50, 66, 171] combined with a low density of traps. [172] Devices relying on PM6, Y6 or slightly modified versions of them currently reach efficiencies of up to 19% and above [173, 174] when fabricated in more complex layers, e.g., in ternary blends.39–44 The phase separation between the donor and acceptor plays a crucial role in efficient charge separation (exciton diffusion length is usually around 20 nm [175, 176]) and is influenced by the miscibility between PM6 and Y6 on the one hand. On the other hand, the properties of the chosen processing solvent and the processing method itself significantly impact the drying kinetics during film formation and therefore can influence the blend morphology. This D/A pairing shows suitable miscibility and interaction parameters for a favorable phase separation, which is beneficial for charge generation. [169]

Despite these advancements, there is an ongoing debate regarding the driving force of free charge generation in PM6:Y6. For fullerene-based OSCs, it is commonly accepted in the community that the HOMO energy offset of the frontier orbitals at the D/A heterojunction must be at least 300 meV to guarantee efficient exciton dissociation. [177, 178] Several recent papers reported efficient charge generation in NFA-based devices with HOMO offsets as small as 50 to 100 meV. [179, 180] The original paper on PM6:Y6 reported a HOMO offset of only 0.09 eV, based on *C-V* scans on neat films of the two components. [20] On the other hand, recent measurements of the ionization energy and electron affinity of neat layers with photoelectron spectroscopy suggested a HOMO offset as large as 0.7 eV. [66] Table B.1 (Supporting Information) provides an overview of the reported HOMO and LUMO energy levels on neat films and on PM6:Y6 blends from the literature. We notice a rather large variation of the energy values for the donor polymer PM6, while the scatter of data for Y6 is much smaller. This may indicate a large effect of the morphology but also of the chosen method on the polymer energetics. Only a few studies concerned the HOMO and LUMO levels of the blend and reported slightly different values as for neat layers; however, none of the studies provided the HOMO offsets and transport in the actual blend.

In this study, we prepared representative PM6:Y6 BHJ solar cells from two different solvent systems, namely CF:CN (chloroform + 0.5 v% chloronaphthalene) and o-xylene. The strong impact of the processing solvent on the active layer morphology has been reported in the literature [164–166] and by choosing CF:CN and o-xylene as different processing solvents we induce two opposing orientations in the bulk of the active layer. As Fig.IV. 2.1(d) demonstrates, the two orientations have a significant influence on the device performance.

PM6:Y6 solar cells produced from CF:CN give an open circuit potential (V_{OC}) of 0.83 V, a fill factor (FF) of 69.3% and a short circuit current (J_{SC}) of 26.4 mA cm^{-2}, with an overall efficiency of 15.02%, matching the literature results. [20] Switching the processing solvent to o-xylene decreases all photovoltaic parameters, most importantly the V_{OC} which decreases to 0.77 V and the J_{SC} which is 22.8 mA cm^{-2}. Overall, the efficiency drops to 11.36%. We have confirmed the difference in the J_{SC} by measuring the photovoltaic external quantum efficiency (EQE_{PV}) spectra (see Fig. B.1, Supporting Information). Here, the o-xylene coated blend displayed a lower photoresponse over the entire spectral range. Also, the integrated photocurrents from the EQE spectra matched the measured J_{SC} within a 5% error margin, highlighting the consistency of the results. Given that both blends yield a fairly small voltage dependence on the light-induced current near short circuit conditions, we rule out inefficient charge extraction as a possible source of a lower J_{SC}, as this loss displays a strong field dependence. More likely, the lower J_{SC} comes from less efficient exciton dissociation or the trapping of photogenerated charge on non-percolated domains. Regarding the V_{OC}, a central question to be answered in this work is whether the lower value for the o-xylene coated sample can be explained by changes of the energy levels of PM6 and Y6 induced by the opposing morphology in the blend or if other aspects must be taken into consideration. Therefore, we utilize a spectroelectrochemical method to determine frontier orbital energies of individual components in PM6:Y6 blend films with different morphologies. The morphology of the blend films will be discussed in detail at first to define the starting point of all the following experiments. The results will be compared to experimental evidence from UPS measurements and discussed regarding device performance in the final section.

IV. 2.3 Result and discussion

IV. 2.3.1 Morphology characterization

As a first step we have studied the morphology of the blend films by a combination of grazing-incidence wide-angle X-ray scattering (GIWAXS) and near-edge X-ray absorption fine-structure (NEXAFS) spectroscopy (see Fig.IV. 2.2).

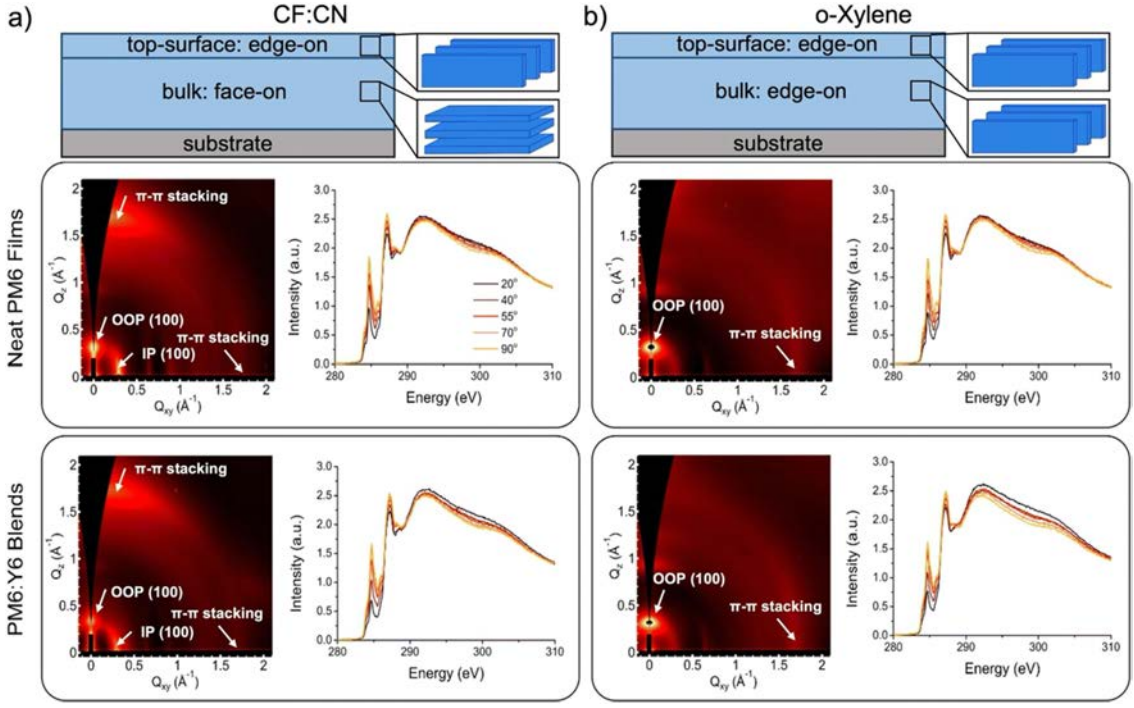

Figure IV. 2.2: Morphology of neat PM6 films and PM6:Y6 blend films (1:1.2 wt%) spin coated from two different solvent systems: (a) CF + 0.5 v% CN and (b) o-xylene. Sketches of the top-surface and bulk morphologies of PM6 as obtained from GIWAXS (bulk) and angle-resolved NEXAFS (top-surface). GIWAXS patterns were plotted on different color scales to properly illustrate all scattering features.

We prepared neat and blend films from two different solvent systems resulting in two different orientations of PM6 in the bulk. GIWAXS data collected at critical angles show that the films spin coated from CF:CN exhibit a dominant face-on orientation in the bulk for both neat PM6 films and blend films with Y6, marked by an intense in-plane (IP) lamellar (100) peak at around 0.3 $Å^{-1}$ and an out-of-plane (OOP) π-π stacking peak at around 1.7 $Å^{-1}$. A minority edge-on orientation is also observed in both neat and blend films as marked by the OOP lamellar (100) peak and IP π-π stacking peak. This matches studies on GIWAXS analysis and peak assignment of neat and blend films of PM6:Y6 processed from different solvents currently present in the literature. [20, 152, 181] From surface-sensitive NEXAFS spectroscopy investigations, an edge-on orientation is found on the surface of the CF:CN-processed films (the average tilt angle of the conjugated backbone is $\langle\alpha\rangle = 64 \pm 1°$). This observation is consistent with the GIWAXS data collected at an angle of incidence below the critical angle which probes surface microstructure, where the ratio of OOP to IP π-πstacking peak intensity decreases with a shallower incident angle (see Fig. B.2, Supporting Information). The existence of different orientations regarding bulk and surface and the strong dependence of morphology on

the processing parameters have already been reported for other conjugated polymers like N2200. [182–184] Processing of PM6 films and blends of PM6:Y6 from o-xylene solutions leads to edge-on orientation throughout the bulk, visible from the weak IP lamellar (100) peak and the corresponding strong OOP (100) signal, Fig.IV. 2.2(b). The surface shows an edge-on orientation as well, with an average tilt angle of the conjugated backbone of $\langle\alpha\rangle = 65 \pm 1°$. In general, the choice of solvent in combination with the processing method has a strong impact on the resulting morphology in the blends. Alternative processing methods like slot-die coating offering different drying kinetics are found in the literature and prove to show how orientations can differ using similar solvents as we do. [185] Regarding Y6, it has a high tendency to pack with a face-on orientation when processed from different processing solvents. [20, 163, 186–189] Here, the literature also gives examples of how small changes on the side groups of Y6 can impact the morphology although solution and processing parameters are kept constant.60 These results underline the importance of the chosen solvent for film preparation since the influence on the morphology and orientation in the film is strong and decides whether there is face-on, edge-on or mixed orientations. [164–166, 189, 190] This difference in morphological orientation of PM6 in PM6:Y6 films fabricated with CF:CN and o-xylene is reflected in the device performances (see Fig.IV. 2.1(d) for the corresponding current density–voltage (*J-V*) characteristics and the Experimental section for the fabrication conditions). Compared to the device with the active layer prepared from CF:CN solution, the blend coated from o-xylene yields a considerably smaller power conversion efficiency, which is mainly due to a lower V_{OC}. Possible reasons for this will be discussed below.

In addition, the NEXAFS results show that the film surface in the blend is enriched with PM6 ($\sim$ 70–80% PM6, see Fig. B.3, Supporting Information). This result is important because the HOMO levels of PM6 from UPS can differ compared to results from cyclic voltammetry. Since UPS is a surface sensitive method, surface morphology should definitely be considered. The impact of the different morphological orientations on the resulting energy levels of the frontier orbitals of both PM6 and Y6 in the blend films is the subject of the following experiments.

IV. 2.3.2 Energy level determination by *in situ* spectroelectrochemistry

The next paragraph presents an in-depth electrochemical analysis by coupling cyclic voltammetry and in situ UV-vis spectroscopy to identify onsets of oxidation and reduction which will be the foundation for the energy level determination. [191] An onset calculation purely based on cyclic voltammetry always suffers from a certain inaccuracy. In general, there is no thermodynamic foundation for an electrochemical onset potential which can vary due to kinetic effects (diffusion of ions into the film) and experimental aspects like background current and chosen electrolyte. [153] In particular, cyclic voltammetry of conjugated polythiophenes like PM6 with its inherent broad redox waves offers much potential for errors when using the onset which is one of the reasons for the high deviations in the HOMO energies from a *C-V* in the literature (see Table B.1, Supporting Information). Additionally, a significant variation in the overall *C-V* quality can be found in the literature, regarding the electrochemical reversibility and the avoidance of charge trapping effects, which unfortunately questions some of the published data. Whilst it does not rule out the general problem of onsets (definition of the threshold value) entirely, our approach excludes errors arising from the electrochemical experiment by

focusing on the spectroscopic response of the material to the applied electrochemical potential, from now on referred to as the spectral onset.

Since most charged species have an individual spectral fingerprint (see Table IV. 2.1), this elegant method allows for a more exact interpretation of the electrochemical processes. To discuss and disentangle multiple overlapping redox processes especially in the context of possible second oxidation steps (creating double charged species) the data from the *C-V* are completed with the in situ spectral information discussed in the next section. A transfer from the neutral to charged form is usually accompanied by a significant change in the UV-vis spectrum, so the onset of spectral change can be used to determine HOMO/LUMO energies. The importance of in situ UV-vis techniques has already been proven in the literature, describing film formation kinetics and analyzing the influence of the processing solvent and conditions on parameters like aggregation, phase separation and crystallinity in blends of PM6 and different NFAs. In this way morphology tuning of the BHJ active layers by annealing can be documented and modified towards increasing the performance of the final device. [192, 193]

Table IV. 2.1: Characteristic absorption maxima of neutral and charged states of neat Y6 and PM6 films. The arrows indicate oxidation and reduction steps

	$Y6^{-\bullet}$	←	**Y6**	→	**$Y6^{+\bullet}$**	→	**$Y6^{2+\bullet}$**
Wavelength/nm	380		830		750		890
	$PM6^{-\bullet}$	←	PM6	→	$PM6^{+\bullet}$	→	$PM6^{2+\bullet}$
Wavelength/nm	850, 1000		580, 625		830		890

Regarding the characterization of blend films our approach offers an additional advantage. The characteristic spectral response of each material allows us to discriminate between the two components in the blend and identify their individual contributions to the result. This means our technique helps us to differentiate between the redox states of the individual components, e.g., whether the second redox wave in the *C-V* scan corresponds to a differently charged state of component A or if it is the actual onset of component B.

In order to avoid errors in the onset determination, the redox behavior of Y6 and PM6 and spectral characteristics of the charged species all need to be understood individually. Before moving on to the complex electrochemical behavior of PM6:Y6 blend films, it is fundamental to understand the redox properties of neat Y6 and PM6 films first. The knowledge on the spectral characteristics of the neat compounds and the blends can also be of great help for other spectroscopic methods like photo-induced absorption (PIA) or transient absorption spectroscopy (TAS). Cyclic voltammograms of the neat material and blend films are presented in Fig.IV. 2.3 and IV. 2.4, giving separate *C-V*s for oxidation and reduction cycles to avoid the charge trapping effects. The presented data in the following section are produced with films processed from CF:CN solutions. The corresponding results of films from o-xylene are found in the Supporting Information (see Fig. B.4 and B.5).

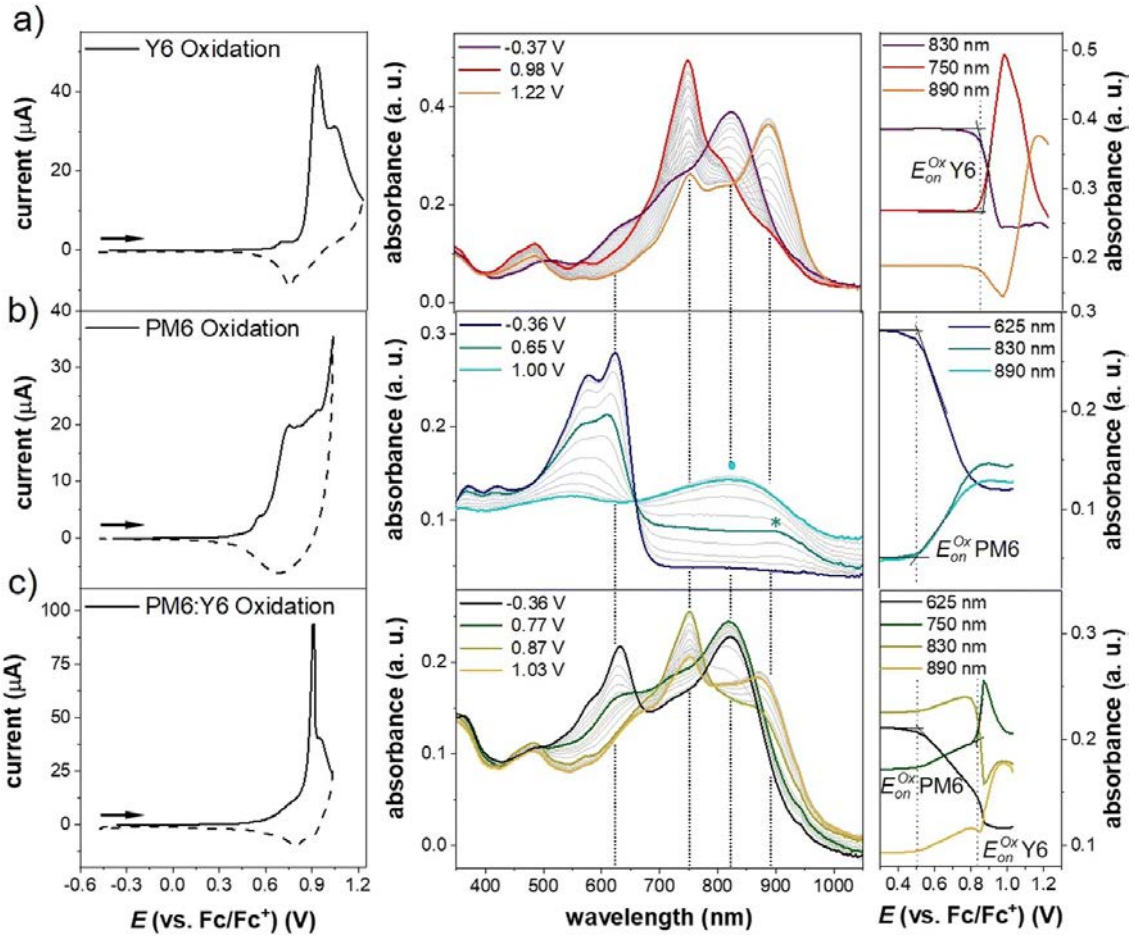

Figure IV. 2.3: In situ *C-V* measurements coupled with UV-vis spectroscopy of (a) neat Y6, (b) neat PM6 and (c) a blend of PM6:Y6 (1:1.2 wt%) films, spin coated from CF:CN (0.5 wt%) solutions. *C-V*s are given on the left (the forward half-cycle is highlighted as a solid line), the spectra of the forward charge half-cycle of the oxidation are presented in the center, completed with peak trends of significant bands on the right side. The peak trends are used for the determination of the spectral onsets which are indicated by dotted lines and obtained via using tangents. Underlying *C-V*s (1st cycles) are measured in 0.1 M $TBAPF_6$/MeCN at 20 mV s^{-1} on ITO substrates.

IV. 2.3.2.1 *HOMO determination*

Y6. The electrochemical behavior of the Y6 acceptor films shows sharp and defined peaks in the *C-V* for the oxidation, shown in Fig.IV. 2.3 a. The oxidation displays an intense wave at 0.92 V with an additional subsignal at 1.04 V. The reduction half-waves are less pronounced showing a weak wave at around 0.8 V. The spectral evolution during the charge half cycle of the oxidation (middle column) and the peak trends of significant absorption bands which are characteristic for the individual redox species (right column) is presented in Fig.IV. 2.3.

The characteristic UV-vis spectrum of a neutral Y6 film is shown in Fig.IV. 2.1 c and IV. 2.3 a in purple color at -0.37 V. When increasing the electrochemical potential, the absorption intensity at 830 nm (neutral band) decreases and a new band develops at 750 nm (red spectrum in Fig.IV. 2.3 a). The new band can be assigned to the first oxidized state (polaron). From the spectral evolution of the neutral species at 830 nm and the polaron species at 750 nm, the spectral onset can be determined via the tangent method

(highlighted in Fig.IV. 2.3 a, right graph). In the case of Y6 this gives a value of 0.84 V. This onset value will be the basis for the calculation of the HOMO energy of neat Y6 films and amounts to -5.64 eV. For the sharp and well-defined wave in the *C-V*, the onset from *C-V* at ~0.85 V (determined by the tangent method) is located quite close to our spectral onset.

Increasing the potential above 1 V, another change in the spectrum becomes visible for Y6. The intensity at 750 nm decreases in favor of a new characteristic peak at 890 nm which we assign to the second oxidized state of Y6 (yellow spectrum at 1.22 V in Fig.IV. 2.3 a). The potential of this spectral change fits to the previously observed signal in the *C-V* at 1.04 V, which can now be assigned to the second oxidation step.

PM6. Moving from the small molecule Y6 to the conjugated donor polymer PM6 distinct differences in the electrochemical behavior are present. In particular the oxidation in Fig.IV. 2.3 b shows the typical broad wave which is characteristic for polydisperse materials like polythiophenes and has been extensively studied for P3HT. [153, 194] In contrast to Y6, the backward half cycle of PM6 can be observed as well, transferring the created oxidized species upon charging back into the neutral form.

Regarding neat PM6 films the absorption spectrum of a neutral film is shown in Fig.IV. 2.1 and IV. 2.3 b in dark blue at -0.36 V. The rather well-defined peak at 625 nm (neutral band) decreases in intensity when extending the potential to positive values. The spectrum of the charged PM6 film now shows a broad absorption around 830 nm with a shoulder at 890 nm. The spectral evolution displays an isosbestic point at 660 nm, indicating a clear transition from the neutral species into the oxidized form. From earlier studies on P3HT we suspect a coexistence of both polaronic and bipolaronic forms at high potentials, since the spectral evolution upon electrochemical doping is similar to polythiophenes like P3HT. [153, 168, 195] Although the absorption shoulder at 890 nm (marked by a teal colored star) might be a feature of the polaron, exact assignment remains difficult due to identical and overlapping bands from both charged species at 830 nm (marked by a blue dot). The extracted spectral onset of the oxidation of neat PM6 is found at 0.50 V which amounts to a HOMO of -5.30 eV. Here, the onset of the *C-V* is located at 0.55 V which is at least 0.05 V further into the direction of positive potentials, caused by the broadening of the obtained *C-V* wave and increased difficulties in finding the correct onset. The same problem also occurs in the *C-V*s from the blend films. This underlines the significant advantage of our method relying on a combination of *C-V* and spectral onset determination.

PM6:Y6 blend. Knowing the electrochemical characteristics of neat Y6 and PM6 films enables the experimental data on PM6:Y6 blends to be interpreted. In general, all the previously described waves and signals can be found in the *C-V*s of the blend films as well. The oxidation in Fig.IV. 2.3 c shows a broad underlying wave with a sharp signal at 0.92 V which can be attributed to the oxidation of Y6. The broad signal underneath can be assigned to the oxidation of PM6.

Following the neat material films, the spectral evolution of the PM6:Y6 blend film is considered. As already described in Fig.IV. 2.1, the absorption of the neutral state of the blend film in Fig.IV. 2.3 c (black spectrum at -0.36 V) is almost a superposition of both neutral absorption bands of Y6 and PM6 with minor shifts occurring probably caused by different packing orders in the blend. This superposition of bands basically applies for the entire doping process and is highlighted by the vertical lines connecting characteristic bands in the neat material and blend films. The spectral onsets of the

individual compounds in the blend are found at 0.50 V for PM6 resulting in a HOMO of -5.30 eV (identical with the neat film) and at 0.83 V for Y6 with a HOMO of -5.63 eV.

For the presented films spin coated from CF:CN only a slight difference in the spectral onset of the oxidation between neat material and blend films can be found in the case of Y6, which can hardly be considered significant.

IV. 2.3.2.2 *LUMO determination*

Y6 The analysis of the spectral evolution of the reduction and the following extraction of spectral onsets for determining the LUMO levels are carried out accordingly.

The *C-V* upon the reduction of Y6 shows a quite sharp wave at -0.92 V, which is more pronounced compared to the oxidation behavior. In both cases (oxidation and reduction) in Fig.IV. 2.3 a and IV. 2.4 a the backward half cycles seem to be less pronounced which questions the electrochemical reversibility at first sight. It is important to mention that these *C-V*s were taken on thin films which are insoluble in the electrolyte in the pristine state. Experiments showed that the solubility properties of Y6 change when charged species of Y6 are being created. After completing the forward half cycle, the fully charged films start to dissolve into the electrolyte leading to a critical loss of electroactive material on the working electrode. As a result, the backward half cycles are weakly pronounced in the case of Y6 oxidation or not visible at all in the case of reduction.

The displayed spectral evolution of the reduction of neat Y6 films in Fig.IV. 2.4 a shows a decrease of the neutral band at 830 nm and a distinct increase at the low wavelength region of the spectrum around 380 nm. The isosbestic points clearly indicate a transition of the neutral state into a reduced form with a characteristic absorption band at 380 nm. The spectral onset of the reduction is located at -0.88 V which yields a LUMO of -3.92 eV.

PM6. The reduction of PM6 shows two separated waves in the *C-V* at -1.65 V and -1.89 V.

The spectral evolution of neat PM6 films shows a unique behavior in the reduction. Upon decreasing the electrochemical potential, the absorption intensity of the neutral band (625 nm) seems to increase at first (spectra from dark blue at -0.35 V to teal color at -1.60 V). This increase of absorption intensity appears at the same potential as the first reduction peak observed in the *C-V*. This is an indication that the PM6 film is slightly oxidized under ambient conditions prior to the experiment. The induced charges – probably originating from the exposure to oxygen – are re-extracted leading to the first reduction signal at around 1.65 V. This is accompanied by an increase of absorbance of the neutral band when the film reaches its fully neutral state. Only after the fully neutral state is reached and the potential is further decreased the typical bleaching of the neutral band is observed together with a broad increase of absorption above 800 nm. Additionally, a weak shoulder can be seen around 900 nm which might be a signature of the negative polaron. A supposed band overlap and the coexistence of different charged species at the same time, which is typical for polythiophenes, make the exact interpretation of this feature difficult.[168, 196] The characteristic absorption of the fully reduced state found at potentials around -1.9 V fits to the second, only relevant, reduction peak in the *C-V* which now completes the description of two reduction peaks in the *C-V* data. Using the spectral onset of this second reduction a value of -1.75 V can be extracted which leads to a LUMO of -3.05 eV for PM6.

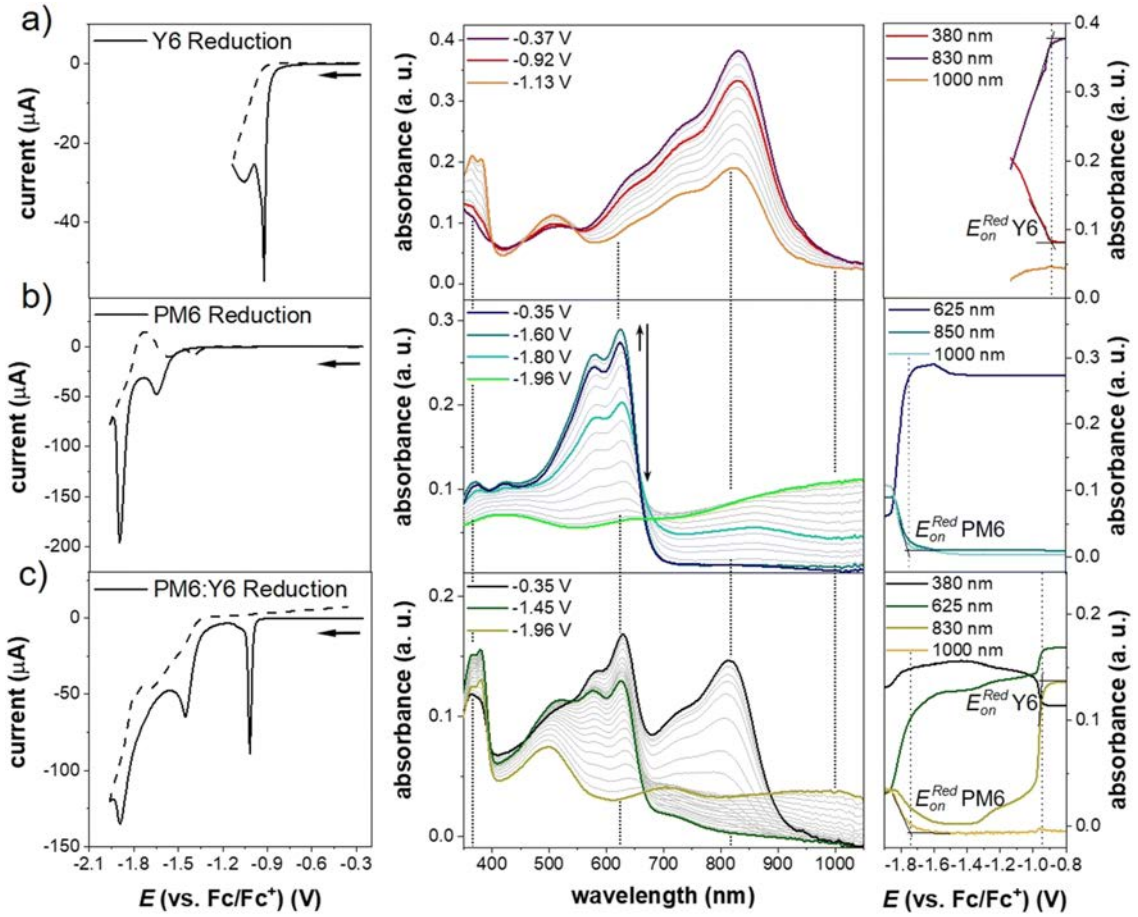

Figure IV. 2.4: In situ *C-V* measurements coupled with UV-vis spectroscopy of (a) neat Y6, (b) neat PM6 and (c) a blend of PM6:Y6 (1:1.2 wt%) films, spin coated from CF:CN (0.5 wt%) solutions. *C-V*s are given on the left (the forward half-cycle is highlighted as a solid line), the spectra of the forward charge half-cycle of the reduction are presented in the center, completed with peak trends of significant bands on the right side. The peak trends are used for the determination of the spectral onsets which are indicated by dotted lines and obtained via using tangents. Underlying *C-V*s (1st cycles) are measured in 0.1 M $TBAPF_6$/MeCN at 20 mV s^{-1} on ITO substrates.

PM6:Y6 blend. The *C-V* of the reduction of the blend films in Fig.IV. 2.4(c) displays three individual signals; one sharp wave (-1.02 V) which can be attributed to the reduction of Y6 and two broader signals (-1.45 V and -1.90 V) which can be seen at similar potentials in the reduction of the neat PM6 film. Evaluating the spectral onsets of the single compounds in the blend film results in a value of -1.74 V for PM6 which yields a LUMO of -3.06 eV and a value of -0.9 V for Y6 corresponding to a LUMO of -3.90 eV. Compared to the results of the neat films a shift of 0.02 V to a lower potential was found for Y6 with respect to the blend. The observed shift of the spectral onset of PM6 is only 0.01 V and therefore not significant.

IV. 2.3.2.3 *Comparison of energy levels, HOMO offsets and transport gaps*

All HOMO and LUMO levels of the neat material films and of the individual compounds inside the blend films (as obtained from the spectral onsets) are summarized in Fig.IV. 2.5.

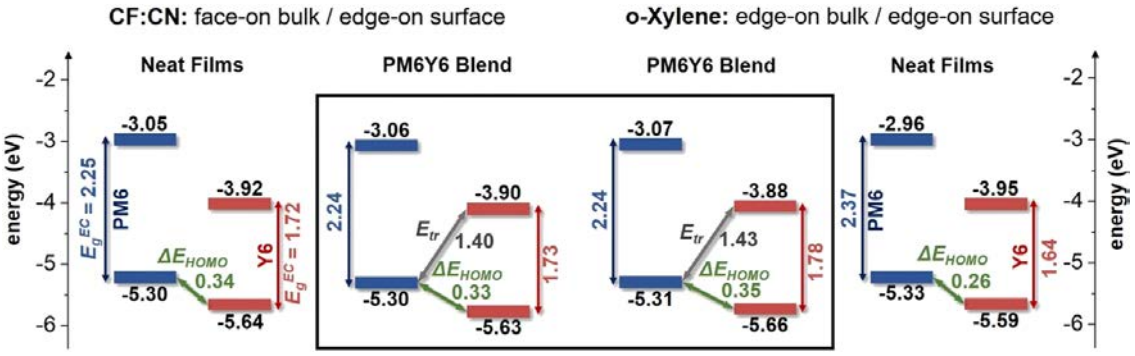

Figure IV. 2.5: Deduced HOMO/LUMO energy levels from the spectral onsets (Fig. IV. 2.2 and IV. 2.3) for films of neat PM6, neat Y6 and the individual compounds in the blend films of PM6:Y6 (1:1.2 wt%) processed from the two solvent systems CF:CN and o-xylene. The potentials were transformed to the Fermi scale using the correction factor of -4.8 eV. Electrochemical band gaps E_g^{EC} of the individual compounds are given as well as HOMO offsets ΔE_{HOMO} and transport gaps E_{tr}.

The determined frontier orbital energies of PM6 and Y6 neat films processed from CF:CN are positioned at -5.30 eV/-3.05 eV (HOMO/LUMO PM6) and at -5.64 eV/-3.92 eV (HOMO/LUMO Y6). The resulting electrochemical band gaps for PM6 are found to be 2.25 eV and 1.72 eV for Y6. The HOMO offset of the two components calculated from the neat films is obtained at 0.34 eV. Compared to the results of the blend prepared from CF:CN, the energy levels of PM6 (-5.30 eV/-3.06 eV) and Y6 (-5.63 eV/-3.90 eV) are located at rather identical values. The blend shows a HOMO offset of 0.33 eV and a transport gap of 1.40 eV. The results for the neat films processed from o-xylene show slight changes in the energy levels. Our experiments yield energy levels of -5.33 eV/-2.96 eV (HOMO/LUMO PM6) and -5.59 eV/-3.95 eV (HOMO/LUMO Y6). This has a direct influence on the HOMO offset which shrinks to 0.26 eV. In the blend processed from o-xylene the HOMO/LUMO levels slightly differ from that of the neat films and are located at -5.31 eV/-3.07 eV (HOMO/LUMO PM6) and at -5.66 eV/-3.88 eV (HOMO/LUMO Y6). This correlates to a HOMO offset of 0.35 eV and a transport gap of 1.43 eV. The calculated energy levels from the spectral onsets for the blend films show a HOMO offset (ΔE_{HOMO}) which is consistently positioned between 0.33 and 0.35 eV.

Comparing textures, in the blend prepared from the CF:CN solution (face-on orientation in bulk), the offset is 0.33 eV, whereas the offset slightly increases to 0.35 eV in the case of blends from o-xylene solutions (in edge-on orientation in bulk). The calculated effective transport gap of 1.4 eV for blend films processed from CF:CN (face-on orientation) is also slightly smaller than for blends from o-xylene solution (edge-on orientation) with an effective transport gap of 1.43 eV.

When comparing the HOMO offset in the neat films with the results of the blend films, differences regarding the solvent systems become visible. While the HOMO offsets remain rather constant for CF:CN films, an increase in the HOMO offset for films prepared from o-xylene solutions is registered. Our study therefore clearly shows that the impact of morphology and molecular orientation on device relevant parameters like HOMO offset and effective transport gaps is small but measurable. In particular, for the investigated materials Y6 and PM6, the results from the spectroelectrochemical experiments lead to the conclusion that blending both components give measurable differences in the energy levels.

The occupied energy levels of the films (HOMO) prepared from different processing solvents (CF:CN and o-xylene) were further measured using ultraviolet photoelectron spectroscopy (UPS). Being a highly surface sensitive technique, UPS results are only influenced by the properties of the top surface of the films and cannot take differing bulk morphologies into account. Since films from CF:CN and o-xylene show identical surface orientations with edge-on orientation (see Fig. IV. 2.2) no difference within the experimental error was measurable, as expected. The UPS spectra of neat PM6 and Y6 films as well as the PM6:Y6 blend processed from CF:CN are shown in Fig.IV. 2.6; the spectra of blends from other processing solvents are shown in the Supporting Information (see Fig. B.6).

The secondary electron cut-off (SECO) spectra in Fig.IV. 2.6(a) are used to calculate the work function of the material and give energies of -4.48 eV for PM6, -4.59 eV for Y6 and -4.54 eV for the PM6:Y6 blend. Adding the work function to the HOMO onsets extracted from the valence band spectra in Fig.IV. 2.6(b) yields the ionization energy of the respective components. The onset used to calculate the binding energy of neat PM6 is rather broad (blue line in Fig.IV. 2.6(b)), while the HOMO of Y6 has a more distinct onset. For binding energies, we extract 0.66 eV for PM6 and 1.09 eV for Y6. This results in ionization energies of the neat films (HOMO levels) of PM6 of -5.14 eV and of Y6 of -5.68 eV (HOMO offset 0.54 eV), in good agreement with the other values reported in the literature from photoelectron spectroscopy on neat layers (see Table B.1 in the Supporting Information).

The Y6 HOMO from UPS at -5.68 eV agrees quite well with the value from the spectral onsets in the in situ *C-V* measurements, while the UPS HOMO of PM6 is shifted by about 0.15 eV to -5.14 eV. This is in line with previously reported data. [172] The reason for this is not clear yet, but we emphasize here that the ionization energy from UPS is very sensitive to the electrostatics at the surface, which will most likely be different in neat and blend films. [197] Therefore, we point out that experiments on neat films have to be taken with caution when they are used to explain the energetics of blend films. To actually access the HOMO energies of the individual components in blend films, we subtract the (scaled) reference valence band spectrum of neat PM6 from the blend spectrum (see Fig.IV. 2.6(c)). The residual intensity resembles the spectral shape of neat Y6, as indicated by the three features labeled H1, H2 and H3. A broadening is observed, which can be caused by the intermixing of the two molecules and the concomitant disorder. [198, 199] A zoom into the HOMO onset region is shown in Fig.IV. 2.6(d) and yields HOMO energies of -5.13 eV and -5.38 eV for PM6 and Y6, respectively. This corresponds to a HOMO offset of 0.25 eV between the two materials, significantly smaller than the HOMO offset determined from the pristine films and in good agreement with the *C-V* and UV-vis results. The difference in the absolute values compared to the *C-V*/UV-vis results could be caused by different electrostatic interactions, e.g., dipole, quadrupole or higher order moments, polarization and screening effects etc., as has been demonstrated before. [200–202]

IV. 2.3.3 Discussion of solar cell performance

With the transport gaps of the neat components and the blends at hand, we now turn to the performance of our PM6:Y6 blend in solar cells. As pointed out earlier, it was proposed that the PM6:Y6 blend exhibits a small barrier for free charge generation.

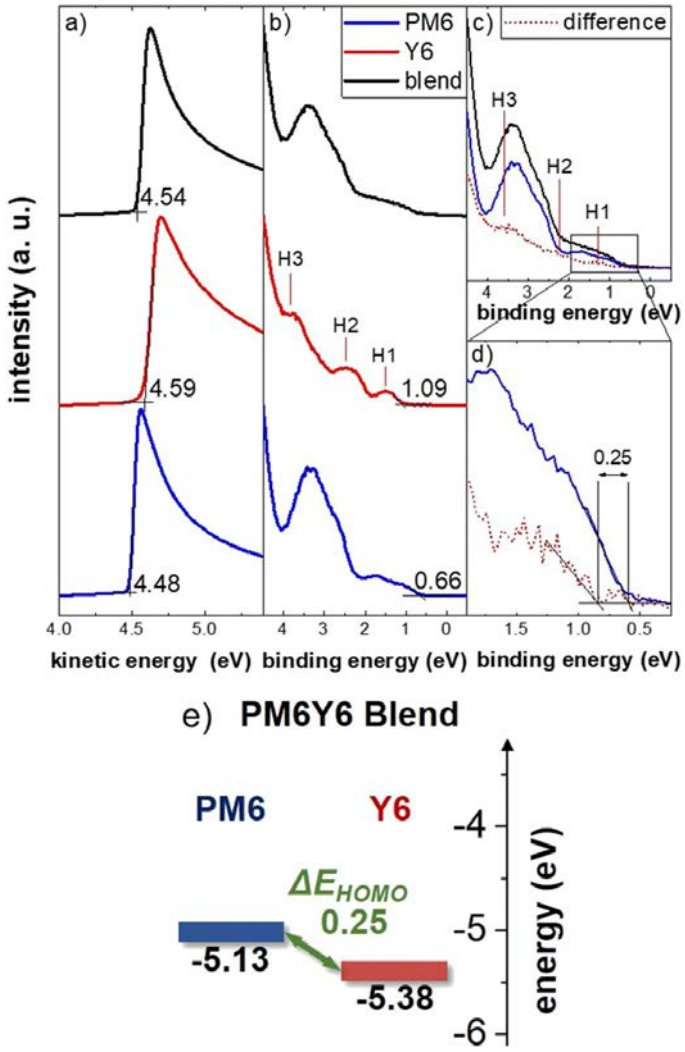

Figure IV. 2.6: (a) Secondary electron cut-off (SECO) and (b) valence band spectra of neat PM6, neat Y6 and PM6:Y6 (1:1.2 wt%) blend films prepared from CF:CN (0.5 wt%). (c) Subtraction of the PM6 valence band spectrum (scaled) from the PM6:Y6 blend spectrum. The residual intensity resembles a broadened Y6 valence band spectrum, as indicated by the HOMO features labeled H1, H2 and H3. (d) Zoom into the valence band onset region marked in (c), yielding a HOMO offset between PM6 and Y6 in the blend of 0.25 eV, significantly smaller than the HOMO offset of the neat films (0.54 eV). Extracted energy levels and HOMO offset (ΔE_{HOMO}) for the blend film are displayed below in (e).

Other groups argued that Y6-based solar devices function efficiently because of a very low or even vanishing exciton binding energy, E_b, of the Y6 singlet exciton. For example, a recent self-consistent quantum mechanics/embedded charge study predicted the energy of Y6 S_1 (ca. 2 eV) to lie 0.1 eV above that of the charge separated state (1.9 eV). There is, indeed, experimental evidence for direct free charge generation in Y6 solid films. [203, 204] Our spectroelectrochemistry data put the electrochemical band gap of Y6 in neat films at 1.72 eV (CF:CN) and 1.64 eV (o-xylene, see Fig.IV. 2.5). This is up to 0.17 eV larger than the mean HOMO–LUMO gap from conventional *C-V* (see Table B.1 , Supporting Information), but compares very well with the gap of 1.7 V determined by photoelectron spectroscopy in the literature. [66] The Y6 band gap is slightly higher in the blend with 1.73 eV from CF:CN and 1.78 eV from o-xylene and consistent with a slight blue shift in absorption, indicating a slightly more distorted structure. On the other hand, we determined the energy of the Y6 singlet energy by the intersection between the

normalized absorption and PL of the blend to be 1.42 ± 0.02 eV (see Fig. B.7, Supporting Information). This yields a Y6 exciton binding energy at 0.33 ± 0.05 eV. This is in the same range as the HOMO offset in the blend, suggesting that the driving force for free charge formation by exciton dissociation is nearly zero. This contrasts the efficient free charge generation of the blend. A similar scenario has been reported by Wu et al. where it was suggested that the formation of free charges is driven by entropy. [172] This is because an electron–hole pair in the charge separated state has many more options to distribute in the blend volume than when it is bound in an exciton or in a charge transfer state. [54] However, our own recent studies showed a pronounced decrease of the free carrier density with temperature, [15] which questions a strong contribution by entropy-driven processes. An alternative approach is to consider the presence of sub-bandgap states not accessible by our spectroscopy. [205–207] Such states will be able to situate the free electron–hole pair at energies well below the singlet exciton of Y6.

We finally address the reason for the significantly lower V_{OC} of the device prepared from o-xylene (0.77 V vs. 0.83 V for the CF:CN). According to Fig.IV. 2.5, the fundamental transport gaps are 1.43 eV and 1.40 eV for the blend prepared from o-xylene and CF:CN, respectively, showing the inverse trend. However, the relation between V_{OC} and the fundamental gap is not straight forward. In general, the V_{OC} of a device is given by the radiative voltage limit reduced by the non-radiative voltage loss: $V_{OC} = V_{OC,rad} - \Delta V_{nr}$. The radiative V_{OC} limit is mainly determined by the ratio of the short circuit current, J_{SC}, and the radiative dark current, $J_{0,rad}$, the latter being proportional to the convolution of the external photovoltaic quantum efficiency (EQE_{PV}) of the device and the blackbody photon flux (ϕ_{BB}) over photon energy: [208] $qV_{OC,rad} = k_B T ln(JSC/J_{0,rad})$ where $J_{0,rad} = q \int \mathrm{EQE}_{PV}(E)\phi_{BB}(E)dE$.

Here, the transport gap may enter indirectly via the onset of the EQE_{PV} spectrum. However, it has been shown before that the low energy tail of PM6:Y6 EQE_{PV} is entirely determined by the Y6 singlet exciton, which has a very similar energy for the two blends. [25] As a consequence, the band-edge of the EQE spectra in Fig.IV. 2.7(a) overlaps almost completely, yielding nearly the same $V_{rad,OC}$ for the two devices (Table B.2 , Supporting Information). Therefore, the difference in V_{OC} of the two devices must be entirely caused by the non-radiative losses (ΔV_{nr}). To confirm this, we measured the external electroluminescence quantum yield (ELQY), which is related to ΔV_{nr} via $q\Delta V_{nr} = -k_B T ln(\mathrm{ELQY})$ (see Fig. B.8 in the Supporting Information for the emission spectra). This measurement revealed an almost 10 times lower ELQY for the device prepared from o-xylene (see Fig.IV. 2.6(b) and Table B.2 , Supporting Information for the values). It has been shown that the ELQY of the PM6:Y6 blend is limited by the non-radiative decay properties of the CT state. [25] In organic solar cells, the predominant non-radiative decay pathway of the CT state is through vibronic coupling to the ground state. [114, 209] There is experimental and theoretical evidence that this process is significantly affected by the interfacial molecular orientation. [210, 211] Our results suggest that this is the determining factor also in our PM6:Y6 devices.

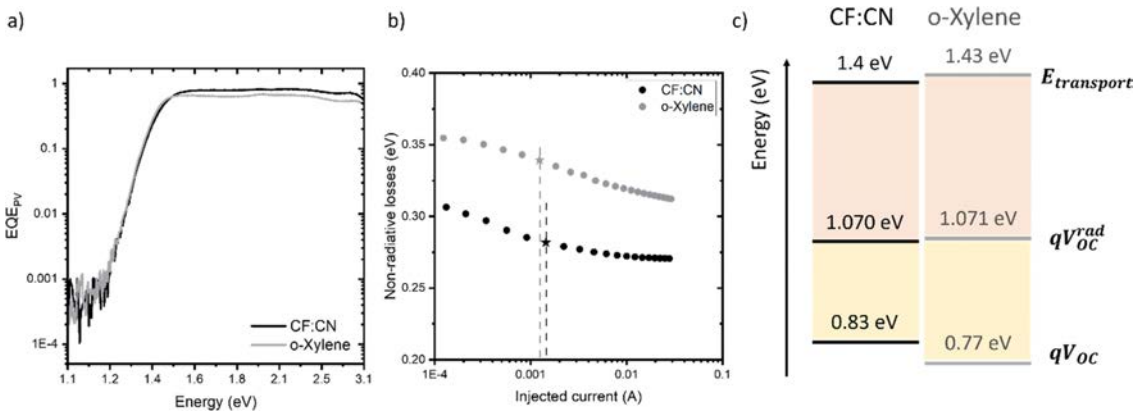

Figure IV. 2.7: EQE_{PV} (a), non-radiative voltage loss as a function of injected current (b), and schematic of relevant energy losses (c) of PM6:Y6 devices fabricated in CF:CN (black) and o-xylene (grey). The dashed lines in (b) indicate when the injected current equals short-circuit current at 1 sun.

IV. 2.4 Conclusions

In summary, this work presents an absorption spectroscopy assisted, spectroelectrochemical approach to determine the frontier orbital energies of PM6 and Y6 in blend films. A central advantage of our technique is the detection of the energy levels of the individual compounds inside the blend films and therefore examines influences arising from blending both materials. By preparing solar cells from two solvent systems resulting in two opposing bulk morphologies we investigated the influence of morphology on the energetics in blend films of the model system PM6:Y6. Our results provided the HOMO/LUMO levels for PM6 of -5.30 eV/-3.06 eV and for Y6 of -5.63 eV/-3.90 eV in blend films processed from CF:CN (face-on morphology in bulk). Respective results for blend films processed from o-xylene (edge-on in bulk) delivered the HOMO/LUMO levels for PM6 of -5.31 eV/-3.07 eV and for Y6 of -5.66 eV/-3.88 eV. Interestingly, these values differ only slightly from the corresponding energies of the neat layers. Our data show that the effect of the different morphologies in the two blends on the energy levels is measurable but too small to explain the distinct difference in device performance. From our spectroelectrochemical measurements, we could determine the HOMO offsets and the transport gaps to be 0.33 eV and 1.4 eV for films from CF:CN and 0.35 eV and 1.43 eV for films from o-xylene, respectively. The HOMO offset was confirmed by UPS measurements on the blend, which yielded a value of 0.25 eV. Notably, the UPS measurements on the neat layers would suggest a HOMO offset of 0.54 eV, indicating that a comparison with neat material films must be taken with care. Finally, we determined the S_1 binding energy of the CF:CN coated Y6 to be 0.33 eV, very similar to the HOMO offset. This suggests that an additional driving force exists for free charge generation. This study exemplifies the importance of precisely determining energy levels in blend films to generate device relevant information.

IV. 3 Toward More Efficient Organic Solar Cells: A Detailed Study of Loss Pathway and Its Impact on Overall Device Performance in Low-Offset Organic Solar Cells

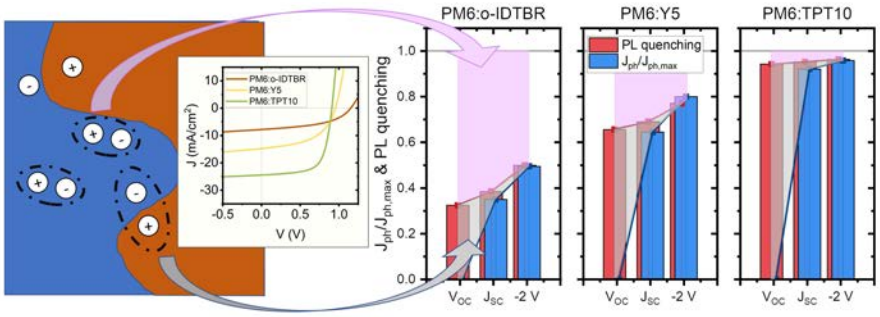

This work provides an insightful understanding of the role of driving force in the overall device performance by performing systematic and detailed loss analyses for each relevant *JV* parameter in a series of NFA-based low-offset OSC systems. The losses via each loss channel are analyzed in detail. In general, this work presents a path towards more efficient organic solar cells.

This chapter is an adapted preprint of:
Bowen Sun, Nurlan Tokmoldin, Obaid Alqahtani, Acacia Patterson, Catherine S. P. De Castro, Drew B. Riley, Manasi Pranav, Ardalan Armin, Frédéric Laquai, Brian A. Collins, Dieter Neher, Safa Shoaee. Toward More Efficient Organic Solar Cells: A Detailed Study of Loss Pathway and Its Impact on Overall Device Performance in Low-Offset Organic Solar Cells. Adv. Energy Mater. (2023), 2300980.

IV. 3.1 Abstract

Low-offset organic solar cell systems have attracted great interest since nonfullerene acceptors came into the picture. While numerous studies have focused on the charge generation process in these low-offset systems, only a few studies have focused on the details of each loss channel in the charge generation process and their impact on the overall device performance. Here, several nonfullerene acceptors are blended with the same polymer donor to form a series of low-offset organic solar cell systems where significant variation in device performance is observed. Through detailed analyses of loss pathways, it is found that: i) the donor:acceptor interfaces of PM6:Y6 and PM6:TPT10 are close to the optimum energetic condition, ii) energetics at the donor:acceptor interface are the most important factor to the overall device performance, iii) exciton dissociation yield can be field-dependent owing to the sufficiently small energetic offset at the donor:acceptor interface, and iv) the change in substituents in the terminal group of Y-series acceptors in this work mainly affects energetics at the donor:acceptor interface instead of the interface density in the active layer. In general, this work presents a path toward more efficient organic solar cells.

IV. 3.2 Introduction

Thanks to the development of nonfullerene acceptors (NFAs), the organic solar cell (OSC) field is currently enjoying a revitalization, with power conversion efficiencies now approaching 20%. [5, 212, 213] Presently, OSC-based NFAs match their inorganic competitors in terms of current production (internal quantum efficiency) owing to their large and complementary absorption, but lag behind with regards to their fill factor (FF) and open-circuit voltage (V_{OC}). [214]

Interestingly, NFA-based solar cells seem to require a smaller driving force for charge generation to work efficiently and simultaneously benefit from a smaller open-circuit voltage loss. In this regard, PM6:Y6 has spurred significant fundamental interest for the possibility of an efficient device with a small energy offset. While initial reports on different NFA systems suggest that efficient charge generation is achievable with a small offset, [22, 50, 133, 215] other in-depth characterization studies of energy levels suggest that a minimum ionization potential offset of 0.3–0.5 eV is required to ensure efficient charge transfer. [66, 129, 131]

With decreasing the highest occupied molecular orbital (HOMO) offset, another observation is that the decreased energy offset between singlet excitons (S_1) and the charge transfer (CT) state of the acceptor ($\Delta E_{S_1\text{-}CT}$) leads to reverse transition from the CT state back to the singlet state (repopulation of singlet excitons). Indeed, the low $\Delta E_{S_1\text{-}CT}$ feature and consequently S_1 reformation in low HOMO-offset systems can lead to interesting and important behaviors in these systems. For this reason, it was observed that the lowest nonradiative voltage losses (ΔV_{nr}) in such low-offset systems are defined by the photoluminescence yield of the acceptor. [117] However, recent work from Neher and co-workers shows that the reduction in ΔV_{nr} due to S_1 repopulation cannot be simply translated into an overall benefit to the V_{OC}. [98] On the other hand, the S_1 reformation feature changes the recombination picture, which can now occur via two channels – CT decay and S_1 decay. Recent work has shown that in PM6:Y6, while the S_1

emission dominates photoluminescence (PL) and electroluminescence (EL), around 99% of the recombination still occurs via the nonradiative CT channel. [25] However, in other systems with even smaller HOMO offset compared to that of PM6:Y6, the loss from the S_1 decay channel may be considerable.

In terms of the charge generation yield (CGY), it has been proposed in previous works that the relation between $\Delta E_{S_1\text{-CT}}$ and CGY can be well described by a model based on the Boltzmann stationary-state equilibrium between the CT and S_1 states when $\Delta E_{S_1\text{-CT}}$ is sufficiently small. [42] Thus, while the minimal energy offset inhibits the rate of charge transfer at the interface, a long exciton lifetime has been suggested to be a key to achieving high generation efficiencies in low $\Delta E_{S_1\text{-CT}}$ systems. [42, 216] However, it has also been observed that other parameters such as the energetic offset between the CT and charge separation (CS) states, the CT decay rate (k_f), and morphology can play an important role in the relation between $\Delta E_{S_1\text{-CT}}$ and CGY. [68, 217] In addition, it was also reported that the low $\Delta E_{S_1\text{-CT}}$ values influence the CT dissociation rate by affecting the energetic offset between the CT and CS states. [67]

Given these complex interplays, the question that arises is whether efficient organic solar cells could be obtained by simply reducing $\Delta E_{S_1\text{-CT}}$. More specifically, how does the reduction of $\Delta E_{S_1\text{-CT}}$ affect the overall performance of an organic solar cell. While a considerable amount of work has focused on the effect of reduced $\Delta E_{S_1\text{-CT}}$ on V_{OC} and on charge generation, limited work has researched the effect of reduced $\Delta E_{S_1\text{-CT}}$ on charge recombination and fill factor and the overall device performance. [218, 219]

In this work, a set of nonfullerene acceptors were judiciously selected and blended with the same polymer donor (PM6) and compared with the reference system PM6:Y6 to study the effect of reduced $\Delta E_{S_1\text{-CT}}$ on the overall performance. The systems in this work present a series of low $\Delta E_{S_1\text{-CT}}$ values with a wide range of device performances. Various steady-state and transient measurements were performed for a detailed study of charge generation, recombination, and V_{OC} losses. An insightful understanding of the role of $\Delta E_{S_1\text{-CT}}$ in the overall device performance in small $\Delta E_{S_1\text{-CT}}$ region is given. For the systems studied herein, we demonstrate that PM6:Y6 and PM6:TPT10 are close to the optimum energetic conditions with respect to their power conversion efficiency (PCE). In the systems where $\Delta E_{S_1\text{-CT}}$ values are further reduced, significant reduction in the short-circuit current (J_{SC}) and FF were observed concurrently with a limited benefit in V_{OC}, although ΔV_{nr} was significantly reduced. It was found that at J_{SC}, the losses mainly originated from inefficient exciton dissociation yield, while the losses via the CT states became more pronounced as the applied voltage reached V_{OC}.

Interestingly, the charge generation process was observed to be field-dependent in systems with sufficiently small $\Delta E_{S_1\text{-CT}}$ values. With further investigation, our data indicated that this field dependence came from field-dependent exciton dissociation at the donor:acceptor interface instead of from the CT states, presenting a different picture from that described by the Onsager–Braun model explaining a field-dependent charge generation in organic solar cells. Furthermore, the bimolecular recombination rate (k_2) increased as $\Delta E_{S_1\text{-CT}}$ was reduced. The field-dependent charge generation together with the increased k_2 leads to the inferior FF and the overall device performance in PM6:Y5 and PM6:o-IDTBR.

IV. 3.3 Results and Discussion

To study the relation between $\Delta E_{S_1\text{-}CT}$ and the device performance, three small NFA molecules are chosen as the acceptors (o-IDTBR, Y5, and TPT10) and PM6 is used as the donor. These three PM6:NFA systems are then compared with the "standardized" PM6:Y6 in terms of their device performances as well as detailed charge generation and recombination mechanisms and dynamics. The chemical structures of the three NFA molecules are given in Figure IV. 3.1a, the full chemical names and device structures can be found in the Supporting Information. Compared to PM6:Y6, the three organic heterojunctions in this work have considerable smaller HOMO offsets, indicating smaller $\Delta E_{S_1\text{-}CT}$ values.

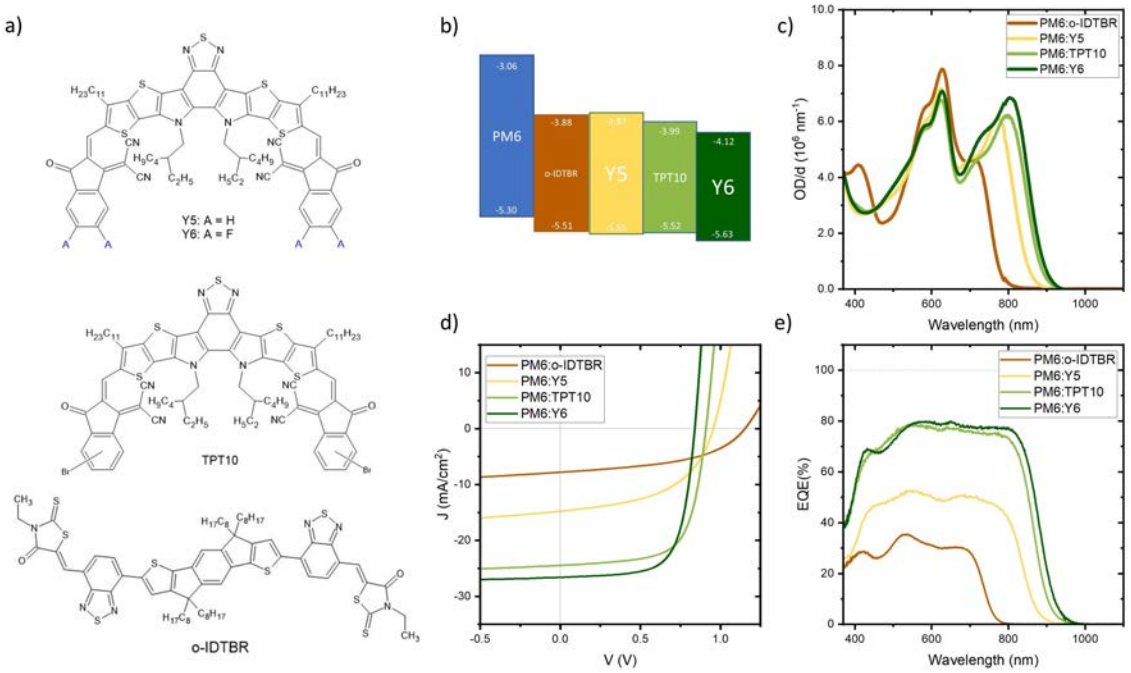

Figure IV. 3.1: Chemical structures, b) energy levels of polymer donor and nonfullerene acceptors reported from previous work, [21, 131, 220–223] c) thickness-normalized optical densities, d) current–voltage (*J-V*) characteristics, and e) external quantum efficiencies (EQEs) of the blends and materials used in this work.

For the studied systems, while the HOMO offsets are only slightly different, significantly different device performances (in J_{SC}, FF, and V_{OC}) were observed. Figure IV. 3.1d shows the currents–voltages (JVs) of the studied systems (detailed *JV* parameters are given in the Supporting Information), where the increase in V_{OC} comes at the cost of the reduction in J_{SC}. Among the studied systems, PM6:TPT10 has the largest J_{SC} (24.4 mA cm^{-2}) and lowest V_{OC} (0.91 V), while the behavior is vice versa for PM6:o-IDTBR (J_{SC} of 7.8 mA cm^{-2}, V_{OC} of 1.15 V). The photovoltaic bandgap of each system is obtained by the first derivative of photovoltaic external quantum efficiency (EQE_{PV}) spectra (Figure C.1, Supporting Information). The low J_{SC} in PM6:o-IDTBR can be partly explained by its large photovoltaic bandgap (1.69 eV) compared to the other studied systems.

However, this is not the whole picture. As is shown in Figure IV. 3.1d, the major difference in the EQE_{PV} spectra is in its amplitude rather than the absorption spectrum. In the

following subsection, the $\Delta E_{S_1\text{-}CT}$ values of each system are first characterized and compared. Thereafter, detailed analyses on the charge generation and recombination are performed to elucidate the underlying origin of the device performance in these systems and give a unified understanding on the role of $\Delta E_{S_1\text{-}CT}$.

IV. 3.3.1 Evaluation of Low $\Delta E_{S_1\text{-}CT}$ Offsets

In evaluating $\Delta E_{S_1\text{-}CT}$ by determining the HOMO–HOMO energetic offset, we are faced with two challenges: 1) difficulty in determining the HOMO values in the blend [153, 154] and 2) lack of information on binding energies for the singlet exciton and CT states. [224–226] To overcome these issues, in particular account of the binding energies, and to study the energetics of the excited species in a working device, we consider using the energy difference between the CT state and the exciton, $\Delta E_{S_1\text{-}CT}$, instead of HOMO–HOMO offset. To this end, we performed temperature-dependent electroluminescence quantum yield (T-ELQY) measurements on working devices. In a system where the HOMO–HOMO offset is estimated to be sufficiently small, the EL spectrum is almost entirely composed of the 0–0 transition of the small bandgap NFA singlet exciton (see Figure C.2 in the Supporting Information). [25] In all three systems studied herein, the PL and EL of the blends resemble the PL of the neat acceptors (see Figure C.2 in the Supporting Information for the comparison of the EL spectra of the blends and the PL spectra of the corresponding neat NFAs) pointing to the presence of the S_1 states and negligible CT contributions in the EL spectra, which is consistent with the energetics of the donor and acceptors.

In a T-ELQY measurement, when fixing the injection current, the quantity of reformed S_1 states is essentially the result of the rate competition between the CT decay and net S_1 repopulation rate from CT. While the rate constant of the CT decay is described by a constant k_f, the rate constant of S_1 reformation from CT can be described by an exponential expression $k_{ref} = k^*_{ref,0} \cdot exp(-\frac{\Delta E_{S_1-CT}}{k_B T})$, where $k^*_{ref,0}$ corresponds to the net CT–S_1 reformation rate k_{ref} at infinite temperature. [25, 49, 58] In this regard, in the studied systems where the EL spectra are almost fully represented by exciton emission, the ELQY values are proportional to the quantity of reformed excitons in the charge injection process

$$ELQY \propto \frac{\#\, exciton}{\#\, injected\ charge} = \frac{k_{ref}(T)}{k_{ref}(T) + k_f} = \left[1 + \frac{k_f}{k_{ref}(T)}\right]^{-1} \qquad \text{(IV. 3.1)}$$

Using the ELQY values, the normalized ELQY*(T) given by ELQY*(T) = ELQY*(T)/ELQY*(T_{max}) is plotted against $1/k_B$T and fitted with the physical model (Equation IV. 3.1), from which $\Delta E_{S_1\text{-}CT}$ is obtained. The data are shown in Figure IV. 3.2a, where a clear trend of the $\Delta E_{S_1\text{-}CT}$ offset in the four involved systems is observed, varying from ≈25 (for PM6:o-IDTBR) to ≈114 meV (for PM6:Y6). The trend in $\Delta E_{S_1\text{-}CT}$ offsets agrees well with the EQE amplitudes (Figure IV. 3.2b), where the smallest EQE corresponds to the smallest $\Delta E_{S_1\text{-}CT}$ offset. As the $\Delta E_{S_1\text{-}CT}$ offset increases, the EQE_{max} first increases accordingly, then saturates at ≈80%.

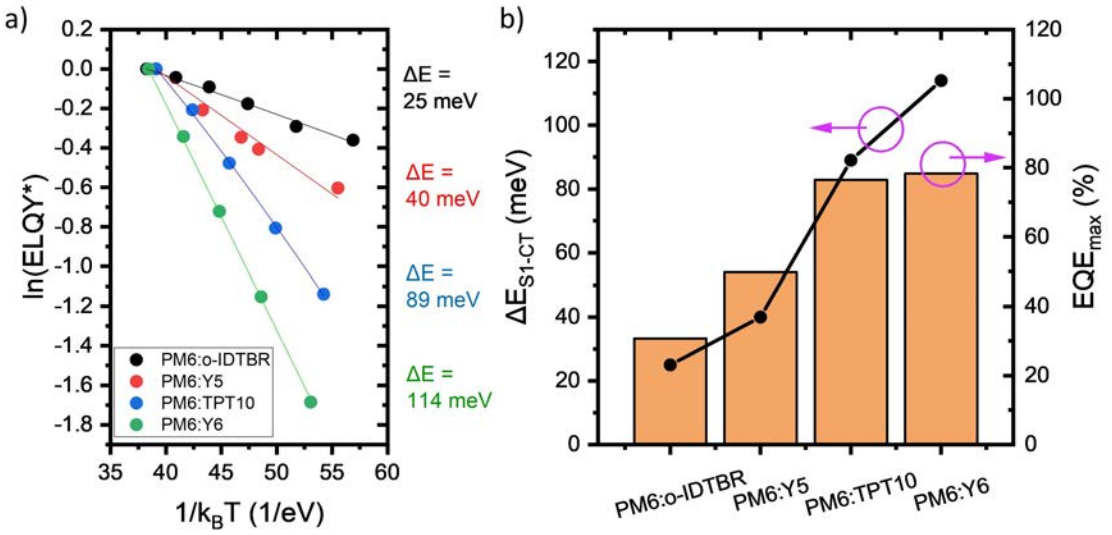

Figure IV. 3.2: a) Temperature-dependent ELQY of the devices, the temperature-dependent ELQY values of PM6:Y6 are taken from a previous paper from our group, [25] and refitted with Equation IV. 3.1. b) The fitted $\Delta E_{S_1\text{-}CT}$ values and EQE amplitude of each system.

IV. 3.3.2 Loss Channels in Low-Offset OSCs

For a deeper understanding of the losses in EQE and photocurrent in the studied systems, charge generation and recombination processes, as well as the interplays between each energy state must be considered (depicted in Figure IV. 3.3). Light absorption by the bulk heterojunction (BHJ) materials generates excitons that diffuse to the donor:acceptor interfaces, where they dissociate into CT states which subsequently form CS states via CT dissociation. Upon the encounter of free charges, CT states are reformed and recombine directly to the ground state thereafter (known as bimolecular recombination). In low-offset OSC systems, the S_1 states can be rather efficiently repopulated via the CT state. The loss mechanism can be described by four channels: 1) exciton loss in the domain during exciton diffusion, [24, 217] 2) decay of excitons at the donor:acceptor interface (energy driven), [24] 3) decay of reformed excitons from the CT states, [68, 98] and 4) decay of the CT states. Channel 1 describes the competition between the domain size and exciton diffusion length, while channel 2 entails the details of the S_1 dissociation rate and exciton lifetime. On the other hand, channel 3 gives information on the competition between exciton reformation and CT decay, and channel 4 includes the rate competition between net CT dissociation, net CT reformation, and CT decay. In the following subsection, the losses from each channel are studied in detail.

IV. 3.3.3 Loss Analysis for J_{SC}

IV. 3.3.3.1 *Losses via S_1 and CT States*

Photoluminescence measurements can be used to probe exciton dissociation. The extent of exciton emission quenching of the blend film relative to the corresponding neat film can be a useful assay of exciton splitting, assigned to the charge transfer from the exciton to the formation of CT states. Herein, photoluminescence quantum yield (PLQY)

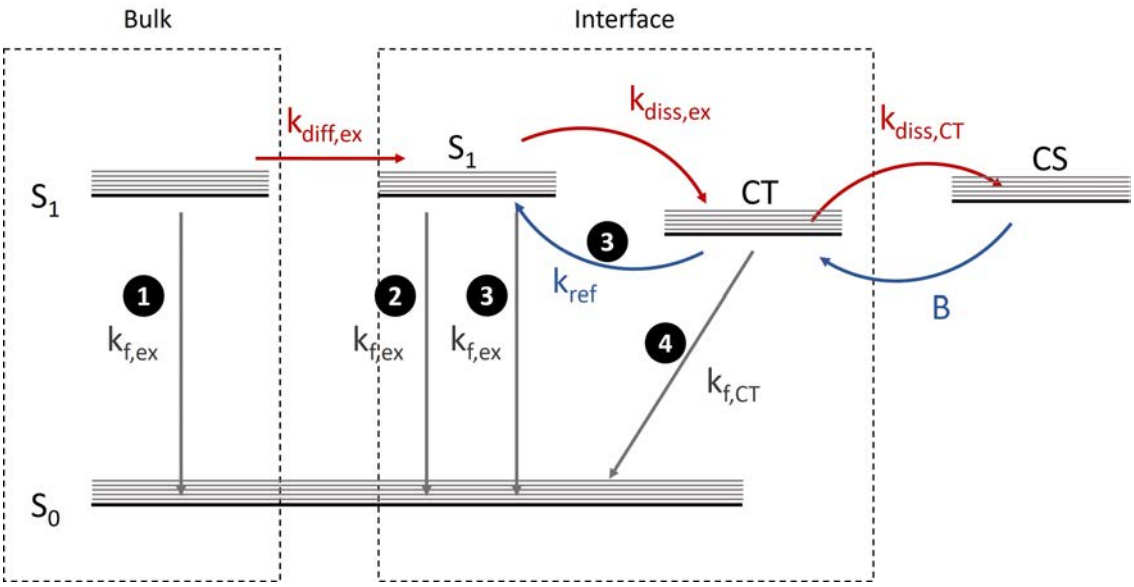

Figure IV. 3.3: Energy diagram describing the generation and decay of S_1 and CT states as well as the interplays between each energy state in low-offset OSCs. $k_{f,ex}$, $k_{diff,ex}$, and $k_{diss,ex}$ are the rate constants of the decay, diffusion, and dissociation of excitons, respectively. $k_{f,CT}$ and $k_{diss,CT}$ are the rate constants of CT decay and CT dissociation, respectively. k_{ref} is the reformation rate constant, and *B* the rate of encounter of free carriers. The singlet excitons generated in the bulk diffuse to the donor:acceptor interface and dissociate to form CT states, and subsequently form free charges (CS) via CT dissociation. The CT and S_1 states can be repopulated upon the encounter of free charges and CT–S_1 reformation, respectively. Losses can occur through four channels: 1) via S_1 decay during the exciton diffusion in the bulk, 2) via S_1 decay during S_1 dissociation at the donor:acceptor interface, 3) via the decay of reformed S_1 from CT states, and 4) via CT decay.

and PL quenching measurements are performed to study the loss via the S_1 decay. For OSC systems with a large HOMO offset, when the blend is illuminated, the PL spectral characteristic is usually understood as a combination of exciton and CT decay. However, as is discussed in Section IV. 3.3.1, as $\Delta E_{S_1\text{-}CT}$ becomes sufficiently low, the CT states can more efficiently repopulate the S_1 state, and hence the PL spectrum is dominated by exciton contribution due to the much higher emissivity of the excitons compared to the CT states. With the PL emission in the studied systems being almost fully contributed by exciton emission (shown in Figure C.2 in the Supporting Information), the PL quenching (PL_{quen}), which is calculated via Equation IV. 3.2, represents the fraction of generated excitons that ultimately decay via nonradiative channels (e.g., CT and triplets). In large offset systems these are typically from the initially photogenerated excitons which do not dissociate to form a CT state, while in low offset systems, in addition to the photogenerated excitons, there is an additional contribution from reformed excitons via the CT state. The PL_{quen} values are tabulated in Table IV. 3.1 (The PLQY values of the blends and neat acceptors can be found in Table C.2 in Supporting Information). As anticipated, exciton quenching becomes less and less efficient with decreasing offset.

$$PL_{quen} = 1 - \frac{PLQY_{Blend}}{PLQY_A} = \frac{\#\,quenched\ exciton}{\#\,generated\ exciton} \qquad \text{(IV. 3.2)}$$

where $PLQY_{Blend}$ and $PLQY_A$ are the photoluminescence quantum yields of the donor:acceptor blend and neat acceptor, respectively.

Table IV. 3.1: The exciton diffusion length ($L_{D,acc}$) of the acceptors measured on neat acceptor films, as well as the characteristic length (L_C), exciton diffusion efficiency ($\eta_{ex,diff}$), and PL quenching (PL_{quen}) of each blend

	$L_{D,acc}$ (nm)	L_C (nm)	Domain purity (N)	$\eta_{ex,diff}$	PL_{quen}
PM6:o-IDTBR	10	60	0.58	0.58	0.32
PM6:Y5	17	85	1	0.67	0.66
PM6:TPT10	17	110	0.7	0.58	0.94

Meanwhile, with the knowledge of optical constants (real refractive index *n* and extinction coefficient *K*) of each blend, the maximum photocurrent ($J_{ph,max}$) can be calculated for each studied system in terms of the optical transfer matrix, [122] under the assumption that all generated excitons are converted into free charges upon light excitation (see Note S2 in the Supporting Information for details). This serves as the upper limit of the photocurrent that the device could theoretically reach, limited by the absorption of the active layer. The ratio of J_{SC} and $J_{ph,max}$ evaluates the fraction of photogenerated excitons that are converted to free charges at the J_{SC} condition. A comparison of $J_{SC}/J_{ph,max}$ and PL_{quen} (at open-circuit voltage) for each system then evaluates the fraction of quenched excitons that results in free charges. As is presented in Figure IV. 3.4c, the close agreement between $J_{SC}/J_{ph,max}$ and PL_{quen} values observed for all systems indicates the main loss channel is the decay of S_1 (loss channels 1–3) rather than the CT state (loss channel 4).

IV. 3.3.3.2 *Exciton Decay in the Bulk during Exciton Diffusion*

While Figure IV. 3.4c manifests the dominance of decay via S_1, we now delve deeper to decouple thermodynamics from kinetics of exciton diffusion in the bulk and charge transfer at the donor:acceptor interface. To address the exciton losses during the exciton diffusion process, a combination of characterizations of morphology, exciton lifetime, and diffusion length is conducted. Resonant soft X-ray scattering (R-SOXS) is a powerful technique to characterize the nanometer scale morphology and provide information of average domain size and domain purity in the active layer of organic solar cells. [227] Through the R-SOXS measurements, it was found that PM6:o-IDTBR has the smallest domain characteristic length (L_C), 60 nm, then PM6:Y5 (85 nm), and then PM6:TPT10 (110 nm). Given that the volume ratio of the donor and acceptor is close to 1 in our studied systems, the domain size in all studied systems is estimated to be half of their corresponding characteristic lengths.

The exciton diffusion lengths (LD) and lifetimes (τ_{ex}) of the acceptors are measured by performing quasi-steady-state pulsed-PLQY measurements and time-resolved photoluminescence (TRPL) measurements on neat acceptor films, respectively (for TRPL measurement, the neat acceptor was diluted with polystyrene (PS), more details can be seen in the Experimental Section in the Supporting Information). The LD of o-IDTBR was determined to be smallest among the three studied acceptors ($\approx$10 nm), while those of Y5 and TPT10 were found to be much larger than that of o-IDTBR, with a similar value of $\approx$17 nm. The result of LD is consistent with the τ_{ex} values obtained from TRPL, being 263, 1280, and 1071 ps for o-IDTBR, Y5, and TPT10, respectively. With the domain size and the

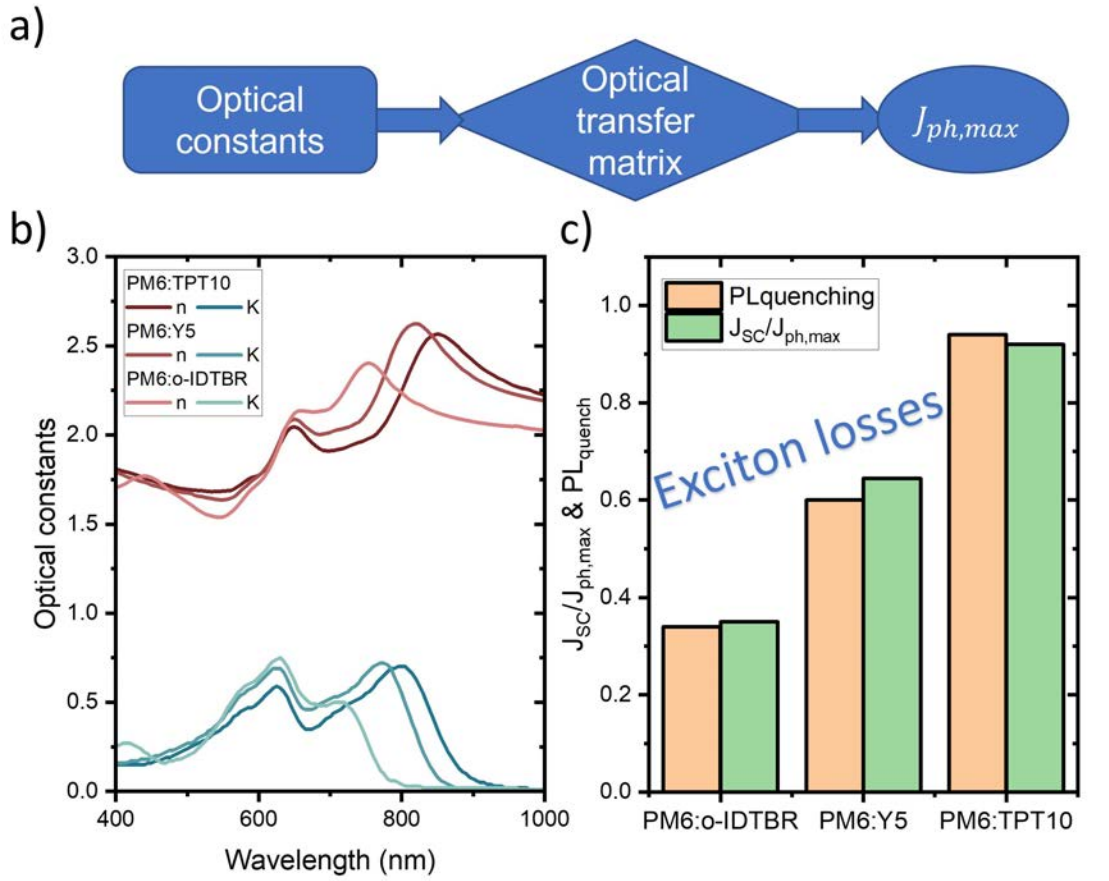

Figure IV. 3.4: a) Calculation of maximum photocurrent ($J_{ph,max}$) in terms of the optical transfer matrix. b) The optical constants of each blend. c) Comparison of $J_{SC}/J_{ph,max}$ and PL quenching (at V_{OC}) of each system.

exciton diffusion lengths, and assuming that the observed domains are 100% pure, the exciton diffusion efficiency ($\eta_{ex,diff}$), representing the probability that an exciton reaches the interface) in each blend can be calculated with Equation IV. 3.3:

$$\eta_{ex,diff} = \frac{2L_D}{\frac{1}{2}L_C} tanh\left[\frac{\frac{1}{2}L_C}{2L_D}\right] \quad \text{(IV. 3.3)}$$

For all studied systems, the $\eta_{ex,diff}$ was found to be close to 0.6, showing no relation between $\eta_{ex,diff}$ and the observed trends in CGY and PL_{quen}. Notably, in PM6:TPT10, the calculated ηexc,diff is much smaller than PL_{quen}. This discrepancy between ηexc,diff and PL_{quen} can be explained by low domain purity in the studied systems. The relative domain purities in a set of binary organic heterojunctions can be estimated by R-SOXS, enabling a qualitative comparison in domain purities among the studied systems. The total scattering intensity (TSI) is related to Δn_{DA}, the contrast function of the donor and acceptor (see Figure C.6 in the Supporting Information), by the relationship Domain purity $\propto \frac{\sqrt{TSI}}{|\Delta n_{DA}|}$. The domain purity was found to be the highest in PM6:Y5, then PM6:TPT10 (Table IV. 3.1). The lowest domain purity was observed in PM6:o-IDTBR. As pointed out in numerous publications, less domain purity assists exciton dissociation by creating more donor:acceptor interfaces, leading to higher PL quenching. [228–232]

Another way of estimating the exciton diffusion efficiency relies on comparison between the saturated photocurrent $J_{ph,sat}$ measured with a high reverse bias and the theoretically calculated maximum photocurrent $J_{ph,max}$. Considering the domain purities, the ratio of $J_{ph,sat}$ over $J_{ph,max}$ represents the lower limit of exciton diffusion efficiency in the blends. Measuring the *JV* response of the three studied systems to obtain the ratio of photocurrent at each voltage $J_{ph}(V)$ and $J_{ph,max}$, it was found that the $J_{ph,sat}/J_{ph,max}$ values of both PM6:TPT10 and PM6:Y5 were close to 1 when measuring $J_{ph,sat}$ at -8 V (Figure C.5, Supporting Information). Since the exciton diffusion process is independent of the applied field, this suggests that all generated excitons can successfully find the donor:acceptor interface in PM6:TPT10 and PM6:Y5. As for PM6:o-IDTBR at -8 V, $J_{ph,sat}/J_{ph,max}$ was found to be 0.73. In fact, considering the smallest domain size and lowest domain purity in PM6:o-IDTBR, it is considered that the actual exciton diffusion efficiency in PM6:o-IDTBR is also close to 1. In the following subsection, a calculation is performed to justify this point.

First, knowing the lower limit of exciton diffusion efficiency and exciton diffusion length, Equation IV. 3.3 gives an estimation of the actual effective L_C in both PM6:TPT10 and PM6:Y5. We found a maximum value of $\approx$25 nm, significantly lower than the directly measured L_C from R-SOXS. According to the R-SOXS results, PM6:o-IDTBR has the smallest domain size and lowest domain purity, so the actual L_C in PM6:o-IDTBR should be even smaller than 25 nm. However, in the following subsection, we use L_C = 25 nm for the calculation to estimate the lowest exciton diffusion efficiency in PM6:o-IDTBR. With L_C = 25 nm and $L_{D,acc}$ = 10 nm (see Table IV. 3.1) for PM6:o-IDTBR, the real exciton diffusion efficiency in PM6:o-IDTBR can be estimated to be at least 90%. Therefore, it could be concluded that in all studied systems, the excitons are able to find the donor:acceptor interface efficiently.

Notably, a relatively high FF of almost 70% is observed for PM6:TPT10 which is close to a Shockley-type charge extraction scenario. [120] This indicates that the charges can still be efficiently extracted in PM6:TPT10 despite its low domain purity, pointing to the formation of a descent intercrossing morphology between each impurity in the domains. Comparing the atomic force microscopy scans of the neat donor and acceptor as well as the blends, it was found that the fibrous feature from PM6 was well preserved in the films of donor:acceptor blends (Figure C.7, Supporting Information). This is consistent with other studies with diluted PM6-based OSC systems, in that efficient charge transportation is ensured due to the high fibrous figure of the PM6 that connects each domain together. [233]

IV. 3.3.3.3 *Exciton Decay at the Interface*

For a better understanding of the mechanism behind the charge generation process, time delayed extraction field (TDCF) measurements were performed under very low fluences to study the field dependence of the charge generation yield (Figure IV. 3.5c). It was found that the charge generation in systems with small $\Delta E_{S_1\text{-}CT}$ (PM6:o-IDTBR and PM6:Y5) is field-dependent, while in PM6:TPT10 and PM6:Y6, where $\Delta E_{S_1\text{-}CT}$ is relatively large, the charge generation is field-independent. [50] This further supports that the field-dependent current density between -2 and 0 V in the *J-V* plot in PM6:o-IDTBR and PM6:Y5 (in Figure IV. 3.1d) is due to actual charge generation processes instead of inefficient competition between charge extraction and recombination.

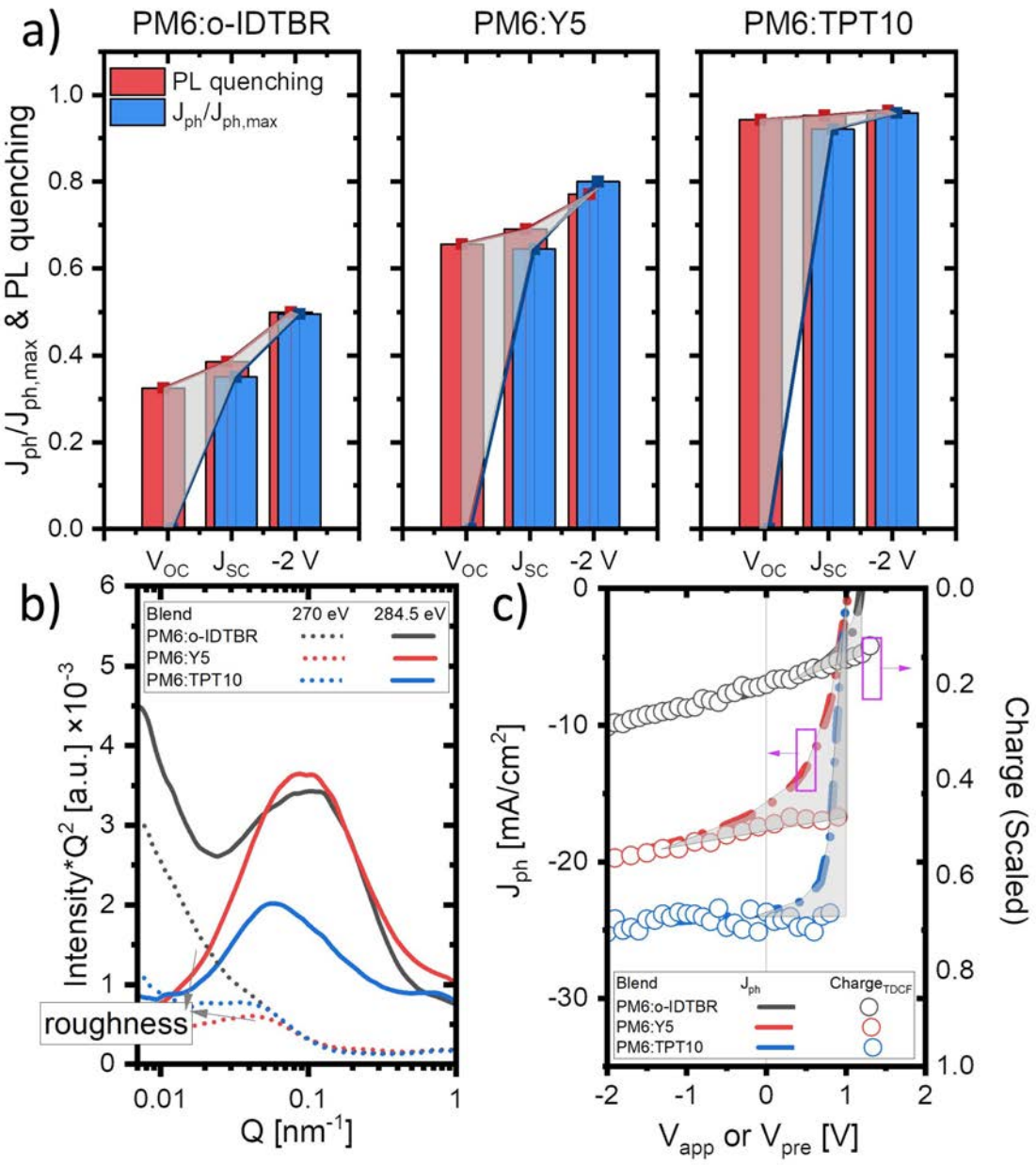

Figure IV. 3.5: Comparison of the PL quenching and $J_{ph}/J_{ph,max}$ in a) V_{OC}, J_{SC}, and reverse bias condition, b) R-SoXS profiles, and c) TDCF generation profile overlaid on J_{ph}-V_{app} for PM6:o-IDTBR, PM6:Y5, and PM6:TPT10.

From the discussion in Sections IV. 3.3.3.1 and IV. 3.3.3.2, it is concluded that the differences in the EQE_{PV} amplitudes among the studied systems observed in Figure IV. 3.1d mainly originate from the exciton losses at the donor–acceptor interface, giving an indication that the field dependence in charge generation originates from field-dependent exciton dissociation at the donor:acceptor interface instead of from field-dependent CT dissociation, as depicted by the Onsager–Braun model. This is further consolidated using comparisons between $J_{ph}/J_{ph,max}$ and PL quenching at three different applied voltages (V_{OC}, J_{SC}, and -2 V) shown in Figure IV. 3.5a. It was observed that both $J_{ph}/J_{ph,max}$ and PL quenching increase while remaining close to each other when the applied bias changed from J_{SC} to -2 V. The similar but increasing PL quenching and $J_{ph}/J_{ph,max}$ values in PM6:Y5 and PM6:o-IDTBR evidence that in systems where $\Delta E_{S_1\text{-}CT}$ is sufficiently small: 1) at J_{SC},

exciton dissociation at the interface limits the photocurrent (through channels 2 and 3), and 2) the exciton dissociation yield at the donor:acceptor interface can be assisted with the application of an extraction bias. The field-dependent exciton dissociation yield, on the one hand, leads to inefficient CGY at J_{SC} and hence low EQE, and on the other hand leads to a reduction in FF.

At the V_{OC} condition where no charge extraction happens, $J_{ph}/J_{ph,max}$ becomes 0 while PL quenching remains relatively high. This indicates that at V_{OC}, the recombination current is mainly contributed by the CT decay (opposite to the situation at the J_{SC} condition).

As is highlighted in gray in Figure IV. 3.5a, when applied voltage approaches V_{OC} from -2 V, recombination via the CT states (channel 4) is found to be more and more pronounced compared to the recombination via S_1. This is consistent with the observed discrepancy between the TDCF generation and *JV* data (Figure IV. 3.5c, area highlighted in gray) showing that nongeminate recombination due to an encounter of free charges becomes more significant as the applied bias approaches V_{OC} from reverse bias. The agreement in the gray highlighted areas in Figure IV. 3.5a,c indicates, for all our studied systems, upon encountering of the free carriers, the decay is more likely to proceed via the CT states than by the CT-S_1 reformation and the consequent S_1 decay.

This is further evidenced by comparing the ELQY of the blends with the PLQY of the neat acceptors. Since the EL spectra of the donor:acceptor blend almost fully consists of the emission of acceptor excitons, ELQY presents the quantum yield of the blend to convert free charges into photons via exciton decay. Relating the PLQY of the neat acceptor (which is the probability that a formed acceptor exciton emits a photon) and the ELQY of the blend, the probability of recombination via exciton reformation and the subsequent exciton decay ($P_{ex,ref}$) upon the encounter of free carriers in each system (Figure IV. 3.3, efficiency of channel 3) can be estimated by Equation IV. 3.4. The ELQY of the blends and the PLQY of the neat acceptors, as well as $P_{ex,ref}$ in each studied system is summarized in Table C.2 (Supporting Information). At near V_{OC}, the calculated $P_{ex,ref}$ in all studied systems is much smaller than 50%, with ≈3% for both PM6:TPT10 and PM6:o-IDTBR and 13% for PM6:Y5, which is consistent with the observation in Figure IV. 3.5a,c that in all studied systems, recombination tends to proceed via channel 4 instead of channel 3 (depicted in Figure IV. 3.3) upon the encounter of free carriers

$$P_{ex,ref} = \frac{ELQY_{blend}}{PLQY_A} \tag{IV. 3.4}$$

IV. 3.3.4 Charge Recombination

As shown in Figure IV. 3.3, upon an encounter of free charges, exciton reformation is in competition with the CT decay process, and both contribute to bimolecular recombination. As derived in previous work, the effective bimolecular recombination rate k_{eff} given by $R_{CS} = k_{eff} n_{CS}^2$ can be obtained via Equation IV. 3.5 for low-offset OSC systems [68]

$$k_{eff} = \left[\frac{1}{k_0} + \frac{1}{k_{CT} + k_S} \right]^{-1} \tag{IV. 3.5}$$

where k_0 is the charge encounter rate coefficient for free charge carriers, $k_{CT} = k_0 k_f / k_d$ is an effective bimolecular recombination coefficient via CT states, and $k_S = k_0 k_{bt}' / k_d$ is

the corresponding effective bimolecular recombination coefficient for charge carriers to ultimately decay via excitons. The ratio between k_{CT} and k_S is given by k_f/k_o. k_f is the CT state recombination rate constant, and k_o is the back-transfer rate constant for CT states to recombine via excitons in the acceptor, which increases exponentially as $\Delta E_{S_1\text{-}CT}$ decreases. As Equation IV. 3.5 indicates, when the CT decay rate constant (k_f) is much faster than k_o, the S_1 reformation process is minor and does not have much effect on the overall recombination process. However, as k_o increases, the S_1 reformation starts to act as a loss channel and contributes to the recombination process. This means when $\Delta E_{S_1\text{-}CT}$ gets small enough, either the CT recombination itself is so fast and dominates the recombination rate, or the S_1 decay acts as another leakage channel to the overall recombination rate. Both of the above-described cases lead to a reduction in FF and hence are not favorable for the overall device performance.

In general, reduced $\Delta E_{S_1\text{-}CT}$ increases k_{eff}, and the significance of this effect depends on the rate competition between CT decay and S_1 reformation, and the subsequent S_1 decay. To study the effect of $\Delta E_{S_1\text{-}CT}$ on the bimolecular recombination rate k_{eff}, bias assisted charge extraction measurements were performed for each system that is studied here. This charge extraction method estimates the carrier density at various fluence at V_{OC} condition and calculates the effective bimolecular recombination rate via $G = R = k_{eff} n_{CS}^2$. As shown in Figure IV. 3.6, it was found that the measured k_{eff} reduces by 1 order from 3×10^{-16} to 1.6×10^{-3} $m^3 s^{-1}$ as $\Delta E_{S_1\text{-}CT}$ increases from 25 to 114 meV which is consistent with the result from Equation IV. 3.5 and the discussion in the previous paragraph.

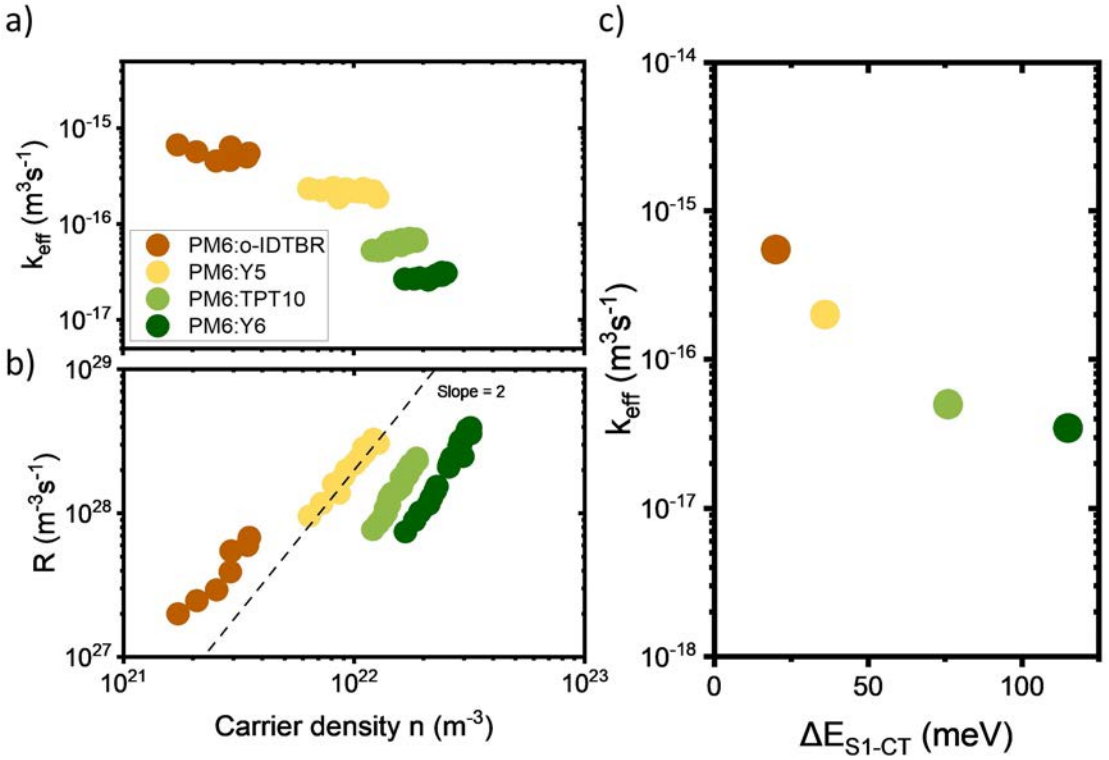

Figure IV. 3.6: a) Effective bimolecular recombination rate coefficient k_{eff} and b) recombination rate R versus carrier density, and c) k_{eff} against $\Delta E_{S_1\text{-}CT}$ for PM6:o-IDTBR, PM6:Y5, PM6:TPT10, and PM6:Y6. The dashed line in (b) represents the slope of 2. The data for PM6:Y6 are taken from previous work from our group. [13]

IV. 3.3.5 V_{OC} Losses in Low-Offset OSCs

It has been found in previous work that the ΔV_{nr} value gets significantly suppressed in systems with low $\Delta E_{S_1\text{-}CT}$, and its lowest limit is defined by the PLQY of the pristine low-optical bandgap material of the blend.[12] In our study, ΔV_{nr} of each system was determined via $\Delta V_{nr} = k_B T \cdot \ln(\text{ELQY})$. The ELQY values in the systems with low $\Delta E_{S_1\text{-}CT}$, PM6:o-IDTBR and PM6:Y5 (1.6×10^{-3} and 3.2×10^{-3}, respectively), were found to be much higher than those in systems with relatively high $\Delta E_{S_1\text{-}CT}$ (PM6:TPT10 and PM6:Y6, with values of 7.4×10^{-4} and 2.7×10^{-5}, respectively), leading to a very low ΔV_{nr} value of 0.16 eV – one of the lowest ΔV_{nr} values in organic solar cells. However, interestingly, when analyzing the overall V_{OC} losses using the difference between the photovoltaic bandgap of the system (E_g) and measured V_{OC}, [234] it was found that the overall V_{OC} losses among the studied systems are very close (Figure IV. 3.7, left panel).

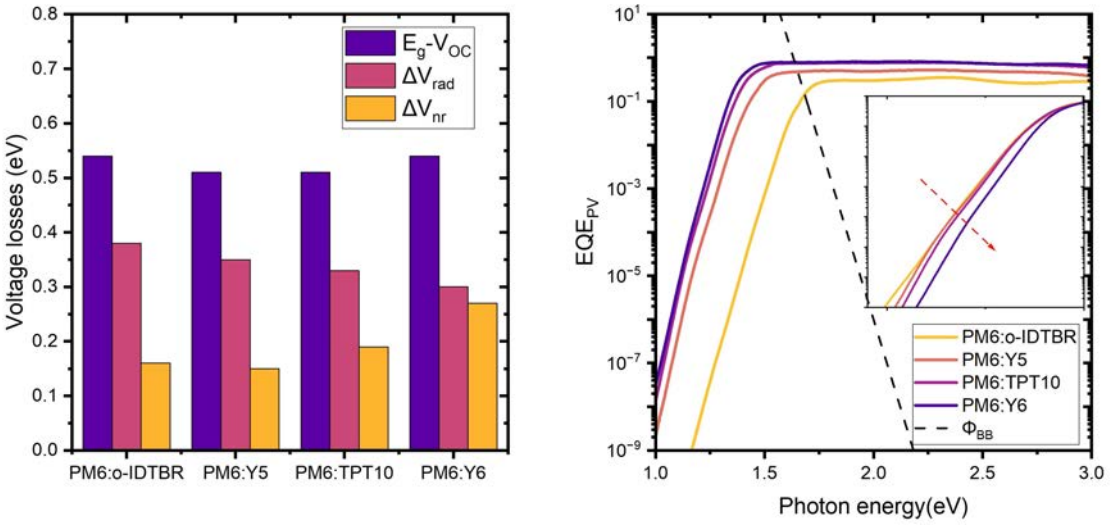

Figure IV. 3.7: Left panel: the overall, radiative, and nonradiative voltage losses of PM6:o-IDTBR, PM6:Y5, PM6:TPT10, and PM6:Y6. The dashed dotted lines are guides to the eye. The data for PM6:Y6 are from previous work from our group. [25] Right panel: the extended EQE_{PV} spectra of PM6:o-IDTBR, PM6:Y5, PM6:TPT10, and PM6:Y6 spectra. Inset, zoomed-in and all the EQE_{PV} spectra are merged at the kink (where sub-bandgap starts) – in order to give a more intuitive comparison on the slope for each system.

To further investigate into the observed discrepancy between the trends in overall V_{OC} losses and ΔV_{nr} among the studied systems, the radiative voltage limit $V_{OC,rad}$ was evaluated for each system with Equation IV. 3.6 [208] (more details about the determination of $V_{OC,rad}$ can be found in the Supporting Information). Getting the radiative voltage loss ΔV_{rad} via $\Delta V_{rad} = E_g - V_{OC,rad}$, and plotting ΔV_{rad} together with ΔV_{nr} for each system, an anticorrelation can be found between these two parameters (Figure IV. 3.7, left panel). From PM6:o-IDTBR to PM6:Y6, while $\Delta E_{S_1\text{-}CT}$ increases, the increase in ΔV_{nr} and reduction in ΔV_{rad} compensate each other and lead to a constant overall V_{OC} loss

$$q \cdot V_{OC,rad} = k_B T \cdot ln(\frac{J_R}{J^0_{rad}}) \quad \text{(IV. 3.6)}$$

where where JR is the total recombination current, $J_{0,rad}$ is the radiative dark saturation current density.

As shown in Figure IV. 3.7 (left panel), there seems to be a relation between $\Delta E_{S_1\text{-}CT}$, ΔV_{nr}, and ΔV_{rad}. This is reminiscent of the relation between the S_1 population and $\Delta E_{S_1\text{-}CT}$ which can affect both ΔV_{nr} and ΔV_{rad} due to the high emissivity of S_1 compared to the CT states. [98] However, in all systems studied here, the $\Delta E_{S_1\text{-}CT}$ is so small that the contributions of the CT state to the EQE_{PV} spectra are nearly negligible. This is evidenced from a) the EL measurements (which is related to EQE_{PV} via reciprocity) showing that the EL spectra are almost entirely contributed by S_1, and b) previous ultrasensitive EQE_{PV} measurements for PM6:Y6 where no observable CT contribution is presented. [50] This means that for all systems, $J_{0,rad}$, and with this $V_{OC,rad}$, is entirely determined by the properties of the singlet exciton and have no "functional" dependence on $\Delta E_{S_1\text{-}CT}$. Instead, the difference in the ΔV_{rad} observed in our systems is found to be due to the subtle difference in the shapes of the tails in the EQE_{PV} spectra. For example, PM6:Y6 gives the sharpest tail while PM6:o-IDTBR has the "flattest" tail, as can be more intuitively found in the inset of Figure IV. 3.7 on the right panel. This affects the calculated $J_{0,rad}$ values when convoluting the EQE_{PV} spectra with the blackbody photon flux and thus the ΔV_{rad}. In other words, the increase of ΔV_{rad} when decreasing $\Delta E_{S_1\text{-}CT}$ comes from a broadening of the EQE_{PV} spectra rather from the S_1 repopulation process. The reason is suspected to be lying in the stiffness of the NFA and detailed blend morphology. Therefore, it is not evident that the observed dependence of ΔV_{rad} on $\Delta E_{S_1\text{-}CT}$ among the systems involved in this study can be generalizable, but it is worth studying this case for more systems in the future.

IV. 3.4 Conclusion

In conclusion, by performing detailed analyses of overall efficiency losses to a series of NFA-based low-offset systems, our work shows that both J_{SC} and FF are severely reduced as $\Delta E_{S_1\text{-}CT}$ becomes sufficiently small, yet the reduction in V_{OC} losses is limited, despite the significantly reduced ΔVnr. In all systems studied herein, the losses in J_{SC} conditions were assigned to exciton dissociation at the donor:acceptor interface. The exciton loss at the donor:acceptor interface was found to be more significant in the systems with the smallest $\Delta E_{S_1\text{-}CT}$ value. Importantly, in the two systems with the lowest $\Delta E_{S_1\text{-}CT}$ values (PM6:o-IDTBR and PM6:Y5), exciton dissociation yield at the donor:acceptor interface was found to be field-dependent, which also leads to a further reduction in the FF. In the forward bias regime where bimolecular recombination becomes significant, recombination via the CT state was found to be increasingly pronounced as the applied bias approached V_{OC}. Thus, despite the presence of S_1 reformation and the consequent decay via S_1, recombination via CT state still serves as the prominent decay channel of the encountered free electrons and holes and severely affects FF, even in the system with very small $\Delta E_{S_1\text{-}CT}$. In addition, consistent with previous theoretical work,[18] it was found that decreasing $\Delta E_{S_1\text{-}CT}$ is not beneficial for achieving low bimolecular recombination coefficients. We anticipate this is due to a stronger binding energy of the CT state (when it becomes closer to the S_1 state), reducing the probability of redissociation. In general, the results in our study support an inferior PCE obtained by simply reducing $\Delta E_{S_1\text{-}CT}$ from PM6:TPT10 and PM6:Y6. In addition, our work provides structure–function information by showing that upon a change of the halogen substituents in the terminal groups of Y5, TPT10, and Y6, the exciton diffusion in their binary heterojunctions with PM6 remain highly efficient, while the very different *JV* performances among these three systems mainly rely on the energetics at the interface.

IV. 4 Wave Optics of Differential Absorption Spectroscopy in Thick-Junction Organic Solar Cells: Optical Artifacts and Correction Strategies

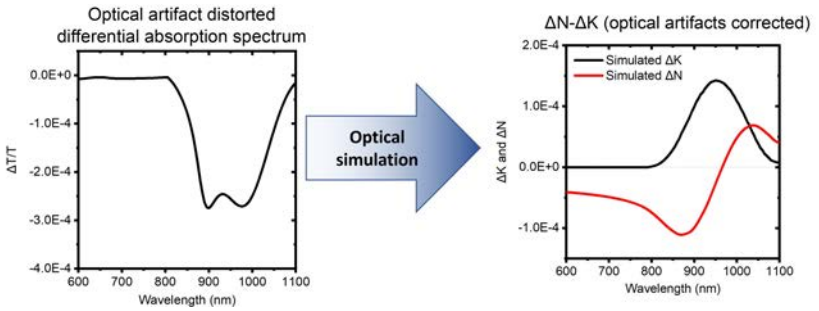

This work presents in detail and systematically how the optical artifacts can manipulate not only the measured spectra, but also the decay dynamics (even for the simplest sample configuration), upon the change of the device thickness and configuration. A generalized methodology based on inverse transfer matrix formalism is provided to correct the distorted spectra and decay dynamics due to optical artifacts.

This chapter is an adapted preprint of:
Bowen Sun, Oskar J. Sandberg, Dieter Neher, Ardalan Armin, and Safa Shoaee. Wave Optics of Differential Absorption Spectroscopy in Thick-Junction Organic Solar Cells: Optical Artifacts and Correction Strategies. Phys. Rev. Applied 17, 054016

IV. 4.1 Abstract

Differential absorption spectroscopy techniques serve as powerful techniques to study the excited species in organic solar cells. However, it has always been challenging to employ these techniques for characterizing thick-junction organic solar cells, especially when a reflective top contact is involved. In this work, we present a detailed and systematic study on how a combination of the presence of the interference effect and a nonuniform charge-distribution profile, severely manipulates experimental spectra and the decay dynamics. Furthermore, we provide a practical methodology to correct these optical artifacts in differential absorption spectroscopies. The results and the proposed correction method generally apply to all kinds of differential absorption spectroscopy techniques and various thin-film systems, such as organics, perovskites, kesterites, and two-dimensional materials. Notably, it is found that the shape of differential absorption spectra can be strongly distorted, starting from 150-nm active-layer thickness; this matches the thickness range of thick-junction organic solar cells and most perovskite solar cells and needs to be carefully considered in experiments. In addition, the decay dynamics of differential absorption spectra is found to be disturbed by optical artifacts under certain conditions. With the help of the proposed correction formalism, differential spectra and the decay dynamics can be characterized on the full device of thin-film solar cells in transmission mode and yield accurate and reliable results to provide design rules for further progress.

IV. 4.2 Introduction

The development of fused-ring electron acceptors (FREAs) has injected new life into the field of organic solar cells (OSC); the state-of-the-art single-junction OSC has now surpassed 18% power conversion efficiency (PCE). So far, FREA-based systems are the most promising candidates to realize commercialization for OSCs due to their impressive PCEs. Unfortunately, it is found that the performance and morphology of FREA systems is quite sensitive to their active-layer thickness. The optimized active-layer thickness for most FREA-based systems is around 100 nm, while significant fill-factor (FF) losses appear when the active-layer thickness exceeds this threshold [9, 13, 20, 235]. This optimized thickness is unfortunately still too thin for reliable production via large-scale printing techniques, such as roll-to-roll processing (requiring around 300 nm) [236, 237]. Due to the high sensitivity of the morphology to fabrication conditions and procedures in many state-of-the-art FREA systems [10–12, 238], it is also not easy for many optoelectronically relevant physical properties (such as mobility, recombination coefficient, recombination order, reduction factor) measured in thin junctions to be directly adapted to thick junctions. There is a range of reports on the exciton lifetime of nonfullerene acceptors (ranging from tens of picoseconds to nanoseconds), which may also arise from the sensitivity to thickness and the morphology-dependent properties of these materials [42, 172, 239–241]. To study the thick-junction devices in detail, it is crucial to perform measurements directly on these thick-junction devices. However, most of the available techniques for organic solar cells are based on assumptions that hold only for thin devices.

One example of such a characterization technique commonly used to assess the generation and recombination of excited species is differential absorption spectroscopy; typical

differential absorption spectroscopy techniques include transient absorption spectroscopy (TAS), photoinduced absorption spectroscopy (PIA), and charge-modulation spectroscopy (CMS) [242–244]. These spectroscopies consist of either an optical or electrical pump and an optical probe and measure the change of the absorption coefficient of the sample when it is excited from the ground state to the excited state. Like many other optical-based experiments [25, 122, 245], differential absorption spectroscopy is sensitive to optical artifacts, primarily the combination of cavity effects (from both pump and probe light) and the inhomogeneous generation profiles. Optical artifacts can be severe, especially with increasing active-layer thickness and in the presence of the top contact [246, 247], and can strongly distort the measured differential transmission ($\Delta T/T$) spectra.

While the cavity effect is usually considered as a light-intensity-independent effect, it is worth pointing out that the decay dynamics of the $\Delta T/T$ signal can be disturbed by interference, under certain conditions, and falsifies the obtained decay constant if not addressed carefully. When considering a thin-film stack with an active layer measured by differential absorption spectroscopy, the change in transmission (ΔT) and reflection (ΔR) can be described by [248–250]

$$\Delta T = \frac{\partial T}{\partial N}\Delta N + \frac{\partial T}{\partial K}\Delta K, \tag{IV. 4.1a}$$

$$\Delta R = \frac{\partial R}{\partial N}\Delta N + \frac{\partial R}{\partial K}\Delta K, \tag{IV. 4.1b}$$

where T and R are the transmission and reflection of the thin-film system, respectively. N and K are the refractive index and extinction coefficient of the active layer, respectively.

The four partial derivative terms in Eqs. IV. 4.1a and IV. 4.1b ($\partial T/\partial N$, $\partial T/\partial K$, $\partial R/\partial N$, $\partial R/\partial K$) can be calculated in terms of optical transfer-matrix calculations [121]. The ratio of the first two and last two derivatives [$(\partial T/\partial N)/(\partial T/\partial K)$ and $(\partial R/\partial N)/(\partial R/\partial K)$] are found to be dependent not only on the wavelength of interest of the probe light, but also on the thickness of the active layer [248]. Subsequently, the measured ΔT in experiments can have more contribution from either ΔN or ΔK, depending on the active-layer thickness and incident-light wavelength.

If there is only the ΔK peak (single or multiple) for one decay dynamic (created upon pump excitation), the decay dynamics of ΔK measured from ΔT will not be disturbed by the derivative terms. This is because the relationship between N and K satisfies the famous Kramers-Kronig relationship [251], which ensures that ΔN follows the same decay dynamics as ΔK.

$$N(\lambda) = 1 + 4c \oint_0^\infty \frac{(2\pi c/(\lambda')^3)K(\lambda')}{(2\pi c/(\lambda')^2 - (2\pi c/(\lambda)^2} \, d\lambda' \tag{IV. 4.2}$$

where λ is the wavelength, c is the speed of light, and $K(\lambda)$ is the extinction coefficient at a given wavelength. Note that λ is a pole on the axis and λ' is the real variable.

As a result, ΔT follows the same decay dynamics as ΔN and ΔK, regardless of the probe wavelength or the active-layer thickness. The decay dynamics is thus independent of device thickness and is not disturbed, even though the shape of the spectrum is distorted by interference, as indicated in previous studies [249]. It should be noted that

this holds under the assumption that the distribution profile of excited species does not alter over time during the experiment, which corresponds to the case when a uniform generation profile is realized. When the distribution profile is nonuniform (e.g., when the optical density of the active layer is larger than 0.5 at the excitation wavelength), the decay dynamics will be disturbed due to the drift and diffusion of the excited species during the measurement.

However, the picture changes when multiple ΔK peaks (e.g., ΔK_1 and ΔK_2) with different decay dynamics are present in the spectrum. In this case, the measured decay dynamics of ΔT_1 can severely deviate from that of its corresponding ΔK_1, even when ΔK_1 and ΔK_2 do not spectrally overlap with each other, as will be discussed below in section IV. 4.3.3. Both the decay dynamics and the shape of the $\Delta T/T$ spectrum are sensitive to the device thickness, even when the distribution profile is not altered during the measurement. Such an effect is found to exist even when no highly reflective layer is present in the sample (for example, when an active layer is sandwiched between two glass substrates). Hence, it is important to consider this effect when comparing supposedly the same parameter, such as the decay dynamics of excitons or free carriers, measured via differential absorption spectroscopy by different groups in the literature. To this end, it is crucial to decode ΔK and ΔN from the measured ΔT or ΔR signal when studying both spectral shape and the decay dynamics of excited species for qualitative or quantitative analyses.

In previous works, it has been proposed to correct the $\Delta T/T$ signal by considering the change in reflection, ΔR, upon pump excitation [252–255]; such a method requires access to both ΔT and ΔR in experiments:

$$-\frac{\Delta T}{T} = d\Delta\alpha + \frac{m}{1-R}\Delta R, \tag{IV. 4.3}$$

where R is the reflectance, α is the absorption coefficient, d is the thickness of the active layer, and m is a factor that depends on the assumed model (m=0 for negligible reflection, m=1 reflection only on the front surface of the active layer, and m=2 for reflection on both surfaces of the active layer). This model assumes the same reflection coefficient for the front and back surfaces of the active layer and does not consider the multiple reflections in the stack, and hence, it is more suitable for simple sample configurations. In addition, errors can be created when the value of m is not carefully and reasonably chosen.

More advanced sample configurations can be incorporated when combining Eqs. IV. 4.1a and IV. 4.1b to calculate ΔN and ΔK [Eqs. IV. 4.4 a and b] [249]. Complicated sample configurations can be taken into account when calculating the derivative terms ($\partial T/\partial N$, $\partial T/\partial K$, $\partial R/\partial N$, $\partial R/\partial K$) via an optical transfer matrix. However, both Eqs. IV. 4.4 a and b severely lose accuracy and result in unavoidable spikes in calculated ΔN and ΔK spectra in the spectral region where the denominator approaches zero. Hence, Eq. (IV. 4.4) is appropriate only over a limited spectral range; post-treatments are required to remove or smooth the spikes. Like Eq. (IV. 4.3), both ΔT and ΔR are to be experimentally measured in this method. In addition, the distribution profile of the excited species cannot be incorporated into this model.

$$\Delta N = \frac{(\partial T/\partial K)\partial R - (\partial R/\partial K)\partial T}{(\partial R/\partial N)(\partial T/\partial K) - (\partial T/\partial N)(\partial R/\partial K)}, \tag{IV. 4.4a}$$

$$\Delta K = \frac{(\partial R/\partial N)\partial T - (\partial T/\partial N)\partial R}{(\partial R/\partial N)(\partial T/\partial K) - (\partial T/\partial N)(\partial R/\partial K)}, \tag{IV. 4.4b}$$

Other efforts have been made to experimentally compensate for the cavity effect in differential absorption spectroscopies, either by adjusting the probe-light incident angle or by modifying standard differential absorption spectroscopy setups; these approaches introduce extra experimental restrictions or difficulties [250, 256].

Here, we illustrate, in detail, how the optical artifacts manipulate the measured differential absorption spectra and decay dynamics and show the extent of these artifacts under various conditions. We also provide a practical methodology based on an inverse transfer matrix to compensate for these artifacts and correct the experimental signal. The proposed correction methodology can be applied for complicated sample configurations with multiple layers; it takes the distribution profile of the excited species into consideration and ensures accuracy over the full spectral range. This correction method has no requirement for the probe-light incident angle and requires only the ΔT signal to be measured with the differential absorption spectroscopy setup. We study both a film (on glass) and a device (with a semitransparent metallic top contact) (keeping everything else the same) for different cavity thicknesses by varying the active-layer thickness in an OSC device. We find that the PIA peak position in the sub-band-gap region can exhibit a large shift due to optical artifacts and, in extreme cases, additional shoulders or peaks, which may be confused with the real peaks, can be resolved. We reproduce the evolution of these thickness-dependent PIA peak features with optical transfer-matrix-model simulations. Simulation results indicate that the additional shoulder or peak features in the measured spectra are a result of optical artifacts and can be present in both devices and films. In addition, the decay dynamics of $\Delta T/T$ is found to be affected by these optical artifacts under certain conditions and deviate from the real decay dynamics of the excited species in both devices and films. Finally, an optical simulation model combining the charge-distribution profile and cavity-effect considerations is proposed to correctly account for these optical artifacts and reveal the real changes in absorption coefficient spectra at each position in the active layer from the experimental differential absorption spectra.

IV. 4.3 Results and Discussion

IV. 4.3.1 Sensitivity of PIA Spectra to Active Layer Thickness

To demonstrate the significant distortion of optical measurements caused by the cavity effect, we employ the state-of-the-art active-layer blend for organic solar cells, PM6 and Y6, and measured the PIA spectra for a range of junction thicknesses (the chemical names and fabrication details are provided in the Supplemental Material).

Figure IV. 4.1 shows the PIA spectra measured on conventionally structured PM6:Y6 devices (for various active-layer thicknesses) under open-circuit conditions. These devices are made to be semitransparent by depositing a very thin Ag layer (35 nm) as

the top contact (not affecting the device performance). As previously assigned by PIA and TAS [83, 257], the spectrum of PM6:Y6 consists of the ground-state bleaching of PM6 (centered at 650 nm) and Y6 (840 nm) as well as photoinduced absorption features between 680 and 810 nm and a peak around 970 nm. The last of these is observed to be highly sensitive to the active-layer thickness. In Fig. IV. 4.1, this PIA peak in the sub-band-gap region is centered at 967 nm for the 100-nm-thick device and is blueshifted by around 10 nm as the active-layer thickness increases from 100 to 260 nm. Upon further increasing the thickness, a double-peak feature emerges. At 330 nm thick, the PIA peak exhibits one pronounced peak at a wavelength of 1012 nm and a shoulder at 919 nm. The latter feature becomes highly pronounced when the thickness of the photoactive layer is increased to 550 nm. To elucidate whether the changes in the PIA peak are due to morphology changes in thick devices, the same experiment is conducted on glass without the electrodes with different thicknesses (Fig. IV. 4.1, inset). In contrast to the observations made on the devices, the double-peak feature is absent in all PIA spectra measured on films. The contrast between PIA features observed on the device and the film strongly points to an optical artifact caused by enhanced optical cavity effects due to the reflective top contact in the devices. These artifacts can strongly manipulate the measured spectrum and lead to inaccurate or even wrong quantitative and qualitative conclusions if not carefully considered.

IV. 4.3.2 Simulating PIA Spectra

To confirm the optical cavity effects in the experimental PIA spectra, we simulate a PIA experiment using optical simulations based on the optical transfer-matrix model. Extending these simulations to a PIA experiment involving pump and probe fields is nontrivial; therefore, we explain the details of these simulations in the following.

In terms of optical transfer-matrix calculations, the transmittance and reflectance of a stack of films, which accounts for interference, can be first obtained, given the thickness and optical constants of each layer, as well as the stack structure [121]. In this way, the transmission spectra on films (glass/PM6:Y6/glass, interlayers are neglected) and on devices (glass/ITO/PM6:Y6/Ag/glass, interlayers are neglected) with varied active-layer thicknesses (from 50 to 600 nm) can be computed, with knowledge of the ground-state optical constants ($\tilde{N} = N + iK$) of the PM6:Y6 blend [258]. Here, N denotes the (real) refractive index, while K is the extinction coefficient. The ground-state optical constants are obtained by a global fitting of experimental reflection and transmission spectra (measured on films on glass) with optical simulations. These results are in agreement with previous studies using ellipsometry to obtain ground-state optical constants of PM6:Y6 blends [259].

The presence of interference can be identified as a violation of the Beer-Lambert law and often shows a wavy feature in transmission (Fabry-Perot oscillation) when varying the active-layer thickness (at a fixed probe wavelength). In simple transmission, interference features can be observed in both films and devices. However, the interference effect is much more pronounced in the device due to the presence of a reflective top contact (Fig. D.2 within the Supplemental Material). In agreement with the experimental observation in Fig. IV. 4.1, the cavity effects are seen to predominantly distort the sub-band-gap region. In the following, using optical simulations, we further consolidate how the cavity effects distort the spectra obtained from differential transmission spectroscopy techniques.

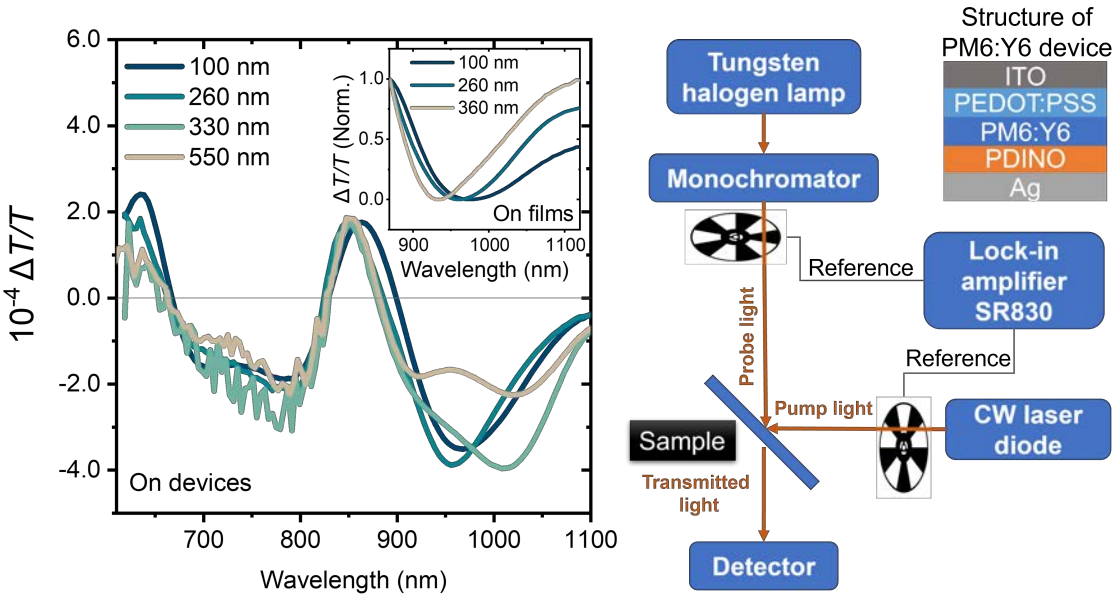

Figure IV. 4.1: Left, PIA spectra of conventional PM6:Y6 device (inset, that of the film). Right, device structure and experimental schematic.

For any thin-film junction, the interference pattern at a fixed probe wavelength is sensitive to the optical constants of each layer in the stack. The dependence of the interference pattern on the optical constants is considered to be the main contribution to the optical artifacts in the experimental differential absorption measurements. In PIA measurements, upon pump excitation, excited species are produced in the material initially in the ground state. The presence of these photogenerated excited species generally results in a different *N*-*K* spectrum from that of the ground-state material. However, the change in the optical constants induces changes in the interference pattern. As a result, both changes in absorption coefficient and in the interference pattern contribute to the experimental differential spectra. The difference between the ground-state and excited-state transmission spectra can therefore be described by T_{exc}-T_{GS}=$\Delta T_{excitation}$+$\Delta T_{interference}$. Here, we propose that this is the primary reason for the high active-layer thickness sensitivity to spectral shape in PIA, and thus, this needs to be carefully considered.

The thickness-dependent PIA feature evolution in Fig. IV. 4.1 can be further consolidated and reproduced by optical simulations, considering the change of interference pattern after excitation and the generation profile (*G*) of excited species induced by the pump light. This can be achieved from knowledge of the device structure, thickness of each layer, and optical constants (*N*-*K* spectra) of the active layer in the ground state and the excited state. A matlab script (denoted PIA_generator) is developed for this PIA signal simulation (for details of the script, see Fig. D.10 within the Supplemental Material).

In the simulation, the transmission spectra of the sample in the ground state (T_{GS}) and excited state (T_{exc}) are computed separately using two sets of *N*-*K* spectra, namely, N_{GS}-K_{GS} and N_{exc}-K_{exc}, respectively. The PIA signal is then calculated by PIA=(T_{exc}-T_{GS})/T_{GS}. N_{GS}-K_{GS} spectra are obtained in a way analogous to that in the simulation for simple transmission. Considering excited-species generation upon pump-light excitation, the N_{exc}-K_{exc} spectra are introduced by adding the artificially designed *N*-*K* spectral features of the photogenerated excited species to the N_{GS}-K_{GS} spectra. For this, the *K* spectral shape of the photogenerated excited species (K_{ES}) is designed and added to K_{GS} to

generate K_{exc} via K_{exc}=K_{ES}+K_{GS}, then a Kramers-Kronig calculation is performed to calculate N_{exc} from K_{exc}, so that the *N*-*K* relationship always satisfies the Kramers-Kronig relationship.

With knowledge of K_{exc}, N_{exc} at each spectral wavelength, λ, can be calculated with Eq. (IV. 4.2). To determine the constant offset for this integration, one needs to find a wavelength where the values of both *N* and *K* are accessible. This is achieved by incorporating one set of *N*-*K* values in the Cauchy regime, where *K* is assumed to be zero and *N* can be calculated by the two-term form of Cauchy's equation [Eq. (IV. 4.5)]:

$$N(\lambda) = N_{Cauchy} + \frac{B}{\lambda^2} \tag{IV. 4.5}$$

where *N* is the refractive index in the Cauchy regime; N_{Cauchy} and *B* are the Cauchy coefficients. The two Cauchy coefficients (N_{Cauchy} and *B*) can be obtained by fitting the transmission and reflection spectra of the sample in the Cauchy region [260]. In PIA_generator, N_{Cauchy} and *B* need to be manually inputted.

To account for the *N*-*K* values in the high-photon-energy region beyond typical measurement wavelength ranges (photon energy larger than ~3.5 eV due to the significant absorption of glass substrates), a Davis and Mott model, which is developed from the classical Tauc model, is applied for the deep valence bands in the material, which become accessible for light absorption in this region [261, 262].

Importantly, a nonuniform generation profile (*G*) is incorporated for a more realistic simulation result. This is achieved by slicing the active layer into multiple slices along the pump-light pathway and considering each slice as a self-standing layer with its local N_{exc}-K_{exc} spectra when computing T_{exc}. The generation rate in each slice (G_s) is calculated by averaging the generation rate of the corresponding positions in the active layer, according to the simulated generation-rate profile *G* (Fig. D.6 within the Supplemental Material). This nonuniform excited-species-generation-rate profile (*G*) is computed by an optical simulation based on the device-structure information, ground-state optical constants of each layer in the stack, and the spectral density of incident light [122]. Increasing the slice number benefits the simulation accuracy.

Assuming the same excited species are generated in all the slices in the active layer, and only the density of the photogenerated excited species in each slice is different, a normalized $K_{ES,norm}$=K_{ES}/K_{ES},max is used to describe only the spectral features of the excited species. The exact change in the *K* spectrum in each slice (ΔK) is scaled from $K_{ES,norm}$ according to G_s in the corresponding slice. For slice *i*, the local $K_{exc}(i)$ can be described by Eq. IV. 4.6:

$$K_{exc}(i) = \Delta K(i) + K_{GS} = f \cdot K_{ES,norm} G_s(i) + K_{GS} \tag{IV. 4.6}$$

where factor *f* is used to relate the generation profile to changes in the *K* spectrum upon excited-species generation (ΔK). This factor *f* is related to the absorption cross section of the excited species (σ_{exc}) and the relationship between the density of excited species and the generation rate. With knowledge of K_{exc} of each slice, N_{exc} for each slice can be calculated by Eq. (IV. 4.2) separately. The change in *N* spectrum upon excited-species generation (ΔN) can be obtained from the difference between N_{exc} and N_{GS} (ΔN=N_{exc}-N_{GS}). It should be noted that Eq. (IV. 4.6) assumes that the density of excited

species is proportional to the generation rate. Under other conditions, this equation can be modified with the help of drift-diffusion simulations or by considering other relationships between generation rate and density of excited species.

PIA_generator is employed to simulate the PIA spectral-shape evolution when varying the active-layer thickness. Designed K_{ES} features are introduced to K_{GS} to realize PIA spectra similar to the experimental spectra for the convenience of comparing the spectral evolution for experimental and simulated data. The K_{ES} peaks here are assumed to be Gaussian (in the energy domain). Apart from the Gaussian bands, various band modeling can also be applied, depending on the measured system (e.g., Drude-Lorentz model).

The PIA simulation is conducted for a film (glass/PM6:Y6/glass, interlayers are neglected) and a device (glass/ITO/PM6:Y6/Ag/glass, interlayers are neglected) with different active-layer thicknesses (Fig. IV. 4.2). For the films [Fig. IV. 4.2(d)], the position of the peak in the sub-band-gap region in computed PIA spectra varies by about 25 nm as the active-layer thickness changes. Notably, even in films, an extra shoulder feature can be resolved. In devices [Fig. IV. 4.2(b)], a significant variation of peak position in the sub-band-gap region by about 65 nm is presented while changing the active-layer thickness. In addition, the double-peak feature is observed in the computed PIA spectra when the active-layer thickness in the device falls into some specific regions (140–200, 310–430, and 500–600 nm), which is in good agreement with the experimental results in Fig. IV. 4.1.

A comparison is made between the simulated [extracted from Fig. IV. 4.2(b)] and experimental PIA signals (Fig. IV. 4.3). Simulated PIA data satisfactorily reproduce the thickness-dependent peak-evolution trend in the sub-band-gap range observed in experiments. This suggests that both the double-peak feature and peak-position shift in experimental data are indeed caused by optical interference rather than a change in excited-species energetic states or the formation of new excited species.

IV. 4.3.3 Effect of Interference on $\Delta T/T$ Decay Dynamics

The optical artifacts, if not carefully addressed, can affect not only the spectral shape of differential absorption spectra, but also the measured decay dynamics under certain conditions. According to the Kramers-Kronig relationship between N and K, when considering only one ΔK peak in the spectrum with certain decay dynamics or multiple ΔK peak for the same decay dynamics, ΔN follows the same dynamics as that of ΔK. As a result, the decay dynamics of ΔT is independent of the value of the derivative terms in Eq. (IV. 4.1) (as the left and right sides of the equation are always scaled by the same factor in time); in this case, the decay dynamics is not affected by interference.

However, when multiple ΔK peaks with different decay dynamics are present in the spectrum, the decay dynamics of ΔT for different peaks can be distorted by interference and reflection and is hence sensitive to active-layer thickness. Assuming two ΔK peaks in two separated spectral regions (ΔK_1 and ΔK_2) decaying exponentially over time, t, with decay constants α_1 and α_2, we have

$$\Delta K_1 = \Delta K_1^0 exp(-\alpha_1 t), \tag{IV. 4.7a}$$

$$\Delta K_2 = \Delta K_2^0 exp(-\alpha_2 t), \tag{IV. 4.7b}$$

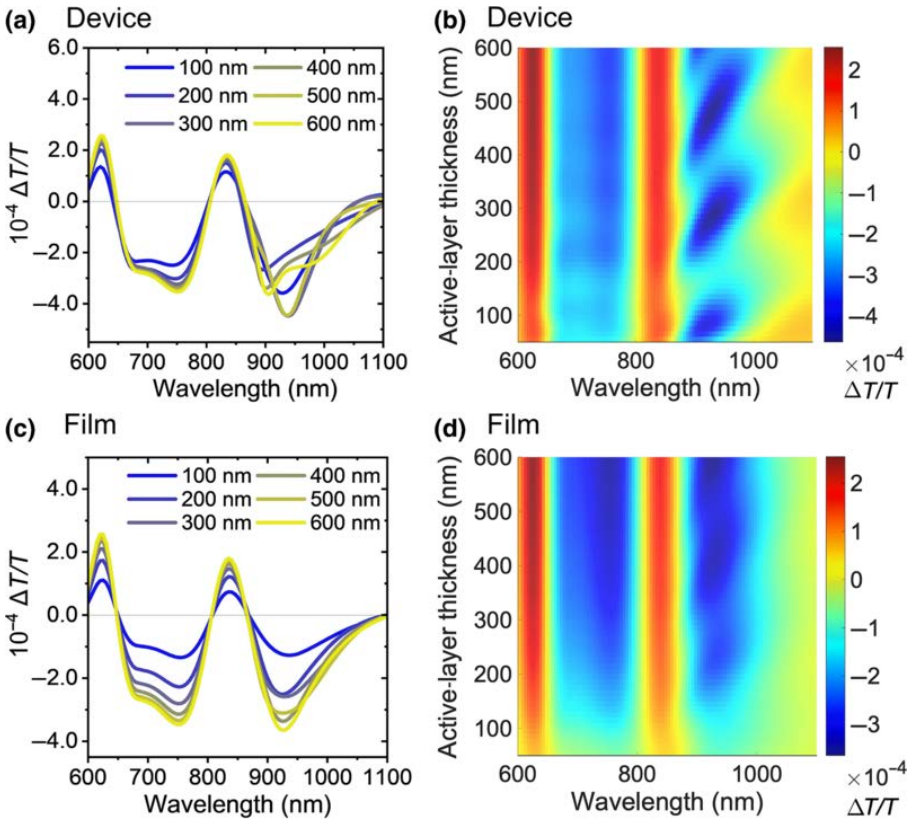

Figure IV. 4.2: Computed PIA spectra of devices [glass/ITO/PM6:Y6/Ag/glass (a),(b)] and films [glass/PM6:Y6/glass, (c),(d)] for different active-layer thicknesses. (a),(c) Simulated PIA spectra for several chosen active-layer thicknesses. (b),(d) Heat maps showing the evolution of PIA spectra when active-layer thickness varies in the range of 50–600 nm. Red indicates a high ground state bleaching signal and blue indicates a high PIA signal.Ag layers in the devices are 35 nm. Five Gaussian peaks centered at 630, 700, 780, 850, and 950 nm are introduced as K_{ES} features.

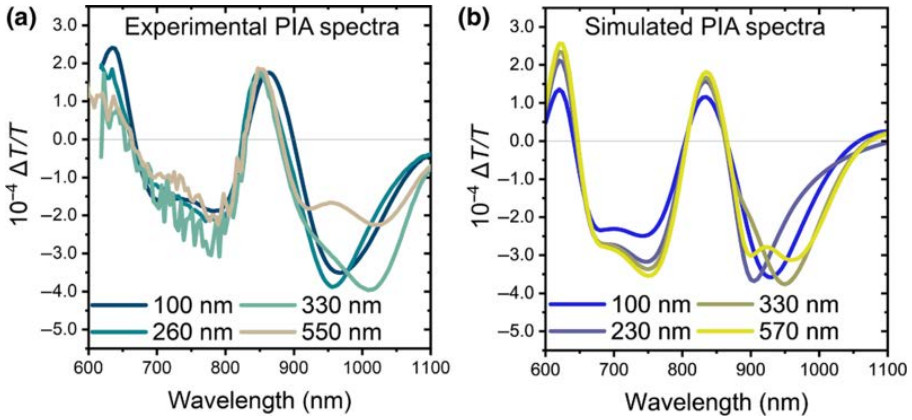

Figure IV. 4.3: Comparing experimental and simulated PIA data; simulated data clearly show similar peak shape and intensity evolution to that observed in experimental data in the sub-band-gap region. (a) Experimental PIA spectra (pumped by 405-nm light with a fluence of 105 mW/cm^2) of PM6:Y6 on devices (ITO/PEDOT:PSS/PM6:Y6/PDINO/Ag) with various active-layer thicknesses. (b) Simulated PIA spectra on a device (glass/ITO/PM6:Y6/Ag/glass, interlayers are neglected) with nonuniform charge-distribution profile and cavity-effect considerations.

where ΔK_1^0 and ΔK_2^0 are ΔK for peaks ΔK_1 and ΔK_2 at t=0, respectively.

According to the Kramers-Kronig relationship, the introduction of ΔK_1 and ΔK_2 leads to ΔN_1 and ΔN_2 (with α_1 and α_2 as decay constants, respectively) over the whole spectral range. Therefore, when probing the ΔK_1 spectral region, the measured ΔT_1 has a contribution not only from ΔK_1 and ΔN_1, but also ΔN_2. Subsequently, the decay dynamics of ΔT_1 is not strictly defined by α_1 and is affected by α_2, even when ΔK_1 and ΔK_2 do not spectrally overlap with each other.

Figure 4 shows the simulated $\Delta T/T$ decay dynamics on devices and films with various active-layer thicknesses when two ΔK peaks [Fig. IV. 4.4(c), centered at 875 and 1025 nm for ΔK_1 and ΔK_2, respectively] with different decay constants (1×10^{10} and 5×10^{9} s^{-1} for α_1 and α_2, respectively) are present in the ΔK spectrum. Four probe wavelengths (875, 925, 975, and 1025 nm) are chosen, which are at the center and shoulder of the peaks [Fig. IV. 4.4(c)]. It is shown in Figs. IV. 4.4(a) and IV. 4.4(b) that the $\Delta T/T$ decay dynamics is affected by the probe wavelength and active-layer thicknesses and strongly deviate from the designed decay dynamics, even though ΔK_1 and ΔK_2 are spectrally separated. It is also found that the extent of deviation is more significant when the probe wavelength gets close to the other peak [Figs. IV. 4.4(a) and IV. 4.4(b), brown and green solid lines]. In addition, the decay dynamics of the peak with a larger decay constant (shorter lifetime) is found to be more sensitive to this effect [Figs. IV. 4.4(a) and IV. 4.4(b), brown and red solid lines].

IV. 4.3.4 ΔN-ΔK Simulation: Benchmark and Experimental Validation

The optical artifacts presented in Figs. IV. 4.2 and IV. 4.4 make it extra challenging to resolve actual changes in absorption coefficients and decay dynamics from measured spectra and to conduct quantitative and qualitative analyses in differential absorption spectroscopies. Here, we propose an inverse transfer-matrix formalism to extract the real K_{ES} spectra from the measured PIA spectra (matlab script denoted as DeltaNK_simulator; for details, see Fig. D.11 within the Supplemental Material). Given the experimental PIA spectrum, device structural information, N_{GS}-K_{GS} spectra, and the pump-light spectral density, the simulator can first calculate the optical generation profile. Then, with the calculated generation profile as another input, the actual changes in the N-K spectra (ΔN-ΔK) at each position in the active layer along the pump-light pathway with optical artifact corrections can be output. Notably, the distribution profile can sometimes deviate from the optical generation profile (e.g., when the excited species are free charges and the device is put under high bias). In this case, a drift-diffusion simulation can be involved to calculate the actual distribution profile more precisely.

The change in extinction coefficient, ΔK, can be easily translated to the change in absorption coefficient ($\Delta\alpha$) via Eq. (IV. 4.8) for conventional PIA analysis. This holds for all quasi-steady-state and transient differential absorption spectroscopies.

$$\alpha = \frac{4\pi K}{\lambda} \tag{IV. 4.8}$$

Figure IV. 4.5 presents a simplified flowchart that intuitively shows the working process of the DeltaNK_simulator. The input PIA spectrum [Fig. IV. 4.5(c)] is extracted directly from Fig. IV. 4.2(b) by choosing a random active-layer thickness and device structure (the PIA of a device with 370-nm active-layer thickness is chosen here as an example). The original ΔN-ΔK used for generating the input PIA spectrum is known but not used as an

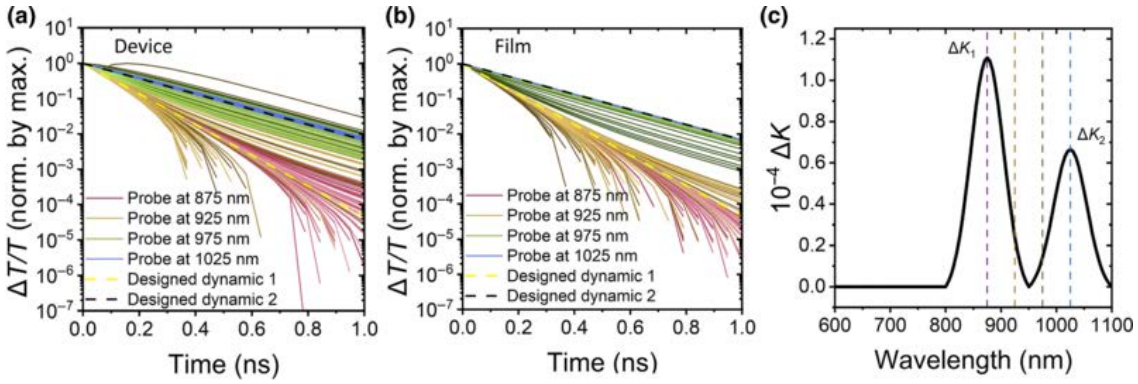

Figure IV. 4.4: Computed apparent decay dynamics obtained from normalized $\Delta T/T$, probing at the center of ΔK_1 (875 nm, red solid lines), right side of ΔK_1 (925 nm, brown solid lines), left side of ΔK_2 (975 nm, green solid lines), and center of ΔK_2 (1025 nm, blue solid lines) on a device (glass/ITO/active layer/Ag/glass) (a) and film (glass/active layer/glass) (b). Yellow and black dashed lines represent the designed decay dynamics of ΔK_1 and ΔK_2, respectively. (c) Designed ΔK_1 and ΔK_2 peaks introduced on top of the ground-state optical constants of the active layer at t=0 (exact amplitude of ΔK_1 and ΔK_2 evolves over time according to α_1 and α_2); four vertical dashed lines, from left to right, indicate the four probe wavelengths at 875, 925, 975, and 1025 nm, respectively.

input for the inverse transfer-matrix calculations. In this way, the output result from the DeltaNK_simulator can be compared with the originally designed ΔN-ΔK to benchmark the fitting result. In Fig. IV. 4.5(e), the simulated ΔN-ΔK in the first slice of the active layer is compared with the corresponding designed ΔN-ΔK of the same slice to show the precision of the fitting result. Figure 5(f) compares the designed and simulated ΔK_{max} at each normalized position ($X_{norm}=X/d$, where x is the real position in the active layer) across the active layer. As shown in Figs. IV. 4.5(e) and IV. 4.5(f), the simulated ΔN-ΔK spectra indeed match the originally designed ΔN-ΔK spectra perfectly. While the input PIA presents a double-peak feature in the sub-band-gap region due to cavity-effect manipulation, the inverse transfer-matrix simulator successfully outputs ΔN-ΔK spectra with a single-peak feature [Figs. IV. 4.5(c) and IV. 4.5(e)]. Such a correction method can also be applied to correct the $\Delta T/T$ dynamics. Taking $\Delta T/T$ spectra probed with each probe wavelength for a device with random thickness in Fig. IV. 4.4(a) as an example (the 150-nm device is chosen here as an example), and using the DeltaNK_simulator to correct the $\Delta T/T$ spectra at each time, the true decay dynamics is thus obtained for all probe wavelengths (Fig. IV. 4.6).

In addition, the simulator shows tolerance against inaccurate input of the active-layer thickness. As shown in Fig. IV. 4.7, DeltaNK_simulator outputs ΔN-ΔK spectra that match the designed ΔN-ΔK spectra, even when the input active-layer thickness deviates from the actual value (by 10 nm in the presented simulation).

The simulation in Fig. IV. 4.5 assumes accurate input of ground-state N-K spectra, which is very challenging in real experiments; the obtained spectra vary in terms of the applied method and labs [259, 263]. In our simulation, the error arising from N_{GS}-K_{GS} is optimized by a global fitting of PIA spectra of devices with various active-layer thicknesses while looping N_{Cauchy} and B values (same N_{Cauchy} and B are simultaneously applied for all spectra in each loop). At least one PIA spectrum measured either on the film or on the device with a very thin active layer (active-layer thickness smaller than 100 nm) is required to help indicate the number of PIA peaks, since previous results have already shown that under these conditions the optical artifacts only slightly affect the peak

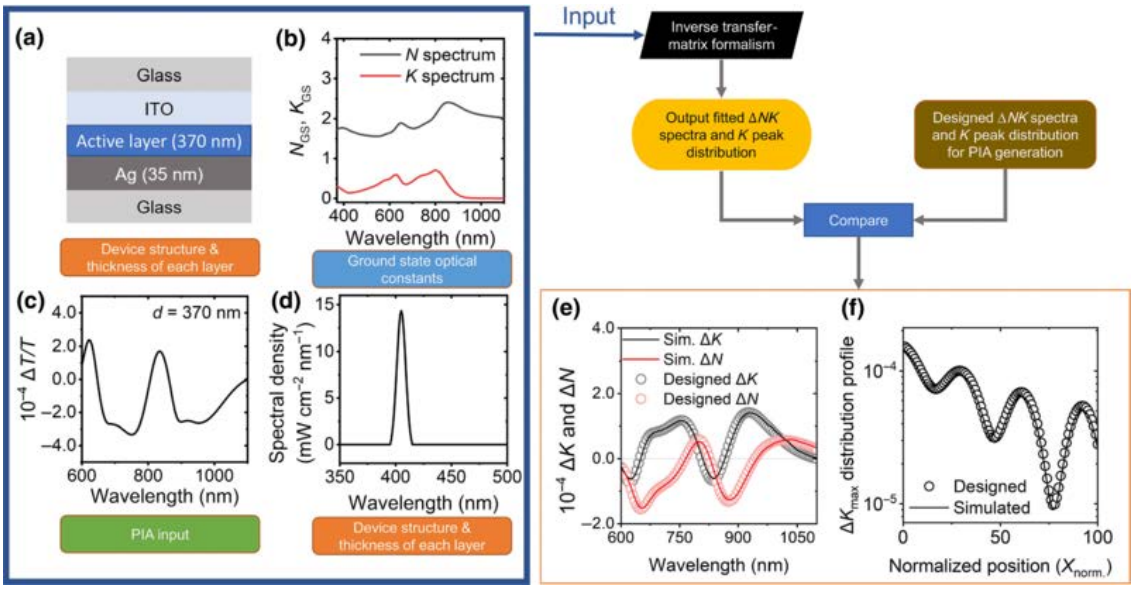

Figure IV. 4.5: Flowchart for Δ*N*-Δ*K* simulation via inverse transfer-matrix formalism (DeltaNK_simulator). (a) Film-stack structure and thicknesses of each layer used. (b) Ground-state optical constants of the active layer together with the optical constants of all the other photoinsensitive layers) as input. (c) PIA signal as input. (d) Spectral density of pump light as input. (e) Comparing designed and computed Δ*N*-Δ*K* in the first slice of the active layer as the output. (f) Comparing the designed and simulated intensity-distribution profile of the peak of Δ*K* (ΔK_{max}) at each position across the active layer as output.

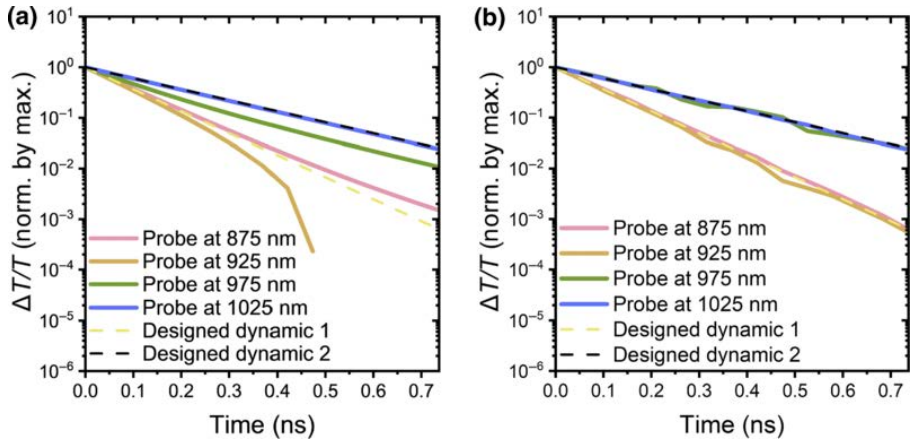

Figure IV. 4.6: Δ*T*/*T* decay dynamics (a) of 150-nm device (glass/ITO/active layer/Ag/glass) probed at various wavelengths extracted from Fig. IV. 4.4 a, and corresponding simulated Δ*K* decay dynamics (b) obtained via DeltaNK_simulator. Yellow and black dashed lines represent designed decay dynamics for ΔK_1 and ΔK_2, respectively.

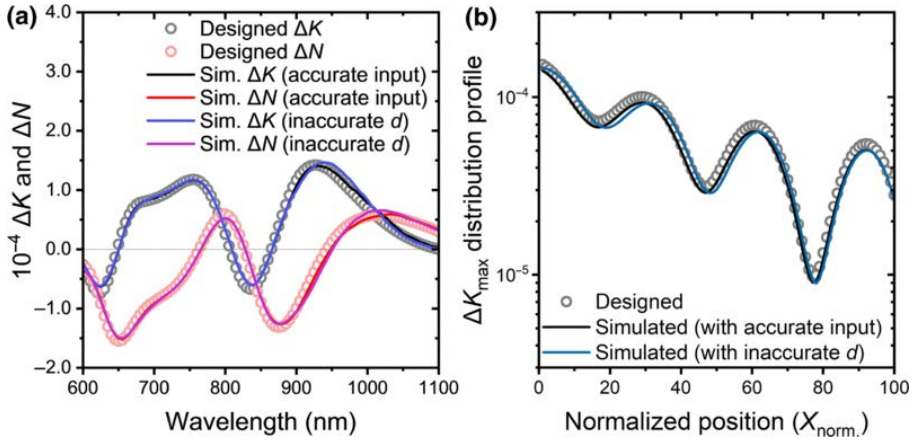

Figure IV. 4.7: Comparing spectral shape in the first slice in the active layer (a) and peak-intensity distribution of Δ*K* at each normalized position, Xnorm, in the active layer (b) of the designed (dots) and simulated Δ*N*-Δ*K* (solid lines) when using accurate and inaccurate active-layer thickness as input of DeltaNK_simulator. Stack structure is glass/ITO/PM6:Y6/Ag/glass, d=370 nm, thickness deviation for inaccurate *d* input is 10 nm.

position and intensity but do not change the number of peaks [Figs. IV. 4.2 (a) and (c)]. At least one input spectrum needs to present the double-peak feature to increase the constraints for the N_{Cauchy} and *B* values. The correct Cauchy coefficients, N_{Cauchy} and *B*, can be determined when the output Δ*K* spectra for all input PIA spectra in the global fitting (especially the ones with double-peak features) give the correct peak number when using the very same N_{Cauchy} and *B* values for all the input PIA spectra. The fitting results will benefit from increasing the number of input PIA spectra for the global fitting, since there are more constraints present for the N_{Cauchy} and *B* values. This fitting strategy can be further adapted to other types of differential absorption spectroscopy techniques as well.

To examine the fitting result of this strategy, two sets of ground state *N*-*K* spectra (N_{GS1}–K_{GS1} and N_{GS2}–K_{GS2}) are used [Fig. IV. 4.8(c)]. PIA data are generated by the PIA_generator using N_{GS1}-K_{GS1}, then fitted in the DeltaNK_simulator using N_{GS2}–K_{GS2} while looping the N_{Cauchy} and *B* values. All other fitting procedures are shown in Fig. IV. 4.5. Simulated Δ*N*-Δ*K* nicely reproduces the designed Δ*N*-Δ*K* in terms of both spectral shape and intensity distribution [Figs. IV. 4.8(a) and IV. 4.8(b)]. This fitting strategy is also employed to fit experimental data in Fig. IV. 4.1 to reveal the spectral shape of Δ*K* and the peak-intensity distribution in the sub-band-gap region (Fig. IV. 4.9). With the fitting results, the experimental PIA spectra can be perfectly reproduced (Fig. D.7 within the Supplemental Material).

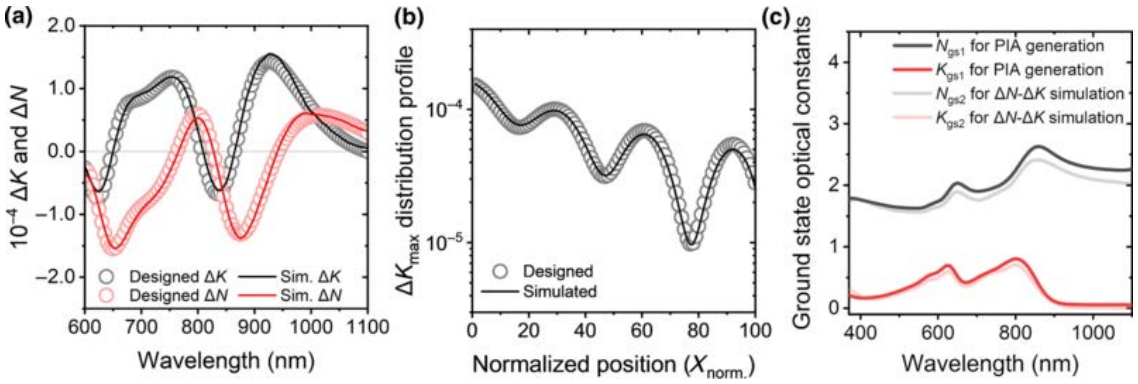

Figure IV. 4.8: Comparing spectral shape of Δ*K* in the first slice in the active layer (a) and peak-intensity distribution of Δ*K* at each normalized position, X_{norm}=X/d, in the active layer (b) of designed (dots) and simulated Δ*N*-Δ*K* (solid lines) when using inaccurate ground-state optical constants as input of DeltaNK_simulator. (c) Ground-state optical constants (*N*-*K*) for PIA generation and Δ*N*-Δ*K* simulation.

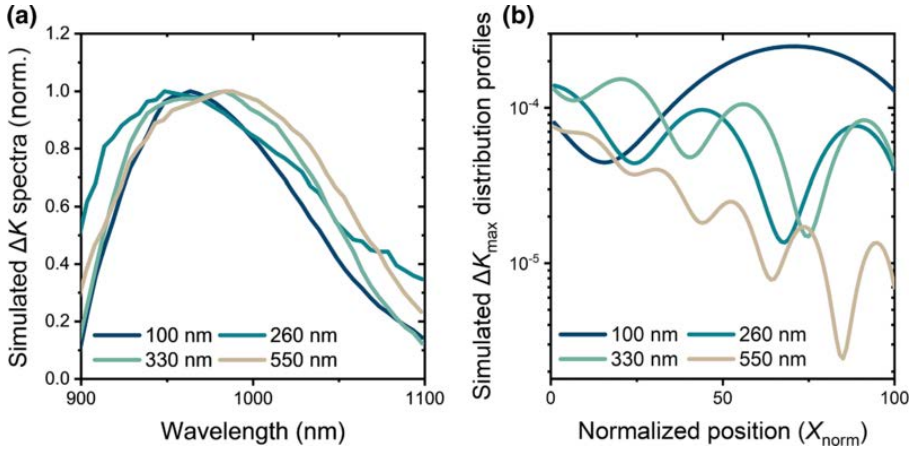

Figure IV. 4.9: The Δ*K* simulation results for experimental PIA spectra on devices with various active layer thicknesses. a) The simulated ΔK spectra in the spectral region from 900 nm to 1100 nm (normalized by peak values) representing the spectral shape of Δ*K*. b) The intensity distribution profile of Δ*K* in at each normalized position X_{norm} = X/d in the active layer.

IV. 4.4 Conclusion

We present a detailed and systematic study on optical artifacts in differential absorption spectroscopies and provide a practical methodology for optical artifact corrections. We clarify how and to what extent the cavity effect and excited-species distribution profile manipulate experimental spectra and decay dynamics in terms of simulations. It is shown that, especially in the sub-band-gap region, the position, intensity, spectral shape, decay dynamics, and even the number of spectral peaks in the measured $\Delta T/T$ spectra can be strongly manipulated by optical artifacts. In both bare films (glass/active layer/glass) and full devices (glass/ITO/active layer/Ag/glass), an extra feature (shoulder or peak) can be introduced to the measured $\Delta T/T$ spectra due to optical artifacts in extreme cases. When multiple Δ*K* peaks with different decay dynamics are present in the spectrum, the $\Delta T/T$ decay dynamics can deviate from the corresponding Δ*K* decay dynamics due to optical artifacts. This artifact in decay dynamics is found to be present in

both devices and films. These artifacts, which should be very carefully considered, bring enormous challenges for peak identification, comparison, and quantitative analyses in differential absorption spectroscopies.

Furthermore, we conclude that these optical artifacts originate from the collective effect of a nonuniform charge-distribution profile and interference effects of the probe light. Finally, we propose an inverse-transfer-matrix formalism to correct these optical artifacts and reveal the actual change in the K spectrum of the sample upon pump excitation. This work can be adapted to all kinds of optical-probe differential absorption spectroscopies and enables accurate determination of the change in absorption coefficient upon pump excitations, for instance, in charge-modulation spectroscopies for studying the electronic properties of semiconductors. More importantly, this work presents a path for directly studying thick-junction organic solar cells and perovskite solar cells with accurate differential absorption spectroscopies.

IV. 5 Discussion, Conclusion and Outlook

This thesis is set against the backdrop of a thriving era in the realm of OSCs, characterized by the rapid development of NFAs. Since the PCE of 15.5% was reported for one famous NFA-based OSC system, PM6:Y6, the NFA-based OSC systems have gained significant attention.

Many of the efficient NFA-based OSC have been shown to be “low-offset systems”. These low-offset systems are promising due to the high charge generation efficiencies despite the observed small HOMO-HOMO offset between the donor and acceptor, which provides the possibility to simultaneously increase the J_{SC} and V_{OC}. The low HOMO-offsets lead to small $\Delta E_{S_1\text{-}CT}$ which plays a critical role in device performance, and inspired many works to reduce the HOMO-offsets for device optimization. Presently, the most efficient single-junction OSC devices based on NFAs have been reported with the PCE of >19% [5, 264], making OSCs closer and closer to the PCE required for commercialization. However, many studies have pointed out the presence of an optimum value for $\Delta E_{S_1\text{-}CT}$, below which charge generation is severely sacrificed and results in inferior overall device performance [24, 42, 217]. As this thesis aims to make a path towards commercialization of OSCs, it provides insights from both physical and technical perspectives. Physics-wise, the thesis intends to make path for further efficiency optimization by understanding the role that $\Delta E_{S_1\text{-}CT}$ plays in the overall device performance in low-offset systems and understand the loss mechanism of each device parameter. From the technical perspective, this thesis emphasizes the importance of carefully addressing the possible violence of assumptions of characterization methods which can lead to measurement artifacts in the practice of converting low-offset OSCs from lab scale towards industrial scales.

The low HOMO-offset OSC systems found to have high emission efficiencies and thus low ΔV_{nr}. Experimental reports have observed that the ELQYs of the low-offset OSC blends are defined by the PLQYs of the lower-bandgap pristine materials in the blends [117]. More detailed studies on the PL and EL emission of the low-offset OSC blends and those of the neat acceptors in the blends has revealed the repopulation of S_1 states from CT states in low-offset OSCs. [25, 42, 98] As a result, as the free electrons and holes encounter each other, exciton decay serves as a parallel recombination channel in addition to CT decay. While the losses via exciton decay was observed to be much lower than that from CT decay in PM6:Y6, the exciton decay channel can serve as one origin of FF losses, which can be considerable when $\Delta E_{S_1\text{-}CT}$ is further reduced. Furthermore, with the energy of CT and S_1 so close to each other, hybridization between CT and S_1 can be induced. While as pointed out by Classen et al. [42], a Boltzmann stationary-state equilibrium model of S_1 and CT can precisely describe the charge generation and reduced ΔV_{nr}, the hybridization between S_1 and CT can affect the CT lifetime and thus, the recombination rate and FF. [265, 266] In addition, the role of other recombination channels such as triplet excitons should not be overlooked. [142] In chapter IV. 1, a systematic study was conducted for three different PM6:NFA blends with a variety of HOMO-offsets. Relating

the ELQY of the blends with the PLQY of corresponding acceptors, the fraction of CT which reforms excitons upon charge injection in the dark condition ($\eta_{ex,ref}$) was evaluated. The interplay among HOMO-offset, $\eta_{ex,ref}$, and the determined k_2 values of PM6:NFA systems was studied and compared. An increase in k_2 was observed with the reduction of the HOMO-offset. However, it should be noted that, while a simultaneous trend in increase of $\eta_{ex,ref}$, and k_2 is observed, the k_2 was found to drastically increase by 30 times (from 1×10^{-17} to 3×10^{-16} m^3/s), while the value of $\eta_{ex,ref}$ remained small, suggesting that exciton reformation, and also the Boltzmann stationary-state equilibrium model of S_1 and CT, alone, does not fully explain the acceleration of bimolecular recombination upon reducing the HOMO-offset in the studied OSC blends. The increased k_2 can possibly have contributions from another dark channel (e.g., triplet excitons), or by enhanced decay rate constant of hybridized CT. Another finding in chapter IV. 1 was the interesting field-dependent generation behavior in PM6:o-IDTBR which is not explainable with the classic Braun-Onsager-type field-dependent CT dissociation model. Such behavior was exemplified with other low-offset systems in chapter IV. 3. The discussion about the decay channels in low-offset OSCs and the field-dependent charge generation will be revisited and discussed in more details in later paragraphs.

Another fact to be noted in chapter IV. 1 is the difficulty in accurately determining energy offsets in low-offset systems. For example, the HOMO-offset in PM6:o-IDTBR determined via *C-V* is -30 meV which is unlikely to still present >30% EQE. Instrumental error plays a role. As for the studies of low-offset OSC systems, the required measurement resolution is very high for the studies for low-offset systems, since the HOMO-offset for these systems are usually lower than 0.5 eV. Taking PM6:Y6 as an example, the ΔE_{HOMO} determined from different labs and methods vary in a large range of 0.08 eV to 0.71 eV (Table. B.1), leaving a large uncertainty about the low driving force characteristic of these systems. While it could be feasible to relatively compare energetic offsets among a series of materials measured in one lab with the same measurement technique, with the measurements operated in similar measurement window, it is still challenging to accurately address the absolute values. In chapter IV. 2, a detailed study on the energetics of PM6:Y6 films fabricated from two different solvents, CF and CB, was conducted with the help of spectroelectrochemistry. Compared to *C-V*, the oxidation and reduction processes of the donor and acceptor can be clearly observed from the change in their corresponding absorption spectra in spectroelectrochemistry. In addition, the injection of electrons from acceptor to donor (vice versa for the injection of holes) at the donor:acceptor interface in the bulk of the active layer can be studied. This serves as an extra advantage of spectroelectrochemistry compared to surface-sensitive methods like UPS. Given the widely observed influence of morphology on the energy level of materials, the effect of morphology was very carefully addressed. It was nicely exemplified in this work how the difference in aggregation can affected the measured HOMO-offsets, which stresses the importance of measuring the HOMO-offset in device-relevant blend films. In addition, the work points out the importance of measuring the energy levels in the bulk for systems with vertical segregations. While the HOMO-offset can be elegantly determined as shown in chapter IV. 2, it is worth to note that the HOMO-offset cannot be immediately translated into $\Delta E_{S_1\text{-}CT}$ due to the binding energies of exciton and CT. While the exciton binding energy can be roughly estimated from the band gap and exciton energy (obtained from absorption and PL emission spectra), it is challenging in getting the binding energy for CT. An indirect way for estimating the $\Delta E_{S_1\text{-}CT}$ of low-offset

OSC systems was presented in chapter IV. 3 in terms of temperature dependent ELQY measurement.

While previous studies from our group concluded that charge generation is not a limiting factor in PM6:Y6, which may be considered as a low offset system, it was shown in chapter IV. 3 that further reduction of $\Delta E_{S_1\text{-}CT}$ lower than a critical point, significantly sacrifices charge generation efficiency and recombination with limited benefit in V_{OC}. This conclusion is consistent with many previous theoretical studies which indicates reduced charge generation efficiencies for low-offset systems due to the vanishing driving force for exciton dissociation [42, 68, 217]. Indeed, in chapter IV. 3 it was found that the different exciton dissociation efficiency at the donor:acceptor interface is the main cause for the drastically different EQE_{PV}s of the studied systems, upon a small variation in the $\Delta E_{S_1\text{-}CT}$. In the applied bias region of $V_{app} \leq 0$, the quantum fraction of the recombination which proceeds via CT decay was found to be negligible compared to that via exciton decay in all studied systems in chapter IV. 3. Importantly and interestingly however, the values of J_{ph} in all studied systems were found to approach their corresponding simulation predicted optical absorption limit $J_{ph,max}$ with the help of bias. This pointed to a picture of field-dependent exciton dissociation yield at the donor:acceptor interface which is different from the traditional picture where such field-dependent charge generation is due to the field-dependent CT dissociation rate and proceeds via the decay of CT states (and is thus highly non-radiative). It is still under debate whether such exciton dissociation yield is caused by a field-assisted exciton dissociation rate (due to e.g., the shift in energetic levels with bias or the disorder of CT) or reduced exciton reformation rate at high collection bias. However, according to our PL/EL results, the reformation fraction of both PM6:Y5 and PM6:o-IDTBR at injection condition when J_{inj}=J_{ph}, were too low to explain the increase from J_{SC} to the saturation current density (J_{sat}) for all systems. One clear consequence of this field-dependent exciton dissociation yield is, though, a limited FF.

The fact that J_{ph} is close to $J_{ph,max}$ at high reverse bias points to unity exciton diffusion efficiencies in all studied systems in chapter IV. 3, however, it should be pointed out that this does not immediately indicate that morphology does not play an important role. From the view of one single exciton, the exciton diffusion and dissociation are two processes in sequence and compete together against the decay of exciton. Thus the diffusion and dissociation efficiencies of excitons can affect one another. For instance, Riley et al. [217] have shown analytically that more driving force (larger $\Delta E_{S_1\text{-}CT}$) is required to reach the same charge generation yield when exciton lifetime is reduced or when domain size is increased in the $\Delta E_{S_1\text{-}CT}$ limiting regime (with all other relevant parameters remaining unchanged). Whilst Classen et al. [42] have shown analytically how exciton lifetime benefits exciton dissociation given the same driving force. In this regard, when excitons require shorter time to reach the donor:acceptor interface, higher exciton dissociation efficiency can be expected with the same exciton dissociation rate and exciton lifetime. In this way, a lower voltage loss from driving force can be achieved with limited sacrifice in charge generation efficiency, given the same exciton lifetime.

Despite the dominating losses via exciton decay in the efficient charge collection regime in *J-V* (from J_{SC} to high reverse bias), in inefficient charge collection regime ($0 \leq V_{app} \leq V_{OC}$), bimolecular recombination plays a considerable role. With *J-V* and PL measurements, it was found that the recombination prefers to occur via a dark recombination channel upon the encounter of two free charges, even in the systems with the lowest $\Delta E_{S_1\text{-}CT}$. Consistent with that presented in chapter IV. 1, the enhanced k_2 was observed

with reduction in $\Delta E_{S_1\text{-}CT}$. It should be noted that although in chapter IV. 1 and IV. 3, a model of exciton, CT and CS was employed for the analyses of loss channels, it is not intended to trivialize the role of other decay channels such as triplet excitons. As pointed out by Gillett et al. [142], the decay via triplet excitons can serve as an important loss channel in V_{OC} condition. In this regard, the dark recombination channel observed in chapter IV. 3 can be a mixture of CT and triplet decay. Given the often-observed low energy for triplet excitons, from the perspective of the energetic and rate model, the losses via these triplet excitons can be understood as another dark state parallel to CT, which is out of the equilibrium and serves as a terminating state. As a conclusion from chapter IV. 1 and IV. 3, the FF of low-offset OSC systems is harmed by both field-dependent exciton dissociation yield, and enhanced CT decay rate.

The highly sought-after reduction in ΔV_{nr} - as presented in chapter IV. 3 - was found not to be advantageous in reducing the loss between V_{OC} and photovoltaic bandgap. The reason here was related to the sharpness of edge of EQE_{PV} spectra. Among the studied PM6:NFA systems it was found that the decreased ΔV_{nr} was accompanied by the broadening of EQE_{PV} tail. Hence the ΔV_{nr} and ΔV_{rad} present a negative correlation. The difference in the sharpness on the EQE_{PV} tail is suspected to be related to the stiffness of the NFA molecules.

Concluded from chapter IV. 1 and IV. 3, as $\Delta E_{S_1\text{-}CT}$ decreases below a critical point ($\Delta E_{S_1\text{-}CT,crit}$), both J_{SC} and FF are strongly sacrificed due to an inefficient and field-dependent exciton dissociation process and enhanced bimolecular recombination. For better understanding of enhanced bimolecular recombination, a model which considers both singlet exciton reformation and triplet excitons is desired. Note that the enhanced bimolecular recombination affects not only the FF, but also V_{OC}. To achieve better FF and V_{OC} in such low-offset systems, it would be important to analyze the dark states in more detail and quantitatively resolve the contribution of CT, and T_1 decay. Here it is stressed that, S_1 decay can play a significant role, since in systems with very low $\Delta E_{S_1\text{-}CT}$ like PM6:o-IDTBR, exciton decay still serves as the main loss channel (response for 70% of carrier losses) even in V_{OC} condition. Regarding the inefficient charge generation for low $\Delta E_{S_1\text{-}CT}$, it is proposed in this thesis that thorough understanding of the mechanism of field-dependent exciton dissociation is the key to bring $\Delta E_{S_1\text{-}CT,crit}$ to a lower value. It is also proposed that long exciton lifetime and small domain size can be beneficial for lowering $\Delta E_{S_1\text{-}CT,crit}$. However, too small domain sizes in BHJ can result into a negative effect on the device performance, since the percolation path for charge extraction is most likely compromised. In this regard, the recently eye-catching pseudo-bilayer organic solar cells fabricated from sequential deposition can be promising as such morphology is believed to be beneficial for charge collections. [186] In addition, this technique has nice compatibility with blade-coating for large-area up-scaling. Overall, the above-mentioned considerations provide a path for pushing the efficiency of low-offset OSCs toward the 20% regime and consequent commercialization.

With the promising perspective for continuously increasing PCE of organic solar cells and attempts being made for up-scaling NFA-based OSCs to an industrial scale, a special note from a technical perspective is given in chapter IV. 4. Indeed, up-scaling and fabricating high-performing OSCs via fabrication techniques which are compatible with industrial production serves as important and tough challenges for the commercialization of OSCs. However, another important and but easily overlooked consideration is the potential artifacts which may become pronounced as the geometry of the device changes. In chapter IV. 4 it has been shown in detail how the effect of low finesse cavity

interference and non-uniform generation profile of the charges collectively distort the observed experimental spectra in differential absorption spectroscopy. Notably, for the same active layer material, the number of the feature peaks can change upon simply varying the device thickness. This consideration becomes extensively essential when considering the high sensitivity of many relevant physical processes and parameters (energy levels, recombination rates, radiative and non-radiative decay constants etc.) to the fabrication conditions. In this regard it is essential to apply the measurements on operational devices on industrial scales. When adapting lab-scale OSC recipes to industrial compatible fabrication techniques such as roll-to-roll processing, the changes in device geometry and configuration are usually required. Therefore, falsified interpretation and analyses can follow if the pronounced optical artifacts are not cautiously addressed. An elegant and feasible way of overcoming the effect of such optical artifacts in differential absorption spectroscopies is to apply corrections based on theoretical calculations. In chapter IV. 4, an inverse optical transfer matrix formalism was provided to minimize the manipulation of cavity effect to experimental result.

In general, at this critical juncture in the maturation of organic photovoltaic technology, and in the context of the global desire to move away from fossil energy, this thesis is intended to pave the way for the commercialization of OSCs, from both the scientific and technical perspective. With this thesis, we propose for deeper study and understanding on the detailed composition of dark loss channels in low-offset OSCs, as well as the role that electric field plays in the exciton dissociation mechanism of these systems, with cautious consideration of applicability and validity of characterization techniques.

Part V

APPENDIX

A Supporting Information to Chapter IV. 1

A.1 Materials and Sample Preparation

The following organic materials were used for photoactive blends.

poly[(2,6-(4,8-bis(5-(2-ethylhexyl-3-fluoro)thiophen-2-yl)-benzo[1,2-b:4,5-b']dith iophene))-alt-(5,5-(1',3'-di-2-thienyl-5',7'-bis(2-ethylhexyl)benzo[1',2'-c:4',5'-c']di thi ophene-4,8-dione)] *(PM6)* was used as a donor, and 2,2'-((2Z,2'Z)-((12,13-bis(2-ethylhexyl)-3,9-diundecyl-12,13-dihydro-[1,2,5]thiadiazolo[3,4-e]thieno[2",3":4',5']thieno[2',3':4,5]pyrrolo[3,2-g]thieno[2',3':4,5]thieno[3,2-b]indole-2,10-diyl)bis(methanylylidene))bis(5,6-difluoro-3-oxo-2,3-dihydro-1H-indene-2,1-diylidene))dimalononitrile *(Y6)*, 3,9-bis(2-methylene-(3-(1,1-dicyanomethylene)-indanone))-5,5,11,11-tetrakis(4-hexylphenyl)-dithieno[2,3-d:2',3'-d']-s-indaceno[1,2-b:5,6-b']dithiophene *(ITIC)*, (5Z,5'Z)-5,5'-((7,7'-(4,4,9,9-tetraoctyl-4,9-dihydro-s-indaceno[1,2-b:5,6-b']dithiophene-2,7-diyl)bis(benzo[c][1,2,5]thiadiazole-7,4-diyl))bis(methanylylidene))bis(3-ethyl-2-thioxothiazolidin-4-one) *(o-IDTBR)* were used as acceptors.

All devices used in the study were fabricated on indium-tin oxide (ITO) coated glass substrates. The photovoltaic cells used the conventional architecture ITO / hole-transport layer (HTL) / blend layer / electron-transport layer (ETL) / Ag with a 30 nm HTL of poly(3,4-ethylenedioxythiophene) polystyrene sulfonate (PEDOT:PSS), spin-coated in air and annealed at 150°C for 15 min, and a 15 nm ETL of N,N'-bis3-[3-(dimethylamino)propylamino]propylperylene-3,4,9,10-tetracarboxylic diimide (PDINN), spin-coated in N2 on top of the photoactive blend layer. The three studied blends of PM6:Y6, PM6:ITIC and PM6:o-IDTBR were dissolved in a mixture of chloroform (99.5 v/v%) and chloronaphtalene (0.5 v/v%) at the D:A weight ratio of 1:1.2 and the total concentration of 16 mg/mL to obtain an approximately 120 nm film. Following spin-coating the films were annealed at 110°C for 10 min in N2. The top Ag electrode with the thickness of 100 nm was thermally evaporated at the base pressure of 1×10-7 mbar. The devices for the space-charge limited current (SCLC) measurements of carrier mobilities utilized two additional architectures: ITO / PEDOT:PSS / active layer / MoO3 / Ag – for hole-only devices, and ITO / ZnO / active layer / PDINN / Ag – for electron-only devices.

A.2 Experimental

Cyclic voltammetry (C-V): Cyclic voltammetry was carried out using an Autolab PG-STAT101 potentiostat with a three-electrode set-up. The reference electrode was Ag/AgCl calibrated against the ferrocene/ferrocenium (Fc/Fc^+) redox couple. Platinum wire was used as a counter electrode, and ITO was the working electrode. Materials were spin coated onto ITO from a 5 mg/mL chloroform solution. Measurements were carried out in anhydrous 0.1 M solution of tetrabutylammonium hexafluorophosphate ($TBAPF_6$) in

acetonitrile, at a scan rate of 50 mV/s. The TBAPF6 electrolyte solution was degassed with nitrogen for 2 hours prior to use.

Grazing-incidence wide-angle X-ray scattering (GIWAXS): Thin films of the active layers and neat materials were prepared for GIWAXS by following the exact procedure of device fabrication. The films were spin coated on silicon substrates. GIWAXS measurements were conducted at the Advanced Light Source (ALS), Berkeley National Lab, at the 7.3.3 beamline [267]. The X-ray energy was 10 keV and the angle of incidence was 0.18°. The scattered photons were collected via a CCD detector.

Resonant soft X-ray scattering (RSoXS): Thin films were prepared similarly to device fabrication, but cast on Na:PSS/Si substrates. Next, the films were floated off in deionized water onto Si_3N_4 membranes to allow for transmission mode measurement. RSoXS measurements were conducted at the ALS 11.0.1.2 beamline[268], or at SST-1 (7-ID-1) beamline of the National Synchrotron Light Source II[269]. The data was collected at X-ray energies of 270 and 284.5 eV. To probe the lateral morphology, the X-ray incident angle was normal to the film surface (90 degrees). To explore the vertical morphology (1_z component), the films were rotated (45 degrees).

Scanning transmission X-ray microscopy (STXM): Films were prepared similar to the RSoXS samples, but mounted onto TEM grids. The STXM measurements were conducted at the ALS 5.3.2 beamline[270]. The data was collected at X-ray energies of 285.2 eV (a resonant energy of the PM6 polymer) and 320 eV (a non-resonant energy). Next, composition analysis of the active layers was performed by following previous procedures[231, 271].

Space-charge limited current (SCLC) measurements: The measurements of carrier mobility μ and transport band disorder σ were performed in the dark using a liquid N2 cryostat and a Keithley 2400 SourceMeter. The J-V measurements on electron-only and hole-only devices at various temperatures enabled extraction of the sought properties by fitting the data to the drift-diffusion model with extended Gaussian disorder[137].

Field-dependent time-resolved photoluminescence (FD-TRPL): TRPL curves were recorded by Fluotime 300, PicoQuant. The sample was first excited by a pulsed laser (402 nm) and then the emission was detected at a set wavelength value, which depends on the PL peak of the material. Time-correlated Single Photon Counting (TCSPC) was used to measure the lifetime in the ps to ms range. For the electric field-dependent measurements, we set a series of reverse voltages in a range from 0 V to 12 V.

Measuring Energetics The difference in the reported energy level values in the literature raises the question about the exact levels and band gaps of blend films. For our study, we preformed CV measurement of neat and blend films. The values obtained from CV for blends differ only slightly from the corresponding energies of the neat layers. This is logical since the orientations of PM6 or the NFAs orientations do not change when blended together (see morphology data).

A.3 SI Notes

Accounting for field-dependence in charge-generation Although both TDCF-Delay and BACE probe the charge recombination rate at the flat-band (or VOC) condition as a function of the collected charge density, $\Delta n/\Delta t$ is determined differently for the two

techniques. Whereas in the former analysis the slope of the total charge versus delay time is calculated, BACE obtains the recombination rate from the expression:

$$\frac{\Delta n}{\Delta t} = \frac{J_G}{qd} \tag{A.1}$$

where J_G is the carrier generation current density and d is the active layer thickness. It is common practice to employ either the J_{SC} or the reverse saturation photocurrent density $J_{ph,sat}$ as a measure of J_G. This approximation is valid for both PM6:ITIC and PM6:Y6, whose charge generation is largely independent of the applied bias. However, as learned from the TDCF-Generation measurements in PM6:o-IDTBR (Figure IV. 1.3b), the amount of charge generated near the VOC reduces significantly compared to the short-circuit condition. In this case, $J_{G,V_{OC}}$ should be approximated as:

$$J_{G,V_{OC}} = J_{SC} \cdot \frac{Q_{G,V_{OC}}}{Q_{G,J_{SC}}} \tag{A.2}$$

where $Q_{G,V_{OC}}/J_{SC}$ are, respectively, the amounts of charge generated at the V_{OC} or J_{SC} conditions.

One detail, which must be taken into account in the charge extraction measurements, such as BACE and TDCF, is the ability to extract all available charges at the appropriate reverse collection bias V_{coll}. Estimation of the carrier drift length using the space-charge limited mobility measurements (Table IV. 1.2) via:

$$l_{dr} = \upsilon \cdot \tau = \mu \cdot \frac{V_0 - V_{coll}}{d} \cdot \frac{1}{n \cdot k_2}, \tag{A.3}$$

where μ is the carrier mobility, k_2 is the bimolecular recombination coefficient, and V_O is the built-in voltage, suggests that, in the case of electrons in PM6:o-IDTBR, above the 1 sun condition the reverse bias of -2 V is insufficient to ensure carrier drift length exceeding the active layer thickness. However, at -4 V, this condition is satisfactorily met.

The appropriate corrections to determine the bimolecular recombination coefficient in PM6:o-IDTBR are shown in Figure A.2(a) and have been introduced in the BACE data in Figure IV. 1.2. To confirm the validity of this correction for the field-dependent PM6:o-IDTBR blend, in Figure A.2(b) we compare the recombination rate versus carrier density dependence for the BACE measurement, corrected according to Eq.A.1 and Eq. A.2, with the TDCF measurement, in which the carrier recombination rate is obtained from a slope of the total charge versus delay time.

Morphology measurements The approximated characteristic length (L_C) values, that are reported in Table IV. 1.3 of the main text, are extracted from Figure A.7(a), where $L_C = 2\pi/q^*$ and q^* is the position of the scattering feature. The secondary feature reported in Figure A.7(a) is consistent with surface roughness considering both energy dependence and STXM thickness maps. Relative domain purity (Table IV. 1.3) is a normalization of phase purity (P): $P \propto \sqrt{TSI/C}$, where TSI is the total scattering intensity calculated as the area under a given Lorentz-corrected RSoXS profile then corrected for a 1_z component by following the 1_z correction procedure in previous work[139]. On the other hand, C is the contrast function between donor and acceptor materials and defined as $C = E^4|\Delta n|^2$,

where E is the X-ray energy and Δn is the difference in the materials' indices of refraction shown in Figure A.7(f). To confirm this relationship of relative domain purity, we have conducted the above analysis at two X-ray energies (284.8 and 285.4 eV, green arrows in Figure A.7(f)) and found similar values of normalized phase purities of 0.68 and 0.61 (at respective energies), where PM6:ITIC has higher relative domain purity than PM6:o-IDTBR. Table IV. 1.3 shows the average of these values. Figure A.8 shows the AFM images of neat PM6, ITIC, o-IDTBR, as well as the PM6:ITIC and PM6: o-IDTBR blends to support the RSoXS measurements.

Morphology-driven driving force for charge generation The model of a morphology-derived driving force for charge generation can be applied to all blends which exhibit ordered (crystalline) domains of the neat compounds. It is assumed that the heterojunction interface area is less ordered. For almost all organic materials, the LUMO (HOMO) depends on the molecular conformation and it is generally larger (smaller) in the aggregated than in the non-aggregated phase. For example, Jamieson and Shoaee reported a ca. 200 meV larger EA for PCBM molecules in a neat film compared to a blend in polystyrene[272]. For PM6:Y6, this topic was recently addressed by the group of Ohkita [273], where the driving force for the downhill process was determined by measuring the HOMO of Y6 in a solution and compared to the HOMO energy of solid Y6 (determined by photoelectron yield spectroscopy, PYS). The change in energy levels between solution and solid state is consistent with the aggregation effects observed from UV-vis measurements on this system by Köhler and co-workers[274]. As such, to assess the impact of NFA aggregation on charge generation in PM6:ITIC and PM6:o-IDTBR, we consider UV-Vis absorption spectra of the acceptors in solution, neat and blend films (Figure A.9). Whilst the Y6 system shows the biggest difference between solution and solid state, ITIC has the smallest. Given previous work on correlation between changes in the absorption and energy level cascade, we anticipate that the aggregation effects may indeed be the strongest in PM6:Y6 but only moderate in PM6:o-IDTBR and hardly present in PM6:ITIC. This observation suggests that mixing with the polymer disrupts aggregation of both o-IDTBR and ITIC, albeit more significantly in the former. The implication on charge generation would then be that the Y6 blend should have the largest driving force, followed by the o-IDTBR and ITIC blends. However, given that the o-IDTBR blend shows field-dependent charge generation, it insinuates that aggregation does not play a role in charge generation in this system. This is consistent with our morphology data. According to the STXM and RSoXS measurements, domain purity in PM6:ITIC is higher than that in PM6:o-IDTBR. Thus, NFA aggregation may play an important role in facilitating free charge generation, following CT state formation at the D/A interface.

Energy offset and non-Langevin recombination The recombination rate can be reduced for several reasons, one being due to the geometrical confinement, as well as other morphological reasons [275] – as such all the different factors are termed together under the reduction term γ_{en} taking into account for any possible mechanism for lowering the encounter rate of the charge carriers. The free charge encounter coefficient k_{en} can be written in terms of geometrically reduced Langevin rate such that

$$k_{en} = fl_{en} k_L, \tag{A.4}$$

where γ_{en} (<1) is the reduction factor due to the confinement of opposite charges in their nano-domains in a bulk heterojunction system, and k_L is the Langevin recombination coefficient:

$$k_L = \frac{q}{\epsilon\epsilon_0}(\mu_e + \mu_h), \tag{A.5}$$

where q is the elementary charge, ε is the relative dielectric constant, ε_0 is the vacuum permittivity, and μ_e and μ_h are, respectively, the electon and hole mobilities. The experimentally observable effective bimolecular recombination coefficient of free carriers to the ground state, k_{rec}, can be related to the free charge encounter coefficient via

$$k_{rec} = \gamma_{CT} k_{en}, \tag{A.6}$$

yielding

$$k_{rec} = \gamma_{CT} k_{en} k_L = \gamma k_L, \tag{A.7}$$

where γ_{CT} is the CT recombination reduction factor and γ is the bimolecular recombination reduction factor. We have previously related γ_{CT} to the rate competition between the decay and dissociation of the CT state[141]. The correlation between the reduction factor and the HOMO-HOMO offset for the systems studied herein (Table A.1) implies that the energetic offset influences the kinetic rates, which in turn influence the reduction factor.

A.4 SI Figures

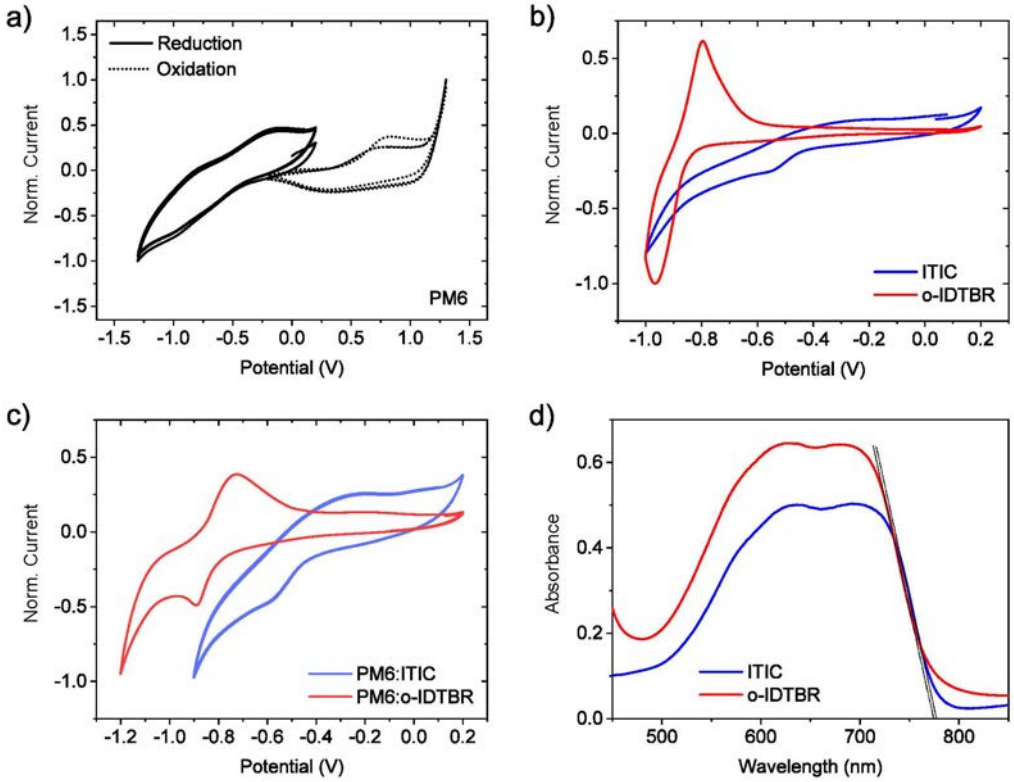

Figure A.1: Cyclic voltammetry measurements of neat PM6 (a), neat ITIC and o-IDTBR (b), PM6:ITIC and PM6:o-IDTBR blends (c), as well as optical absorption spectra of neat ITIC and o-IDTBR (d).

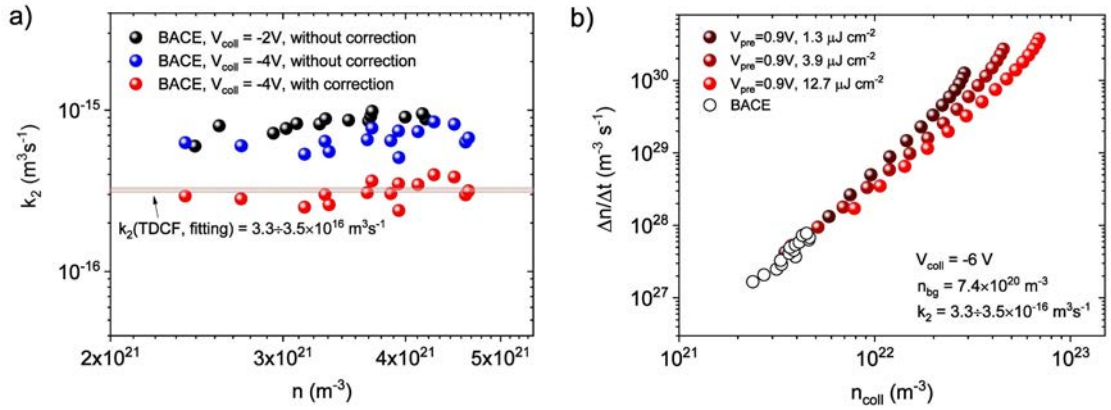

Figure A.2: a) Correction of the bimolecular carrier recombination coefficient k_2 in PM6:o-IDTBR due to the field-dependent charge generation, as well as insufficient charge extraction; b) comparison of carrier recombination rate vs. carrier density measurements between TDCF (at various fluences) and corrected BACE measurements for PM6:o-IDTBR.

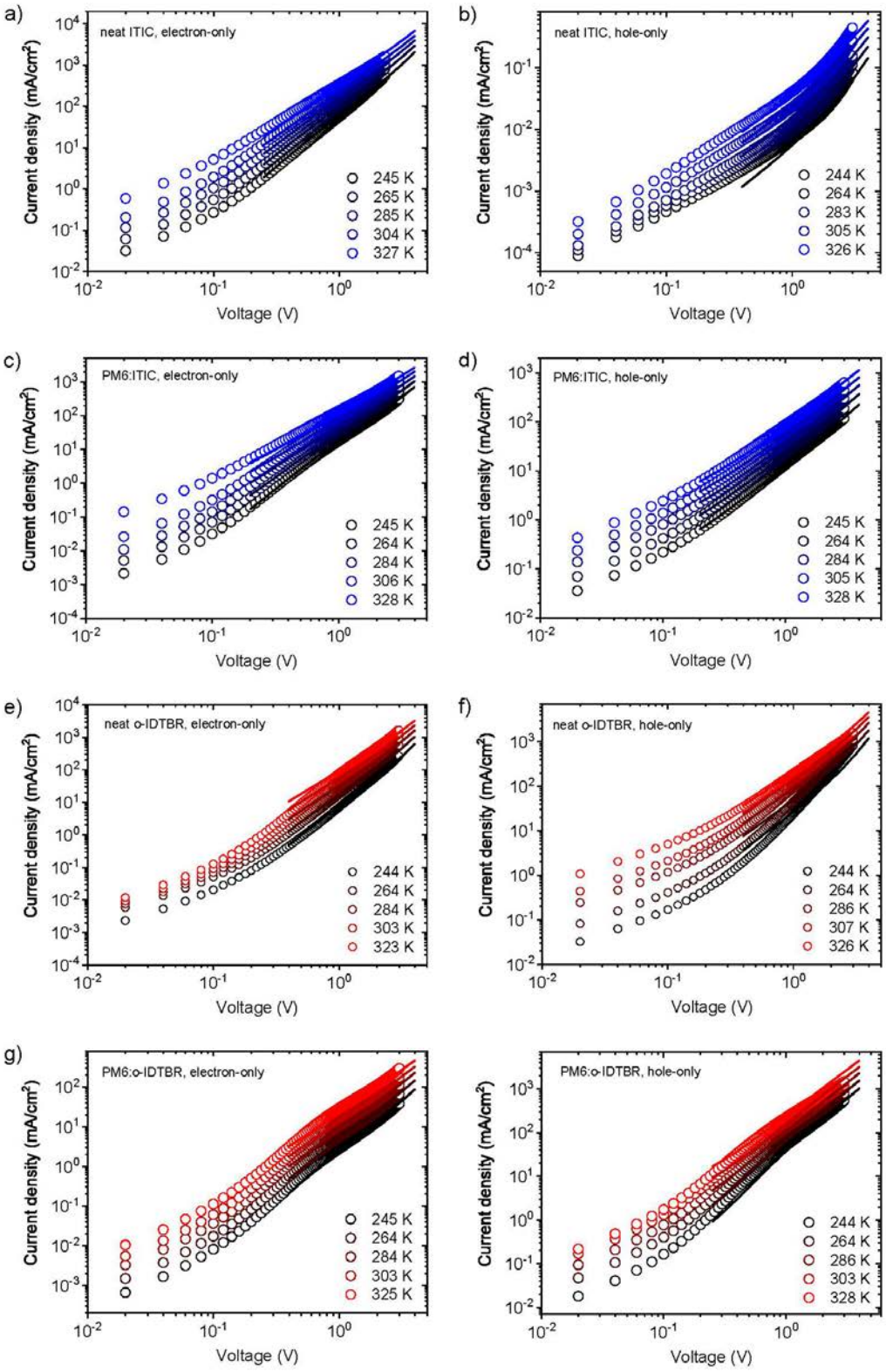

Figure A.3: Space-charge limited current (SCLC) data of electron-only (a, c, e and f) and hole-only (b, d, f and h) devices: neat ITIC (a and b); PM6:ITIC (c and d); neat o-IDTBR (e and f); PM6:o-IDTBR (g and h).

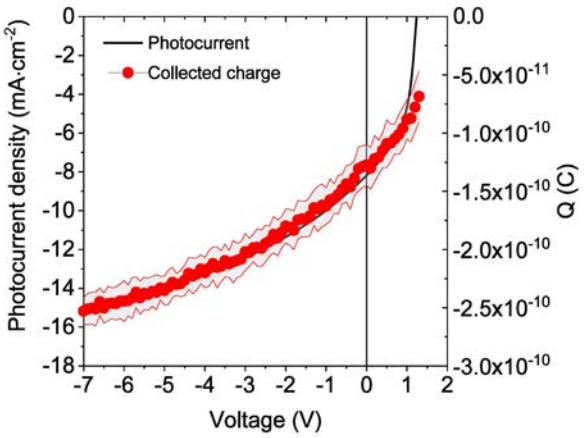

Figure A.4: Overlap between the voltage dependence of photocurrent density (left axis) and the collected charge (right axis) curves for the PM6:o-IDTBR solar cell.

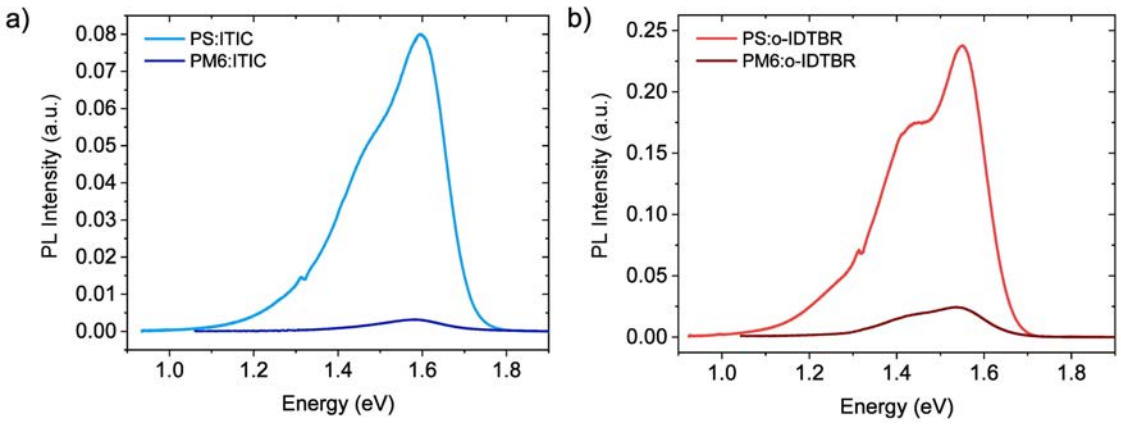

Figure A.5: Photoluminescence measurements of PS:ITIC vs. PM6:ITIC (a) and PS:o-IDTBR vs. PM6:o-IDTBR (b), demonstrating the quenching of the acceptor emission upon blending with the donor material.

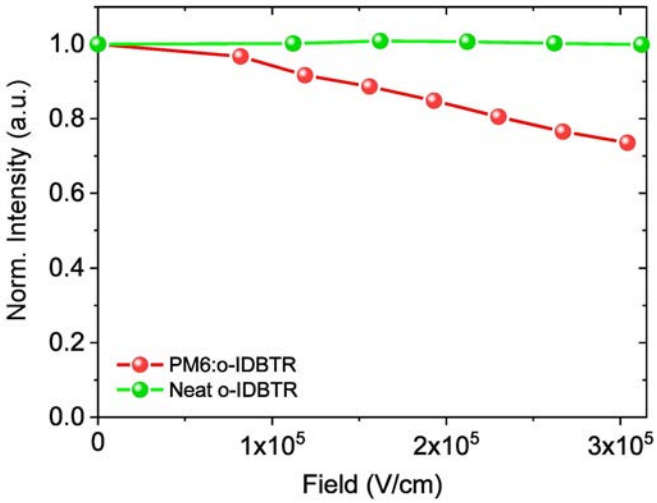

Figure A.6: Comparison of normalised photoluminescence intensity vs. electric field for PM6:o-IDTBR and neat o-IDTBR.

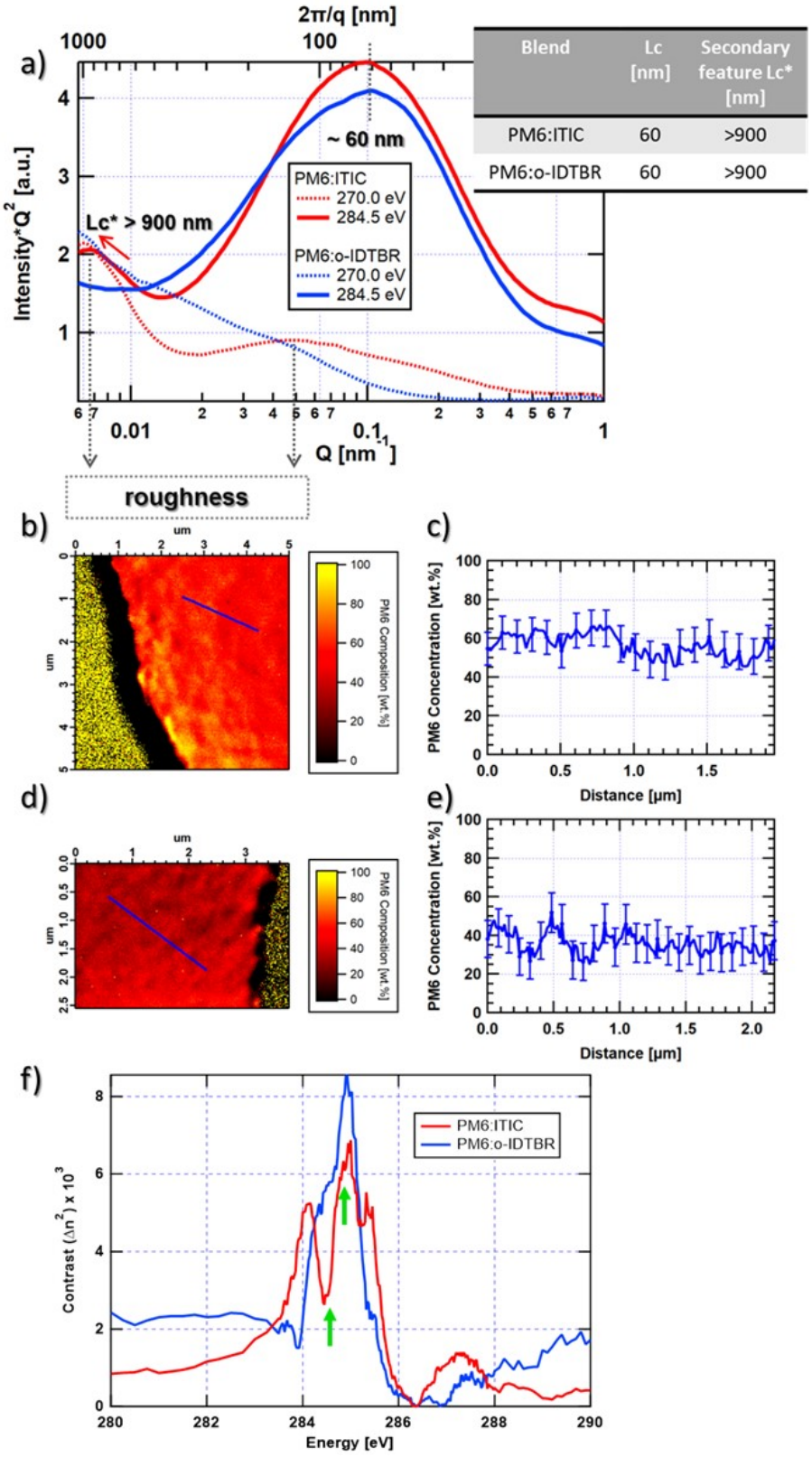

Blend	Lc [nm]	Secondary feature Lc* [nm]
PM6:ITIC	60	>900
PM6:o-IDTBR	60	>900

Figure A.7: Comparison of morphological measurements for PM6:ITIC and PM6:o-IDTBR: a) 1D Lorentz-corrected scattering profiles of PM6:ITIC and PM6:o-IDTBR, measured using resonant soft X-ray scattering (RSoXS); b) scanning transmission X-ray microscopy (STXM) composition map of PM6:ITIC; c) spatial distribution of the PM6 concentration in PM6:ITIC; d) STXM composition map of PM6:o-IDTBR; e) spatial distribution of the PM6 concentration in PM6:o-IDTBR; f) X-ray index contrast Δn^2 for the two systems of interest.

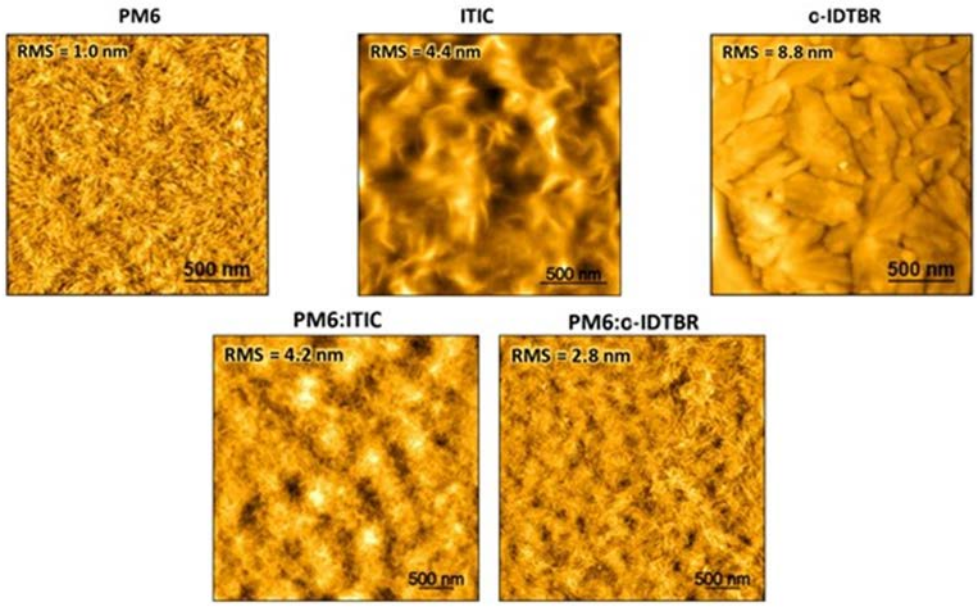

Figure A.8: Atomic force microscopy (AFM) images of neat PM6, ITIC, o-IDTBR, as well as the PM6:ITIC and PM6: o-IDTBR blends.

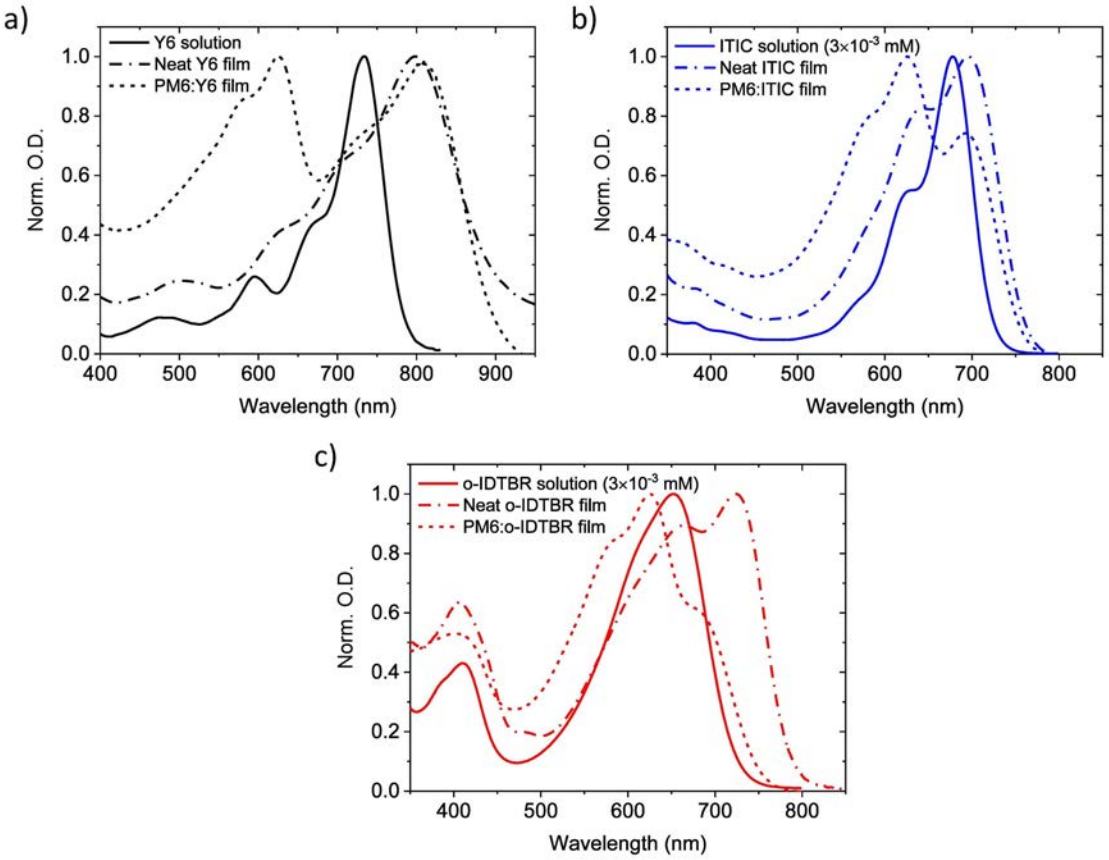

Figure A.9: Comparison of UV-Vis absorption spectra for Y6 (a), ITIC (b) and o-IDTBR (c) in a solution, in a PM6-blended film and in a neat film. The data for a) is adapted from the work by Perdigón-Toro et al.[50]

A.5 SI Tables

Table A.1: Relationship between the blend HOMO-HOMO energy offsets ΔE_{HOMO} and bimolecular recombination coefficient k_2 (obtained via bias-assisted charge extraction (BACE)), Langevin recombination coefficient k_L (obtained via space-charge limited current (SCLC) mobility measurements) and non-Langevin prefactor $\gamma = k_2 / k_L$ (assuming the relative dielectric constant of ε = 3) for the PM6:Y6, PM6:ITIC and PM6:o-IDTBR organic solar cells. The energy offsets determined in this work via cyclic voltammetry (*C-V*) are compared with the offsets obtained via cyclic voltammetry (*C-V*) and photoelectron spectroscopy in the air (PESA) in a study by Bertrandie et al.[129].

Blend	$\Delta E_{HOMO,C\text{-}V}$ meV	ΔE_{HOMO} ,C-V (PESA) meV	k_2 m^3/s	k_L m^3/s	γ (eV)
PM6:Y6	410	170 (600)	1.4×10^{-17}	5.8×10^{-16}	0.024
PM6:ITIC	70	90 (500)	1.2×10^{-16}	1.7×10^{-16}	0.7
PM6:o-IDTBR	-30	-100 (400)	3.1×10^{-16}	3.2×10^{-16}	0.96

B Supporting Information to Chapter IV. 2

B.1 Materials and Sample Preparation

Materials PM6 (Mn ~100 kg mol^{-1}, PDI ~2.3) and Y6 (1451.94 g mol^{-1}) were both purchased from 1-Material and used without further purification. All used solvents were purchased from Sigma-Aldrich and used as received.

Film Preparation and Treatment Thin films of neat PM6, neat Y6 and a blend of PM6:Y6 (1:1.2 wt%) were spin-coated from CF:CN (0.5 wt%) and o-xylene to obtain ~30 nm thick films on ITO substrates. The solutions were stirred at elevated temperatures (40 °C for CF:CN and 70 °C for o-xylene) to guarantee good solution quality before spin coating under a dry nitrogen atmosphere. All ITO substrates were previously cleaned by ultrasonication in isopropanol and acetone. The samples fabricated with CF:CN were annealed for 10 min at 110 °C under a dry nitrogen atmosphere right after the deposition of the active layer. For the samples fabricated with o-xylene, the active layer solution and substrate were heated up to 100 °C and 110 °C, respectively, prior to spin coating. The deposition of an active layer was conducted with hot solution and hot substrate.

Device Geometry All PM6:Y6 devices were prepared in the same conventional structure (ITO/PEDOT:PSS/PM6:Y6/PDINO/Ag). Patterned ITO substrates (Psiotec, UK) were sonicated in Hellmanex, deionized water, acetone, and isopropanol for 20 min, 20 min, 10 min and 10 min, respectively. The cleaned ITO substrates were then treated with O_2 plasma (200 W, 4 min). Filtered (through 0.2 µm PA filter) PEDOT:PSS (Clevios, AL4083) was spin coated on the plasma treated ITO substrates at 5000 rpm for 30 s under ambient conditions to form the hole transport layer. The PEDOT:PSS layer was then thermally annealed at 150 °C for 25 min. The rest of the fabrication was conducted in a glovebox. The PM6:Y6 active layers made with CF:CN (0.5 wt%) and o-xylene were prepared, deposited, and treated on the top of the PEDOT:PSS layer exactly as described in the film preparation and treatment section. After the deposition and treatment of the active layer, a thin layer of PDINO (~10 nm) was spin coated on the top of the active layer to form the electron transport layer. Silver was then thermally evaporated through a patterned mask on the top of the PDINO layer to complete the devices with a pixel area of 0.06 cm^2.

B.2 Experimental

Electrochemical measurements Cyclic voltammograms were recorded in an electrochemical three-electrode setup under inert conditions. ITO substrates were used as working electrodes against a Pt counter electrode. An AgCl covered Ag wire was used as a pseudo reference electrode in 0.1 M $TBAPF_6$ (electrochemical grade) in MeCN as the standard electrolyte. All potentials were referenced against the Fc/Fc^+ redox couple

(added after the measurements) as the internal standard. The experiments were carried out on a PGSTAT204 potentiostat from Metrohm. The working electrodes were positioned in the beam path of a UV-vis spectrometer to collect the in situ spectral data. The modular diode array spectrometer system from Zeiss was provided with an MCS621 vis II detector and a CLH600 F halogen lamp.

Grazing-incidence wide-angle X-ray scattering (GIWAXS) GIWAXS measurements were performed at the SAXS/WAXS beamline at the Australian Synchrotron. [276] A photon energy of 15 keV was used with 2D scattering patterns recorded using a Pilatus 2M detector. The sample-to-detector-distance was 742 mm calibrated using a silver behenate reference standard. The sample and detector were enclosed in a vacuum chamber to suppress air scatter. Scattering patterns were measured as a function of the angle of incidence, with the bulk-sensitive data acquired with an angle of incidence near the critical angle that maximized scattering intensity from the sample, and the surface-sensitive data acquired below the critical angle. The experimentally determined critical angles range from 0.105° to 0.13°. The difference in these apparent critical angles is within the acceptable range of error, which is defined by the resolution of incident angle alignment with a value of 0.02°. Data reduction and analysis were performed using a modified version of NIKA, [277] implemented in Igor Pro.

Near-edge X-ray absorption fine-structure (NEXAFS) spectroscopy NEXAFS measurements were performed under high vacuum conditions at the Soft X-ray beamline at the Australian Synchrotron.[278] Data were acquired in the partial electron yield (PEY) mode whereby X-ray absorption was detected via the measurement of the energetic photons that were ejected from the sample that were detected by a channeltron detector. Data were calibrated and normalized using the so-called “stable monitor method” that uses an upstream gold mesh to monitor the beam intensity whose response is calibrated by measuring the signal at the sample position with a photodiode. Data analysis was performed in QANT,[279] with further details of data analysis procedures provided elsewhere.[280]

Ultraviolet photoelectron spectroscopy (UPS) All samples were transferred to a UHV system with a base pressure of 10^{-10} mbar without air exposure. A HIS 13 helium discharge lamp from ScientaOmicron equipped with a monochromator was used for excitation, yielding a reduced UV flux and therefore minimum degradation of the samples. The kinetic energy of the emitted photoelectrons was measured using a Specs Phoibos 100 hemispherical analyzer and pass energies of 5 eV or 2 eV for the valence band or the secondary electron cut-off (SECO) spectra, respectively. A bias of -10 V was applied between the sample and the analyzer during SECO measurements. The binding energy axis was calibrated by measuring the Fermi-edge of a polycrystalline gold sample and setting its center to 0 eV. The resolution of the setup in this configuration was 0.15 eV as determined from the width of the Fermi-edge.

B.3 SI Figures

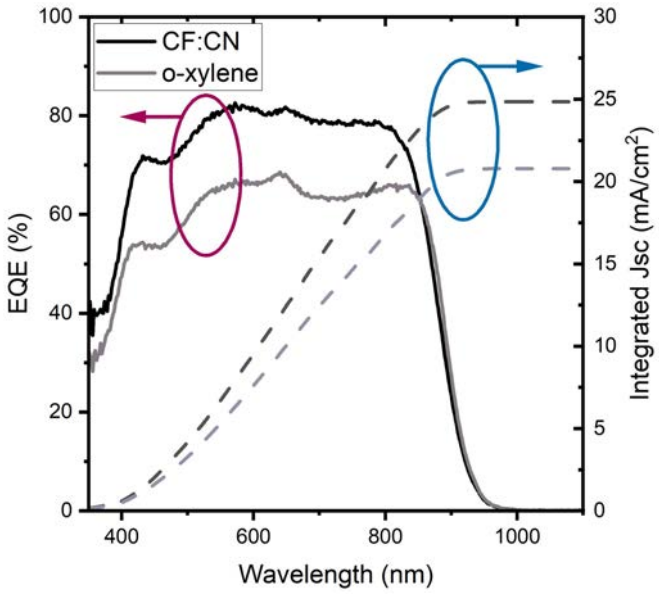

Figure B.1: External quantum efficiency (EQE) spectrum of PM6:Y6 devices fabricated with CF:CN and o-xylene as the solvent for the active layer.

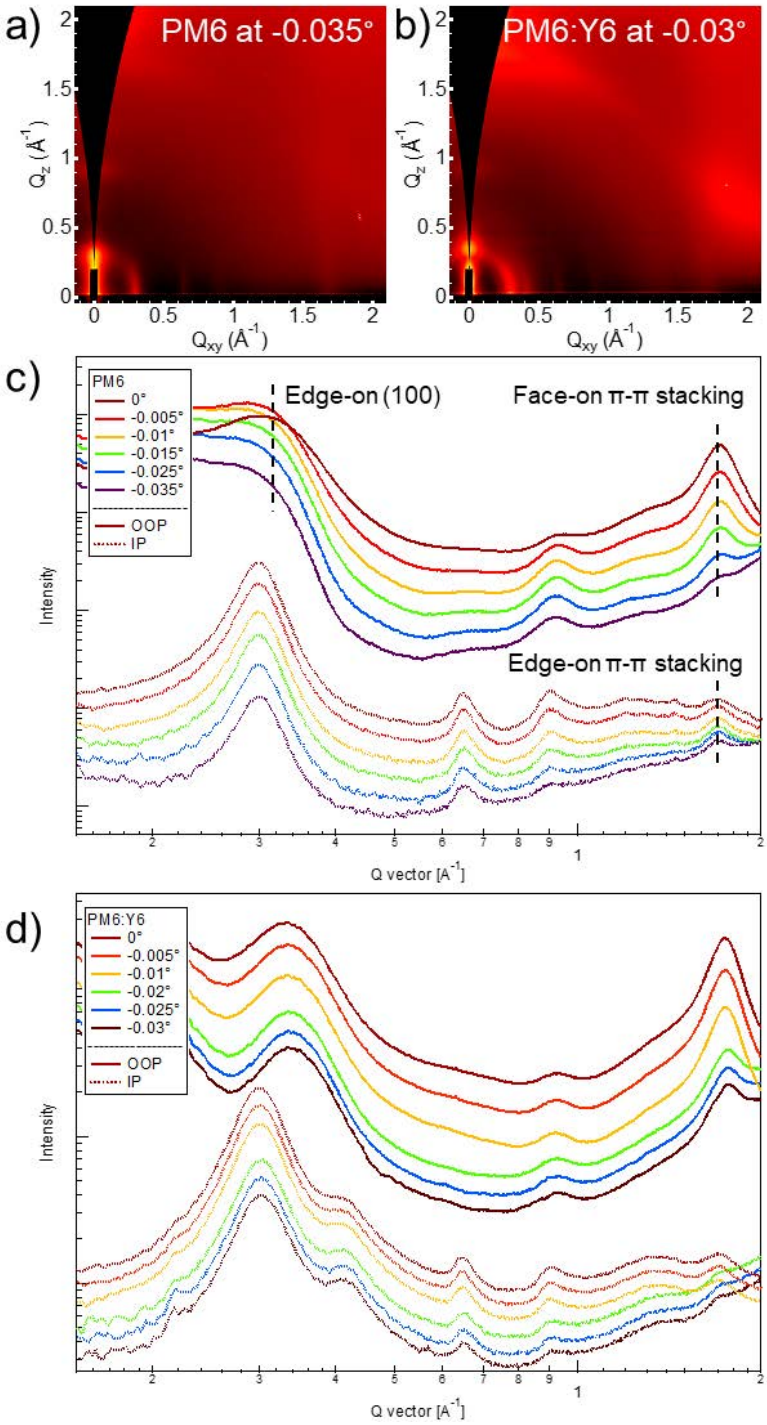

Figure B.2: (a-b) 2D GIWAXS patterns and (c-d) the corresponding incident-angle-dependent 1D plots of neat PM6 films and PM6:Y6 blend films (1:1.2 wt%) spin-coated from CF + 0.5 v% CN solvent system. The angles of incidence are labelled relative to critical angle; the 0° data corresponds to the critical angle whereas negative values refer to measurements below the critical angle. In both neat and blend films, GIWAXS data collected at shallower incident angle observed weaker out-of-plane (OOP) π-π stacking peak relative to OOP (100) lamellar stacking peak and in-plane (IP) π-π stacking peak indicating the improved ratio of edge-on oriented PM6 crystallites, which is consistent with the NEXAFS findings. At -0.03° incident angle, the blend film observes stronger OOP π-π stacking peak than that in the neat film due to the π-π stacking order of face-on oriented Y6 crystallites.

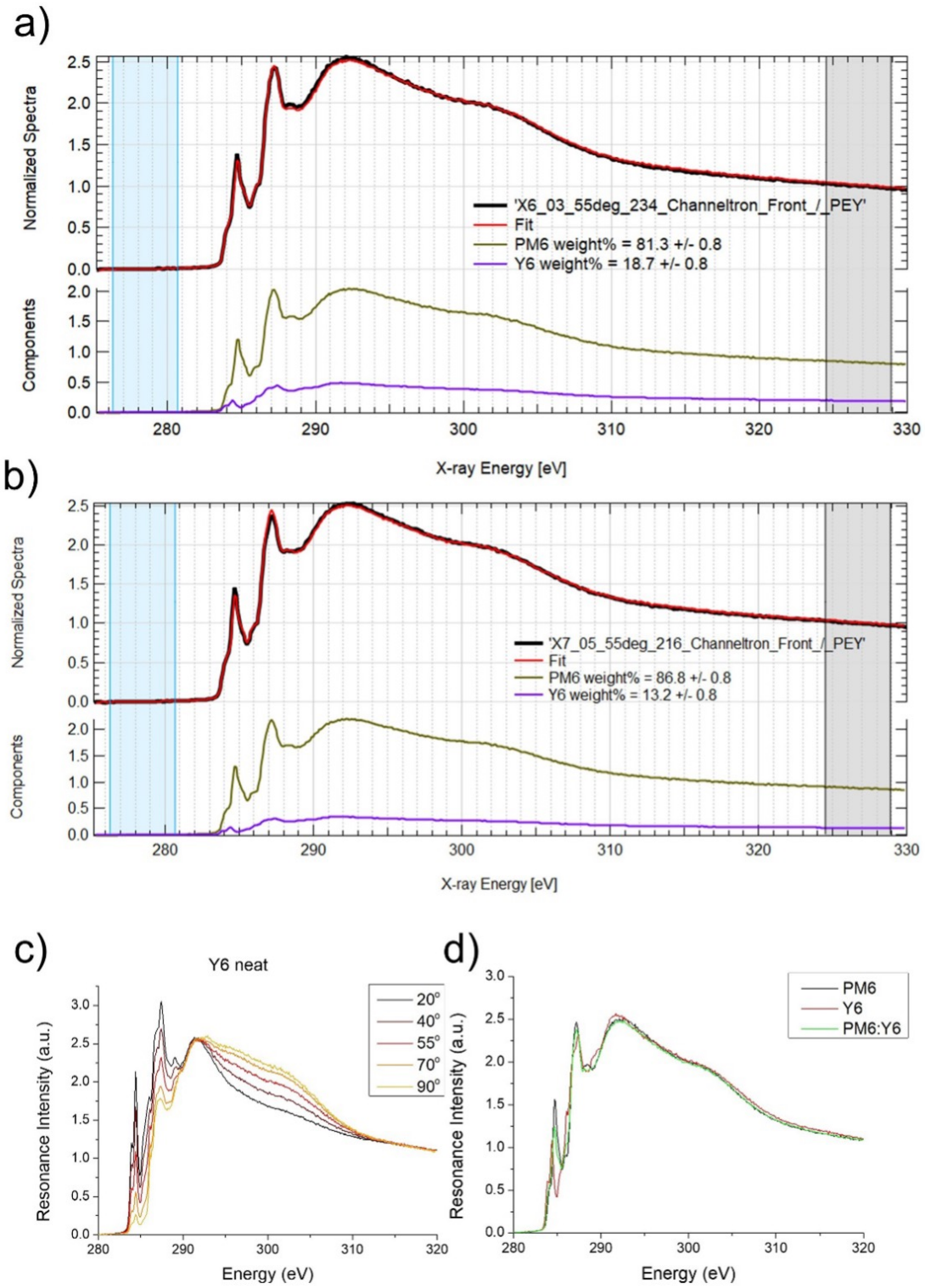

Figure B.3: Angle-resolved NEXAFS spectra of PM6:Y6 blend films (1:1.2 wt%, 30 nm) processed from a) CF:CN (CF + 0.5 v% CN) and b) o-xylene solutions. Spectra of the neat compounds are given in c) and d).

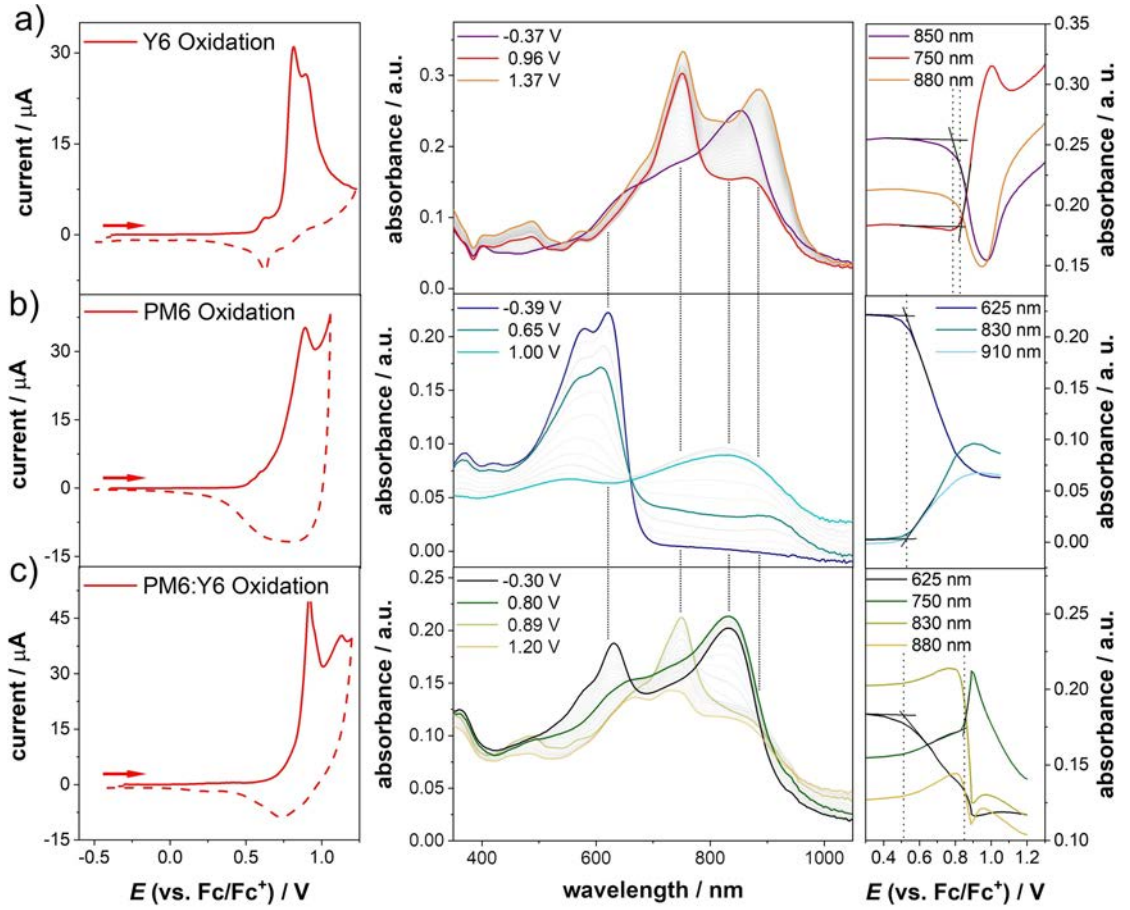

Figure B.4: In situ CV measurements coupled with UV-vis spectroscopy of a) neat Y6, b) neat PM6 and c) a blend of PM6:Y6 (1:1.2 wt%) films, spin coated and annealed from o-xylene solutions. CVs are given on the left, the spectra of the charge half-cycle of the oxidation are presented in the center, completed with peak trends of significant bands on the right side. Spectral onsets of the oxidation are indicated by dotted lines and obtained via tangent method. Underlying CVs (1_{st} cycles) are measured in 0.1 M $TBAPF_6$/MeCN at 20 mVs^{-1} on ITO substrates.

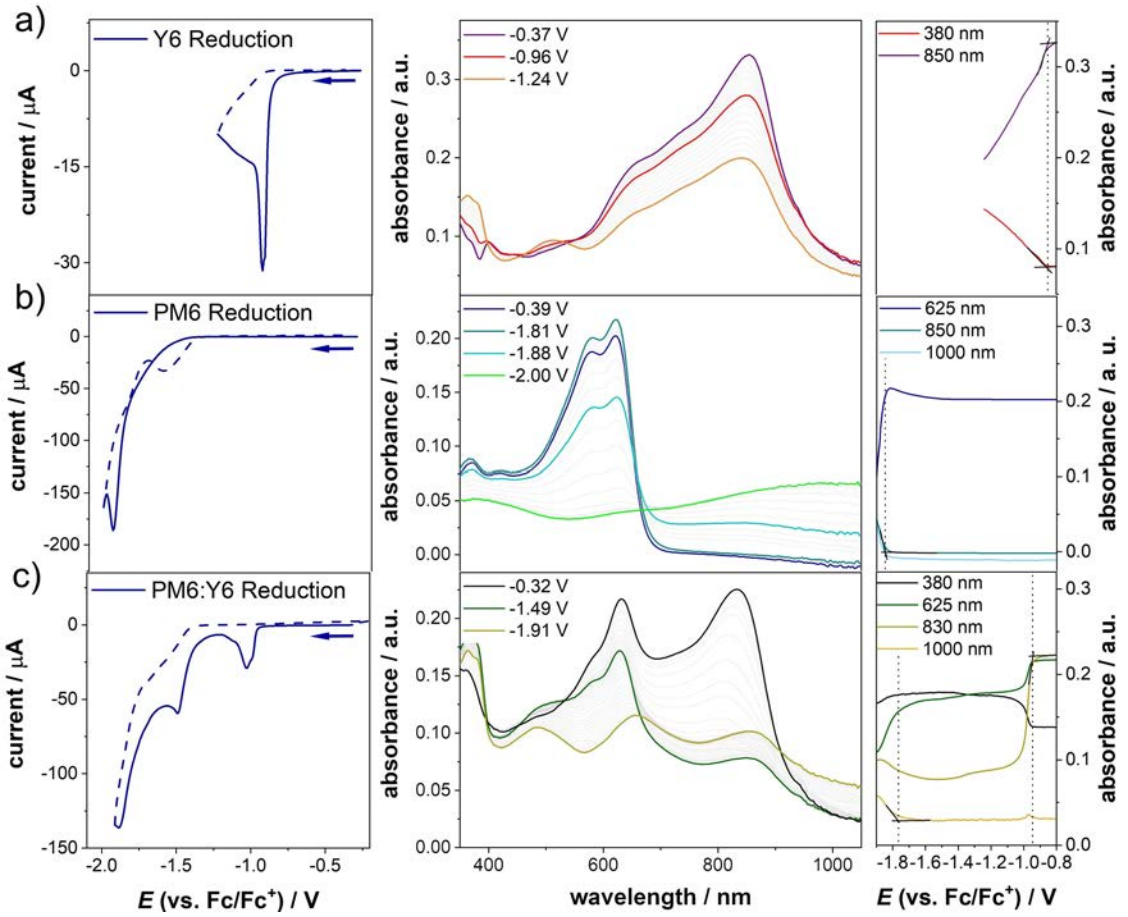

Figure B.5: In situ CV measurements coupled with UV-vis spectroscopy of a) neat Y6, b) neat PM6 and c) a blend of PM6:Y6 (1:1.2 wt%) films, spin coated and annealed from o-xylene solutions. CVs are given on the left, the spectra of the charge half-cycle of the oxidation are presented in the center, completed with peak trends of significant bands on the right side. Spectral onsets of the reduction are indicated by dotted lines and obtained via tangent method. Underlying CVs (1st cycles) are measured in 0.1 M $TBAPF_6$/MeCN at 20 mVs^{-1} on ITO substrates.

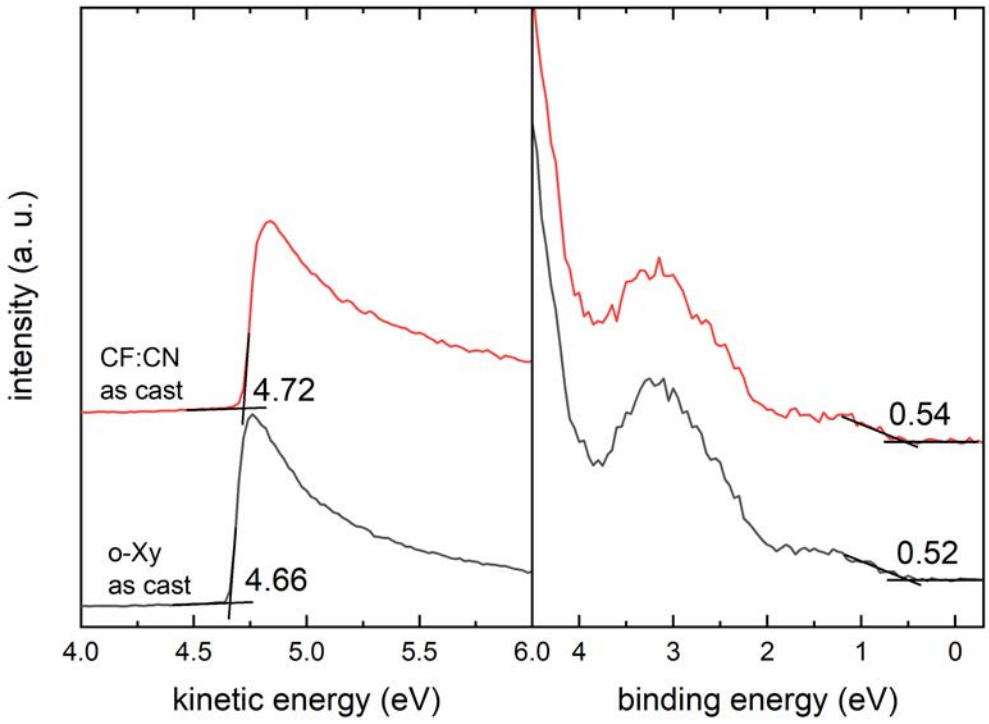

Figure B.6: UPS spectra from PM6:Y6 blend films (1:1.2 wt%) processed from different solvent systems. Secondary electron cut-off (SECO) and valence band spectra of PM6:Y6 blend films prepared from CF:CN (0.5 wt%) and o-xylene.

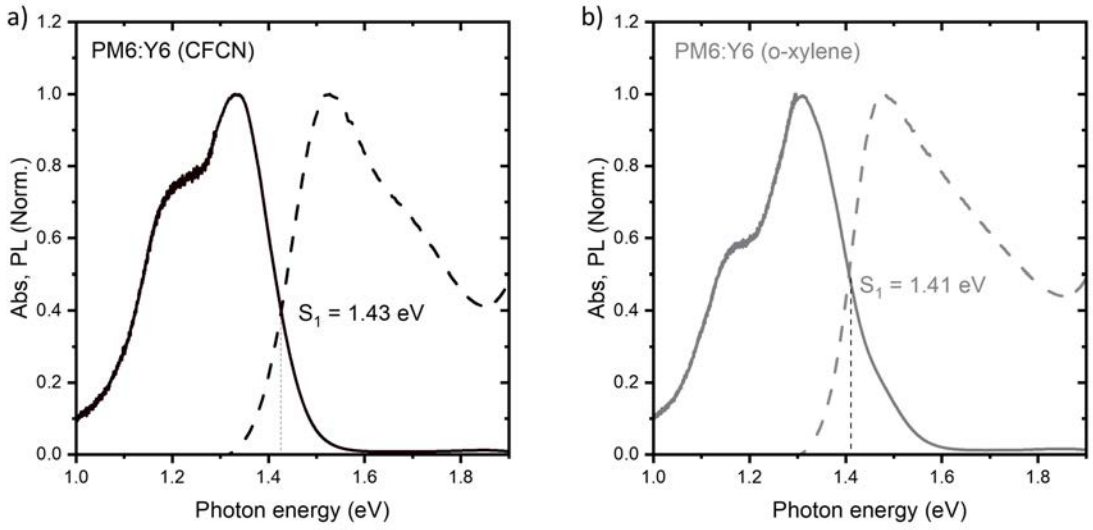

Figure B.7: Normalized absorption and photoluminescence (PL) spectra of PM6:Y6 film fabricated with a) CF:CN and b) o-xylene as the solvent.

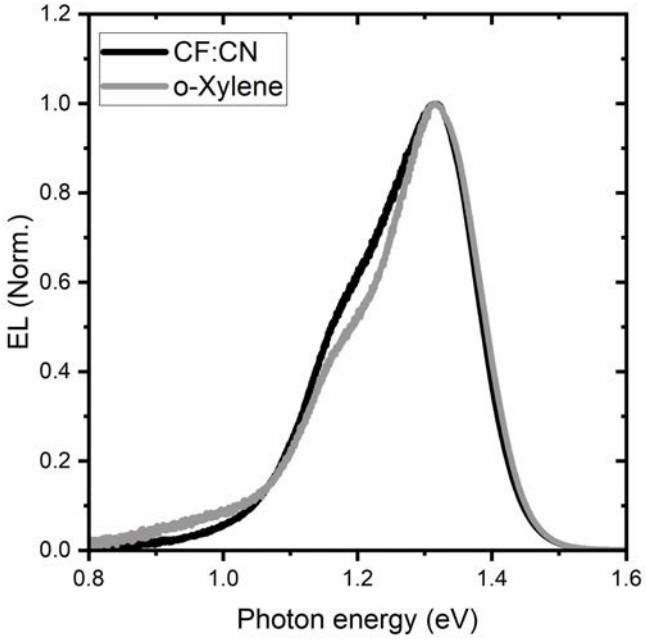

Figure B.8: The normalized electroluminescence (EL) spectra of PM6:Y6 devices fabricated with CF:CN and o-xylene as the solvent for the active layer.

B.4 SI Tables

Table B.1: Published HOMO and LUMO levels of PM6 and Y6 in the literature, determined by various experimental techniques from recent years. Electrochemical band gaps as well as the transport energy is given as well. If known, the correction factor for transferring the CV onset into the energy scale is given in brackets.

PM6			Y6						
HOMO (eV)	LUMO (eV)	E_g^{EC} (eV)	HOMO (eV)	LUMO (eV)	E_g^{EC} (eV)	ΔE_{HOMO} (eV)	E_{tr} (eV)	Method	Ref
-5.30	-3.05	2.25	-5.64	-3.92	1.72	0.34	1.38	SPC	our work
-5.30	-3.06	2.24	-5.63	-3.90	1.73	0.33	1.40	SPC	our work*
-5.56	-3.50	2.06	-5.65	-4.10	1.55	0.09	1.46	CV (4.36 eV) +	[20]
-5.05	-3.59	1.46	-5.61	-4.10	1.51	0.56	0.95	CV (4.73 eV)	[281]
-5.45	-3.20	2.25	-	-	-	-	-	CV (4.8 eV)	[282]
-5.18	-	-	-	-	-	-	-	PESA	[282]
-5.54	-3.65	1.89	-5.62	-4.11	1.51	0.08	1.43	CV	[283]
-5.13	-3.28	-	-5.66	-4.29	-	0.53	0.84	UPS + E_{opt}	[284]
-5.45	-3.65	1.80	-	-	-	-	-	CV (4.71 eV) + E_{opt}	[164]
-5.50	-3.61	1.89	-	-	-	-	-	CV (4.29 eV)	[181]
-5.10	-3.10	-	-5.81	-4.10	-	0.71	1.00	UPS + IEPS	[66]
-5.43	-3.47	1.96	-5.69	-3.96	1.73	0.26	1.47	CV	[172]
-5.53	-	-	-	-3.92	1.73	0.26	1.47	CV	[172]*
-5.50	-3.50	2.00	-	-	-	-	-	CV	[63]
-5.56	-3.48	2.08	-5.67	-4.08	1.59	0.11	1.48	CV (4.44 eV)	[285]
-	-	-	-5.65	-4.10	1.55	-	-	CV	[188]

Table B.2: Voltage losses for PM6:Y6 devices fabricated with different solvents. The ELQY is measured at 1 sun injection condition ($J_{int} = J_{SC,1\ sun}$)

Device	$J_{0,rad}$ (A/m^2)	$V_{OC,rad}$ (V)	V_{OC} (V)	$DV^{nr}_{OC,calc}$ (eV)	ELQY	$DV^{nr}_{OC,meas}$ (eV)
PM6:Y6 (CF:CN)	2.81×10^{-16}	1.070	0.83	0.24	1.85×10^{-5}	0.28
PM6:Y6 (o-xylene)	2.36×10^{-16}	1.071	0.77	0.30	2.36×10^{-5}	0.34

C Supporting Information to Chapter IV. 3

C.1 Materials and Sample Preparation

Device Fabrication The polymer donor PM6 (Poly[(2,6-(4,8-bis(5-(2-ethylhexyl-3-fluoro)thiophen-2-yl)-benzo[1,2-b:4,5-b']dithiophene))-alt-(5,5-(1',3'-di-2-thienyl-5',7'-bis(2-ethylhexyl) benzo [1',2'-c:4',5'c'] dithiophene-4,8-dione)]), small molecular acceptors o-IDTBR ((5Z,5'Z)-5,5'-((7,7'-(4,4,9,9-tetraoctyl-4,9-dihydro-s-indaceno[1,2-b:5,6-b'] dithiophene-2,7-diyl)bis(benzo[c][1,2,5]thiadiazole-7,4-diyl))bis(methanylylidene)) bis(3-ethyl-2-thioxothiazolidin-4-one)), Y5 ((2,2'-((2Z,2'Z)-((12,13-bis(2-ethylhexyl)-3,9-diundecyl-12,13-dihydro[1,2,5]thiadiazolo[3,4e]thieno [2",3":4',5'] thieno[2',3':4,5] pyrrolo[3,2-g] thieno[2',3':4,5]thieno[3,2-b]indole-2,10-diyl)bis(methanylylidene))bis(3-oxo-2,3-dihydro1H-indene-2,1-diylidene))dimalononitrile)), and TPT10 (2,2'- [[12,13-Bis(2-ethylhexyl)-12,13-dihydro-3,9-dinonylbisthieno[2",3":4',5']thieno[2',3':4,5] pyrrolo[3,2-e:2',3'-g][2,1,3]benzothiadiazole-2,10-diyl]bis[methylidyne(5 or 6-bromo-3-oxo-1H-indene-2,1(3H)-diylidene)]]bis[propanedinitrile]), as well as the electron transport material PDINO (3,3'-(1,3,8,10-Tetraoxoanthra[2,1,9-def:6,5,10-d'e'f']diisoquinoline-2,9(1H,3H,8H,10H)-diyl)bis(N,N-dimethylpropan-1-amine oxide)) were all purchased from 1-Material Inc. The hole transport material PEDOT:PSS aqueous solution (Clevios, AL4083). The solvent chloroform ($CHCl_3$) was purchased from Carl Roth and Alfa Aesar, respectively.

All devices were fabricated with a structure of glass/ITO/PEDOT:PSS/active layer/PDINO/Ag. For the device fabrication, patterned ITO substrates (Psiotec, UK) were first sonicated in Hellmanex, deionized water, acetone, and isopropanol one after another for 20 min, 20 min, 10 min and 10 min, respectively. O2 plasma treatment (200 W, 4 min) was performed on the cleaned substrates right after the cleaning procedure. PEDOT:PSS solution was filtered through a 0.45 µm PTFE filter and then spin coated on cleaned ITO substrates with 5000 rpm for 30 s to form a $\sim$35 nm film. The PEDOT:PSS layers were then annealed at 150 °C for 25 min on a hot plate. The rest of the fabrication process was performed in a glovebox. Solutions of PM6:o-IDTBR, PM6:Y5 and PM6:TPT10 were all prepared with a total concentration of 12 mg/ml and with a donor-acceptor weight ratio of 1:1.2. All solutions were stirred at room temperature for 3 hours, then spin coated on the PEDOT:PSS layers with 2000 rpm spin speed to form $\sim$100 nm-thick active layers. PDINO solution was prepared in methanol with the concentration 1 mg/ml and spin coated on top of the active layers to form an electron transport layer of $\sim$10 nm. Afterwards, silver was thermally evaporated through a mask to the top of PDINO as a top contact to complete the device. The size of each pixel was 0.06 cm^2.

All film samples were fabricated by spin coating the neat acceptor or blend solution on glass substrates. The glass substrates were cleaned with the same procedure as that for ITO substrates. All neat acceptor solutions were prepared by dissolving the acceptor molecule in chloroform with the concentration of 14 mg/ml. All blend solutions were

prepared in the same way as described above for the device fabrications. All solutions were stirred at room temperature for 3 hours prior to spin coating.

For time-resolved photoluminescence (TRPL) measurements, blends of polystyrene (PS, purchased from Sigma Aldrich) and acceptors were used, and spin coated on glass substrates. The neat acceptors were blended with polystyrene with a PS-acceptor weight ratio of 1:1.2, and dissolved in chloroform by stirring the solution at room temperature for 3 hours prior to spin coating.

C.2 Experimental

Pulsed PLQY Exciton diffusion lengths of neat films were measured using the pulsed-PLQY technique described in detail elsewhere[41]. The samples were held under a constant flow of nitrogen gas and excited with a ~300 fs, 25 kHz repetition rate laser pulse of wavelength 515 nm (Pharos PHM02-2H-3H). The unfocused beam had a spot size of 1030 µm incident on the sample and is modulated with an acousto-optic modulator at 273 Hz. The photoluminescence is captured on an amplified photodiode (Femto OE-300-Si-30) and the signal is recorded on a lock-in amplifier (Stanford Research Systems SR860) with reference frequency dictated by the acousto-optic modulator. The thickness of each sample was measured via ellipsometry while the absorbed power is measured in situ. To calculate the exciton diffusion length, the capture radius is assumed to be equivalent to the d_{100} spacing determined from GIWAXS.

Resonant soft X-ray scattering (R-SOXS) Films of the PM6:NFA active layers were casted following the aforementioned procedure in the device fabrication section. The thin films were spin casted on Na:PSS/Si substrates then floated off in deionized water onto Si3N4 membranes. RSoXS measurements were conducted at the SST-1 (7-ID-1) beamline of the National Synchrotron Light Source II[269] or at the Advanced Light Source 11.0.1.2 beamline[268]. The data was collected at a resonant X-ray energy (284.5 eV) and a non-resonant energy (270 eV) in a normal transmission geometry to probe the lateral structure. To probe the vertical morphology (Qz component), the films were rotated at 45 degrees then R-SOXS data was collected at the selected X-ray energies. The results of the propping the Q_z component then used to correct for the total scattering intensity by following a previous procedure[139].

Time-resolved photoluminescence (TRPL) The TRPL measurements of the polystyrene (PS):NFA films were performed at low fluence (from 0.6 to 2.5 nJ/cm^2 – at which no fluence dependence was observed) in vacuum using the output of a Modelocked Ti:Sa (Chameleon Ultra I from Coherent) fs laser operating at 80 MHz repetition rate, at 690 nm. The PL of the samples was collected by an optical telescope (consisting of two plano-convex lenses), focused on the slit of a spectrograph (Princeton Instrument Spectra Pro SP2300) and detected with a Streak Camera (Hamamatsu C10910) system, a long-pass filter (700 nm) was used. The data were acquired in photon counting mode using the Streak Camera software (HPDTA) and exported to Origin 2021 for further analysis. The TRPL decays were analysed with a sum of exponentials and the amplitude weighted average lifetime calculated.

Grazing-incidence wide-angle X-ray scattering (GIWAXS) GIWAXS measurements were conducted on samples of neat and blend films that were cast on silicon substrates. The GIWAXS measurements were conducted at the 7.3.3 beamline, Advanced Light Source

(ALS), Berkeley National Lab[267]. The X-ray wavelength was 1.24 Å at an incident angle of 0.2° with respect to the sample surface. A CCD detector was used to collect the scattered photons. Data collected by the CCD then processed and reduced into 1D GIWAXS profiles via Niak software[277].

Atomic force microscopy (AFM) Samples for AFM scanning were prepared similar to the GIWAXS samples. Film roughness was scanned via a Bruker microscope with a SCANASYST-AIR silicon tip on nitride lever with k=0.4 N m^{-1} and fo = 70 kHz. Next, the AFM scans were processed using NanoScope Analysis 3.0 software to extract the root-mean square (RMS) roughness values.

C.3 SI Notes

Note 1. Calculation of optical constants from the transmission and reflection spectra. The optical constants of PM6:o-IDTBR, PM6:Y5, and PM6:TPT10 were obtained from the UV-VIS spectroscopy as described in detail in previous work from Armin and co-workers[259][10]. For each system, two bare films with different thicknesses were spin coated on glass substrates (in the structure of glass/film/glass, the encapsulation was made on the side). The transmission and reflection spectra of both films (from 300 nm to 1600 nm) were then measured via UV-VIS with an integrating sphere. Employing a two-term Cauchy model where n= n_{Cauchy}+ B_{Cauchy}/λ^2 for a global fitting in the UV-VIS spectra of the two films with different thicknesses, the exact thickness of each film as well as the global fitting parameter n_{Cauchy} and B_{Cauchy} can be obtained. Thereafter, an inverse transfer matrix formalism can be performed and the complex refractive index $\overline{n} = n + iK$ can consequently be obtained. This method enables accurate determination of optical constants and is particularly suited for organics and organohalide perovskites.

Note 2. Calculation for $J_{ph,max}$ via optical transfer matrix.

With the knowledge of optical constants in each system, and by defining the device structure as glass/ITO/PEDOT:PSS/active layer/Ag (the ultra-thin organic interlayer PDINO was neglected), an optical transfer matrix calculation can be performed to calculate the energy dissipation of the electromagnetic field at each position in the active layer[122, 286, 287]. Assuming the internal quantum yield of the system being unity, the total exciton generation rate in the active layer and therefore $J_{ph,max}$ can be calculated by integrating the energy dissipation over wavelength and space.

Note 3. Calculation of radiative voltage limit $V_{OC,rad}$ and radiative voltage loss ΔV_{rad}.

To calculate V_{rad}, we first extend the measured EQEPV spectra to low photon energies by applying reciprocity relation from Rau[208].

$$EL(E) = Q_e(E) \cdot \phi_{BB}(E) \cdot \left[exp(\frac{qV_{int}}{k_B T}) - 1 \right] = A \cdot EQE_{PV}(E) \cdot \phi_{BB} \tag{C.1}$$

where E is the photon energy, $\phi_{BB}(E)$ the black body radiation flux, V_{int} the internal voltage which is defined as the quasi-Fermi-level splitting, $Q_e(E)$ is the partial external quantum efficiency which quantitatively equals EQE_{PV} when measured under normal incidence. A is a prefactor.

After obtaining extended EQE_{PV} (E) in the low photon energy range, the radiative dark recombination current $J_{o,rad}$ can be obtained by relating $EQE_{PV}(E)$ and $\phi_{BB}(E)$ together via equation C.2.

$$J_{0,rad} = \int_0^\infty Q_e(E)\phi_{BB}(E)dE = q\int_0^\infty EQE_{PV}(E)\phi_{BB}(E)\,dE \tag{C.2}$$

In the end, the $V_{OC,rad}$ can be obtained by:

$$V_{OC,rad} = \frac{k_B T}{q} ln \frac{J_{ph}}{J_{rad}^0} \tag{C.3}$$

To evaluate ΔV_{rad}, $V_{OC,rad}$ was referred to the photovoltaic bandgap E_g determined from the first derivative of EQE_{PV} spectrum (ΔV_{rad}=E_g-$V_{OC,rad}$)[234].

C.4 SI Figures

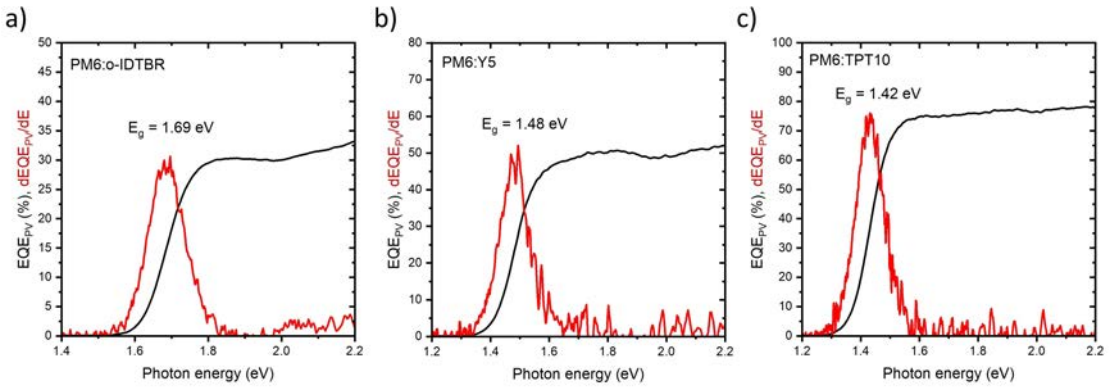

Figure C.1: Photovoltaic bandgap of PM6:o-IDTBR, PM6:Y5, and PM6:TPT10, obtained from the peak of the first derivative of EQE_{PV}.

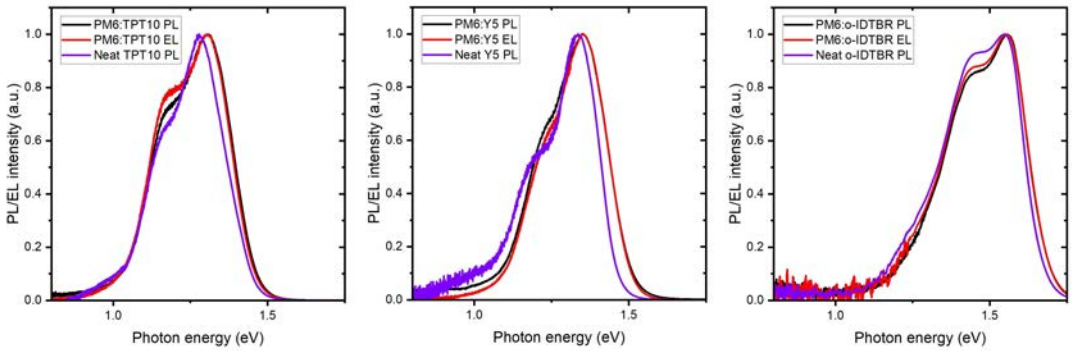

Figure C.2: PL and EL of the blends compared to PL of the neat acceptor. This is due to the strong emission property of the S1 state, when S1 reformation happens, the contribution of CT emission in the PL and EL spectra of the device becomes negligible[25].

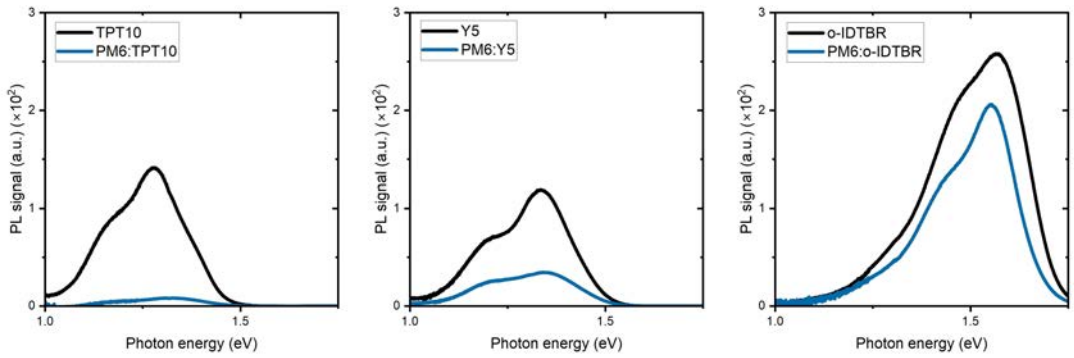

Figure C.3: Comparison of PL emission signal in the PLQY measurement of the neat acceptors and the blends at 1 sun equivalent condition, measured in integrating sphere.

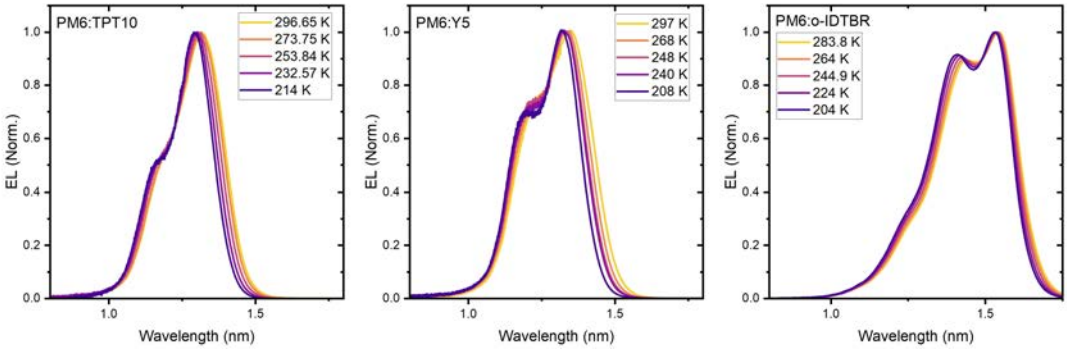

Figure C.4: Normalized temperature dependent EL spectra measured in Cryostat for PM6:o-IDTBR, PM6:Y5 and PM6:TPT10. It is observed that the shape of EL emission spectra does not change in all the three studied systems.

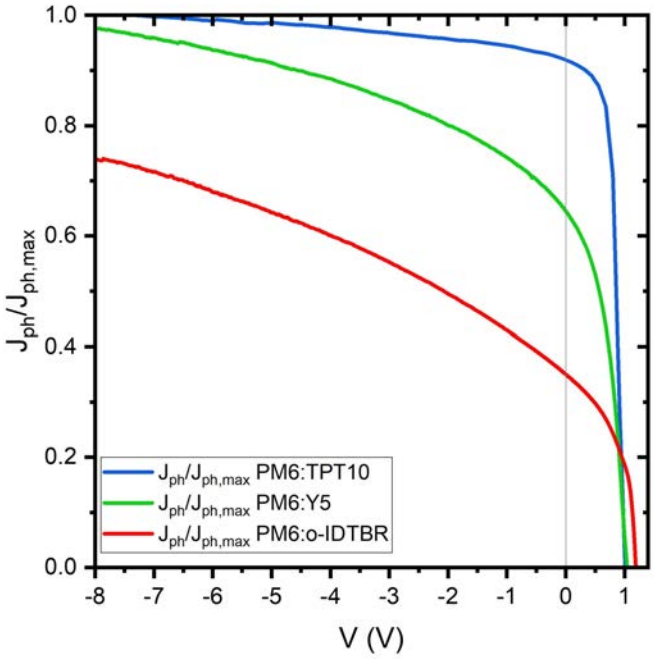

Figure C.5: The ratio of J_{ph} and $J_{ph,max}$ versus applied voltage for PM6:o-IDTBR, PM6:Y5 and PM6:TPT10.

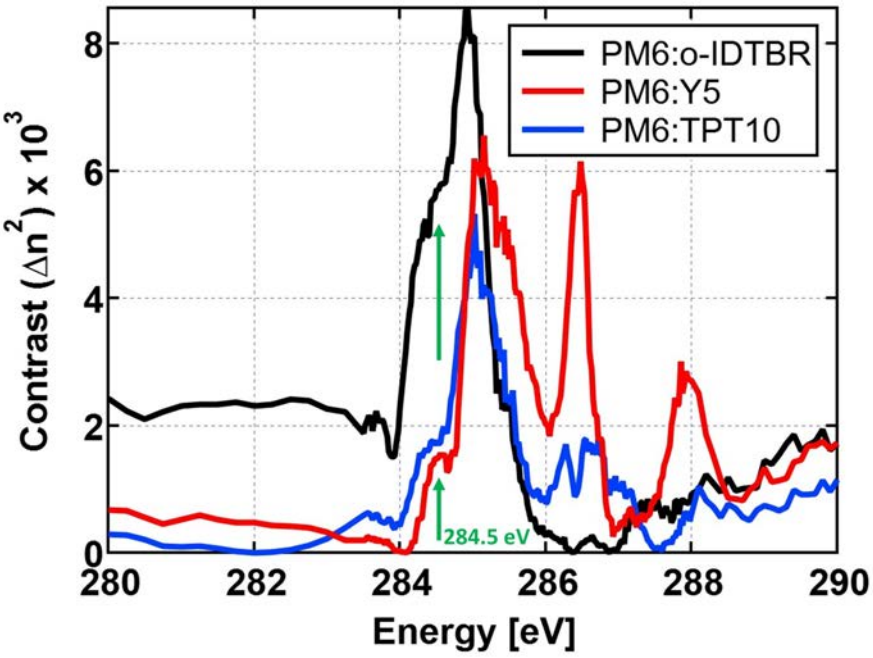

Figure C.6: The X-ray index contrast Δn_2 between the donor and acceptor materials of the investigated OSC systems. The green arrows point to the contrast values at X-ray energy of 284.5 eV, which is the used resonant energy in the R-SOXS experiment.

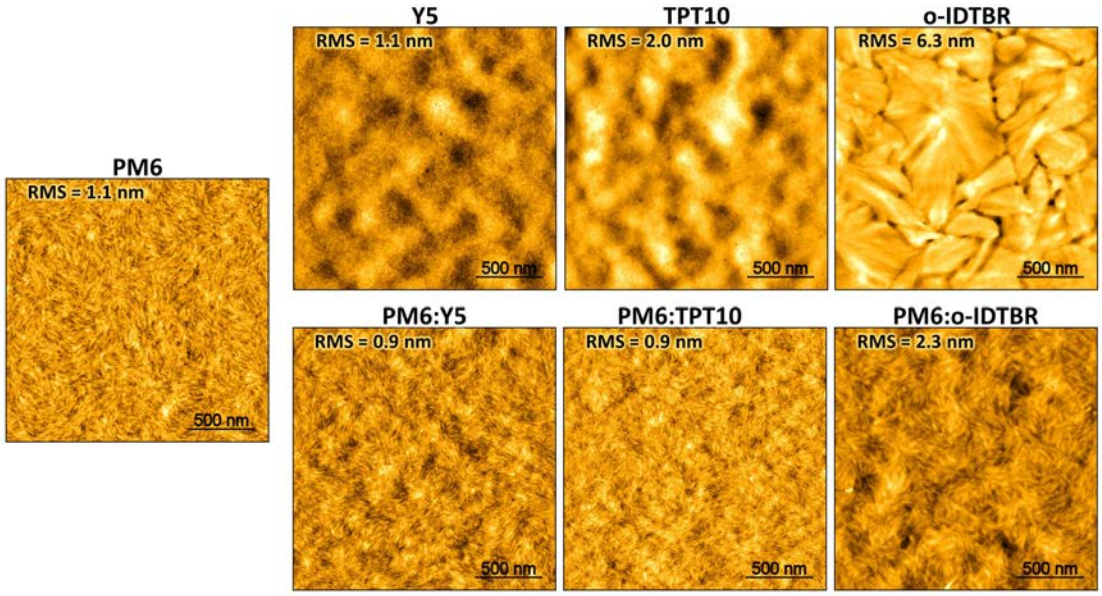

Figure C.7: The AFM scans of neat PM6, Y5, TPT10 and o-IDTBR as well as the blends.

C.5 SI Tables

Table C.1: *J-V* parameters for PM6:o-IDTBR, PM6:Y5, PM6:TPT10 and PM6:Y6.

	V_{OC} (V)	J_{SC} (nm/cm²)	FF	PCE%
PM6:o-IDTBR	1.15	7.80	0.48	4.20
PM6:Y5	0.95	14.78	0.51	7.20
PM6:TPT10	0.91	24.44	0.67	15.10
PM6:Y6	0.84	26.6	0.69	15.40

Table C.2: PLQY of the blends and neat acceptors, ELQY of the blends, and $\eta_{ex,ref}$) in PM6:o-IDTBR, PM6:Y5, PM6:TPT10 and PM6:Y6 chapter [25].

	$PLQY_{blend}$	$PLQY_{acceptor}$	$ELQY_{blend}$	Repopulation (%)
PM6:o-IDTBR	4.15×10^{-2}	6.1×10^{-2}	1.6×10^{-3}	2.5
PM6:Y5	8.0×10^{-3}	2.4×10^{-2}	3.2×10^{-3}	13.3
PM6:TPT10	1.6×10^{-3}	2.7×10^{-2}	7.4×10^{-4}	2.7
PM6:Y6	3.1×10^{-4}	7.0×10^{-3}	2.7×10^{-5}	0.4

Table C.3: V_{OC} loss analysis for each involved systems in this study. The data for PM6:Y6 comes from previous work from our group [25].

	$J_{o,rad}$ (A/m²)	E_g (eV)	$V_{OC,rad}$ (V)	V_{OC} (V)	ΔV_{nr} (V)	E_g-qV_{OC} (eV)
PM6:o-IDTBR	6.95×10^{-21}	1.69	1.31	1.15	0.16	0.54
PM6:Y5	1.83×10^{-17}	1.48	1.13	0.97	0.15	0.51
PM6:TPT10	1.3×10^{-16}	1.42	1.09	0.91	0.19	0.51
PM6:Y6	2.0×10^{-20}	1.38	1.08	0.84	0.27	0.54

D Supporting Information to Chapter IV. 4

D.1 Materials and Sample Preparation

Material The PM6 polymer (Poly[(2,6-(4,8-bis(5-(2-ethylhexyl-3-fluoro)thiophen-2-yl)-benzo[1,2-b:4,5-b']dithiophene))-alt-(5,5-(1',3'-di-2-thienyl-5',7'-bis(2-ethylhexyl)benzo[1',2'-c:4',5'c']dithiophene-4,8-dione)]), small molecule Y6 (2,2'-[[12,13-Bis(2-ethylhexyl)-12,13-dihydro-3,9-diundecylbisthieno[2",3":4',5'] thieno[2',3':4,5]pyrrolo[3,2-e:2',3'-g][2,1,3]benzothiadiazole-2,10-diyl]bis[methylidyne(5,6-difluoro-3-oxo-1H-indene-2,1(3H)diylidene)]]bis[propanedinitrile]) and PDINO (2,9-Bis[3-(dimethyloxidoamino)propyl]anthra[2,1,9-def:6,5,10-d'e'f']diisoquinoline-1,3,8,10(2H,9H)-tetrone) are purchased from 1-Material Inc. The solvent chloroform ($CHCl_3$) and additive 1-Chloronaphthalene (CN) is purchased from Carl Roth and Alfa Aesar, respectively.

Sample Preparation Semitransparent devices are fabricated in a regular configuration and with a structure ITO/PEDOT:PSS/PM6:Y6/PDINO/Ag. The bare films were fabricated on glass substrates with a structure of glass/PM6:Y6/glass. Patterned ITO substrates (Psiotec, UK) and glass substrates were sonicated in Hellmanex, deionized water, acetone, and isopropanol for 20 min, 20 min, 10 min and 10 min, respectively. The cleaned ITO substrates were then treated with O2 plasma at 200 W for 4 min. Subsequently, PEDOT:PSS solution (Clevios, AL4083) was filtered with 0.2 µm PA filter and deposited on ITO substrates via spin coating at 5000 rpm for 30 s in ambient condition and thermal annealed at 150 °C for 25 min. The rest of the procedure was conducted in the glovebox. PM6 and Y6 were blended with 1:1.2 wt. ratio and dissolved in $CHCl_3$ (with 0.5 vl% CN) in the concentration of 12 mg/ml and 25 mg/ml to form the active layer solutions. PDINO was dissolved in methanol with the concentration of 1 mg/ml to form the electron transport layer solution. Then, the PM6:Y6 solutions were deposited onto the PEDOT:PSS layers with different concentrations and spin speeds to form 100 nm, 260 nm, 360 nm and 550 nm active layers. The samples were then thermal annealed at 110 °C for 10 nm. PDINO layers were deposited on PM6:Y6 layers afterwards at 1500 rpm for 40 s. 35 nm of Ag was evaporated on the PDINO layers consequently to complete the devices. Additionally, the active layer solutions were spin coated onto the cleaned glass substrates with the same spin coating conditions as that for device fabrications to form 100 nm, 260 nm, and 360 nm PM6:Y6 films.

D.2 SI Figures

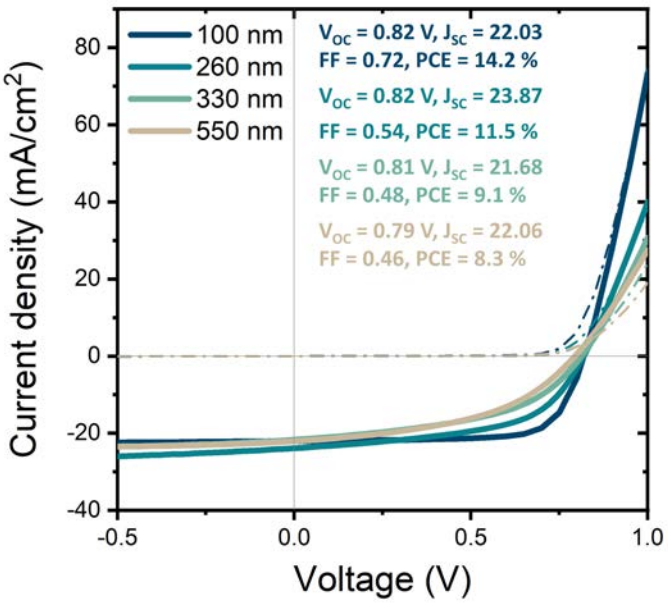

Figure D.1: Current density-voltage (*J-V*) characteristics of the semitransparent devices with various active layer thicknesses (100 nm, 260 nm, 330 nm and 550 nm) under simulated AM1.5G light (solid lines) and in dark condition (dash dot lines).

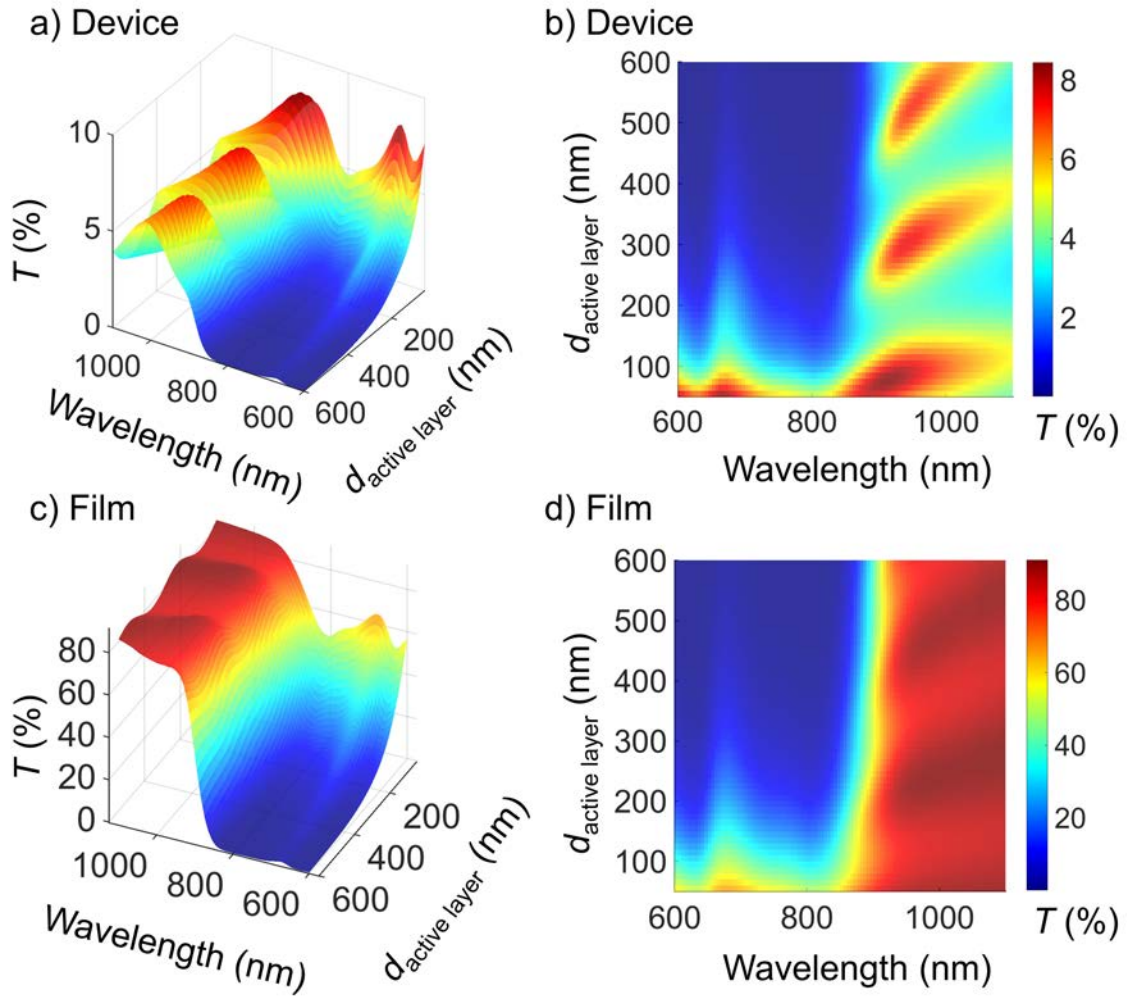

Figure D.2: Computed transmission spectra of glass/ITO/PM6:Y6/Ag/glass junction (a and b) and glass/PM6:Y6/glass (c and d) with active layer thickness varying between 50-600 nm. a and c are the 3D plots showing the evolution of the transmission spectra as active layer thickness varies. b and d are the heatmaps of a and c, respectively. Red color stands for high transmission and blue color for low transmission. The Ag layer is 35 nm.

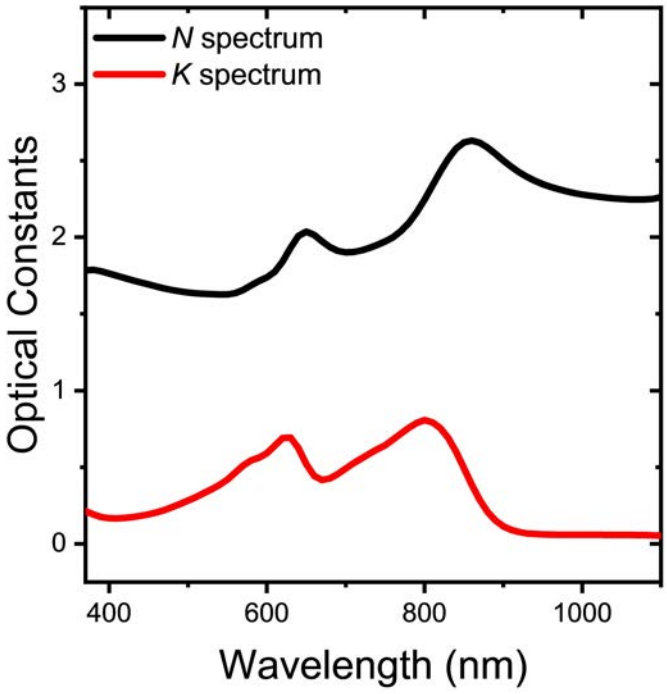

Figure D.3: Ground state optical constants of PM6:Y6 blend (1:1.2 wt. ratio) obtained from the global fitting of the transmission and reflection spectra of an 80 nm and a 110 nm PM6:Y6 bare film via transfer matrix simulation.

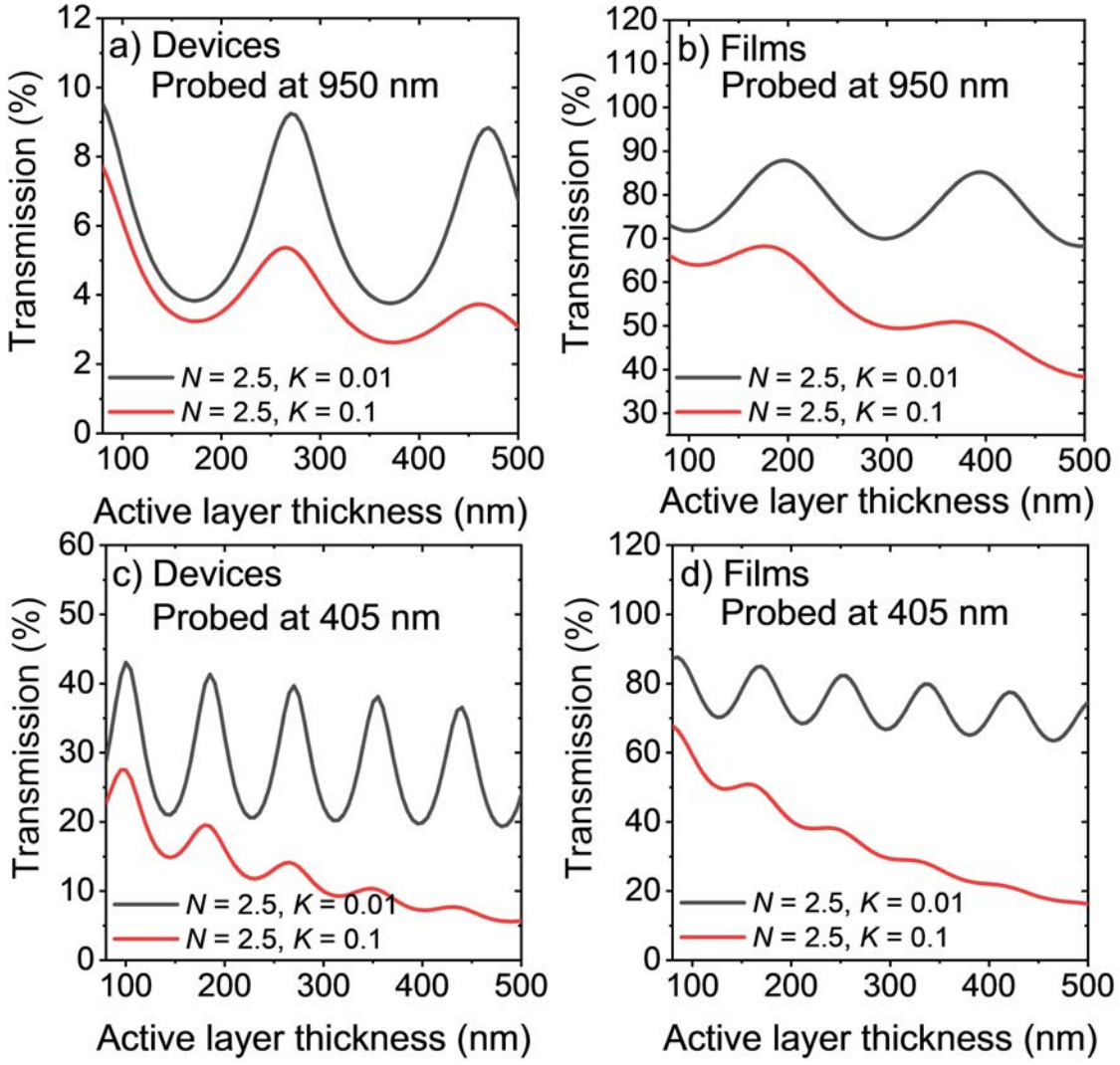

Figure D.4: Transmission of monochromatic light (950 nm and 405 nm) for sample materials with various *N*-*K* values (varying *K*) and thicknesses, and in the stack structure with top contact (glass/sample material/top contact/glass) and without top contact (glass/sample material/-glass). The top contact is 35 nm Ag. It is shown that interference pattern is sensitive to changes in *K*.

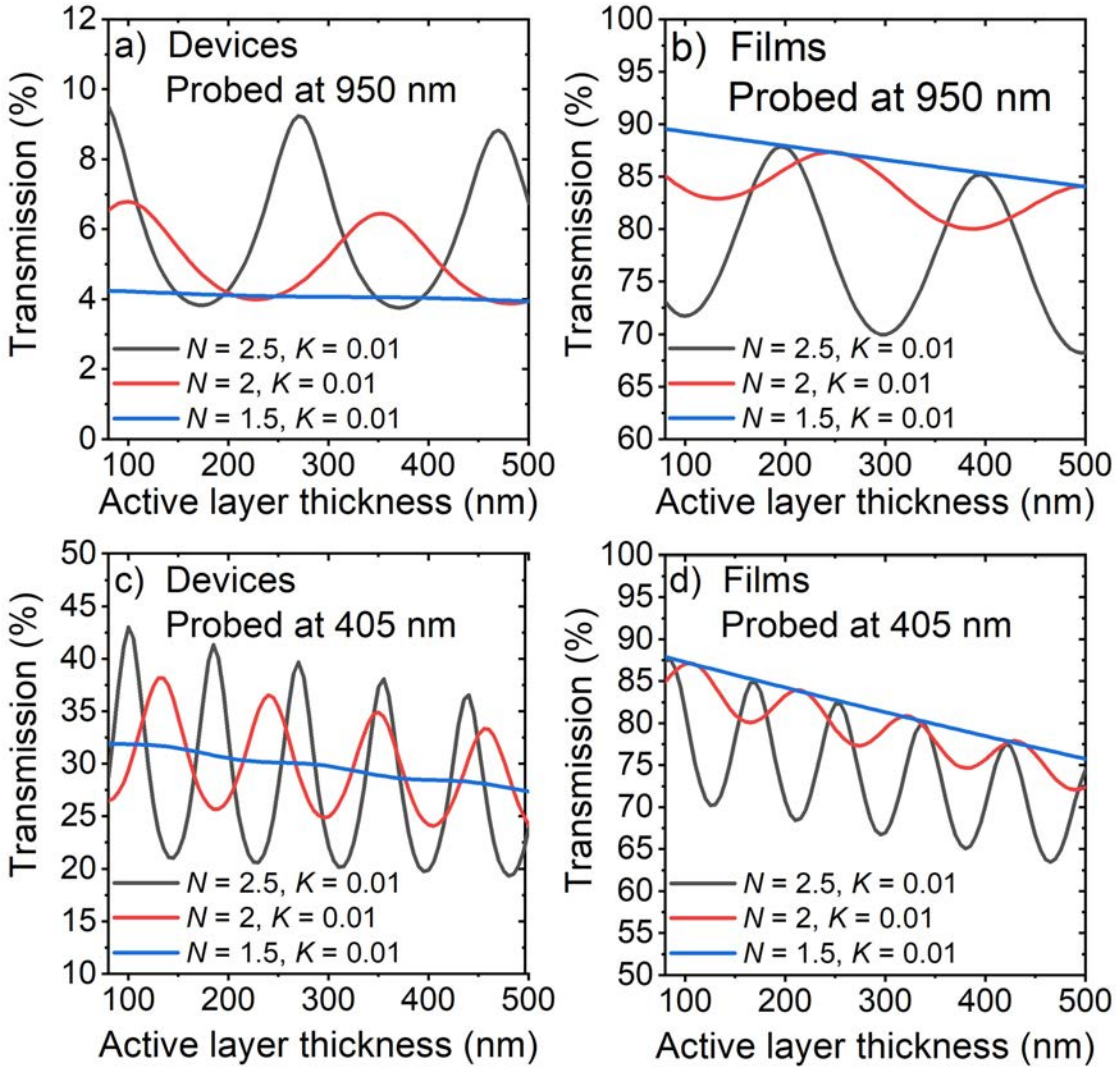

Figure D.5: Transmission of monochromatic light (950 nm and 405 nm) for sample materials with various *N*-*K* values (varying *N*) and thicknesses, and in the stack structure with top contact (glass/sample material/top contact/glass) and without top contact (glass/sample material/glass). The top contact is 35 nm Ag. It is shown that interference pattern is sensitive to changes in *K*.

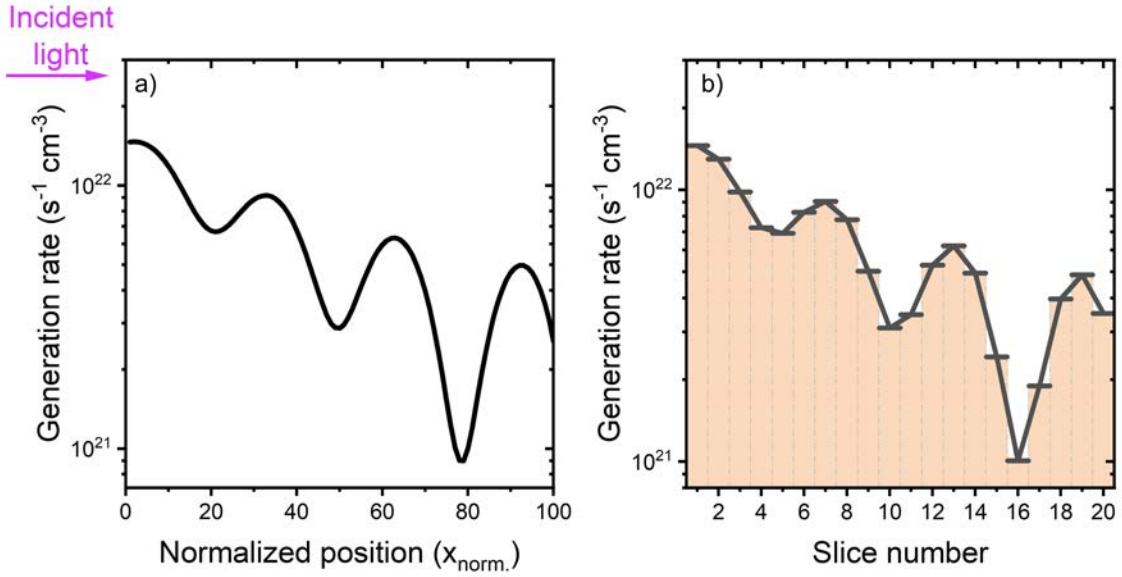

Figure D.6: Translating simulated generation rate profile in the device G (a) into the generation rate in each slice G_s (b) (active layer is sliced into 20 pieces).

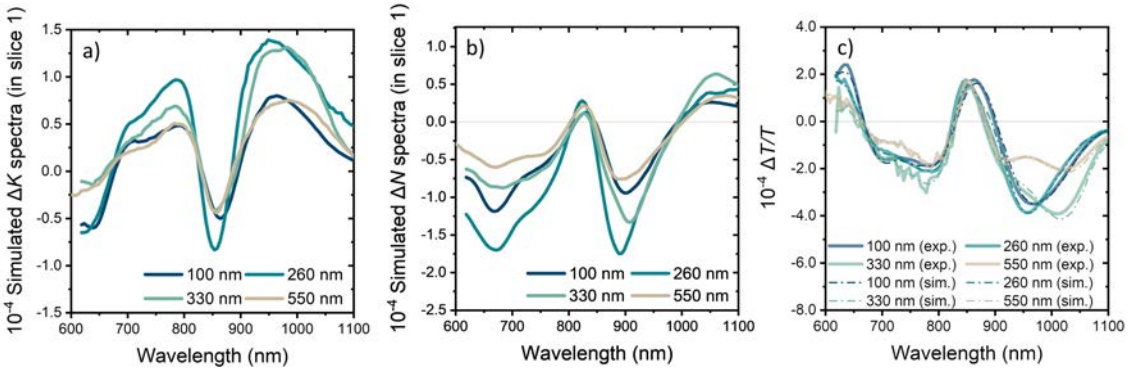

Figure D.7: The ΔK (a) and ΔN (b) simulation results (in the first slice in the active layer) for devices with various active layer thicknesses. c) Comparing the simulated PIA spectra and experimental spectra. The residual sum of squares (RSS) of the fitting for 100 nm, 260 nm, 330 nm and 550 nm experimental data are 2.3×10^{-8}, 2.9×10^{-8}, 6.4×10^{-8} and 3.4×10^{-8}, respectively.

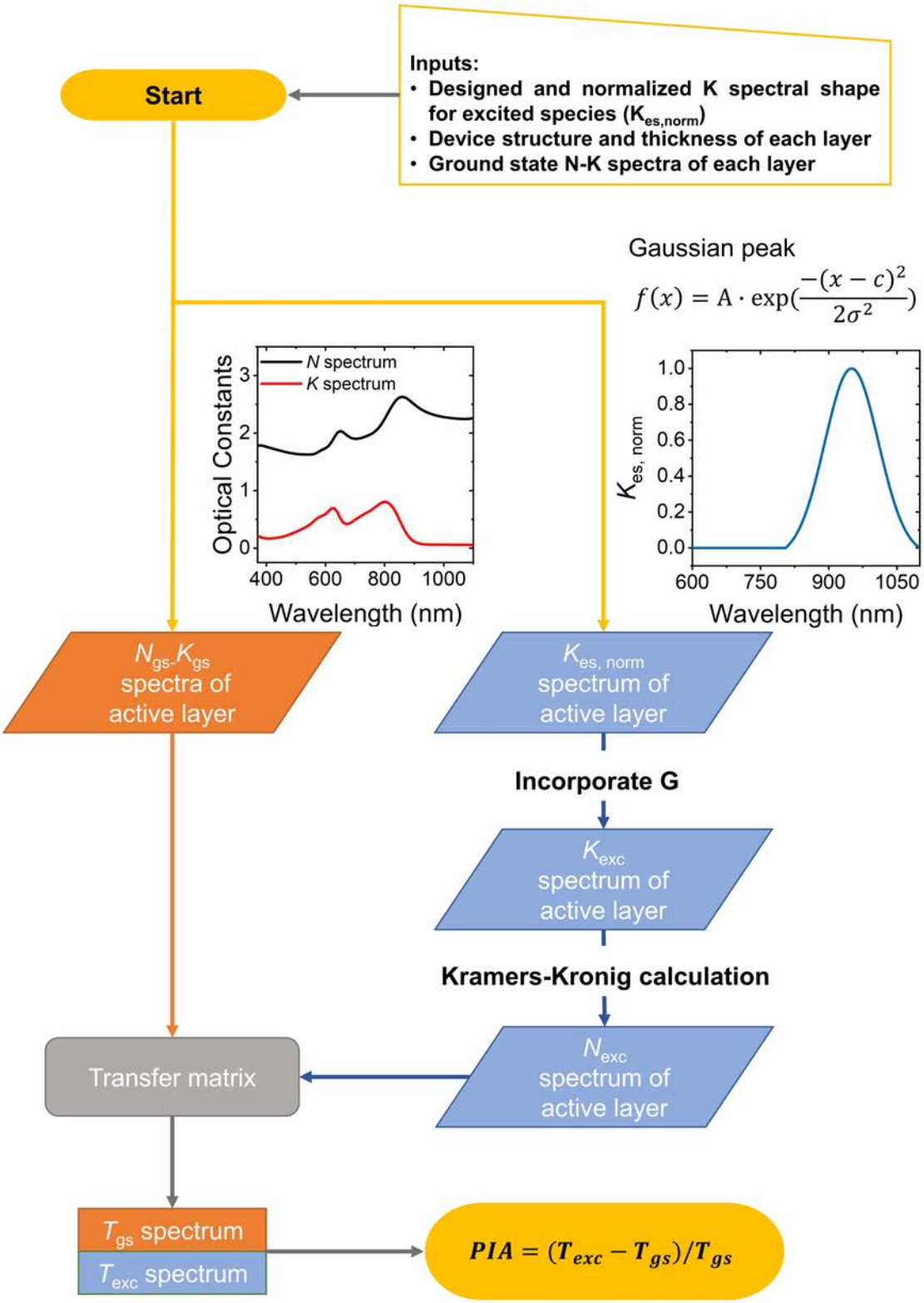

Figure D.8: Flowchart for PIA signal generation for various stack structures and active layer thicknesses with cavity effect considerations. For the simplicity of presenting, only one peak is defined for K_{es} here.

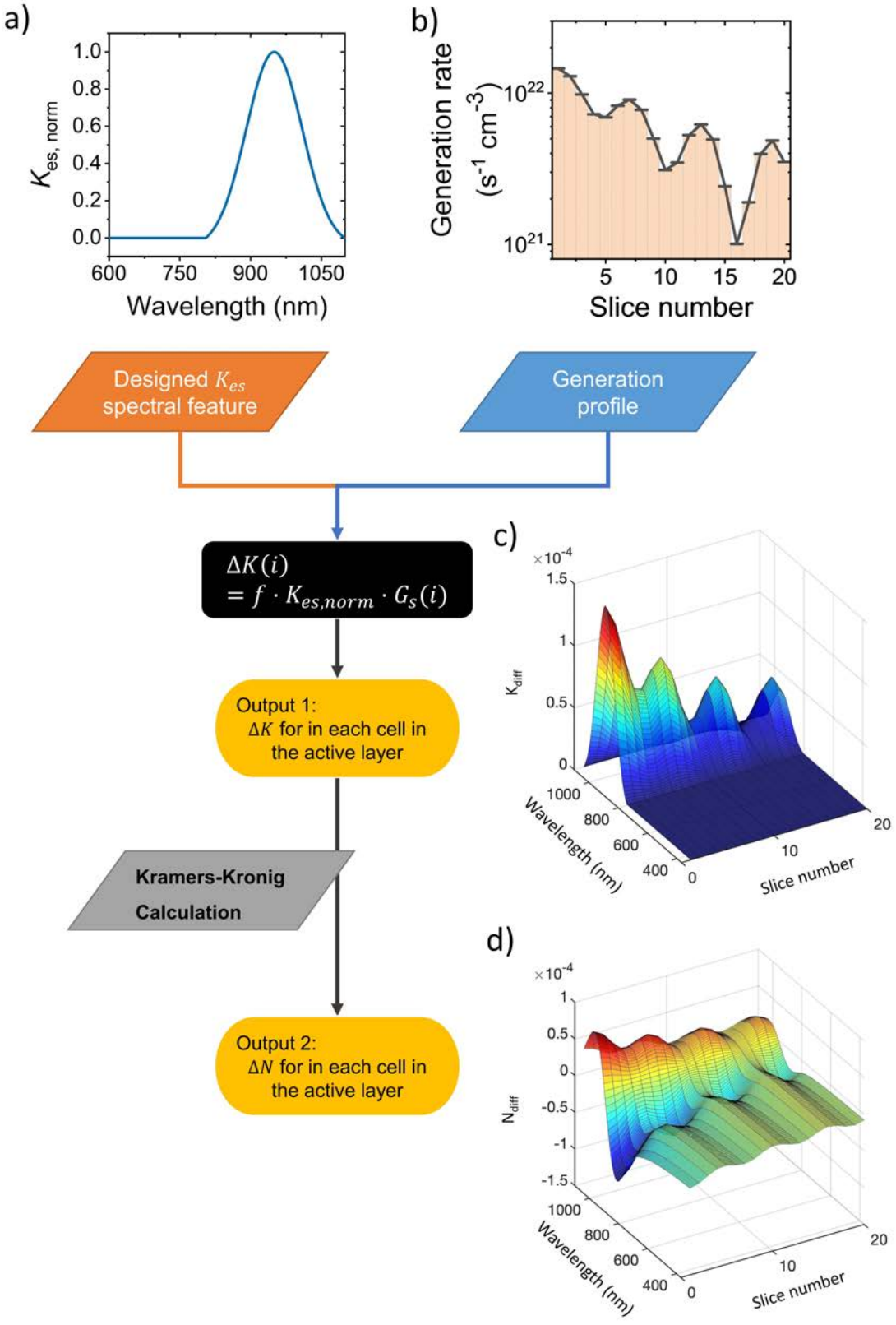

Figure D.9: Flowchart for incorporating generation profile in PIA simulation. a) Designed spectral shape ($K_{es,norm}$) for generated excited species. b) Generation profile in each slice G_x. c) ΔK spectra for each slice in the active layer. d) Δ*N* spectra for each slice in the active layer. The stack structure is glass/ITO/PM6:Y6/Ag/glass, d = 390 nm. For the simplicity of presenting, only one peak is defined for K_{es} here.

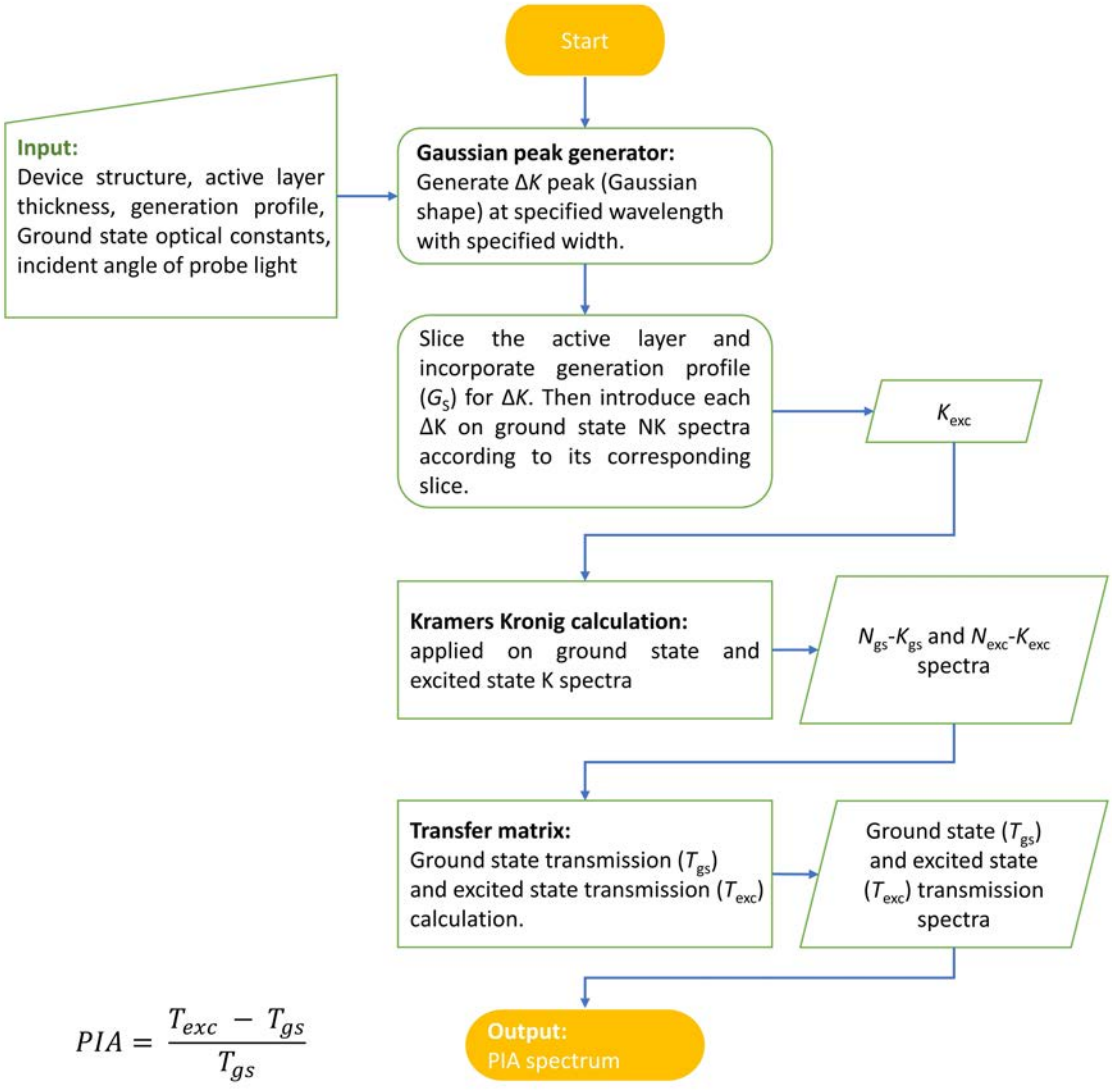

Figure D.10: Flowchart for MATLAB script PIA_generator.

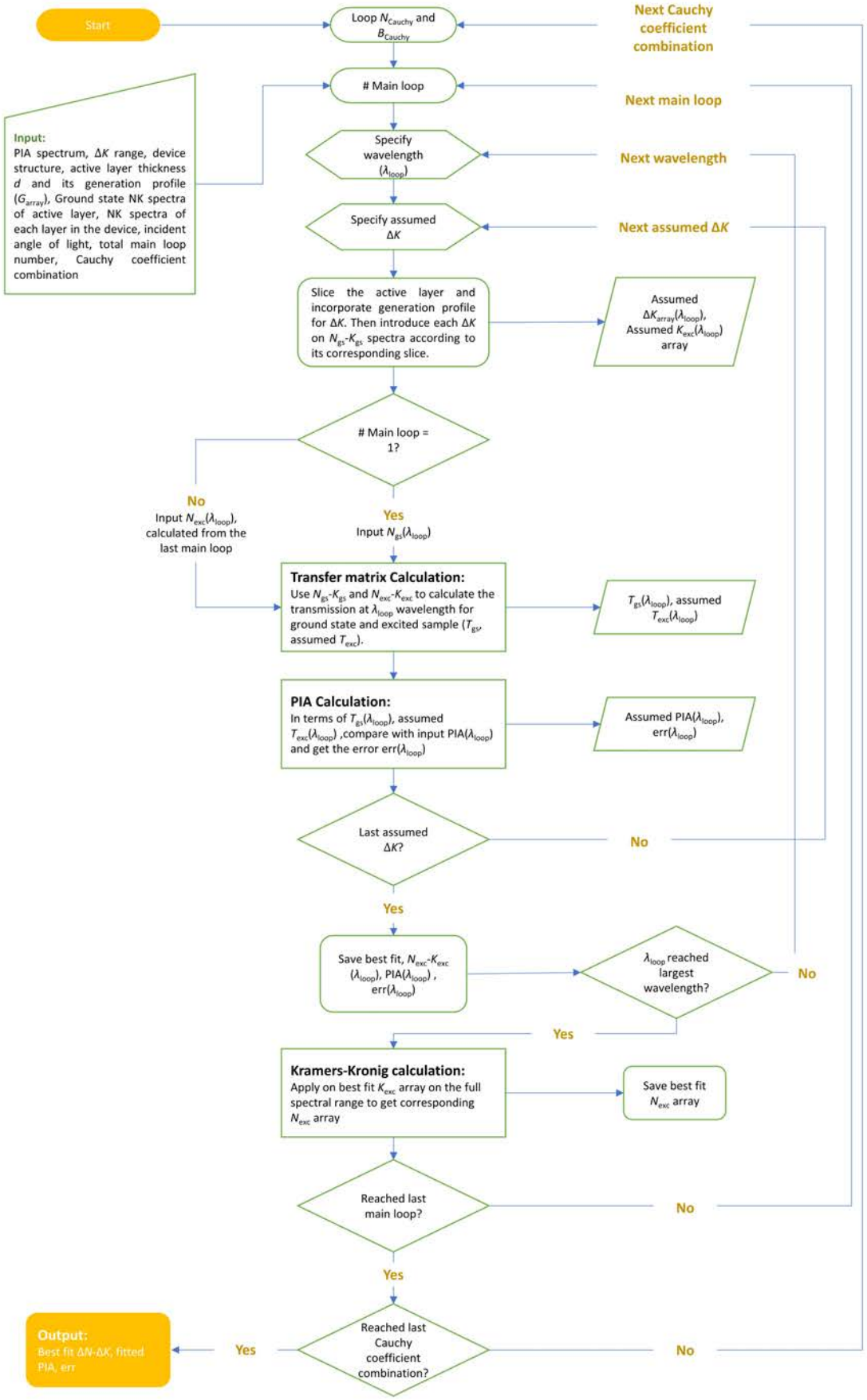

Figure D.11: Flowchart for MATLAB script DeltaNK_simulator.

E List of Symbol

The list of Symbol is summarized in this chapter.

PM6	Poly[(2,6-(4,8-bis(5-(2-ethylhexyl-3-fluoro)thiophen-2-yl)-benzo[1,2-b:4,5-b’] dithiophene))-alt-(5,5-(1’,3’-di-2-thienyl-5’,7’-bis(2-ethylhexyl)benzo[1’,2’-c:4’,5’ -c’]dithiophene-4,8-dione)]
Y5	(2,2’-((2Z,2’Z)-((12,13-bis(2-ethylhexyl)-3,9-diundecyl-12,13-dihydro[1,2,5]thiadi azolo[3,4e]thieno[2”,3”:4’,5’] thieno[2’,3’:4,5]pyrrolo[3,2-g] thieno[2’,3’:4,5]thien o[3,2-b]indole-2,10-diyl)bis(methanylylidene))bis(3-oxo-2,3-dihydro1H-inden e-2,1-diylidene))dimalononitrile)
Y6	2,2’-((2Z,2’Z)-((12,13-bis(2-ethylhexyl)-3,9-diundecyl-12,13-dihydro-[1,2,5]thiadi azolo[3,4-e]thieno[2",3”:4’,5’]thieno[2’,3’:4,5]pyrrolo[3,2-g]thieno[2’,3’:4,5]thien o[3,2-b]indole-2,10-diyl)bis(methanylylidene))bis(5,6-difluoro-3-oxo-2,3-dihy dro-1H-indene-2,1-diylidene))dimalononitrile
TPT10	2,2’- [[12,13-Bis(2-ethylhexyl)-12,13-dihydro-3,9-dinonylbisthieno[2”,3”:4’,5’]thi eno[2’,3’:4,5]pyrrolo[3,2-e:2’,3’-g][2,1,3]benzothiadiazole-2,10-diyl]bis[methylid yne(5 or 6-bromo-3-oxo-1H-indene-2,1(3H)-diylidene)]]bis[propanedinitrile]
o-IDTBR	(5Z,5’Z)-5,5’-((7,7’-(4,4,9,9-tetraoctyl-4,9-dihydro-s-indaceno[1,2-b:5,6-b’]dithi ophene-2,7-diyl)bis(benzo[c][1,2,5]thiadiazole-7,4-diyl))bis(methanylylidene)) bis(3-ethyl-2-thioxothiazolidin-4-one)
ITIC	3,9-bis(2-methylene-(3-(1,1-dicyanomethylene)-indanone))-5,5,11,11-tetrakis(4-hexylphenyl)-dithieno[2,3-d:2’,3’-d’]-s-indaceno[1,2-b:5,6-b’]dithiophene
d	Distance or thickness
q	Elementary charge
ε	Dielectric Constant
c	Speed of light
k_B	Boltzmann constant
$h(\hbar)$	Reduced Planck constant
ϕ_{BB}	Black body photon flux
n	Carrier density
n_e	Electron density
n_h	Hole density
V_{OC}	Open Circuit voltage
V_{bi}	Built-in voltage
V_{pre}	Prebias is TDCF and BACE measurements
V_{coll}	Collection voltage
t_{delay}	Delay time in TDCF measurement
n_{id}	Ideality factor
R_{sh}	Shunt resistance
R_s	Series resistance
J_o	Dark saturation current density
J_{light}	Current density in light condition

J_{dark}	Current density in light condition
J_{SC}	Short-circuit current density
J_{ph}	Photocurrent density
J_{sat}	Saturation current density
J_{gen}	Photo-generation current density
J_{rec}	Recombination current density
J_{inj}	Injection current density
V_{MPP}	Voltage at maximum power point
P_{MPP}	Maximum output power density
P_{out}	Electrical output power density
P_{in}	Input power density of radiation
FF	Fill-factor
E_b	Binding energy
E_{CT}	CT energy
E_t	trap energy
E_{tr}	Transport gap
ΔE_{HOMO}	Energetic offset of the HOMO levels of the donor and acceptor.
$\Delta E_{S_1\text{-}CT}$	Energetic offset between S_1 and CT
E_g^{EC}	Electrochemical band gap
$I_{ph,trans}$	Transient photocurrent
$I_{light,trans}$	Transient current in the light condition
Q_{ph}	Photogenerated charge
δ	Order of recombination
R	Recombination rate of free carriers (band-to-band)
R_{SRH}	SRH recombination rate
C_e/C_h	Capture coefficient for electrons/holes
N_C	Effective density of states for electrons
N_V	Effective density of states for holes
G	Generation rate (if not specified)
$k_{diff,exc}$	Exciton diffusion rate constant
$k_{diss,exc}$	Exciton dissociation rate constant
$k_{f,exc}$	Exciton decay rate constant
$k_{diss,CT}$	CT dissociation rate constant
$k_{f,CT}$	CT decay rate constant
k_{ref}	S_1 reformation rate constant from CT
B	Rate constant of encounter of free charge
k_L	Langevin recombination rate coefficient
k_2	Bimolecular recombination coefficient
k_{eff}	Effective bimolecular recombination coefficient
k_{SRH}	SRH recombination rate coefficient
θ	Recombination-to-extraction parameter
α	Figure-of-merit of solar cell
υ	Drift velocity of charges
μ	Carrier mobility
$D_{e/h}$	Diffusion coefficient for electrons/holes
θ	Energetic disorder
F	Electric field
η_{abs}	Efficiency for light absorption
$\eta_{diff,exc}$	Efficiency for exciton diffusion

$\eta_{\text{diss,exc}}$	Efficiency for exciton dissociation
$\eta_{\text{diss,CT}}$	Efficiency for CT dissociation
η_{coll}	Efficiency for charge collection
$\eta_{\text{quen,exc}}$	Exciton quenching efficiency
N	Refractive index
K	Extinction coefficient
T_{GS}	Transmission spectrum of the ground state material
T_{exc}	Transmission spectrum of the excited material
ΔV_{nr}	Non-radiative voltage loss
T	Temperature or transmission

Bibliography

[1] *IEA, Share of cumulative power capacity by technology, 2010-2027, IEA, Paris https://www.iea.org/data-and-statistics/charts/share-of-cumulative-power-capacity-by-technology-2010-2027, IEA. Licence: CC BY 4.0*.

[2] *IEA (2022), Buildings, IEA, Paris https://www.iea.org/reports/buildings, License: CC BY 4.0*.

[3] J. Jing, S. Dong, K. Zhang, Z. Zhou, Q. Xue, Y. Song, Z. Du, M. Ren, and F. Huang, "Semitransparent Organic Solar Cells with Efficiency Surpassing 15%," Advanced Energy Materials **12**, 2200453 (2022).

[4] J. W. Yoon, H. Bae, J. Yang, J.-W. Ha, C. Lee, J. Lee, S. C. Yoon, H. Choi, and S.-J. Ko, "Semitransparent organic solar cells with light utilization efficiency of 4% using fused-cyclopentadithiophene based near-infrared polymer donor," Chemical Engineering Journal **452**, 139423 (2023).

[5] L. Zhu, M. Zhang, J. Xu, C. Li, J. Yan, G. Zhou, W. Zhong, T. Hao, J. Song, X. Xue, Z. Zhou, R. Zeng, H. Zhu, C.-C. Chen, R. C. I. MacKenzie, Y. Zou, J. Nelson, Y. Zhang, Y. Sun, and F. Liu, "Single-junction organic solar cells with over 19% efficiency enabled by a refined double-fibril network morphology," Nature Materials **21**, 656–663 (2022).

[6] F. Yang, Y. Huang, Y. Li, and Y. Li, "Large-area flexible organic solar cells," npj Flexible Electronics **5**, 30 (2021).

[7] Y. Lin, Y. Firdaus, F. H. Isikgor, M. I. Nugraha, E. Yengel, G. T. Harrison, R. Hallani, A. El-Labban, H. Faber, C. Ma, X. Zheng, A. Subbiah, C. T. Howells, O. M. Bakr, I. McCulloch, S. D. Wolf, L. Tsetseris, and T. D. Anthopoulos, "Self-Assembled Monolayer Enables Hole Transport Layer-Free Organic Solar Cells with 18% Efficiency and Improved Operational Stability," ACS Energy Letters **5**, 2935–2944 (2020).

[8] Y. Cui, H. Yao, J. Zhang, K. Xian, T. Zhang, L. Hong, Y. Wang, Y. Xu, K. Ma, C. An, C. He, Z. Wei, F. Gao, and J. Hou, "Single-Junction Organic Photovoltaic Cells with Approaching 18% Efficiency," Advanced Materials **32**, 1908205 (2020).

[9] A. L. Jones, C. H. Y. Ho, P. R. Riley, I. Angunawela, H. Ade, F. So, and J. R. Reynolds, "Investigating the active layer thickness dependence of non-fullerene organic solar cells based on PM7 derivatives," Journal of Materials Chemistry C **8**, 15459–15469 (2020).

[10] Y. Zheng, J. Huang, G. Wang, J. Kong, D. Huang, M. Mohadjer Beromi, N. Hazari, A. D. Taylor, and J. Yu, "A highly efficient polymer non-fullerene organic solar cell enhanced by introducing a small molecule as a crystallizing-agent," Materials Today **21**, 79–87 (2018).

[11] X. Song, N. Gasparini, and D. Baran, "The Influence of Solvent Additive on Polymer Solar Cells Employing Fullerene and Non-Fullerene Acceptors," Advanced Electronic Materials **4**, 1700358 (2018).

[12] W. Zhu, A. P. Spencer, S. Mukherjee, J. M. Alzola, V. K. Sangwan, S. H. Amsterdam, S. M. Swick, L. O. Jones, M. C. Heiber, A. A. Herzing, G. Li, C. L. Stern, D. M. DeLongchamp, K. L. Kohlstedt, M. C. Hersam, G. C. Schatz, M. R. Wasielewski, L. X. Chen, A. Facchetti, and T. J. Marks, "Crystallography, Morphology, Electronic Structure, and Transport in Non-Fullerene/Non-Indacenodithienothiophene Polymer:Y6 Solar Cells," Journal of the American Chemical Society **142**, 14532–14547 (2020).

[13] S. M. Hosseini, N. Tokmoldin, Y. W. Lee, Y. Zou, H. Y. Woo, D. Neher, and S. Shoaee, "Putting Order into PM6:Y6 Solar Cells to Reduce the Langevin Recombination in 400 nm Thick Junction," Solar RRL **4**, 2000498 (2020).

[14] N. Tokmoldin, S. M. Hosseini, M. Raoufi, L. Q. Phuong, O. J. Sandberg, H. Guan, Y. Zou, D. Neher, and S. Shoaee, "Extraordinarily long diffusion length in PM6:Y6 organic solar cells," Journal of Materials Chemistry A **8**, 7854–7860 (2020).

[15] L. Perdigón-Toro, L. Q. Phuong, F. Eller, G. Freychet, E. Saglamkaya, J. I. Khan, Q. Wei, S. Zeiske, D. Kroh, S. Wedler, A. Köhler, A. Armin, F. Laquai, E. M. Herzig, Y. Zou, S. Shoaee, and D. Neher, "Understanding the Role of Order in Y-Series Non-Fullerene Solar Cells to Realize High Open-Circuit Voltages," Advanced Energy Materials **12**, 2103422 (2022).

[16] L. Q. Phuong, S. M. Hosseini, C. W. Koh, H. Y. Woo, and S. Shoaee, "Measuring Competing Recombination Losses in a Significantly Reduced Langevin System by Steady-State Photoinduced Absorption and Photocurrent Spectroscopy," Journal of Physical Chemistry C **123**, 27417–27422 (2019).

[17] J. A. Moon and J. Tauc, "Interference effects in pump-probe spectroscopy of thin films," Journal of Applied Physics **73**, 4571–4578 (1993).

[18] J. Kniepert, A. Paulke, L. Perdigón-Toro, J. Kurpiers, H. Zhang, F. Gao, J. Yuan, Y. Zou, V. M. Le Corre, L. J. A. Koster, and D. Neher, "Reliability of charge carrier recombination data determined with charge extraction methods," J. Appl. Phys. **126**, 205501 (2019).

[19] M. A. Green, E. D. Dunlop, G. Siefer, M. Yoshita, N. Kopidakis, K. Bothe, and X. Hao, "Solar cell efficiency tables (Version 61)," Progress in Photovoltaics: Research and Applications **31**, 3–16 (2023).

[20] J. Yuan, Y. Zhang, L. Zhou, G. Zhang, H.-L. L. Yip, T.-K. K. Lau, X. Lu, C. Zhu, H. Peng, P. A. Johnson, M. Leclerc, Y. Cao, J. Ulanski, Y. Li, and Y. Zou, "Single-Junction Organic Solar Cell with over 15% Efficiency Using Fused-Ring Acceptor with Electron-Deficient Core," Joule **3**, 1140–1151 (2019).

[21] S. Chen, Y. Wang, L. Zhang, J. Zhao, Y. Chen, D. Zhu, H. Yao, G. Zhang, W. Ma, R. H. Friend, P. C. Chow, F. Gao, and H. Yan, "Efficient Nonfullerene Organic Solar Cells with Small Driving Forces for Both Hole and Electron Transfer," Advanced Materials **30**, 10.1002/adma.201804215 (2018).

[22] Y. Zhong, M. Causa', G. J. Moore, P. Krauspe, B. Xiao, F. Günther, J. Kublitski, R. Shivhare, J. Benduhn, E. BarOr, S. Mukherjee, K. M. Yallum, J. Réhault, S. C. B. Mannsfeld, D. Neher, L. J. Richter, D. M. DeLongchamp, F. Ortmann, K. Vandewal, E. Zhou, and N. Banerji, "Sub-picosecond charge-transfer at near-zero driving force in polymer:non-fullerene acceptor blends and bilayers," Nature Communications **11**, 833 (2020).

[23] S. Li, C.-Z. Li, M. Shi, and H. Chen, "New Phase for Organic Solar Cell Research: Emergence of Y-Series Electron Acceptors and Their Perspectives," ACS Energy Letters **5**, 1554–1567 (2020).

[24] A. Armin, W. Li, O. J. Sandberg, Z. Xiao, L. Ding, J. Nelson, D. Neher, K. Vandewal, S. Shoaee, T. Wang, H. Ade, T. Heumüller, C. Brabec, and P. Meredith, "A History and Perspective of Non-Fullerene Electron Acceptors for Organic Solar Cells," Advanced Energy Materials **11**, 2003570 (2021).

[25] L. Perdigón-Toro, L. Q. Phuong, S. Zeiske, K. Vandewal, A. Armin, S. Shoaee, and D. Neher, "Excitons Dominate the Emission from PM6:Y6 Solar Cells, but This Does Not Help the Open-Circuit Voltage of the Device," ACS Energy Letters **6**, 557–564 (2021).

[26] S. S. Li, "Classification of solids and crystal structure," in *Semiconductor physical electronics*, edited by S. S. Li (Springer New York, New York, NY, 2006), pp. 1–25.

[27] A. Köhler and H. Bässler, *Electronic Processes in Organic Semiconductors* (2015).

[28] S. Sze and K. K. Ng, "Thyristors and Power Devices," in *Phys. semicond. devices* (John Wiley & Sons, Inc., Hoboken, NJ, USA, Apr. 2006), pp. 548–598.

[29] W. Tress, "The device physics of organic solar cells," PhD thesis (Technical University of Dresden, 2011).

[30] H. I. Afridi, T. G. Kazi, A. G. Kazi, F. Shah, S. K. Wadhwa, N. F. Kolachi, A. Q. Shah, J. A. Baig, and N. Kazi, "Levels of Arsenic, Cadmium, Lead, Manganese and Zinc in Biological Samples of Paralysed Steel Mill Workers with Related to Controls," Biol. Trace Elem. Res. **144**, 164–182 (2011).

[31] S. Sze and K. K. Ng, "Physics and Properties of Semiconductors-A Review," in *Physics of semiconductor devices* (John Wiley & Sons, Inc., Hoboken, NJ, USA, 2006), pp. 5–75.

[32] N. Ueno, "Electronic Structure of Molecular Solids: Bridge to the Electrical Conduction," in *Physics of organic semiconductors: second edition* (Wiley, 2013), pp. 65–89.

[33] T. J. Dawidczyk, H. Kong, and H. E. Katz, "Organic semiconductors (OSCs) for electronic chemical sensors," in *Handbook of organic materials for optical and (opto)electronic devices: properties and applications* (Elsevier, 2013), pp. 577–596.

[34] V. Coropceanu, J. Cornil, D. A. da Silva Filho, Y. Olivier, R. Silbey, and J. L. Brédas, *Charge transport in organic semiconductors*, 2007.

[35] W. Brütting, *Physics of Organic Semiconductors*, edited by W. Brütting (Wiley, 2005), pp. 1–536.

[36] C. A. Gueymard, D. Myers, and K. Emery, "Proposed reference irradiance spectra for solar energy systems testing," Solar Energy **73**, 443–467 (2002).

[37] W. Tress, A. Merten, M. Furno, M. Hein, K. Leo, and M. Riede, "Correlation of Absorption Profile and Fill Factor in Organic Solar Cells: The Role of Mobility Imbalance," Advanced Energy Materials **3**, 631–638 (2013).

[38] B. Lüssem, M. Riede, and K. Leo, "Doping of Organic Semiconductors," in *Physics of organic semiconductors* (Wiley, 2012), pp. 425–496.

[39] K. W. Böer and U. W. Pohl, "Excitons," in *Semiconductor physics* (Springer International Publishing, Cham, 2015), pp. 1–41.

[40] H. Ibach and H. Lüth, "Dielectric Properties of Materials," in *Solid-state physics* (Springer Berlin Heidelberg, Berlin, Heidelberg, 2009), pp. 371–418.

[41] D. B. Riley, O. J. Sandberg, W. Li, P. Meredith, and A. Armin, "Quasi-Steady-State Measurement of Exciton Diffusion Lengths in Organic Semiconductors," Physical Review Applied **17**, 024076 (2022).

[42] A. Classen, C. L. Chochos, L. Lüer, V. G. Gregoriou, J. Wortmann, A. Osvet, K. Forberich, I. McCulloch, T. Heumüller, and C. J. Brabec, "The role of exciton lifetime for charge generation in organic solar cells at negligible energy-level offsets," Nature Energy **5**, 711–719 (2020).

[43] S. D. Dimitrov, B. C. Schroeder, C. B. Nielsen, H. Bronstein, Z. Fei, I. McCulloch, M. Heeney, and J. R. Durrant, "Singlet exciton lifetimes in conjugated polymer films for organic solar cells," Polymers **8**, 14 (2016).

[44] L. J. A. Koster, S. E. Shaheen, and J. C. Hummelen, "Pathways to a New Efficiency Regime for Organic Solar Cells," Advanced Energy Materials **2**, 1246–1253 (2012).

[45] R. A. Marcus and N. Sutin, "Electron transfers in chemistry and biology," Biochimica et Biophysica Acta (BBA) - Reviews on Bioenergetics **811**, 265–322 (1985).

[46] Y. Yi, V. Coropceanu, and J.-L. Brédas, "A comparative theoretical study of exciton-dissociation and charge-recombination processes in oligothiophene/fullerene and oligothiophene/perylenediimide complexes for organic solar cells," Journal of Materials Chemistry **21**, 1479 (2011).

[47] T. Liu and A. Troisi, "Absolute Rate of Charge Separation and Recombination in a Molecular Model of the P3HT/PCBM Interface," The Journal of Physical Chemistry C **115**, 2406–2415 (2011).

[48] K. Thomas, "Generalized detailed balance theory of solar cells," PhD thesis (Forschungszentrum Jülich GmbH, 2009).

[49] W. Li, S. Zeiske, O. J. Sandberg, D. B. Riley, P. Meredith, and A. Armin, "Organic solar cells with near-unity charge generation yield," Energy and Environmental Science **14**, 6484–6493 (2021).

[50] L. Perdigón-Toro, H. Zhang, A. Markina, J. Yuan, S. M. Hosseini, C. M. Wolff, G. Zuo, M. Stolterfoht, Y. Zou, F. Gao, D. Andrienko, S. Shoaee, and D. Neher, "Barrierless Free Charge Generation in the High-Performance PM6:Y6 Bulk Heterojunction Non-Fullerene Solar Cell," Advanced Materials **32**, 1906763 (2020).

[51] C. Poelking and D. Andrienko, "Design Rules for Organic Donor–Acceptor Heterojunctions: Pathway for Charge Splitting and Detrapping," Journal of the American Chemical Society **137**, 6320–6326 (2015).

[52] S. Verlaak, D. Beljonne, D. Cheyns, C. Rolin, M. Linares, F. Castet, J. Cornil, and P. Heremans, "Electronic structure and geminate pair energetics at organic-organic interfaces: the case of pentacene/ C60 heterojunctions," Advanced Functional Materials **19**, 3809–3814 (2009).

[53] B. A. Gregg, "Entropy of Charge Separation in Organic Photovoltaic Cells: The Benefit of Higher Dimensionality," The Journal of Physical Chemistry Letters **2**, 3013–3015 (2011).

[54] S. N. Hood and I. Kassal, "Entropy and Disorder Enable Charge Separation in Organic Solar Cells," The Journal of Physical Chemistry Letters **7**, 4495–4500 (2016).

[55] J. I. Khan, M. A. Alamoudi, N. Chaturvedi, R. S. Ashraf, M. N. Nabi, A. Markina, W. Liu, T. A. Dela Peña, W. Zhang, O. Alévêque, G. T. Harrison, W. Alsufyani, E. Levillain, S. De Wolf, D. Andrienko, I. McCulloch, and F. Laquai, "Impact of Acceptor Quadrupole Moment on Charge Generation and Recombination in Blends of IDT-Based Non-Fullerene Acceptors with PCE10 as Donor Polymer," Advanced Energy Materials **11**, 2100839 (2021).

[56] M. Saladina, P. Simón Marqués, A. Markina, S. Karuthedath, C. Wöpke, C. Göhler, Y. Chen, M. Allain, P. Blanchard, C. Cabanetos, D. Andrienko, F. Laquai, J. Gorenflot, and C. Deibel, "Charge Photogeneration in Non-Fullerene Organic Solar Cells: Influence of Excess Energy and Electrostatic Interactions," Advanced Functional Materials **31**, 2007479 (2021).

[57] V. D. Mihailetchi, L. J. A. Koster, J. C. Hummelen, and P. W. M. Blom, "Photocurrent Generation in Polymer-Fullerene Bulk Heterojunctions," Physical Review Letters **93**, 216601 (2004).

[58] C. L. Braun, "Electric field assisted dissociation of charge transfer states as a mechanism of photocarrier production," The Journal of Chemical Physics **80**, 4157–4161 (1984).

[59] S. Sze and K. K. Ng, "Metal-Semiconductor Contacts," in *Physics of semiconductor devices*, 3rd ed. (Oct. 2006), pp. 134–196.

[60] V. D. Mihailetchi, H. Xie, B. de Boer, L. M. Popescu, J. C. Hummelen, P. W. M. Blom, and L. J. A. Koster, "Origin of the enhanced performance in poly(3-hexylthiophene): [6,6]-phenyl C61-butyric acid methyl ester solar cells upon slow drying of the active layer," Applied Physics Letters **89**, 012107 (2006).

[61] V. D. Mihailetchi, H. X. Xie, B. de Boer, L. J. A. Koster, and P. W. M. Blom, "Charge Transport and Photocurrent Generation in Poly(3-hexylthiophene): Methanofullerene Bulk-Heterojunction Solar Cells," Advanced Functional Materials **16**, 699–708 (2006).

[62] D. Liraz and N. Tessler, "Charge dissociation in organic solar cells—from Onsager and Frenkel to modern models," Chemical Physics Reviews **3**, 031305 (2022).

[63] Y. Liu, J. Zhang, G. Zhou, F. Liu, X. Zhu, and F. Zhang, "Electric Field Facilitating Hole Transfer in Non-Fullerene Organic Solar Cells with a Negative HOMO Offset," The Journal of Physical Chemistry C **124**, 15132–15139 (2020).

[64] A. Weu, T. R. Hopper, V. Lami, J. A. Kreß, A. A. Bakulin, and Y. Vaynzof, "Field-Assisted Exciton Dissociation in Highly Efficient PffBT4T-2OD:Fullerene Organic Solar Cells," `10.1021/acs.chemmater.8b00094` (2018).

[65] K. Nakano, Y. Chen, B. Xiao, W. Han, J. Huang, H. Yoshida, E. Zhou, and K. Tajima, "Anatomy of the energetic driving force for charge generation in organic solar cells," Nature Communications **10**, 2520 (2019).

[66] S. Karuthedath, J. Gorenflot, Y. Firdaus, N. Chaturvedi, C. S. P. D. Castro, G. T. Harrison, J. I. Khan, A. Markina, A. H. Balawi, T. Archie, D. Peña, W. Liu, R.-Z. Liang, A. Sharma, S. H. K. Paleti, W. Zhang, Y. Lin, E. Alarousu, D. H. Anjum, P. M. Beaujuge, S. D. Wolf, I. McCulloch, T. D. Anthopoulos, D. Baran, D. Andrienko, F. Laquai, C. S. P. De Castro, G. T. Harrison, J. I. Khan, A. Markina, A. H. Balawi, T. A. D. Peña, W. Liu, R.-Z. Liang, A. Sharma, S. H. K. Paleti, W. Zhang, Y. Lin, E. Alarousu, S. Lopatin, D. H. Anjum, P. M. Beaujuge, S. De Wolf, I. McCulloch, T. D. Anthopoulos, D. Baran, D.

Andrienko, and F. Laquai, "Intrinsic efficiency limits in low-bandgap non-fullerene acceptor organic solar cells," Nature Materials **20**, 378–384 (2021).

[67] M. Azzouzi, N. P. Gallop, F. Eisner, J. Yan, X. Zheng, H. Cha, Q. He, Z. Fei, M. Heeney, A. A. Bakulin, and J. Nelson, "Reconciling models of interfacial state kinetics and device performance in organic solar cells: impact of the energy offsets on the power conversion efficiency†," Energy and Environmental Science **15**, 1256–1270 (2022).

[68] O. J. Sandberg and A. Armin, "Energetics and Kinetics Requirements for Organic Solar Cells to Break the 20% Power Conversion Efficiency Barrier," The Journal of Physical Chemistry C **125**, 15590–15598 (2021).

[69] H. Bässler, "Charge Transport in Disordered Organic Photoconductors a Monte Carlo Simulation Study," physica status solidi (b) **175**, 15–56 (1993).

[70] D. Mendels and N. Tessler, "Thermoelectricity in Disordered Organic Semiconductors under the Premise of the Gaussian Disorder Model and Its Variants," The Journal of Physical Chemistry Letters **5**, 3247–3253 (2014).

[71] S. M. Hosseini, S. Wilken, B. Sun, F. Huang, S. Y. Jeong, H. Y. Woo, V. Coropceanu, and S. Shoaee, "Relationship between Energetic Disorder and Reduced Recombination of Free Carriers in Organic Solar Cells," Advanced Energy Materials **13**, 2203576 (2023).

[72] E. M. Conwell, "Impurity Band Conduction in Germanium and Silicon," Physical Review **103**, 51–61 (1956).

[73] N. F. Mott, "On the transition to metallic conduction in semiconductors," Canadian Journal of Physics **34**, 1356–1368 (1956).

[74] A. Miller and E. Abrahams, "Impurity Conduction at Low Concentrations," Physical Review **120**, 745–755 (1960).

[75] M. Kuik, G.-j. A. H. Wetzelaer, H. T. Nicolai, N. I. Craciun, D. M. De Leeuw, and P. W. M. Blom, "25th Anniversary Article: Charge Transport and Recombination in Polymer Light-Emitting Diodes," Advanced Materials **26**, 512–531 (2014).

[76] D. L. Huber, "Diffusion of optical excitation at finite temperatures," The Journal of Chemical Physics **78**, 2530–2532 (1983).

[77] U. Larsen, "Time scale of thermally activated diffusion in random systems: A new law of thermal activation," Physical Review B **32**, 1772–1777 (1985).

[78] Y. J. Chen and G. M. Carter, "Measurement of third order nonlinear susceptibilities by surface plasmons," Applied Physics Letters **41**, 307–309 (1982).

[79] P. N. Murgatroyd, "Theory of space-charge-limited current enhanced by Frenkel effect," Journal of Physics D: Applied Physics **3**, 308 (1970).

[80] W. F. F Pasveer, J. Cottaar, C. Tanase, R. Coehoorn, P. A. A Bobbert, P. W. M. W. M. Blom, D. M. de Leeuw, M. A. J. A. J. Michels, D. M. D. Leeuw, and M. A. J. A. J. Michels, "Unified Description of Charge-Carrier Mobilities in Disordered Semiconducting Polymers," Physical Review Letters **94**, 206601 (2005).

[81] A. Rahimi Chatri, S. Torabi, V. M. Le Corre, and L. J. A. Koster, "Impact of Electrodes on Recombination in Bulk Heterojunction Organic Solar Cells," ACS Applied Materials & Interfaces **10**, 12013–12020 (2018).

[82] J. Kurpiers and D. Neher, "Dispersive Non-Geminate Recombination in an Amorphous Polymer:Fullerene Blend," Scientific Reports **6**, 26832 (2016).

[83] L. Q. Phuong, S. M. Hosseini, O. J. Sandberg, Y. Zou, H. Y. Woo, D. Neher, and S. Shoaee, "Quantifying Quasi-Fermi Level Splitting and Open-Circuit Voltage Losses in Highly Efficient Nonfullerene Organic Solar Cells," Solar RRL **5**, 2000649 (2021).

[84] S. R. Cowan, W. L. Leong, N. Banerji, G. Dennler, and A. J. Heeger, "Identifying a threshold impurity level for organic solar cells: Enhanced first-order recombination via well-defined PC84BM traps in organic bulk heterojunction solar cells," Advanced Functional Materials **21**, 3083–3092 (2011).

[85] C. M. Proctor, M. Kuik, and T.-Q. Nguyen, "Charge carrier recombination in organic solar cells," Progress in Polymer Science **38**, 1941–1960 (2013).

[86] S. M. Hosseini, J. Kurpiers, Z. Chen, K. Zhang, F. Huang, A. Armin, D. Neher, and S. Shoaee, "Impact of Bimolecular Recombination on the Fill Factor of Fullerene and Nonfullerene-Based Solar Cells : A Comparative Study of Charge Generation and Extraction," 10.1021/acs.jpcc.8b11669 (2019).

[87] D. Bartesaghi, I. D. C. Pérez, J. Kniepert, S. Roland, M. Turbiez, D. Neher, and L. J. A. Koster, "Competition between recombination and extraction of free charges determines the fill factor of organic solar cells," Nature Communications **6**, 7083 (2015).

[88] N. Karl and G. Sommer, "Field Dependent Losses of Electrons and Holes by Bimolecular Volume Recombination in the Excitation Layer of Anthracene Single Crystals Studied by Drift Current Pulses," Physica Status Solidi (a) **6**, 231–241 (1971).

[89] T. M. Burke, S. Sweetnam, K. Vandewal, and M. D. Mcgehee, "Beyond Langevin Recombination : How Equilibrium Between Free Carriers and Charge Transfer States Determines the Open-Circuit Voltage of Organic Solar Cells," 1–12 (2015).

[90] O. J. Sandberg, *Charge collection in thin-film devices based on low-mobility semiconductors Charge collection in thin-film devices based on low-mobility semiconductors* ().

[91] S. Shoaee, M. Stolterfoht, and D. Neher, "The Role of Mobility on Charge Generation, Recombination, and Extraction in Polymer-Based Solar Cells," Advanced Energy Materials **8**, 1703355 (2018).

[92] S. Albrecht, W. Schindler, J. Kurpiers, J. Kniepert, J. C. Blakesley, I. Dumsch, S. Allard, K. Fostiropoulos, U. Scherf, and D. Neher, "On the Field Dependence of Free Charge Carrier Generation and Recombination in Blends of PCPDTBT/PC 70 BM: Influence of Solvent Additives," The Journal of Physical Chemistry Letters **3**, 640–645 (2012).

[93] L. J. Koster, V. D. Mihailetchi, and P. W. Blom, "Bimolecular recombination in polymer/fullerene bulk heterojunction solar cells," Applied Physics Letters **88**, 1–3 (2006).

[94] C. Groves and N. C. Greenham, "Bimolecular recombination in polymer electronic devices," Physical Review B **78**, 155205 (2008).

[95] M. C. Heiber, C. Baumbach, V. Dyakonov, and C. Deibel, "Encounter-Limited Charge-Carrier Recombination in Phase-Separated Organic Semiconductor Blends," Physical Review Letters **114**, 136602 (2015).

[96] L. J. A. Koster, E. C. P. Smits, V. D. Mihailetchi, and P. W. M. Blom, "Device model for the operation of polymer/fullerene bulk heterojunction solar cells," Physical Review B **72**, 085205 (2005).

[97] W. Tress, K. Leo, and M. Riede, "Optimum mobility, contact properties, and open-circuit voltage of organic solar cells: A drift-diffusion simulation study," Physical Review B **85**, 1–11 (2012).

[98] T. Fritsch, J. Kurpiers, S. Roland, N. Tokmoldin, S. Shoaee, T. Ferron, B. A. Collins, S. Janietz, K. Vandewal, and D. Neher, "On the Interplay between CT and Singlet Exciton Emission in Organic Solar Cells with Small Driving Force and Its Impact on Voltage Loss," Advanced Energy Materials **12**, 2200641 (2022).

[99] Y. Tamai, R. Shirouchi, T. Saito, K. Kohzuki, and S.-i. Natsuda, "Role of the energy offset in the charge photogeneration and voltage loss of nonfullerene acceptor-based organic solar cells," J. Mater. Chem. A, – (2023).

[100] M. Xie, Y. Shi, H. Zhang, J. Pan, J. Zhang, Z. Wei, and K. Lu, "Aryl-substituted-indanone end-capped nonfullerene acceptors for organic solar cells with a low nonradiative loss," Chemical Communications **58**, 4877–4880 (2022).

[101] W. Shockley and W. T. Read, "Statistics of the Recombinations of Holes and Electrons," Physical Review **87**, 835–842 (1952).

[102] P. Würfel, U. Würfel, Peter Würfell, Uli Würfel, P. Würfel, U. Würfel, Peter Würfell, and Uli Würfel, *Physics of Solar Cells - From Basic Principles to Advanced Concepts (3rd ed.)* 3rd Ed. (Wiley-VCH, 2016), p. 289.

[103] A. Hofacker and D. Neher, "Dispersive and steady-state recombination in organic disordered semiconductors," Physical Review B **96**, 10.1103/PhysRevB.96.245204 (2017).

[104] S. Dongaonkar, K. Y, D. Wang, M. Frei, S. Mahapatra, and M. A. Alam, "On the nature of shunt leakage in amorphous silicon p-i-n solar cells," IEEE Electron Device Letters **31**, 1266–1268 (2010).

[105] U. Würfel, D. Neher, A. Spies, S. Albrecht, U. Wu, D. Neher, A. Spies, and S. Albrecht, "Impact of charge transport on current–voltage characteristics and power-conversion efficiency of organic solar cells," Nature Communications **6**, 6951 (2015).

[106] J. D. Servaites, M. A. Ratner, and T. J. Marks, "Organic solar cells: A new look at traditional models," Energy & Environmental Science **4**, 4410 (2011).

[107] A. Cheknane, H. S. Hilal, F. Djeffal, B. Benyoucef, and J.-P. Charles, "An equivalent circuit approach to organic solar cell modelling," Microelectronics Journal **39**, 1173–1180 (2008).

[108] B. Mazhari, "An improved solar cell circuit model for organic solar cells," Solar Energy Materials and Solar Cells **90**, 1021–1033 (2006).

[109] A. Bou, A. Pockett, D. Raptis, T. Watson, M. J. Carnie, and J. Bisquert, "Beyond Impedance Spectroscopy of Perovskite Solar Cells: Insights from the Spectral Correlation of the Electrooptical Frequency Techniques," Journal of Physical Chemistry Letters **11**, 8654–8659 (2020).

[110] G. Grancini, M. Maiuri, D. Fazzi, A. Petrozza, H.-J. Egelhaaf, D. Brida, G. Cerullo, and G. Lanzani, "Hot exciton dissociation in polymer solar cells," Nature Materials **12**, 29–33 (2013).

[111] A. Armin, Y. Zhang, P. L. Burn, P. Meredith, A. Pivrikas, and E. Grancini, "Measuring internal quantum efficiency to demonstrate hot exciton dissociation," Nature Materials **12**, 593–593 (2013).

[112] A. Armin, M. Velusamy, P. Wolfer, Y. Zhang, P. L. Burn, P. Meredith, and A. Pivrikas, "Quantum Efficiency of Organic Solar Cells: Electro-Optical Cavity Considerations," ACS Photonics **1**, 173–181 (2014).

[113] A. Armin, N. Zarrabi, O. J. Sandberg, C. Kaiser, S. Zeiske, W. Li, and P. Meredith, "Limitations of Charge Transfer State Parameterization Using Photovoltaic External Quantum Efficiency," Advanced Energy Materials **10**, 2001828 (2020).

[114] M. Azzouzi, J. Yan, T. Kirchartz, K. Liu, J. Wang, H. Wu, and J. Nelson, "Nonradiative Energy Losses in Bulk-Heterojunction Organic Photovoltaics," Physical Review X **8**, 031055 (2018).

[115] J. Benduhn, K. Tvingstedt, F. Piersimoni, S. Ullbrich, Y. Fan, M. Tropiano, K. A. Mcgarry, O. Zeika, M. K. Riede, C. J. Douglas, S. Barlow, S. R. Marder, D. Neher, D. Spoltore, and K. Vandewal, "Intrinsic non-radiative voltage losses in fullerene-based organic solar cells," **17053**, 10.1038/nenergy.2017.53 (2017).

[116] R. Englman and J. Jortner, "The energy gap law for radiationless transitions in large molecules," Molecular Physics **18**, 145–164 (1970).

[117] X.-K. Chen, D. Qian, Y. Wang, T. Kirchartz, W. Tress, H. Yao, J. Yuan, M. Hülsbeck, M. Zhang, Y. Zou, Y. Sun, Y. Li, J. Hou, O. Inganäs, V. Coropceanu, J.-L. Bredas, and F. Gao, "A unified description of non-radiative voltage losses in organic solar cells," Nature Energy **6**, 799–806 (2021).

[118] D. Qian, Z. Zheng, H. Yao, W. Tress, T. R. Hopper, S. Chen, S. Li, J. Liu, S. Chen, J. Zhang, X. K. Liu, B. Gao, L. Ouyang, Y. Jin, G. Pozina, I. A. Buyanova, W. M. Chen, O. Inganäs, V. Coropceanu, J. L. Bredas, H. Yan, J. Hou, F. Zhang, A. A. Bakulin, and F. Gao, "Design rules for minimizing voltage losses in high-efficiency organic solar cells," Nature Materials **17**, 703–709 (2018).

[119] F. D. Eisner, M. Azzouzi, Z. Fei, X. Hou, T. D. Anthopoulos, T. J. S. Dennis, M. Heeney, and J. Nelson, "Hybridization of Local Exciton and Charge-Transfer States Reduces Nonradiative Voltage Losses in Organic Solar Cells," Journal of the American Chemical Society **141**, 6362–6374 (2019).

[120] D. Neher, J. Kniepert, A. Elimelech, and L. J. A. Koster, "A New Figure of Merit for Organic Solar Cells with Transport-limited Photocurrents," Scientific Reports **6**, 24861 (2016).

[121] B. Harbecke, "Coherent and incoherent reflection and transmission of multilayer structures," Applied Physics B Photophysics and Laser Chemistry **39**, 165–170 (1986).

[122] G. F. Burkhard, E. T. Hoke, and M. D. McGehee, "Accounting for Interference, Scattering, and Electrode Absorption to Make Accurate Internal Quantum Efficiency Measurements in Organic and Other Thin Solar Cells," Advanced Materials **22**, 3293–3297 (2010).

[123] A. Y. B. Meneau, Y. Olivier, T. Backlund, M. James, D. W. Breiby, J. W. Andreasen, and H. Sirringhaus, "Temperature Dependence of Charge Localization in High-Mobility, Solution-Crystallized Small Molecule Semiconductors Studied by Charge Modulation Spectroscopy," Advanced Functional Materials **26**, 2326–2333 (2016).

[124] "Interaction of light with matter," in *Semiconductor optics* (Springer Berlin Heidelberg, Berlin, Heidelberg, 2005), pp. 37–72.

[125] S. Roland, "Charge Carrier Recombination and Open Circuit Voltage in Organic Solar Cells: From Bilayer-Model Systems to Hybrid Multi-Junctions," PhD thesis (University of Potsdam, 2017).

[126] Y. Lin and X. Zhan, "Non-fullerene acceptors for organic photovoltaics: an emerging horizon," Materials Horizons **1**, 470–488 (2014).

[127] C. Yan, S. Barlow, Z. Wang, H. Yan, A. K.-Y. Jen, S. R. Marder, and X. Zhan, "Non-fullerene acceptors for organic solar cells," Nature Reviews Materials **3**, 18003 (2018).

[128] S. Yoon, E.-Y. Shin, N.-K. Cho, S. Park, H. Y. Woo, and H. J. Son, "Progress in morphology control from fullerene to nonfullerene acceptors for scalable high-performance organic photovoltaics," Journal of Materials Chemistry A **9**, 24729–24758 (2021).

[129] J. Bertrandie, J. Han, C. S. P. De Castro, E. Yengel, J. Gorenflot, T. Anthopoulos, F. Laquai, A. Sharma, and D. Baran, "The Energy Level Conundrum of Organic Semiconductors in Solar Cells," Advanced Materials **34**, 2202575 (2022).

[130] S. Shoaee, F. Deledalle, P. Shakya Tuladhar, R. Shivanna, S. Rajaram, K. S. Narayan, and J. R. Durrant, "A Comparison of Charge Separation Dynamics in Organic Blend Films Employing Fullerene and Perylene Diimide Electron Acceptors," The Journal of Physical Chemistry Letters **6**, 201–205 (2015).

[131] D. Neusser, B. Sun, W. L. Tan, L. Thomsen, T. Schultz, L. Perdigón-Toro, N. Koch, S. Shoaee, C. R. McNeill, D. Neher, and S. Ludwigs, "Spectroelectrochemically determined energy levels of PM6:Y6 blends and their relevance to solar cell performance," Journal of Materials Chemistry C **10**, 11565–11578 (2022).

[132] C. Yang, J. Zhang, N. Liang, H. Yao, Z. Wei, C. He, X. Yuan, and J. Hou, "Effects of energy-level offset between a donor and acceptor on the photovoltaic performance of non-fullerene organic solar cells," Journal of Materials Chemistry A **7**, 18889–18897 (2019).

[133] S. Li, L. Zhan, C. Sun, H. Zhu, G. Zhou, W. Yang, M. Shi, C. Z. Li, J. Hou, Y. Li, and H. Chen, "Highly Efficient Fullerene-Free Organic Solar Cells Operate at Near Zero Highest Occupied Molecular Orbital Offsets," J. Am. Chem. Soc. **141**, 3073–3082 (2019).

[134] D. Veldman, Ö. İpek, S. C. J. Meskers, J. Sweelssen, M. M. Koetse, S. C. Veenstra, J. M. Kroon, S. S. van Bavel, J. Loos, and R. A. J. Janssen, "Compositional and Electric Field Dependence of the Dissociation of Charge Transfer Excitons in Alternating Polyfluorene Copolymer/Fullerene Blends," Journal of the American Chemical Society **130**, 7721–7735 (2008).

[135] U. Würfel and M. Unmüssig, "Apparent Field-Dependence of the Charge Carrier Generation in Organic Solar Cells as a Result of (Bimolecular) Recombination," Solar RRL **2**, 1800229 (2018).

[136] J. Kniepert, I. Lange, N. J. van der Kaap, L. J. A. Koster, and D. Neher, "A Conclusive View on Charge Generation, Recombination, and Extraction in As-Prepared and Annealed P3HT:PCBM Blends: Combined Experimental and Simulation Work," Advanced Energy Materials **4**, 1301401 (2014).

[137] N. Felekidis, A. Melianas, and M. Kemerink, "Automated open-source software for charge transport analysis in single-carrier organic semiconductor diodes," Organic Electronics **61**, 318–328 (2018).

[138] E. Sağlamkaya, A. Musiienko, M. S. Shadabroo, B. Sun, S. Chandrabose, O. Shargaieva, G. Lo Gerfo M, N. F. van Hulst, and S. Shoaee, "What is special about Y6; the working mechanism of neat Y6 organic solar cells," Materials Horizons **10**, 1825–1834 (2023).

[139] T. Ferron, M. Pope, and B. A. Collins, "Spectral Analysis for Resonant Soft X-Ray Scattering Enables Measurement of Interfacial Width in 3D Organic Nanostructures," Physical Review Letters **119**, 167801 (2017).

[140] S. Mukherjee, C. M. Proctor, G. C. Bazan, T.-Q. Nguyen, and H. Ade, "Significance of Average Domain Purity and Mixed Domains on the Photovoltaic Performance of High-Efficiency Solution-Processed Small-Molecule BHJ Solar Cells," Advanced Energy Materials **5**, 1500877 (2015).

[141] S. Shoaee, A. Armin, M. Stolterfoht, S. M. Hosseini, J. Kurpiers, and D. Neher, "Decoding Charge Recombination through Charge Generation in Organic Solar Cells," Solar RRL **3**, 1900184 (2019).

[142] A. J. Gillett, A. Privitera, R. Dilmurat, A. Karki, D. Qian, A. Pershin, G. Londi, W. K. Myers, J. Lee, J. Yuan, M. K. Riede, F. Gao, G. C. Bazan, A. Rao, D. Beljonne, R. H. Friend, S. J. Ko, M. K. Riede, F. Gao, G. C. Bazan, A. Rao, T. Q. Nguyen, D. Beljonne, and R. H. Friend, "The role of charge recombination to triplet excitons in organic solar cells," Nature **597**, 666–671 (2021).

[143] S. Karuthedath, J. Gorenflot, A. Melianas, Z. Kan, M. Kemerink, and F. Laquai, "Buildup of Triplet-State Population in Operating TQ1:PC 71 BM Devices Does Not Limit Their Performance," The Journal of Physical Chemistry Letters **11**, 2838–2845 (2020).

[144] A. Armin, J. R. Durrant, and S. Shoaee, "Interplay Between Triplet-, Singlet-Charge Transfer States and Free Charge Carriers Defining Bimolecular Recombination Rate Constant of Organic Solar Cells," The Journal of Physical Chemistry C **121**, 13969–13976 (2017).

[145] T. M. Swager, "50th Anniversary Perspective : Conducting/Semiconducting Conjugated Polymers. A Personal Perspective on the Past and the Future," Macromolecules **50**, 4867–4886 (2017).

[146] O. Inganäs, "Organic Photovoltaics over Three Decades," Advanced Materials **30**, 1800388 (2018).

[147] S. Ludwigs, *P3HT Revisited – From Molecular Scale to Solar Cell Devices*, edited by S. Ludwigs, Vol. 265, Advances in Polymer Science (Springer Berlin Heidelberg, Berlin, Heidelberg, 2014).

[148] K. A. Mazzio and C. K. Luscombe, "The future of organic photovoltaics," Chemical Society Reviews **44**, 78–90 (2015).

[149] B. Kippelen and J.-L. Brédas, "Organic photovoltaics," Energy & Environmental Science **2**, 251 (2009).

[150] O. Doat, B. H. Barboza, A. Batagin-Neto, D. Bégué, and R. C. Hiorns, "Review: materials and modelling for organic photovoltaic devices," Polymer International **71**, 6–25 (2022).

[151] A. Facchetti, "π-Conjugated Polymers for Organic Electronics and Photovoltaic Cell Applications," Chemistry of Materials **23**, 733–758 (2011).

[152] J. Wu, Y. Meng, X. Guo, L. Zhu, F. Liu, and M. Zhang, "All-polymer solar cells based on a novel narrow-bandgap polymer acceptor with power conversion efficiency over 10%," Journal of Materials Chemistry A **7**, 16190–16196 (2019).

[153] K. Bruchlos, D. Trefz, A. Hamidi-Sakr, M. Brinkmann, J. Heinze, A. Ruff, and S. Ludwigs, "Poly(3-hexylthiophene) revisited – Influence of film deposition on the electrochemical behaviour and energy levels," Electrochimica Acta **269**, 299–311 (2018).

[154] M. Schwarze, W. Tress, B. Beyer, F. Gao, R. Scholz, C. Poelking, K. Ortstein, A. A. Günther, D. Kasemann, D. Andrienko, and K. Leo, "Band structure engineering in organic semiconductors," Science **352**, 1446–1449 (2016).

[155] L. Zhu, M. Zhang, W. Zhong, S. Leng, G. Zhou, Y. Zou, X. Su, H. Ding, P. Gu, F. Liu, and Y. Zhang, "Progress and prospects of the morphology of non-fullerene acceptor based high-efficiency organic solar cells," Energy & Environmental Science **14**, 4341–4357 (2021).

[156] A. Wadsworth, M. Moser, A. Marks, M. S. Little, N. Gasparini, C. J. Brabec, D. Baran, and I. McCulloch, "Critical review of the molecular design progress in non-fullerene electron acceptors towards commercially viable organic solar cells," Chemical Society Reviews **48**, 1596–1625 (2019).

[157] A. Distler, T. Sauermann, H.-J. Egelhaaf, S. Rodman, D. Waller, K.-S. Cheon, M. Lee, and D. M. Guldi, "The Effect of PCBM Dimerization on the Performance of Bulk Heterojunction Solar Cells," Advanced Energy Materials **4**, 1300693 (2014).

[158] G. Zhang, X.-K. Chen, J. Xiao, P. C. Y. Chow, M. Ren, G. Kupgan, X. Jiao, C. C. S. Chan, X. Du, R. Xia, Z. Chen, J. Yuan, Y. Zhang, S. Zhang, Y. Liu, Y. Zou, H. Yan, K. S. Wong, V. Coropceanu, N. Li, C. J. Brabec, J.-L. Bredas, H.-L. Yip, and Y. Cao, "Delocalization of exciton and electron wavefunction in non-fullerene acceptor molecules enables efficient organic solar cells," Nature Communications **11**, 3943 (2020).

[159] A. Mishra and P. Bäuerle, "Small Molecule Organic Semiconductors on the Move: Promises for Future Solar Energy Technology," Angewandte Chemie International Edition **51**, 2020–2067 (2012).

[160] J. Roncali, P. Leriche, and P. Blanchard, "Molecular Materials for Organic Photovoltaics: Small is Beautiful," Advanced Materials **26**, 3821–3838 (2014).

[161] C. Malacrida, A. H. Habibi, S. Gámez-Valenzuela, I. Lenko, P. S. Marqués, A. Labrunie, J. Grolleau, J. T. López Navarrete, M. C. Ruiz Delgado, C. Cabanetos, P. Blanchard, and S. Ludwigs, "Impact of the Replacement of a Triphenylamine by a Diphenylmethylamine Unit on the Electrochemical Behavior of Pentaerythritol-Based Push-Pull Tetramers," ChemElectroChem **6**, 4215–4228 (2019).

[162] Q. Wei, W. Liu, M. Leclerc, J. Yuan, H. Chen, and Y. Zou, "A-DA'D-A non-fullerene acceptors for high-performance organic solar cells," Science China Chemistry **63**, 1352–1366 (2020).

[163] K. Jiang, Q. Wei, J. Y. L. Lai, Z. Peng, H. K. Kim, J. Yuan, L. Ye, H. Ade, Y. Zou, and H. Yan, "Alkyl Chain Tuning of Small Molecule Acceptors for Efficient Organic Solar Cells," Joule **3**, 3020–3033 (2019).

[164] M. Zhang, X. Guo, W. Ma, H. Ade, and J. Hou, "A Large-Bandgap Conjugated Polymer for Versatile Photovoltaic Applications with High Performance," Advanced Materials **27**, 4655–4660 (2015).

[165] Q. Fan, T. Liu, W. Gao, Y. Xiao, J. Wu, W. Su, X. Guo, X. Lu, C. Yang, H. Yan, M. Zhang, and Y. Li, "Overcoming the energy loss in asymmetrical non-fullerene acceptor-based polymer solar cells by halogenation of polymer donors," Journal of Materials Chemistry A **7**, 15404–15410 (2019).

[166] X. Xu, L. Yu, H. Yan, R. Li, and Q. Peng, "Highly efficient non-fullerene organic solar cells enabled by a delayed processing method using a non-halogenated solvent," Energy & Environmental Science **13**, 4381–4388 (2020).

[167] E. J. W. Crossland, K. Tremel, F. Fischer, K. Rahimi, G. Reiter, U. Steiner, and S. Ludwigs, "Anisotropic Charge Transport in Spherulitic Poly(3-hexylthiophene) Films," Advanced Materials **24**, 839–844 (2012).

[168] D. Neusser, C. Malacrida, M. Kern, Y. M. Gross, J. van Slageren, and S. Ludwigs, "High Conductivities of Disordered P3HT Films by an Electrochemical Doping Strategy," Chemistry of Materials **32**, 6003–6013 (2020).

[169] R. Ma, G. Li, D. Li, T. Liu, Z. Luo, G. Zhang, M. Zhang, Z. Wang, S. Luo, T. Yang, F. Liu, H. Yan, and B. Tang, "Understanding the Effect of End Group Halogenation in Tuning Miscibility and Morphology of High-Performance Small Molecular Acceptors," Solar RRL **4**, 2000250 (2020).

[170] Q. Guo, Q. Guo, Y. Geng, A. Tang, M. Zhang, M. Du, X. Sun, and E. Zhou, "Recent advances in PM6:Y6-based organic solar cells," Materials Chemistry Frontiers **5**, 3257–3280 (2021).

[171] Z. Tu, G. Han, and Y. Yi, "Barrier-Free Charge Separation Enabled by Electronic Polarization in High-Efficiency Non-fullerene Organic Solar Cells," The Journal of Physical Chemistry Letters **11**, 2585–2591 (2020).

[172] J. Wu, J. Lee, Y.-C. Chin, H. Yao, H. Cha, J. Luke, J. Hou, J.-S. Kim, and J. R. Durrant, "Exceptionally low charge trapping enables highly efficient organic bulk heterojunction solar cells," Energy & Environmental Science **13**, 2422–2430 (2020).

[173] Y. Cui, Y. Xu, H. Yao, P. Bi, L. Hong, J. Zhang, Y. Zu, T. Zhang, J. Qin, J. Ren, Z. Chen, C. He, X. Hao, Z. Wei, and J. Hou, "Single-Junction Organic Photovoltaic Cell with 19% Efficiency," Advanced Materials **33**, 2102420 (2021).

[174] K. Chong, X. Xu, H. Meng, J. Xue, L. Yu, W. Ma, and Q. Peng, "Realizing 19.05% Efficiency Polymer Solar Cells by Progressively Improving Charge Extraction and Suppressing Charge Recombination," Advanced Materials **34**, 2109516 (2022).

[175] P. E. Shaw, A. Ruseckas, and I. D. W. Samuel, "Exciton Diffusion Measurements in Poly(3-hexylthiophene)," Advanced Materials **20**, 3516–3520 (2008).

[176] O. V. Mikhnenko, H. Azimi, M. Scharber, M. Morana, P. W. M. Blom, and M. A. Loi, "Exciton diffusion length in narrow bandgap polymers," Energy & Environmental Science **5**, 6960 (2012).

[177] M. C. Scharber, D. Mühlbacher, M. Koppe, P. Denk, C. Waldauf, A. J. Heeger, and C. J. Brabec, "Design Rules for Donors in Bulk-Heterojunction Solar Cells—Towards 10 % Energy-Conversion Efficiency," Advanced Materials **18**, 789–794 (2006).

[178] C. Deibel and V. Dyakonov, "Polymer–fullerene bulk heterojunction solar cells," Reports on Progress in Physics **73**, 096401 (2010).

[179] G. Zhou, M. Zhang, Z. Chen, J. Zhang, L. Zhan, S. Li, L. Zhu, Z. Wang, X. Zhu, H. Chen, L. Wang, F. Liu, and H. Zhu, "Marcus Hole Transfer Governs Charge Generation and Device Operation in Nonfullerene Organic Solar Cells," ACS Energy Letters **6**, 2971–2981 (2021).

[180] R. Jasiunas, H. Zhang, J. Yuan, X. Zhou, D. Qian, Y. Zou, A. Devižis, J. Šulskus, F. Gao, and V. Gulbinas, "From Generation to Extraction: A Time-Resolved Investigation of Photophysical Processes in Non-fullerene Organic Solar Cells," The Journal of Physical Chemistry C **124**, 21283–21292 (2020).

[181] X. Li, R. Ma, T. Liu, Y. Xiao, G. Chai, X. Lu, H. Yan, and Y. Li, "Fine-tuning HOMO energy levels between PM6 and PBDB-T polymer donors via ternary copolymerization," Science China Chemistry **63**, 1256–1261 (2020).

[182] H. Yan, Z. Chen, Y. Zheng, C. Newman, J. R. Quinn, F. Dötz, M. Kastler, and A. Facchetti, "A high-mobility electron-transporting polymer for printed transistors," Nature **457**, 679–686 (2009).

[183] D. Trefz, Y. M. Gross, C. Dingler, R. Tkachov, A. Hamidi-Sakr, A. Kiriy, C. R. McNeill, M. Brinkmann, and S. Ludwigs, "Tuning Orientational Order of Highly Aggregating P(NDI2OD-T 2) by Solvent Vapor Annealing and Blade Coating," Macromolecules **52**, 43–54 (2019).

[184] Y. M. Gross, D. Trefz, C. Dingler, D. Bauer, V. Vijayakumar, V. Untilova, L. Biniek, M. Brinkmann, and S. Ludwigs, "From Isotropic to Anisotropic Conductivities in P(NDI2OD-T 2) by (Electro-)Chemical Doping Strategies," Chemistry of Materials **31**, 3542–3555 (2019).

[185] H. Zhao, H. B. Naveed, B. Lin, X. Zhou, J. Yuan, K. Zhou, H. Wu, R. Guo, M. A. Scheel, A. Chumakov, S. V. Roth, Z. Tang, P. Müller-Buschbaum, and W. Ma, "Hot Hydrocarbon-Solvent Slot-Die Coating Enables High-Efficiency Organic Solar Cells with Temperature-Dependent Aggregation Behavior," Advanced Materials **32**, 2002302 (2020).

[186] H. Fu, W. Gao, Y. Li, F. Lin, X. Wu, J. H. Son, J. Luo, H. Y. Woo, Z. Zhu, and A. K. Jen, "A Generally Applicable Approach Using Sequential Deposition to Enable Highly Efficient Organic Solar Cells," Small Methods **4**, 2000687 (2020).

[187] Y. Qin, Y. Xu, Z. Peng, J. Hou, and H. Ade, "Low Temperature Aggregation Transitions in N3 and Y6 Acceptors Enable Double-Annealing Method That Yields Hierarchical Morphology and Superior Efficiency in Nonfullerene Organic Solar Cells," Advanced Functional Materials **30**, 2005011 (2020).

[188] Z. Wang, Z. Peng, Z. Xiao, D. Seyitliyev, K. Gundogdu, L. Ding, and H. Ade, "Thermodynamic Properties and Molecular Packing Explain Performance and Processing Procedures of Three D18:NFA Organic Solar Cells," Advanced Materials **32**, 2005386 (2020).

[189] W. Zhong, M. Zhang, G. Freychet, G. M. Su, L. Ying, F. Huang, Y. Cao, Y. Zhang, C. Wang, and F. Liu, "Decoupling Complex Multi-Length-Scale Morphology in Non-Fullerene Photovoltaics with Nitrogen K-Edge Resonant Soft X-ray Scattering," Adv. Mater. **34**, 2107316 (2022).

[190] J. Zhan, L. Wang, M. Zhang, L. Zhu, T. Hao, G. Zhou, Z. Zhou, J. Chen, W. Zhong, C. Qiu, S. Leng, Y. Zou, Z. Shi, H. Zhu, W. Feng, M. Zhang, Y. Li, Y. Zhang, and F. Liu, "Manipulating Crystallization Kinetics of Conjugated Polymers in Nonfullerene Photovoltaic Blends toward Refined Morphologies and Higher Performances," Macromolecules **54**, 4030–4041 (2021).

[191] S. Albrecht, K. Vandewal, J. R. Tumbleston, F. S. U. Fischer, J. D. Douglas, J. M. J. Fréchet, S. Ludwigs, H. Ade, A. Salleo, and D. Neher, "On the Efficiency of Charge Transfer State Splitting in Polymer:Fullerene Solar Cells," Advanced Materials **26**, 2533–2539 (2014).

[192] R. Ma, C. Yan, P. W.-K. Fong, J. Yu, H. Liu, J. Yin, J. Huang, X. Lu, H. Yan, and G. Li, "In situ and ex situ investigations on ternary strategy and co-solvent effects towards high-efficiency organic solar cells," Energy & Environmental Science **15**, 2479–2488 (2022).

[193] X. Jiang, P. Chotard, K. Luo, F. Eckmann, S. Tu, M. A. Reus, S. Yin, J. Reitenbach, C. L. Weindl, M. Schwartzkopf, S. V. Roth, and P. Müller-Buschbaum, "Revealing Donor–Acceptor Interaction on the Printed Active Layer Morphology and the Formation Kinetics for Nonfullerene Organic Solar Cells at Ambient Conditions," Advanced Energy Materials **12**, 2103977 (2022).

[194] M. Skompska and A. Szkurłat, "The influence of the structural defects and microscopic aggregation of poly(3-alkylthiophenes) on electrochemical and optical properties of the polymer films: discussion of an origin of redox peaks in the cyclic voltammograms," Electrochimica Acta **46**, 4007–4015 (2001).

[195] C. Enengl, S. Enengl, S. Pluczyk, M. Havlicek, M. Lapkowski, H. Neugebauer, and E. Ehrenfreund, "Doping-Induced Absorption Bands in P3HT: Polarons and Bipolarons," ChemPhysChem **17**, 3836–3844 (2016).

[196] J. Heinze, B. A. Frontana-Uribe, and S. Ludwigs, "Electrochemistry of Conducting Polymers—Persistent Models and New Concepts," Chemical Reviews **110**, 4724–4771 (2010).

[197] X. Li, Q. Zhang, J. Yu, Y. Xu, R. Zhang, C. Wang, H. Zhang, S. Fabiano, X. Liu, J. Hou, F. Gao, and M. Fahlman, "Mapping the energy level alignment at donor/acceptor interfaces in non-fullerene organic solar cells," Nature Communications **13**, 2046 (2022).

[198] P. Li, G. Ingram, J.-J. Lee, Y. Zhao, and Z.-H. Lu, "Energy disorder and energy level alignment between host and dopant in organic semiconductors," Communications Physics **2**, 2 (2019).

[199] Y. Nakayama, S. Kera, and N. Ueno, "Photoelectron spectroscopy on single crystals of organic semiconductors: experimental electronic band structure for optoelectronic properties," Journal of Materials Chemistry C **8**, 9090–9132 (2020).

[200] K. Ortstein, S. Hutsch, M. Hambsch, K. Tvingstedt, B. Wegner, J. Benduhn, J. Kublitski, M. Schwarze, S. Schellhammer, F. Talnack, A. Vogt, P. Bäuerle, N. Koch, S. C. B. Mannsfeld, H. Kleemann, F. Ortmann, and K. Leo, "Band gap engineering in blended organic semiconductor films based on dielectric interactions," Nature Materials **20**, 1407–1413 (2021).

[201] K. Ortstein, S. Hutsch, A. Hinderhofer, J. Vahland, M. Schwarze, S. Schellhammer, M. Hodas, T. Geiger, H. Kleemann, H. F. Bettinger, F. Schreiber, F. Ortmann, and K. Leo, "Energy Level Engineering in Organic Thin Films by Tailored Halogenation," Advanced Functional Materials **30**, 2002987 (2020).

[202] S. Duhm, G. Heimel, I. Salzmann, H. Glowatzki, R. L. Johnson, A. Vollmer, J. P. Rabe, and N. Koch, "Orientation-dependent ionization energies and interface dipoles in ordered molecular assemblies," Nature Materials **7**, 326–332 (2008).

[203] L. Zhu, J. Zhang, Y. Guo, C. Yang, Y. Yi, and Z. Wei, "Small Exciton Binding Energies Enabling Direct Charge Photogeneration Towards Low-Driving-Force Organic Solar Cells," Angewandte Chemie International Edition **60**, 15348–15353 (2021).

[204] M. B. Price, P. A. Hume, A. Ilina, I. Wagner, R. R. Tamming, K. E. Thorn, W. Jiao, A. Goldingay, P. J. Conaghan, G. Lakhwani, N. J. L. K. Davis, Y. Wang, P. Xue, H. Lu, K. Chen, X. Zhan, and J. M. Hodgkiss, "Free charge photogeneration in a single component high photovoltaic efficiency organic semiconductor," Nature Communications **13**, 2827 (2022).

[205] I. N. Hulea, H. B. Brom, A. J. Houtepen, D. Vanmaekelbergh, J. J. Kelly, and E. A. Meulenkamp, "Wide Energy-Window View on the Density of States and Hole Mobility in Poly(<math display="inline"> <mi>p</mi> </math> -Phenylene Vinylene)," Physical Review Letters **93**, 166601 (2004).

[206] T. Sueyoshi, H. Fukagawa, M. Ono, S. Kera, and N. Ueno, "Low-density band-gap states in pentacene thin films probed with ultrahigh-sensitivity ultraviolet photoelectron spectroscopy," Applied Physics Letters **95**, 10.1063/1.3258351 (2009).

[207] S. Athanasopoulos, H. Bässler, and A. Köhler, "Disorder vs Delocalization: Which Is More Advantageous for High-Efficiency Organic Solar Cells?" The Journal of Physical Chemistry Letters **10**, 7107–7112 (2019).

[208] U. Rau, "Reciprocity relation between photovoltaic quantum efficiency and electroluminescent emission of solar cells," Physical Review B **76**, 085303 (2007).

[209] Z. Tang, B. Liu, A. Melianas, J. Bergqvist, W. Tress, Q. Bao, D. Qian, O. Inganäs, and F. Zhang, "A New Fullerene-Free Bulk-Heterojunction System for Efficient High-Voltage and High-Fill Factor Solution-Processed Organic Photovoltaics," Advanced Materials **27**, 1900–1907 (2015).

[210] N. A. Ran, S. Roland, J. A. Love, V. Savikhin, C. J. Takacs, Y.-T. Fu, H. Li, V. Coropceanu, X. Liu, J.-L. Brédas, G. C. Bazan, M. F. Toney, D. Neher, and T.-Q. Nguyen, "Impact of interfacial molecular orientation on radiative recombination and charge generation efficiency," Nature Communications **8**, 79 (2017).

[211] X.-K. Chen, M. K. Ravva, H. Li, S. M. Ryno, and J.-L. Brédas, "Effect of Molecular Packing and Charge Delocalization on the Nonradiative Recombination of Charge-Transfer States in Organic Solar Cells," Advanced Energy Materials **6**, 1601325 (2016).

[212] Y. Wei, Z. Chen, G. Lu, N. Yu, C. Li, J. Gao, X. Gu, X. Hao, G. Lu, Z. Tang, J. Zhang, Z. Wei, X. Zhang, and H. Huang, "Binary Organic Solar Cells Breaking 19% via Manipulating the Vertical Component Distribution," Advanced Materials **34**, 10.1002/adma.202204718 (2022).

[213] W. Gao, F. Qi, Z. Peng, F. R. Lin, K. Jiang, C. Zhong, W. Kaminsky, Z. Guan, C. Lee, T. J. Marks, H. Ade, and A. K. Jen, "Achieving 19% Power Conversion Efficiency in Planar-Mixed Heterojunction Organic Solar Cells Using a Pseudosymmetric Electron Acceptor," Advanced Materials **34**, 2202089 (2022).

[214] M. A. Green, E. D. Dunlop, J. Hohl-Ebinger, M. Yoshita, N. Kopidakis, and X. Hao, "Solar cell efficiency tables (version 56)," Progress in Photovoltaics: Research and Applications **28**, 629–638 (2020).

[215] R. Wang, J. Yuan, R. Wang, G. Han, T. Huang, W. Huang, J. Xue, H. Wang, C. Zhang, C. Zhu, P. Cheng, D. Meng, Y. Yi, K. Wei, Y. Zou, and Y. Yang, "Rational Tuning of Molecular Interaction and Energy Level Alignment Enables High-Performance Organic Photovoltaics," Advanced Materials **31**, 1904215 (2019).

[216] T. F. Hinrichsen, C. C. S. Chan, C. Ma, D. Paleček, A. Gillett, S. Chen, X. Zou, G. Zhang, H.-L. Yip, K. S. Wong, R. H. Friend, H. Yan, A. Rao, and P. C. Y. Chow, "Long-lived and disorder-free charge transfer states enable endothermic charge separation in efficient non-fullerene organic solar cells," Nature Communications **11**, 5617 (2020).

[217] D. B. Riley, P. Meredith, A. Armin, and O. J. Sandberg, "Role of Exciton Diffusion and Lifetime in Organic Solar Cells with a Low Energy Offset," The Journal of Physical Chemistry Letters **13**, 4402–4409 (2022).

[218] X. Zhang, N. Yao, R. Wang, Y. Li, D. Zhang, G. Wu, J. Zhou, X. Li, H. Zhang, J. Zhang, Z. Wei, C. Zhang, H. Zhou, F. Zhang, and Y. Zhang, "On the understanding of energy loss and device fill factor trade-offs in non-fullerene organic solar cells with varied energy levels," Nano Energy **75**, 105032 (2020).

[219] A. Karki, J. Vollbrecht, A. J. Gillett, P. Selter, J. Lee, Z. Peng, N. Schopp, A. L. Dixon, M. Schrock, V. Nádaždy, F. Schauer, H. Ade, B. F. Chmelka, G. C. Bazan, R. H. Friend, and T. Nguyen, "Unifying Charge Generation, Recombination, and Extraction in Low-Offset Non-Fullerene Acceptor Organic Solar Cells," Advanced Energy Materials **10**, 2001203 (2020).

[220] R. Qin, D. Wang, G. Zhou, Z.-P. Yu, S. Li, Y. Li, Z.-X. Liu, H. Zhu, M. Shi, X. Lu, C.-Z. Li, and H. Chen, "Tuning terminal aromatics of electron acceptors to achieve high-efficiency organic solar cells," Journal of Materials Chemistry A **7**, 27632–27639 (2019).

[221] Q. Fan, Q. An, Y. Lin, Y. Xia, Q. Li, M. Zhang, W. Su, W. Peng, C. Zhang, F. Liu, L. Hou, W. Zhu, D. Yu, M. Xiao, E. Moons, F. Zhang, T. D. Anthopoulos, O. Inganäs, and E. Wang, "Over 14% efficiency all-polymer solar cells enabled by a low bandgap polymer acceptor with low energy loss and efficient charge separation," Energy & Environmental Science **13**, 5017–5027 (2020).

[222] J. Yuan, Y. Zhang, L. Zhou, C. Zhang, T. Lau, G. Zhang, X. Lu, H. Yip, S. K. So, S. Beaupré, M. Mainville, P. A. Johnson, M. Leclerc, H. Chen, H. Peng, Y. Li, and Y. Zou, "Fused Benzothiadiazole: A Building Block for n-Type Organic Acceptor to Achieve High-Performance Organic Solar Cells," Advanced Materials **31**, 1807577 (2019).

[223] C. Sun, S. Qin, R. Wang, S. Chen, F. Pan, B. Qiu, Z. Shang, L. Meng, C. Zhang, M. Xiao, C. Yang, and Y. Li, "High Efficiency Polymer Solar Cells with Efficient Hole Transfer at Zero Highest Occupied Molecular Orbital Offset between Methylated Polymer Donor and Brominated Acceptor," Journal of the American Chemical Society **142**, 1465–1474 (2020).

[224] C. M. Cardona, W. Li, A. E. Kaifer, D. Stockdale, and G. C. Bazan, "Electrochemical Considerations for Determining Absolute Frontier Orbital Energy Levels of Conjugated Polymers for Solar Cell Applications," Advanced Materials **23**, 2367–2371 (2011).

[225] J. Sworakowski, J. Lipiński, and K. Janus, "On the reliability of determination of energies of HOMO and LUMO levels in organic semiconductors from electrochemical measurements. A simple picture based on the electrostatic model," Organic Electronics **33**, 300–310 (2016).

[226] R. E. M. Willems, C. H. L. Weijtens, X. de Vries, R. Coehoorn, and R. A. J. Janssen, "Relating Frontier Orbital Energies from Voltammetry and Photoelectron Spectroscopy to the Open-Circuit Voltage of Organic Solar Cells," Advanced Energy Materials **9**, 1803677 (2019).

[227] B. A. Collins and E. Gann, "Resonant soft X-ray scattering in polymer science," Journal of Polymer Science **60**, 1199–1243 (2022).

[228] O. Alqahtani, M. Babics, J. Gorenflot, V. Savikhin, T. Ferron, A. H. Balawi, A. Paulke, Z. Kan, M. Pope, A. J. Clulow, J. Wolf, P. L. Burn, I. R. Gentle, D. Neher, M. F. Toney, F. Laquai, P. M. Beaujuge, and B. A. Collins, "Mixed Domains Enhance Charge Generation and Extraction in Bulk-Heterojunction Solar Cells with Small-Molecule Donors," Advanced Energy Materials **8**, 1702941 (2018).

[229] N. A. Ran, J. A. Love, M. C. Heiber, X. Jiao, M. P. Hughes, A. Karki, M. Wang, V. V. Brus, H. Wang, D. Neher, H. Ade, G. C. Bazan, and T. Nguyen, "Charge Generation and Recombination in an Organic Solar Cell with Low Energetic Offsets," Advanced Energy Materials **8**, 1701073 (2018).

[230] K. D. Rosenthal, M. P. Hughes, B. R. Luginbuhl, N. A. Ran, A. Karki, S. Ko, H. Hu, M. Wang, H. Ade, and T. Nguyen, "Quantifying and Understanding Voltage Losses Due to Nonradiative Recombination in Bulk Heterojunction Organic Solar Cells with Low Energetic Offsets," Advanced Energy Materials **9**, 1901077 (2019).

[231] B. A. Collins, Z. Li, J. R. Tumbleston, E. Gann, C. R. McNeill, and H. Ade, "Absolute Measurement of Domain Composition and Nanoscale Size Distribution Explains Performance in PTB7:PC 71 BM Solar Cells," Advanced Energy Materials **3**, 65–74 (2013).

[232] L. Ye, S. Li, X. Liu, S. Zhang, M. Ghasemi, Y. Xiong, J. Hou, and H. Ade, "Quenching to the Percolation Threshold in Organic Solar Cells," Joule **3**, 443–458 (2019).

[233] N. Yao, J. Wang, Z. Chen, Q. Bian, Y. Xia, R. Zhang, J. Zhang, L. Qin, H. Zhu, Y. Zhang, and F. Zhang, "Efficient Charge Transport Enables High Efficiency in Dilute Donor Organic Solar Cells," The Journal of Physical Chemistry Letters **12**, 5039–5044 (2021).

[234] Y. Wang, D. Qian, Y. Cui, H. Zhang, J. Hou, K. Vandewal, T. Kirchartz, and F. Gao, "Optical Gaps of Organic Solar Cells as a Reference for Comparing Voltage Losses," Advanced Energy Materials **8**, 1801352 (2018).

[235] B. Fan, P. Zhu, J. Xin, N. Li, L. Ying, W. Zhong, Z. Li, W. Ma, F. Huang, and Y. Cao, "High-Performance Thick-Film All-Polymer Solar Cells Created Via Ternary Blending of a Novel Wide-Bandgap Electron-Donating Copolymer," Advanced Energy Materials **8**, 1703085 (2018).

[236] L. Zhang, H. Zhao, B. Lin, J. Yuan, X. Xu, J. Wu, K. Zhou, X. Guo, M. Zhang, and W. Ma, "A blade-coated highly efficient thick active layer for non-fullerene organic solar cells," Journal of Materials Chemistry A **7**, 22265–22273 (2019).

[237] W. Li, K. H. Hendriks, W. S. Roelofs, Y. Kim, M. M. Wienk, and R. A. Janssen, "Efficient small bandgap polymer solar cells with high fill factors for 300 nm thick films," Advanced Materials **25**, 3182–3186 (2013).

[238] S. H. Park, I. S. Jin, H. Ahn, and J. W. Jung, "Non-halogenated additive engineering for morphology optimization in environmental-friendly solvent processed non-fullerene organic solar cells," Organic Electronics **86**, 105893 (2020).

[239] L. Zhan, S. Li, T. K. Lau, Y. Cui, X. Lu, M. Shi, C. Z. Li, H. Li, J. Hou, and H. Chen, "Over 17% efficiency ternary organic solar cells enabled by two non-fullerene acceptors working in an alloy-like model," Energy and Environmental Science **13**, 635–645 (2020).

[240] S. D. Dimitrov, Z. Huang, F. Deledalle, C. B. Nielsen, B. C. Schroeder, R. S. Ashraf, S. Shoaee, I. McCulloch, and J. R. Durrant, "Towards optimisation of photocurrent from fullerene excitons in organic solar cells," Energy and Environmental Science **7**, 1037–1043 (2014).

[241] S. Liang, S. Li, Y. Zhang, T. Li, H. Zhou, F. Jin, C. Sheng, G. Ni, J. Yuan, W. Ma, and H. Zhao, "Efficient Hole Transfer via Delocalized Excited State in Small Molecular Acceptor: A Comparative Study on Photodynamics of PM6:Y6 and PM6:ITIC Organic Photovoltaic Blends," Advanced Functional Materials **31**, 2102764 (2021).

[242] G. Grancini, D. Polli, D. Fazzi, J. Cabanillas-Gonzalez, G. Cerullo, and G. Lanzani, "Transient absorption imaging of P3HT:PCBM photovoltaic blend: Evidence for interfacial charge transfer state," Journal of Physical Chemistry Letters **2**, 1099–1105 (2011).

[243] H. Ohkita, S. Cook, Y. Astuti, W. Duffy, S. Tierney, W. Zhang, M. Heeney, I. McCulloch, J. Nelson, D. D. C. Bradley, and J. R. Durrant, "Charge Carrier Formation in Polythiophene/Fullerene Blend Films Studied by Transient Absorption Spectroscopy," Journal of the American Chemical Society **130**, 3030–3042 (2008).

[244] R. Wang, C. Zhang, Q. Li, Z. Zhang, X. Wang, and M. Xiao, "Charge Separation from an Intra-Moiety Intermediate State in the High-Performance PM6:Y6 Organic Photovoltaic Blend," Journal of the American Chemical Society **142**, 12751–12759 (2020).

[245] S. R. Scully and M. D. McGehee, "Effects of optical interference and energy transfer on exciton diffusion length measurements in organic semiconductors," Journal of Applied Physics **100**, 034907 (2006).

[246] C. Kaiser, S. Zeiske, P. Meredith, and A. Armin, "Determining Ultralow Absorption Coefficients of Organic Semiconductors from the Sub-Bandgap Photovoltaic External Quantum Efficiency," Advanced Optical Materials **8**, 1901542 (2020).

[247] A. Armin, A. Yazmaciyan, M. Hambsch, J. Li, P. L. Burn, and P. Meredith, "Electro-Optics of Conventional and Inverted Thick Junction Organic Solar Cells," ACS Photonics **2**, 1745–1754 (2015).

[248] H. T. Grahn, C. Thomsen, and J. Tauc, "Influence of interference on photoinduced changes in transmission and reflection," Optics Communications **58**, 226–230 (1986).

[249] H. P. Pasanen, P. Vivo, L. Canil, A. Abate, and N. Tkachenko, "Refractive index change dominates the transient absorption response of metal halide perovskite thin films in the near infrared," Physical Chemistry Chemical Physics **21**, 14663–14670 (2019).

[250] M. Kubinyi, R. Allott, A. Grofcsik, and W. J. Jones, "Elimination of interference effects from photoinduced-transmission decay curves of thin silicon films," Applied Optics **34**, 2949–2954 (1995).

[251] K.-E. Peiponen and E. M. Vartiainen, "Kramers-Kronig relations in optical data inversion," Physical Review B **44**, 8301–8303 (1991).

[252] S. D. Phillips, R. Worland, G. Yu, T. Hagler, R. Freedman, Y. Cao, V. Yoon, J. Chiang, W. C. Walker, and A. J. Heeger, "Electroabsorption of polyacetylene," Physical Review B **40**, 9751–9759 (1989).

[253] T. Liu, Y. Foo, J. A. Zapien, M. Li, and S. W. Tsang, "A generalized Stark effect electromodulation model for extracting excitonic properties in organic semiconductors," Nature Communications **10**, 5089 (2019).

[254] S. J. Martin, D. D. C. Bradley, P. A. Lane, H. Mellor, and P. L. Burn, "Linear and nonlinear optical properties of the conjugated polymers PPV and MEH-PPV," Physical Review B **59**, 15133–15142 (1999).

[255] K. Lee, E. K. Miller, N. S. Sariciftci, J. C. Hummelen, F. Wudl, and A. J. Heeger, "Photoinduced absorption and photoinduced reflectance in conducting polymer/methanofullerene films: Nonlinear-optical changes in the complex index of refraction," Physical Review B **54**, 10525–10529 (1996).

[256] R. R. Tamming, J. Butkus, M. B. Price, P. Vashishtha, S. K. K. Prasad, J. E. Halpert, K. Chen, and J. M. Hodgkiss, "Ultrafast Spectrally Resolved Photoinduced Complex Refractive Index Changes in CsPbBr 3 Perovskites," ACS Photonics **6**, 345–350 (2019).

[257] A. Karki, J. Vollbrecht, A. J. Gillett, S. S. Xiao, Y. Yang, Z. Peng, N. Schopp, A. L. Dixon, S. Yoon, M. Schrock, H. Ade, G. N. M. Reddy, R. H. Friend, and T.-Q. Nguyen, "The role of bulk and interfacial morphology in charge generation, recombination, and extraction in non-fullerene acceptor organic solar cells," Energy & Environmental Science **13**, 3679–3692 (2020).

[258] C. C. Katsidis and D. I. Siapkas, "General transfer-matrix method for optical multilayer systems with coherent, partially coherent, and incoherent interference," Applied Optics **41**, 3978–3987 (2002).

[259] R. Kerremans, C. Kaiser, W. Li, N. Zarrabi, P. Meredith, and A. Armin, "The Optical Constants of Solution-Processed Semiconductors—New Challenges with Perovskites and Non-Fullerene Acceptors," Advanced Optical Materials **8**, 2000319 (2020).

[260] D. Poelman and P. F. Smet, "Methods for the determination of the optical constants of thin films from single transmission measurements: a critical review," Journal of Physics D: Applied Physics **36**, 1850–1857 (2003).

[261] B. D. Viezbicke, S. Patel, B. E. Davis, and D. P. Birnie, "Evaluation of the Tauc method for optical absorption edge determination: ZnO thin films as a model system," physica status solidi (b) **252**, 1700–1710 (2015).

[262] E. A. Davis and N. F. Mott, "Conduction in non-crystalline systems V. Conductivity, optical absorption and photoconductivity in amorphous semiconductors," Philosophical Magazine **22**, 0903–0922 (1970).

[263] N. Schopp, V. V. Brus, J. Lee, G. C. Bazan, and T. Nguyen, "A Simple Approach for Unraveling Optoelectronic Processes in Organic Solar Cells under Short-Circuit Conditions," Advanced Energy Materials **11**, 2002760 (2021).

[264] R. Sun, Y. Wu, X. Yang, Y. Gao, Z. Chen, K. Li, J. Qiao, T. Wang, J. Guo, C. Liu, X. Hao, H. Zhu, and J. Min, "Single-Junction Organic Solar Cells with 19.17% Efficiency Enabled by Introducing One Asymmetric Guest Acceptor," Advanced Materials **34**, 2110147 (2022).

[265] R. Shivari and N. Banerji, "Photophysics and Charge Generation in Low Energy-offset Blends for Organic Solar Cells," CHIMIA **75**, 862 (2021).

[266] V. Coropceanu, X.-K. Chen, T. Wang, Z. Zheng, and J.-L. Brédas, "Charge-transfer electronic states in organic solar cells," Nature Reviews Materials **4**, 689–707 (2019).

[267] A. Hexemer, W. Bras, J. Glossinger, E. Schaible, E. Gann, R. Kirian, A. MacDowell, M. Church, B. Rude, and H. Padmore, "A SAXS/WAXS/GISAXS Beamline with Multilayer Monochromator," Journal of Physics: Conference Series **247**, 012007 (2010).

[268] E. Gann, A. T. Young, B. A. Collins, H. Yan, J. Nasiatka, H. A. Padmore, H. Ade, A. Hexemer, and C. Wang, "Soft x-ray scattering facility at the Advanced Light Source with real-time data processing and analysis," Review of Scientific Instruments **83**, 045110 (2012).

[269] E. Gann, T. Crofts, G. Holland, P. Beaucage, T. McAfee, R. J. Kline, B. A. Collins, C. R. McNeill, D. A. Fischer, and D. M. DeLongchamp, "A NIST facility for resonant soft x-ray scattering measuring nano-scale soft matter structure at NSLS-II," Journal of Physics: Condensed Matter **33**, 164001 (2021).

[270] A. L. D. Kilcoyne, T. Tyliszczak, W. F. Steele, S. Fakra, P. Hitchcock, K. Franck, E. Anderson, B. Harteneck, E. G. Rightor, G. E. Mitchell, A. P. Hitchcock, L. Yang, T. Warwick, and H. Ade, "Interferometer-controlled scanning transmission X-ray microscopes at the Advanced Light Source," Journal of Synchrotron Radiation **10**, 125–136 (2003).

[271] B. A. Collins and H. Ade, "Quantitative compositional analysis of organic thin films using transmission NEXAFS spectroscopy in an X-ray microscope," Journal of Electron Spectroscopy and Related Phenomena **185**, 119–128 (2012).

[272] S. Shoaee, S. Subramaniyan, H. Xin, C. Keiderling, P. S. Tuladhar, F. Jamieson, S. A. Jenekhe, and J. R. Durrant, "Charge Photogeneration for a Series of Thiazolo-Thiazole Donor Polymers Blended with the Fullerene Electron Acceptors PCBM and ICBA," Advanced Functional Materials **23**, 3286–3298 (2013).

[273] S.-i. Natsuda, T. Saito, R. Shirouchi, Y. Sakamoto, T. Takeyama, Y. Tamai, and H. Ohkita, "Cascaded energy landscape as a key driver for slow yet efficient charge separation with small energy offset in organic solar cells," Energy & Environmental Science **15**, 1545–1555 (2022).

[274] D. Kroh, F. Eller, K. Schötz, S. Wedler, L. Perdigón-Toro, G. Freychet, Q. Wei, M. Dörr, D. Jones, Y. Zou, E. M. Herzig, D. Neher, and A. Köhler, "Identifying the Signatures of Intermolecular Interactions in Blends of PM6 with Y6 and N4 Using Absorption Spectroscopy," Advanced Functional Materials **32**, 2205711 (2022).

[275] J. Gorenflot, M. C. Heiber, A. Baumann, J. Lorrmann, M. Gunz, A. Kämpgen, V. Dyakonov, and C. Deibel, "Nongeminate recombination in neat P3HT and P3HT:PCBM blend films," Journal of Applied Physics **115**, 144502 (2014).

[276] N. M. Kirby, S. T. Mudie, A. M. Hawley, D. J. Cookson, H. D. T. Mertens, N. Cowieson, and V. Samardzic-Boban, "A low-background-intensity focusing small-angle X-ray scattering undulator beamline," Journal of Applied Crystallography **46**, 1670–1680 (2013).

[277] J. Ilavsky, "Nika : software for two-dimensional data reduction," Journal of Applied Crystallography **45**, 324–328 (2012).

[278] B. C. C. Cowie, A. Tadich, L. Thomsen, R. Garrett, I. Gentle, K. Nugent, and S. Wilkins, "The Current Performance of the Wide Range (90–2500 eV) Soft X-ray Beamline at the Australian Synchrotron," in (2010), pp. 307–310.

[279] E. Gann, C. R. McNeill, A. Tadich, B. C. C. Cowie, and L. Thomsen, "Quick AS NEXAFS Tool (QANT): a program for NEXAFS loading and analysis developed at the Australian Synchrotron," Journal of Synchrotron Radiation **23**, 374–380 (2016).

[280] M. M. Nahid, E. Gann, L. Thomsen, and C. R. McNeill, "NEXAFS spectroscopy of conjugated polymers," European Polymer Journal **81**, 532–554 (2016).

[281] J. Wu, G. Li, J. Fang, X. Guo, L. Zhu, B. Guo, Y. Wang, G. Zhang, L. Arunagiri, F. Liu, H. Yan, M. Zhang, and Y. Li, "Random terpolymer based on thiophene-thiazolothiazole unit enabling efficient non-fullerene organic solar cells," Nature Communications **11**, 4612 (2020).

[282] W. Peng, Y. Lin, S. Y. Jeong, Z. Genene, A. Magomedov, H. Y. Woo, C. Chen, W. Wahyudi, Q. Tao, J. Deng, Y. Han, V. Getautis, W. Zhu, T. D. Anthopoulos, and E. Wang, "Over 18% ternary polymer solar cells enabled by a terpolymer as the third component," Nano Energy **92**, 106681 (2022).

[283] K. Li, Y. Wu, Y. Tang, M. Pan, W. Ma, H. Fu, C. Zhan, and J. Yao, "Ternary Blended Fullerene-Free Polymer Solar Cells with 16.5% Efficiency Enabled with a Higher-LUMO-Level Acceptor to Improve Film Morphology," Adv. Energy Mater. **9**, 1901728 (2019).

[284] M. Zhang, L. Zhu, G. Zhou, T. Hao, C. Qiu, Z. Zhao, Q. Hu, B. W. Larson, H. Zhu, Z. Ma, Z. Tang, W. Feng, Y. Zhang, T. P. Russell, and F. Liu, "Single-layered organic photovoltaics with double cascading charge transport pathways: 18% efficiencies," Nature Communications **12**, 309 (2021).

[285] S. Tu, L. Zhang, X. Lin, L. Xiao, W. Wang, and Q. Ling, "Modifying polymer PM6 by incorporating a third component for an enhanced short-circuit current density," J. Mater. Chem. C **10**, 2026–2033 (2022).

[286] L. A. A. Pettersson, L. S. Roman, and O. Inganäs, "Modeling photocurrent action spectra of photovoltaic devices based on organic thin films," J. Appl. Phys. **86**, 487–496 (1999).

[287] P. Peumans, A. Yakimov, and S. R. Forrest, "Small molecular weight organic thin-film photodetectors and solar cells," J. Appl. Phys. **93**, 3693–3723 (2003).

Publication List

1. M. Pranav, T. Hultzsch, A. Musiienko, **B. Sun**, A. Shukla, F. Jaiser, S. Shoaee, and D. Neher, "Anticorrelated Photoluminescence and Free Charge Generation Proves Field-Assisted Exciton Dissociation in Low-Offset PM6:Y5 Organic Solar Cells," APL Materials 11, 061111 (2023)
2. **B. Sun**, N. Tokmoldin, O. Alqahtani, A. Patterson, C. S. P. De Castro, D. B. Riley, M. Pranav, A. Armin, F. Laquai, B. A. Collins, D. Neher, and S. Shoaee, "Toward More Efficient Organic Solar Cells: A Detailed Study of Loss Pathway and Its Impact on Overall Device Performance in Low-Offset Organic Solar Cells," Advanced Energy Materials, 2300980 (2023).
3. N. Tokmoldin, **B. Sun**, F. Moruzzi, A. Patterson, O. Alqahtani, R. Wang, B. A. Collins, I. McCulloch, L. Lüer, C. J. Brabec, D. Neher, and S. Shoaee, "Elucidating How Low Energy Offset Matters to Performance of Nonfullerene Acceptor-Based Solar Cells," ACS Energy Letters 8, 2552–2560 (2023).
4. M. Raoufi, S. Rühl, S. Chandrabose, A. Shukla, **B. Sun**, E. Kratochvil, S. Blumstengel, and D. Neher (2023), Fast Photoresponse from Hybrid Monolayer MoS2/Organic Photodetector. Physica Status Solidi (a) 2300107.
5. E. Sağlamkaya, A. Musiienko, M. S. Shadabroo, **B. Sun**, S. Chandrabose, O. Shargaieva, G. Lo Gerfo M, N. F. van Hulst, and S. Shoaee, "What is special about Y6; the working mechanism of neat Y6 organic solar cells," Materials Horizons 10, 1825–1834 (2023).
6. M. Raoufi, S. Chandrabose, R. Wang, **B. Sun**, N. Zorn Morales, S. Shoaee, S. Blumstengel, N. Koch, E. List-Kratochvil, and D. Neher, "Influence of the Energy Level Alignment on Charge Transfer and Recombination at the Monolayer-MoS 2 /Organic Hybrid Interface," The Journal of Physical Chemistry C 127, 5866–5875 (2023).
7. S. M. Hosseini, S. Wilken, **B. Sun**, F. Huang, S. Y. Jeong, H. Y. Woo, V. Coropceanu, and S. Shoaee, "Relationship between Energetic Disorder and Reduced Recombination of Free Carriers in Organic Solar Cells," Advanced Energy Materials 13, 2203576 (2023).
8. F. Ye, S. Zhang, J. Warby, J. Wu, E. G.-Partida, F. Lang, S. Shah, E. Sağlamkaya, **B. Sun**, F.-S. Zu, S. Shoaee, H. Wang, B. Stiller, D. Neher, W.-H. Zhu, M. Stolterfoht, and Y. Wu, "Overcoming C60-induced interfacial recombination in inverted perovskite solar cells by electron-transporting carborane," Nature Communications 13, 7454 (2022).
9. D. Neusser, **B. Sun**, W. L. Tan, L. Thomsen, T. Schultz, L. Perdigón-Toro, N. Koch, S. Shoaee, C. R. McNeill, D. Neher, and S. Ludwigs, "Spectroelectrochemically determined energy levels of PM6:Y6 blends and their relevance to solar cell performance," Journal of Materials Chemistry C 10, 11565–11578 (2022).

10. J. Vollbrecht, N. Tokmoldin, **B. Sun**, V. V. Brus, S. Shoaee, and D. Neher, "Determination of the charge carrier density in organic solar cells: A tutorial," Journal of Applied Physics 131, 221101 (2022).

11. **B. Sun**, O. J. Sandberg, D. Neher, A. Armin, and S. Shoaee, "Wave Optics of Differential Absorption Spectroscopy in Thick-Junction Organic Solar Cells: Optical Artifacts and Correction Strategies," Physical Review Applied 17, 054016 (2022).

12. J. Marin-Beloqui, G. Zhang, J. Guo, J. Shaikh, T. Wohrer, S. M. Hosseini, **B. Sun**, J. Shipp, A. J. Auty, D. Chekulaev, J. Ye, Y.-C. Chin, M. B. Sullivan, A. J. Mozer, J.-S. Kim, S. Shoaee, and T. M. Clarke, "Insight into the Origin of Trapping in Polymer/Fullerene Blends with a Systematic Alteration of the Fullerene to Higher Adducts," The Journal of Physical Chemistry C 126, 2708–2719 (2022).

13. N. Tokmoldin, J. Vollbrecht, S. M. Hosseini, **B. Sun**, L. Perdigón-Toro, H. Y. Woo, Y. Zou, D. Neher, and S. Shoaee, "Explaining the Fill-Factor and Photocurrent Losses of Nonfullerene Acceptor-Based Solar Cells by Probing the Long-Range Charge Carrier Diffusion and Drift Lengths," Advanced Energy Materials 11, 2100804 (2021).

日月出矣，而爝火不息

— <庄子·逍遥游>

Acknowledgments

Nearly four years of my life have been consumed by the captivating odyssey of a PhD, a cherished voyage that I hold in the highest regard. On this rainy night, amidst the rumble of thunder in the sky, I am sitting before the luminous glow of my computer screen, filled with a profound sense of happiness and a tapestry of intricate emotions. As I type this long-awaited chapter, I cannot help but reflect on the decision I made four years ago, a decision that has led me to this moment. I am keenly aware that without the support and assistance of many, I would not have arrived here. This thesis belongs not only to me but also to them.

I would like to send my sincere gratitude to my supervisor Prof. Dr. Safa Shoaee, who took me immediately at the very moment I applied to go for PhD and keeps giving me so much patience and trust to work on my studies in all these years ever since. I extend my deep appreciation to my second supervisor Prof. Dr. Dieter Neher for engaging in countless discussions, suggestions, and offering continuous support.

I am immensely grateful to all of my collaborators, I would not have made it to finish this thesis without your support. I would like to give special thanks to Prof. Dr. Ardalan Armin who provided valuable suggestions for my first publication, which holds significant meaning to me.

Thanks very much to Prof. Dr. Jan Anton Koster for agreeing to review my thesis.

I extend my heartfelt thanks to our dedicated technician and administration team, Frank Jaiser, Thomas Hultzsch, Andreas Pucher, Burkhard Stiller, Florian Dornack, and Elke Derlig. The lab would not have run so smoothly without the exceptional effort from you.

I owe my thanks to my brilliant colleagues in our joint research group of "Optoelectronics of Disordered Semiconductors", "Soft Matter Physics and Optoelectronics", "PotsdamPero" and "ROSI". I am particularly grateful to Mehrdad who trained me for my very first solar cell, and Phuong who gave me the very first PIA training. Thanks to Lorena who is always willing to help and provide her great knowledge. Thanks to Vincent who offer so much help and guidance to me in simulations. I am also thankful to Guangzheng for all his important advice at the early stage of my PhD, and Nurlan for so many discussions and experience sharing that we had. Thanks to Manasi for sharing so many wise thoughts and advice, both personally and professionally. And thanks a lot to Fangyuan, Pacho, and Meysam, for expanding my perspective on solar cell research from organics solar cells to perovskites, transistors, 2-D materials and so on, through so many valuable discussions and sharing of lab experiences. I would like to thank Elifnaz, Joachim, Atul, Jonas, Emilio, Thorben, Felix, Martin, Max, Jarla, Jonny, Christian, Sahil, Guorui, Sema, Yonglin, Sercan, Biruk, Julian... for all the good time that we spend together, the chance

to work with you outstanding people has consistently motivated me in my research endeavors.

Special thanks to Manasi, Atul, and Thorben for helping me proof-read this thesis.

I deeply thank all my friends in Germany - Abu, Ming-Hsuan, Nishant, Mehray, Lisa, Désirée, Seif, Haimeng, Xiaoxuan, Vivien, Dan, and others - for enriching my life and creating all those cherished memories. Interacting with each of you has provided me with a broader perspective on life. Special thanks to Abu for being my best hiking and barbecue companion, I had pretty much learned most of the philosophies about PhD in those hikes. And to Ming-Hsuan for keep offering life suggestions whenever I feel confused. Thanks to Nishant for being my wonderful friend and flatmate at the same time...

I would like to convey my special thanks to Yue, meeting you is one of the greatest things happened in my life. Thank you so much for filling up the tenderest part of my heart and constantly reminding me how fortunate I am. However far away, we have always closely connected to each other.

Finally, I would like to express my deepest gratitude to my parents for their unwavering support and immense pride in me throughout the past 29 years of my life. Your constant encouragement means the world to me, and I am equally proud of you.

Declaration

I declare that this thesis is composed of my original work and does not contain material previously published or written by another person other than those mentioned or referenced. I have fully reference all text directly or indirectly quoted from a source. The contribution from co-authors in this work has been clarified. This thesis was not submitted to another university.

Potsdam, Germany, December 20, 2023

Bowen Sun